From Ink to CCM: Interplay of Process Influences in Ink Processing, Membrane Direct Coating, and Drying in Fuel Cell Manufacturing

Zur Erlangung des akademischen Grades eines

DOKTORS DER INGENIEURWISSENSCHAFTEN

von der KIT-Fakultät für Chemieingenieurwesen und Verfahrenstechnik des Karlsruher Instituts für Technologie (KIT)
genehmigte

DISSERTATION

von

Philipp Quarz

Tag der mündlichen Prüfung: 20.04.2026

Erstgutachter: Prof. Dr.-Ing. Dr. h. c. Wilhelm Schabel

Zweitgutachter: Prof. Dr. rer. nat. Norbert Willenbacher

This document is licensed under a Creative Commons
Attribution 4.0 International License (CC BY 4.0):
https://creativecommons.org/licenses/by/4.0/deed.en
Excluded from this license are chapter 6.2 and parts of chapter 9.5, which are marked with a footnote in the text. They contain material reprinted under author rights from Taylor & Francis, originally published under CC BY-NC 4.0.

For my family, with love and gratitude

"The whole is greater than the sum of its parts." – Aristotle

Kurzfassung

Brennstoffzellen sind eine vielversprechendes System im angestrebten Energiewandel. Für eine breite Markteinführung müssen die Systeme jedoch günstiger und hinsichtlich Performance und Langlebigkeit weiter verbessert werden. Herzstück der breit einsetzbaren Polymer-Elektrolyt-Membran Brennstoffzelle (PEMFC) ist die beidseitig Katalysator-beschichtete Membran (CCM, engl.: *catalyst-coated membrane*). Hier finden im Betrieb die elektrochemischen Reaktionen sowie der entscheidende Stofftransport der Reaktanten statt. An der CCM lassen sich die Kosten und Leistungsparameter des Gesamtsystems optimieren. Diese Eigenschaften werden durch die CCM-Herstellung beeinflusst. Im Herstellungsprozess liegt daher ein großer Hebel zur Kosteneinsparung und Leistungs- sowie Lebensdauererhöhung der CCM und damit der gesamten Brennstoffzelle. Dafür notwendig sind ein besseres Verständnis des Herstellungsprozesses und eine systematische Untersuchung der zugrundeliegenden Effekte.

Die vorliegende Arbeit beschäftigt sich mit der Herstellung von CCM für PEMFC und leistet einen Beitrag zu den oben benannten Zielen sowie zu einem besseren Prozessverständnis. Konkret wird die Herstellung von *Pt/C*-basierten Katalysatortinten und ihre Applikation auf die protonenleitende Membran erforscht. Dabei werden drei zentrale Aspekte der CCM-Produktion untersucht: die Formulierung und Herstellung der Katalysatortinte, die Herausforderungen bei der Membrandirektbeschichtung (MDC) sowie die Trocknung der Lösemittel aus der sich bilden Katalysatorschichten der CCM.

Die Katalysatortinte besteht aus Katalysatorpartikeln, Ionomer (einem ionisch leitenden Polymer), und mehreren Lösemitteln sowie ggfs. weiteren Additiven. Häufig in der Literatur und auch in der vorliegenden Arbeit wird das Lösemittelsystem 1-Propanol-Wasser verwendet. Während die Tintenformulierung oft Gegenstand wissenschaftlicher Untersuchungen ist, gilt dies bislang nur bedingt für die Tintenprozessierung. Die Katalysatorpartikel liegen im Ausgangsmaterial als

agglomeriertes Pulver vor und müssen aufgebrochen und mit den anderen Tintenkomponenten vermischt werden. In der vorliegenden Arbeit wird der Einfluss verschiedener Prozessparameter (Mahldauer und Drehzahl) bei der Tintenherstellung in einer Kugelmühle systematisch untersucht. In den durchgeführten Experimenten zeigt sich, dass die Belastungszahl (*SN*, von engl.: *Stress Number*), in die Mahldauer und Drehzahl einfließen, die Prozessfunktion für die Partikelgrößenverteilung (PGV) einer Tinte darstellt.

Aus den Katalysatortinten werden durch Beschichtung der Membran und anschließende Trocknung Katalysatorschichten hergestellt. Die PGV der Tinten bestimmt wesentlich die Schichteigenschaften wie die Porendurchmesser-Verteilung und die Qualität der aus ihr hergestellten Schicht. Die Qualität einer Schicht wird anhand der in der fertigen Elektrode auftretenden Risse bewertet. Elektrochemische Tests sind kein Teil der Untersuchungen dieser Arbeit. Es zeigt sich, dass die PGV die Verknüpfung zwischen Tintenprozessierung und Schichteigenschaften bildet. Ähnliche PGV, egal wie genau erzeugt, führen zu ähnlichen Schichteigenschaften (Porendurchmesser und Risse). Es konnte eine optimale Mahldauer bzw. PGV für möglichst Riss-arme Schichten experimentell identifiziert werden. Durch das Mahlen werden große Partikelagglomerate in der Tinte aufgebrochen, die oftmals Ausgangspunkt für Risse in den trocknenden Schichten sind. Mit zu vielen kleinen Partikeln wird jedoch ein ausgeprägtes Rissnetzwerk beobachtet. Als Erklärung wird die Verteilung des Ionomers in der Tinte und der daraus entstehenden Schicht diskutiert. Unterschieden wird an die Partikeloberfläche gebundenes Ionomer und freies Ionomer. Tinten mit unterschiedlicher PGV haben unterschiedliche für das Ionomer zugängliche Partikeloberflächen, was dessen Verteilung beeinflusst. Freies Ionomer benetzt während des Mahlprozesses neu gebildete Partikeloberflächen, welche dadurch stabilisiert werden. Eine ausreichende Versorgung der Partikel mit gebundenem Ionomer und weiteres noch verfügbares freies Ionomer kompensiert bei der Filmverfestigung im Tintentrocknungsschritt auftretende Spannungen und reduziert so die Rissentstehung. Ist die erzeugte Partikeloberfläche zu groß, reicht das vorhandene Ionomer nicht mehr aus, die Partikel ausreichend zu stabilisieren. Der höhere Bedarf an Ionomer bei kleinen PGV (mehr kleine Partikel) kann durch einen höheren Ionomeranteil bei der Tintenformulierung kompensiert werden. Es wird erstmals geschlussfolgert,

dass der in der Tintenformulierung eingestellte Ionomeranteil (in Form des Ionomer zu Kohlenstoff Verhältnisses (*I/C*)) und die Tintenprozessierung zusammen betrachtet und aufeinander abgestimmt werden müssen, um rissfreie Schichten herzustellen.

Die Arbeit beforscht die Membrandirektbeschichtung. Diese herausfordernde Prozessroute birgt diverse Vorteile im Brennstoffzellenbetrieb, wie etwa die Reduzierung der Kontaktwiderstände. Darüber hinaus wird im Vergleich zum etablierten CCM-Herstellungsweg, dem Decal-Prozess, ein Prozessschritt eliminiert und das Material der Decal-Folie eingespart. Die größte Herausforderung ist das Quellen der Membran durch den Kontakt mit den Tintenlösemitteln. Dies hat Auswirkungen auf die Membranhandhabung und die Rissbildung in der applizierten Katalysatorschicht. Bislang wird häufig sprühbeschichtet. Für das Scale-up ist die Rolle-zu-Rolle-Beschichtung und dabei die Schlitzdüsenbeschichtung potentiell vielversprechend. Hierbei wird die Tinte in einem (mehrere) hundert Mikrometer dicken Nassfilm aufgetragen. Die Lösemittelexposition der Membran ist hoch und besonders herausfordernd. Der Nassfilmauftrag wird in der vorliegenden Arbeit mittels Rakel-Beschichtung durchgeführt. Diese Beschichtungsmethode eignet sich gut, um die grundlegenden Effekte bei der Schlitzdüsenbeschichtung nachzubilden und ermöglicht gleichzeitig eine größere Probenvariation mit kleineren Probenvolumina (weniger Totvolumen) und kürzeren Reinigungszeiten.

Starke Quellung der Membran wird insbesondere bei Kontakt mit 1-Propanol beobachtet. Es zeigt sich, dass sich die Membran ohne Einschränkung durch eine stützende Schutzfolie oder Befestigung auf einer Beschichtungsplatte stärker verformt. Diese Verformung ist bei der anschließenden Trocknung und Schrumpfung der Membran reversibel. Es wurde beobachtet, dass bei fehlender Fixierung der Membran während der Trocknung weniger Risse in der Katalysatorschicht entstehen als bei fixierter Membran. Dies wird damit erklärt, dass durch die Fixierung der Membran Spannungen in der quellenden und schrumpfenden Membran entstehen, die in die darüberliegende Schicht induziert werden und so die Rissentstehung fördern. Ohne Fixierung treten diese Spannungen nicht auf.

Die Katalysatortinten bestehen aus mehreren Lösemitteln. Nach dem Tintenauftrag auf die Membran, bei der anschließenden Trocknung kann es zur bevorzugten

Entfernung eins Lösemittels gegenüber des/der anderen Lösemittel kommen. Dies führt zu einer kontinuierlichen Veränderung der Lösemittelzusammensetzung im Prozess. Dies beeinflusst wiederum die Eigenschaften (Konformation, Agglomeration, etc.) des Ionomers, der Partikel und ihrer Wechselwirkungen in der sich bildenden Schicht sowie letztendlich auch der Schicht selbst, beispielsweise in Form von auftretenden Rissen. Es werden zwei unterschiedliche Phänomene beobachtet: selektive Trocknung und selektive Lösemittelaufnahme der Membran durch Quellung. Beide Effekte werden diskutiert.

Grundlage der Untersuchungen ist das Lösemittelsystem 1-Propanol-Wasser. 1-Propanol und Wasser weisen ähnliche Siedetemperaturen auf und die Dampfdruckkurven weichen nur wenig voneinander ab. Darüber hinaus wechselwirken die beiden Lösemittel in einem Gemisch stark miteinander und bilden ein Azeotrop. Am Azeotrop haben die Flüssig- und die Gasphase die gleiche Zusammensetzung. Es wird experimentell gezeigt und theoretisch begründet, dass das Azeotrop bei der Filmtrocknung jedoch nicht die unselektiv, d.h. ohne Veränderung der Lösemittelzusammensetzung trocknende, Zusammensetzung vollständig beschreibt. Stattdessen verschiebt sich die unselektiv trocknende Zusammensetzung hin zum dynamischen Azeotrop, dem sogenannten Arheotrop. Die Stofftransportkinetik der Lösemittel in die Luft beeinflusst maßgeblich die Selektivität der Trocknung. Experimentell und auf analytischen Überlegungen aufbauend gefundene Einflussfaktoren sind die initiale Lösemittelzusammensetzung, die Temperatur und die Interaktionsdauer der Flüssigphase und der Trocknungsluft, ausgedrückt im Verhältnis des Verdunstungsstroms zum Stoffstrom der Trocknungsluft. Einen großen Einfluss hat die Vorbeladung der Trocknungsluft mit Lösemittel, hier im Fall von Wasser als relative Luftfeuchte gezeigt. Die gefundenen Einflussgrößen und Faktoren verdeutlichen die Bedeutung genauer Kenntnisse der Trocknungsbedingungen für die Herstellung gewünschter, reproduzierbarer Schichten. Sie sind gleichzeitig Herausforderung und Chance zur gezielten Prozessbeeinflussung.

Es werden Überströmungsexperimente durchgeführt und die Lösemittelzusammensetzung während der Trocknung zunächst über die Gemischdichte und später in-situ während der Trocknung ortsaufgelöst im Film mit der inversen Mikro

Raman Spektroskopie (IMRS) bestimmt. Dabei wird erstmals die IMRS auf die Trocknung eines Lösemittelgemischs, bei der alle Komponenten verdunsten, angewendet. Dies funktioniert mit hoher quantitativer Genauigkeit und kann zukünftig auch auf andere Stoffsysteme und Fragestellungen angewendet werden. Je nach bevorzugt verdunstender Komponente werden unterschiedliche Auswirkungen auf die Ausbildung von Konzentrationsgradienten im Lösemittelgemisch beobachtet.

Die einzelnen Schritte der CCM-Herstellung – Tintenprozessierung, Membrandirektbeschichtung (MDC) und Filmtrocknung – werden vorwiegend separat untersucht und analysiert. Dabei werden diverse Effekte und Einflussgrößen besser verstanden. Es zeigt sich jedoch auch, dass die verschiedenen Effekte in den einzelnen Prozessschritten miteinander verschränkt sind und sich gegenseitig beeinflussen. So beeinflusst die in der Tintenprozessierung eingestellte Partikelgrößenverteilung die Verteilung des Ionomers in Tinte und Schicht. Die Modifikation des Ionomers hängt auch von der Lösemittelzusammensetzung ab. Die Lösemittelzusammensetzung verändert sich nach der Beschichtung durch selektive Trocknung und Lösemittelaufnahme der Membran. Beide sind wiederum von der aktuellen Lösemittelzusammensetzung abhängig und somit miteinander gekoppelt. Die Produktion einer CCM ist ein komplexer Prozess, der in seinen Einzelheiten im Rahmen dieser Arbeit untersucht wird, um ihn besser zu verstehen.

Abstract

Fuel cells are a promising technology for the desired energy transition. However, to be adopted more widely, the systems must be cheaper and improved in terms of performance and durability. At the heart of the widely applicable polymer electrolyte membrane fuel cell (PEMFC) is the double-sided catalyst-coated membrane (CCM). This is where the crucial mass transport of the reactants and the electrochemical reactions take place during operation. The costs and performance parameters of the overall system are optimized at the CCM. The CCM production process influences these properties. Therefore, the manufacturing process is a key factor in reducing costs and enhancing the performance and service life of the CCM, and consequently, the entire fuel cell. This requires a better understanding of the manufacturing process and a systematic investigation of the underlying effects.

This study focuses on the production of CCM for PEMFCs, contributing to the aforementioned goals and enhancing the understanding of the manufacturing process. Specifically, it investigates the production of *Pt/C*-based catalyst inks and their application to the proton-conducting membrane. Three key aspects of CCM production are examined: the formulation and processing of the catalyst ink; the challenges of membrane direct coating (MDC); and solvent evaporation from the catalyst layers of the CCM.

The catalyst ink consists of catalyst particles, ionomer (an ionically conductive polymer) and several solvents, as well as optional additives. The 1-propanol/water solvent system is frequently used in the literature and in the present work. Although the ink formulation is often the subject of scientific research, this has so far only been applied to a limited extent to the ink process. The catalyst particles are present in the starting material as an agglomerated powder and must be broken up and mixed with the other ink components. This study systematically investigates the influence of various process parameters, namely grinding time and rotational speed, on the production of ink in a ball mill. Experiments show that the stress

number (*SN*), which incorporates grinding time and rotational speed, is the process function for the particle size distribution (PSD) of an ink.

Catalyst layers are produced by membrane direct coating (MDC) and subsequent drying of catalyst inks. The PSD of the inks determines the properties of the layers, such as pore diameter distribution, and the quality of the layer formed. The quality of a layer is assessed based on cracks that occur in the finished electrode. Electrochemical tests are not part of the investigation in this thesis. It has been found that the PSD forms the link between ink processing and layer properties. Similar PSDs lead to similar coating properties (pore diameter and cracks), no matter how they are produced. It was possible to identify an optimum grinding time or PSD for coatings with as few cracks as possible through experimentation. Grinding breaks up large particle agglomerates in the ink, which often initiate cracks in the drying layers. However, with too many small particles, a pronounced crack network is observed. As explanation, the distribution of the ionomer in the ink and the resulting layer is discussed. A distinction is made between ionomer that is bound to the particle surface and ionomer that is free. The distribution of ionomer is influenced by the different particle surfaces accessible to it in inks with different PSDs. Free ionomer wets newly formed particle surface areas during the grinding process, stabilizing them in the process. A sufficient supply of bound ionomer to the particles, alongside additional free ionomer, compensates for stresses that occur during film solidification in the ink drying step, thereby reducing the formation of cracks. However, if the generated particle surface is too large, the available ionomer is insufficient to stabilize the particles adequately. The higher ionomer requirement for a low PSD (i.e. more small particles) can be met by increasing the ionomer content in the ink formulation. For the first time, it is concluded that the ionomer content set in the ink formulation (in the form of the ionomer-to-carbon ratio (*I/C*)) and ink processing must be considered and coordinated together in order to produce low-crack and crack-free coatings.

The work investigates membrane direct coating. This challenging manufacturing process offers several advantages for fuel cell operation, including reduced contact resistance. Compared to the established CCM manufacturing process, one process step is eliminated and the decal film material is saved. The biggest

challenge is the membrane swelling due to contact with ink solvents. This impacts membrane handling and the formation of cracks in the applied catalyst layer. Spray coating has often been used up to now. For scale-up, roll-to-roll and slot die coating are promising options. Here, the ink is applied in a wet film several hundred micrometers thick. The membrane's exposure to solvents is high and particularly challenging. In the present study, wet film application is carried out using doctor blade coating. This method is well suited to replicating the basic effects of slot die coating, while also allowing for greater sample variation with smaller sample volumes (less dead volume) and shorter cleaning times.

Strong swelling of the membrane is observed, particularly on contact with 1-propanol. Without the restriction of a supporting protective film or attachment to a coating plate, it can be seen that the membrane deforms more strongly. This deformation is reversible during subsequent drying and shrinkage of the membrane. If the membrane is not fixed during drying, fewer cracks appear in the catalyst layer. This is explained by the stresses induced in the swelling and shrinking membrane by fixing the membrane, which promote the formation of cracks in the overlying layer. Without fixation, these stresses do not occur.

The catalyst inks consist of several solvents. After the ink has been applied to the membrane, one solvent may be removed during the subsequent drying process. This results in an ongoing change in the solvent composition throughout the process. This, in turn, influences the properties (conformation, agglomeration, etc.) of the ionomer, the particles, and their interactions in the forming layer. Ultimately, it also affects the layer itself, for example by causing cracks to form. Two phenomena are observed: selective drying and the selective absorption of solvents by the membrane through swelling. Both effects are discussed.

The investigations are based on the solvent system of 1-propanol and water. The boiling temperatures of 1-propanol and water are similar, and their vapor pressure curves differ only slightly from one another. Furthermore, the two solvents interact strongly with each other when mixed, forming an azeotrope. At the azeotrope, the liquid and gas phases have the same composition. Experimentally and theoretically, it has been shown and argued that the azeotrope in film drying does not fully describe non-selective drying, i.e. drying without changing the solvent

composition. Instead, the non-selective drying composition shifts towards the dynamic azeotrope, the so called arheotrope. The mass transport kinetics of the solvents into the air significantly influence the selectivity of drying. Experimentally observed and analytically derived influencing factors include the initial solvent composition, temperature, and interaction time of the liquid phase and drying air, expressed as the ratio of evaporation flow to drying air flow. Preloading the drying air with solvent (shown here in the case of water as relative air humidity) has a significant impact. These findings illustrate the importance of precise knowledge of the drying conditions for producing desired, reproducible coatings. They simultaneously present a challenge and an opportunity to influence the process in a targeted manner.

Overflow experiments are carried out to determine the solvent composition during drying, first via the mixture density and then spatially in situ during drying of the film using inverse micro Raman spectroscopy (IMRS). This is the first time that IMRS has been used to study the drying of a solvent mixture in which all components evaporate. The method is highly quantitative and can also be applied to other material systems and issues in the future. Depending on the preferred evaporating component, different effects on the formation of concentration gradients in the solvent mixture are observed.

The individual steps of CCM production – ink processing, membrane direct coating (MDC) and film drying – are primarily investigated and analyzed separately. This approach provides a better understanding of the various effects and influencing variables. However, it is also becoming apparent that these effects are interlinked and influence each other within the individual process steps. For instance, the particle size distribution established during ink processing affects the ionomer distribution in the ink and coating. The modification of the ionomer also depends on the solvent composition. The solvent composition changes after coating due to selective drying and solvent absorption of the membrane. These two processes are dependent on the current solvent composition and are therefore linked to each other. The production of a CCM is a complex process, the details of which are examined in this work in order to better understand it.

Table of Contents

Symbols & Abbreviations

Latin Letters

Symbol	Unit	Meaning
A	m²	Surface area
A_{Ph}	m²	Liquid-gas-interphase
$\tilde{c}_{\mathrm{p,g}}$	J mol^{-1} K^{-1}	Molar heat capacity of the gas at const. pressure
D	wt%	Deviation in the quality analysis of Raman experiments
d	nm	Shell thickness of the ionomer around particles
d_{GD}	cm	Diameter of the grinding disk
d_{GM}	mm	Diameter of the grinding media
d_i	µm	Particle size / equivalent diameter
d_{P}	Nm	Diameter of the pores within a catalyst layer
d_{10}	µm	10 % percentile of the particle size distribution
d_{50}	µm	50 % percentile of the particle size distribution
d_{90}	µm	90 % percentile of the particle size distribution
d_{99}	µm	99 % percentile of the particle size distribution
G	MPa	Shear modulus of the particles
g	m s^{-2}	Gravimetric constant (9.81)
$K_{1,2}$	g g^{-1}	Calibration constant in Raman analysis
h	µm	Film height
I_i	a.u.	Raman intensity of component *i*
I/C	g g^{-1}	Gravimetric ionomer-to-carbon ratio
$\tilde{M}_i$	g mol^{-1}	Molar weight of component *i*
m	g	Mass
m_i	g	Mass of component *i*
$m_{\mathrm{I,total}}$	g	Total amount of ionomer
$\dot{m}_i$	g m^{-2} s^{-1}	Mass flow of component *i*

N_C	-	Number of grinding media contacts
N_i	-	Number of particles of specific particle size x_i
N_P	-	Number of particles in the ball milling system
$\dot{N}_i$	mol s^{-1}	Molar flux of component *i*
n	rpm	Rotational speed of the grinding disk
n_CB	-	Refractive index of carbon black
n_sol	-	Refractive index of the solvent mixture
n_Lewis	-	Lewis flow parameter
P_S	m^{-1}	Probability of impact in ball milling
p	Pa or bar	Pressure
p_i^*	Pa	Partial pressure of component *i*
p_max	Pa	Maximum capillary pressure
Q_3	-	Cumulative volumetric particle size distribution
q_3	µm^{-1}	Volume-weighted particle size distribution density
r	µm	Particle radius
$\dot{r}_i$	$\frac{\mathrm{g\ s^{-1}}}{\mathrm{g\ s^{-1}}}\%$	Relative evaporative mass flow of component *i*
$\tilde{\dot{r}}_i$	$\frac{\mathrm{mol\ s^{-1}}}{\mathrm{mol\ s^{-1}}}\%$	Relative evaporative molar flow of component *i*
S_i	wt%	Gravimetric selectivity of component *i*
$\tilde{S}_i$	mol%	Molar selectivity of component *i*
S_V	µm^{-1}	Specific surface area
SN	m^{-1}	Stress number
SI	J	Stress intensity of the milling process
SI_GM	J	Stress intensity of the grinding media
s	nm	Shell thickness of ionomer covering a particle
s_i	µm	Thickness of the substrate
T	K	Temperature
t	s, min or h	Time
V	ml	Introduced mercury volume during pore diameter analysis
V_i	cm^3	Volume of component *i*
$\dot{V}_\mathrm{g}$	l s^{-1}	Standard volumetric flow rate of the gas

v_{GM}	cm min^{-1}	Velocity of the grinding media
WT	N cm^{-1}	Web tension per width
w	mm	Width of the substrate
$X_{1,2}$	g g^{-1}	1-propanol to water mass ratio in Raman analysis
x_i	wt%	Mass fraction of component *i* in the liquid
$\tilde{x}_i$	mol%	Molar fraction of component *i* in the liquid
y_i	wt%	Mass fraction of component *i* in the gas phase
$\tilde{y}_i$	mol%	Molar fraction of component *i* in the gas phase
$\tilde{z}_i$	mol%	Molar fraction of component *i*

Greek Letters

Symbol	Unit	Meaning
α	W m^{-2} K^{-1}	Heat transfer coefficient
$\beta_{i,j}$	m s^{-1}	Mass transfer coefficient of component *i* in *j*
γ_i	-	Activity coefficient of component *i*
γ_L	N m^{-1}	Surface tension of the solvent
$\Delta\nu_i$	cm^3 mol^{-1}	Structural diffusion volume increment of component *i*
$\delta_{i,j}$	m^2 s^{-1}	Diffusion coefficient of component *i* in medium *j*
ε	vol%	Porosity
ε_r	-	Dielectric constant resp. relative permittivity
ξ	-	Correction factor for incomplete surface coverage and geometric deviations
λ_g	W m^{-1} K^{-1}	Thermal conductivity of the gas
ρ_i	g cm^{-3}	Density of component *i*
ρ_{GM}	g cm^{-3}	Density of the grinding media
$\tilde{\rho}_i$	mol m^{-3}	Molar density of component *i*
σ	N cm^{-2}	Tensile stress within the substrate
Φ_V	vol%	Volumetric fraction
φ	%	Relative humidity of the drying air
φ_{GM}	vol%	Volumetric filling ratio of grinding media to ink
ω_i	-	Weighting factor of component *i* in Raman analysis

Subscripts

0	Start
1	1-Propanol
2	Water
∞	Bulk
A, B	Different cases
air	Into the air
ar	Arheotrope
az	Azeotrope
C	Catalyst
decal	In the decal process
dry	Dry
drying	Due to drying
ex-situ	Ex-situ
film	Film
g	Gas
GD	Grinding disk
I	Ionomer
I,binder	Ionomer present as free ionomer
I, porosity	Immobilized ionomer within porous agglomerates or porous primary particles
I,surface	Adsorbed and immobilized ionomer on the primary particle or agglomerate surface
i, j	Component *i* resp. *j*
IMRS	Inverse micro Raman spectroscopy
in-situ	In-situ
L	Liquid
Lewis	Lewis
Ph	Phase boundary
max	Maximum
membrane	Membrane
mix	Mixture
rcp	Random close packing

solid	Solid
Sol	Solvent
swelling	Swelling
weighted	Weighted
total	Total

Dimensionless Numbers

Le_i	Lewis number of component *i*
M	Coordination number in fracture mechanics
$NTU_{i,\mathrm{g}}$	Number of transfer units of component *i* into the gas phase g
pH	Measure of the acidity of an aqueous solution
Pr	Prandtl number
Sc_i	Schmidt number of component *i*

Chemical symbols

C	Carbon
CH_3OH	Methanol
CO_2	Carbon dioxide
e^-	Electron
F	Fluor
H_2	Hydrogen
H_2O	Water
H_3O^+	Hydronium
H^+	Proton
IrO_2	Iridium oxide
O_2	Oxygen
Pt	Platinum
$-SO_3H$	Sulfonic acid group

Abbreviations

1D	One-dimensional
^{1}H NMR	Proton nuclear magnetic resonance
3D	Three-dimensional
AFC	Alkaline fuel cells
BOS	German and Austrian authorities and organizations with security tasks (German: *Behörden und Organisationen mit Sicherheitsaufgaben*)
BP	Bipolar plates
CCM	Catalyst-coated membrane
CCS	Catalyst-coated substrate
CCT	Critical crack thickness
CCUS	Carbon capture, utilization and storage
CHP	Combined heat and power
CL	Catalyst layers
CNT	Carbon nanotubes
CV-SANS	Contrast-variation small-angle neutron scattering
DMFC	Direct methanol fuel cells
EoFS	End of film shrinkage
EW	Equivalent weight
FCEV	Fuel cell electric vehicles
FTIR	Fourier Transform Infrared Spectroscopy
GDE	Gas diffusion electrode
GDL	Gas diffusion layer
GISAXS	Grazing incidence small-angle X-ray scattering
GM	Grinding media
HBPS	High boiling point solvent
HSA carbon	High surface area carbon
HTC	Heat transfer coefficient
HWT	Higher web tension
IMRS	Inverse micro Raman spectroscopy
LT	Layer thickness
LWT	Lower web tension

M	Membrane
MCFC	Molten carbonate fuel cells
MDC	Membrane direct coating
MEA	Membrane electrode assembly
M w/ S	Membrane with supporting backing foil
M w/o S	Membrane without supporting backing foil
PAFC	Phosphoric acid fuel cells
PC	Primary cracks
PEM	Polymer electrolyte membrane
PEMFC	Polymer electrolyte membrane fuel cell
PEMWE	Polymer electrolyte membrane water electrolysis
PET	Polyethylene terephthalate
PFAS	Per- and polyfluorinated alkyl substances
PFSA	Perfluoro sulphonic acid
PSD	Particle size distribution
PTFE	Polytetrafluoroethylene
R2R	Roll-to-roll
SEM	Scanning electron microscopy
SOFC	Solid-oxide fuel cells
TPB	Triple-phase boundaries
VHF radio	Very high frequency radio
VLE	Vapor-liquid equilibrium
μPTV	Micro particle tracking velocity

Preface

This thesis is the result of my work as a research assistant in the Thin Film Technology (TFT) working group at the Karlsruhe Institute of Technology (KIT) from November 2019 to October 2025. With the start shortly before the corona pandemic, the sometimes uncomfortable phase during it and the time after it was overcome, this period was also characterized by many other ups and downs. I would like to thank all those who accompanied and supported me during this time. Without them, this work would not have been possible.

I would like to thank Prof. Dr.-Ing. Dr. h.c. Wilhelm Schabel and Dr.-Ing. Philip Scharfer for their support, their confidence and the space they gave me to conduct my work. I was able to learn and grow a lot in numerous discussions and conversations. I furthermore thank both of them for the flexible time management during the writing process and am also grateful for the opportunity to present my research at numerous national and international conferences. It certainly helped that I/we first had to find a suitable and established conference on the topic of hydrogen fuel cells and electrolyzers, which was new to the working group. But I never imagined that this job would take me to three continents. And each time the effort was worth it, thanks to interesting discussions with renowned international experts and, of course, the spectacular conference side events, such as a visit to a platinum mine at a depth of 800 m, a trip on a paddle steamer on the Mississippi or a night cruise on the Seine in Paris.

I thank Prof. Dr. rer. nat. Norbert Willenbacher for taking over the co-supervision of this thesis.

A big thank you goes to Margit Morvay for her constant helpfulness and administrative support in the TFT secretariat. I would also like to thank her for always being a calm and understanding anchor of stability in the group during challenging times with her great experience and caring instinct. I also thank Ulrike Lossow for her administrative support and helpfulness and wish her much success and patience in her future work.

Special thanks go to my colleagues Alexander, Alexandra, Andreas, Anna-Lena, David, Jana, Jochen, Johannes, Jonas, Julian B., Julian K., Kevin, Linus, Lisa, Lukas, Max, Nadine, Philipp, Ralf, Sandro, Simon, Thilo, Tobias, Víctor and the colleagues at TVT. They all have been with me for different lengths of time, but they have all left their mark on me thanks to the good professional cooperation, the collegial and discussion-friendly working atmosphere and the strong group cohesion. Various events, extended conference stays and ski trips have also been highlights of my time here. So I can say with satisfaction that many of my colleagues have become friends.

Thanks to Kevin, who has been with me for over 12 years since the first day at university, and Thilo and Víctor, with whom I have experienced so much. From chasing bike thieves and legendary long-distance hikes through the idyllic Black Forest to indulging in regional cultural traditions. Special thanks go to Linus and especially Nadine, with whom I built up our "Team Brennstoffzelle" and worked on and supervised many projects and student theses together. We really complemented each other very well. Thank you also for the personal support in difficult times. It's great that "Team Brennstoffzelle" is now further growing with Alexandra.

A big thank you to "my" students: Adrian, Ahmad, Angela, Athanasios, Camila, Chiara, Christoph, Dennis, Ellen, Frank, Grecia, Jana, Jara, Jialiang, Jonas, Ludger, Lukas, Marc, Marek, Martin, Meike, Nico, Nicolas, Niklas Be., Niklas Bu., Niklas F., Niklas K., Philipp, Rafael, Vincent, and especially August and Anna. In 15 Bachelor's and eight Master's theses and as student assistants, they have spent many hours in the laboratory, preparing and post-processing experiments, researching and discussing, all contributing to the success of this thesis. Even though there were sometimes up to ten of them at a time and it was difficult to keep track of each project and supervise them appropriately, I really enjoyed working with them all.. I have learnt a lot from mentoring so many young adults and I am sure that each of them has taken something away from the collaboration.

I also thank Prof. Dr.-Ing. Matthias Kind and Prof. Dr.-Ing. Thomas Wetzel of the TVT for the opportunity to be involved in student teaching in collaboration

with the TFT. Thanks also go to Michael Wachter and the employees of the TVT workshop, who quickly and easily completed and adapted various small components for the experiments.

Thanks go to the BioHealing team. The collaboration in this interdisciplinary group and the visionary project goal was very rewarding and always gave me great pleasure. Even though the funding situation was challenging at times, our results are impressive. It's nice to meet up with old kindergarten friends again through projects like this.

I also like to thank Karsten Seidel for his constructive cooperation on an equal footing and his distinctive ability to always ask good new questions, to find illustrative comparative examples from the household and to push me into new areas of research.

I would like to acknowledge the financial support of part of my research provided by the Forschungsvereinigung Umwelttechnik via the Allianz für Industrie und Forschung (AiF) within the framework of the program for the promotion of joint industrial research and development (IGF) of the Federal Ministry of Economics and Technology (BMWK) on the basis of a resolution of the German Bundestag (GraphenBlocker, grant number 20738). Also by the Ministry of Economic Affairs, Labor and Housing Baden-Württemberg (WM BW) (KliMEA, grant number 3-4332.62-KIT/14) and the Innovation Campus Mobility of the Future and KIT Future Fields (BioHealing). My thanks also goes to the KIT-Publication Fund for the partial funding of my publications.

Finally, I want to thank all my friends and family members for supporting me with and distracting me from all work-related issues during all ups and downs accompanying my years of PhD work. I especially want to thank Steffi for being there for me with unwavering faith and unconditional support, in good times and in bad. Thank you!

Karlsruhe, December 16, 2025

Philipp Quarz

1 Introduction and state of the art

Fuel cells and electrolyzers are two important systems on the way to the desired energy transition and a sustainable circular hydrogen economy [1–3]. (Excess) energy can be converted into hydrogen as a chemical energy carrier in electrolyzers and thus be stored and transported. The chemically stored energy is efficiently converted into electricity using hydrogen fuel cells. The process involves the catalytic splitting of hydrogen, which is then recombined with oxygen to form water as sole emission. When green hydrogen[1] is used, there are no greenhouse gas emissions in the production and usage of this.

Fuel cells are highly efficient, combined heat and power (CHP) systems, making them attractive for various applications. Fuel cell systems have high energy density, long range, and short refueling times, which are comparable to those of conventional combustion vehicles. This makes them a promising option for the transportation sector. They can power cars, trucks, buses and, in the future, it is intended to fuel ships and aircrafts [7]. They are also used as emergency power generators or in public safety communications[2] [9].

The fuel cell dates back to 1838/39, when Christian Friedrich Schönbein (1799–1868) and Sir William Grove (1811–1896) almost simultaneously and independently of each other demonstrated the reverse electrolysis of water [10,11]. Since then, it has taken some time for fuel cells to gain popularity and technical application [12]. Today, there are essentially six different types of

[1] Hydrogen is labelled with different colors depending on its origin. Green hydrogen is produced by electrolysis using renewable energy and is considered the main resource of a sustainable circular hydrogen economy with applications, e.g. in steel reduction [4,5], ammoniac synthesis, or reconverted directly into electrical energy in fuel cells [6]. An overview of the colors and thus the origins of hydrogen is provided in Appendix 9.1.

[2] For public safety communication, German and Austrian authorities and organizations with security tasks (German abbr. BOS) use a non-public VHF radio service [8]. BOS radio is operated using radio masts powered by fuel cells.

fuel cells, which differ in the type of electrolyte and fuel used, as well as their operating temperature: polymer electrolyte membrane fuel cells (PEMFC), direct methanol fuel cells (DMFC), alkaline fuel cells (AFC), phosphoric acid fuel cells (PAFC), solid-oxide fuel cells (SOFC), and molten carbonate fuel cells (MCFC). SOFC and MCFC are high-temperature types [13]. Depending on the power requirement, different types are suitable [14] (Figure 1).

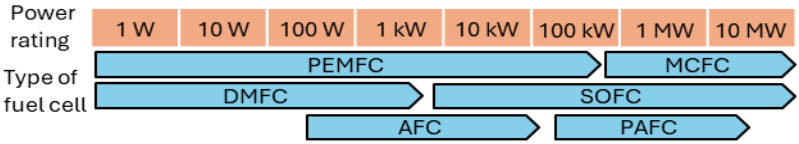

Figure 1: Different types of fuel cells and their operation power ranges. Adapted with permission from [14]. https://creativecommons.org/licenses/by/4.0/

This thesis focuses on polymer electrolyte fuel cells (PEMFC). The advantages of this type of fuel cell are fast start-up, relatively low operating temperatures, reduced electrolyte corrosion, and fewer electrolyte management problems due to the solid electrolyte used compared to liquid electrolytes in other types of fuel cells. The reported efficiency of a PEMFC varies and is in the range around 53 – 58 % for pure electricity and between 70 – 90 % for CHP, using the generated electricity and the exhaust heat [13]. By way of comparison, the efficiency of internal combustion engines in transport applications is in the order of 30 % (gasoline), 45 % (diesel) and that of batteries around 65 % [15]. Taking hydrogen provision into account reduces the overall efficiency of a fuel cell. Including the entire process chain, from hydrogen production in an electrolyzer to storage, transportation and usage in a fuel cell, well-to-wheel efficiencies of around 26 % are reported for fuel cell electric vehicles (FCEVs) using green hydrogen [16]. This is better than well-to-wheel efficiencies of combustion engines (11 – 26 % for gasoline) including all fuel supply losses [17]. All efficiencies are approximate and vary with the exact process and conditions. The high gravimetric energy density of hydrogen (higher heating value: 143 MJ kg^{-1}) is particularly advantageous in e.g. heavy-duty transportation. A volumetric energy density of 5.6 MJ L^{-1} is achieved when hydrogen is pressurized to 700 bar [18]. For an overview of engine efficiencies and energy densities of different fuels, see Appendix 9.1.

1.1 Components and structure of a PEMFC

A PEMFC stack consists of several repeating units. An individual unit consists of: two bipolar plates (BP) surrounding the membrane electrode assembly (MEA) (Figure 2). The MEA consists of a polymer electrolyte membrane (PEM), two catalyst layers (CL) as anode and cathode and two gas diffusion layers (GDL). The membrane and both CL together form the catalyst-coated membrane (CCM).

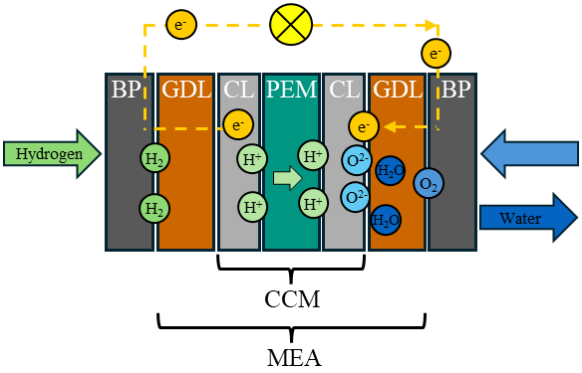

Figure 2: Structure of a single polymer electrolyte membrane fuel cell (PEMFC) unit consisting of bipolar plates (BP), gas diffusion layers (GDL), catalyst layers (CL) and polymer electrolyte membrane (PEM). The PEM and the two CLs form the catalyst-coated membrane (CCM). Adding the two GDLs builds the membrane electrode assembly (MEA). In addition, the occurring reactants are given: Hydrogen H_2, Oxygen O_2, Water H_2O, Protons H^+ and Electrons e^-.

For the energy converting reaction, the educts (hydrogen H_2 and oxygen O_2) are supplied through the bipolar plates and further distributed over the surface by the gas diffusion layers. In the anode, the H_2 is split into two protons H^+ and two electrons e^- (Eq. 1.1). The electrons are conducted through the bipolar plate and can be used as electrical current via a consumer. The protons pass through the electrolyte membrane to the cathode. There, O_2 is supplied. It recombines with the protons and electrons, which are also conducted via the

bipolar plate, to form water (Eq. 1.2). The product water is removed via the GDL and the flow field in the bipolar plate. The overall reaction is shown in Eq. 1.3. It gives a theoretical reversible cell voltage of 1.23 V with a reaction enthalpy of 286.0 kJ mol^{-1} and a free enthalpy of 237.3 kJ mol^{-1} under standard conditions at 25 °C [19].

Anode:	$2\,H_2$	$\rightleftarrows$	$4\,H^+ + 4\,e^-$	1.1
Cathode:	$O_2 + 4\,H^+ + 4\,e^-$	$\rightleftarrows$	$2\,H_2O$	1.2
Redox:	$2\,H_2 + O_2$	$\rightleftarrows$	$2\,H_2O$	1.3

The bipolar plates are also responsible for heat dissipation, water management and mechanical stability. However, the most important mass transport processes for the reactions and electrochemistry take place in the CCM. This is shown in more detail in Figure 3. The two electrodes are microporous networks of catalyst particles and ionomer, which is a proton-conducting polymer and binder for the catalyst particles. The catalyst particles are nanometer-sized platinum grains doped onto a carbon carrier. This structure saves on expensive platinum while maintaining a high electrochemically active surface and good electrical conductivity. This simultaneously improves the electrical conductivity and porosity of the layer. Many so-called triple-phase boundaries (TPB) are important for high performance. The catalytically active platinum must be in contact with all reaction partners. It must therefore be in contact with the gas space for the supply of gaseous reactants and the removal of water produced on the cathode side. Electrons and protons must also be transported to and from the platinum. The conduction of the electrons takes place via the carbon support particles and the conduction of the protons via the ionomer and the membrane. The ionomer material in the catalyst layer and in the membrane are often the same, although it is not necessarily required to be identical [20].

The optimal operating conditions require, among other things, a high degree of distribution and good accessibility of the platinum nano-particles. A good contact between the ionomer of the catalyst layer and the membrane is also

required for good proton conductivity [19]. As a brief digression, the design of the CCM in PEM electrolyzers is very similar, so many of the conclusions from fuel cell manufacturing can be applied to electrolyzer manufacturing. Further details can be found in Appendix 9.1.

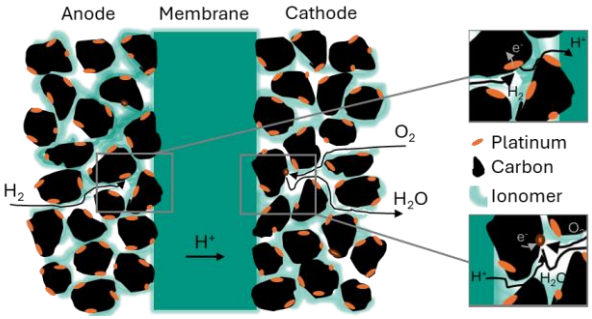

Figure 3: Schematic illustration of a catalyst-coated membrane (CCM) consisting of porous anode and cathode electrode and a proton conducting membrane. Additionally zoom into the triple-phase boundaries (TPB) where the Redox reactions occur on the right.

The desired properties of the involved system components result from the used materials and their processing. A brief outline on the state of research of the materials and production of CCM is given in the following.

1.2 CCM and MEA fabrication

There are different ways to manufacture the membrane electrode assembly (MEA) (Figure 4). The membrane and GDLs are typically prefabricated and purchased. The process begins with the liquid catalyst ink.[1] Two process routes are distinguished: manufacturing via the catalyst-coated substrate (CCS) and via the catalyst-coated membrane (CCM). CCS and CCM are the respective

[1] In the less common direct membrane deposition, the membrane is coated from an ionomer suspension onto the electrode and dried there to form the membrane. The electrode is previously manufactured on the GDL (CCS process) [21–26] or onto an inert substrate (decal process) [27].

intermediate products. In the CCS process (Figure 4 I)), the catalyst ink is applied onto the gas diffusion layer (GDL) and forms the CCS, sometimes referred to as gas diffusion electrode (GDE). The MEA is formed by two CCS with a membrane in between [28]. Although hot-pressing is often used to reduce contact resistance, it is not mandatory during assembly [29].

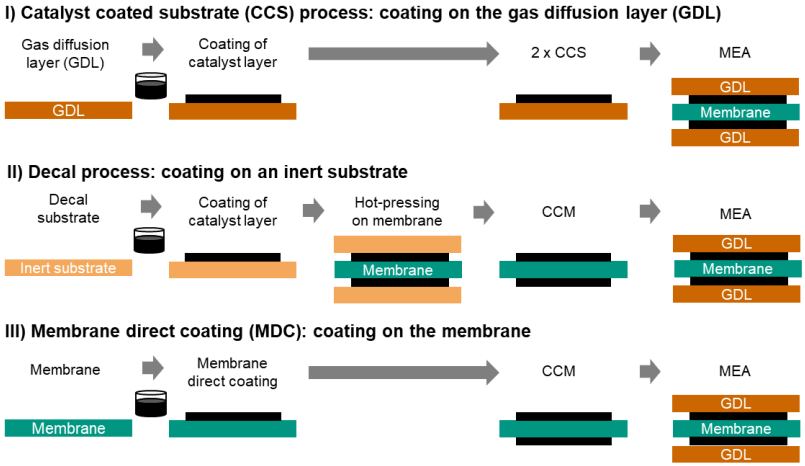

Figure 4: Process routes to produce a membrane electrode assembly (MEA): I) catalyst-coated substrate (CCS) process, as well as II) decal process and III) membrane direct coating via the intermediate product of the catalyst-coated membrane (CCM). I) In the CCS process, the catalyst ink (black) is coated and dried on two gas diffusion layers (GDL) (brown) to form the CCS. Both are assembled with the membrane (petrol) to form the MEA. II) In the decal process, the catalyst ink is coated and dried on two inert decal substrates (orange) and then applied to both sides of the membrane in a hot-pressing step. Then, assembling the GDLs forms the MEA. III) Using advanced membrane direct coating (MDC), the ink is coated and dried directly onto the membrane. Again, assembling the GDLs then forms the MEA. Reused and supplemented from [30].

It is different for the process routes via the CCM. Here, the CCM is produced first and the GDLs are added later, forming the MEA. The CCM approach is further differentiated in two production methods: the decal process (Figure 4 II)) and the membrane direct coating (MDC) (Figure 4 III)). In the decal

process, the catalyst ink is applied to an inert substrate and dried. The resulting electrode is then hot-pressed onto both sides of the membrane to form the CCM. Additional hot-pressing of the GDLs onto the CCM builds the MEA. The second approach for CCM manufacturing is membrane direct coating (MDC). The ink is applied directly to the membrane on both sides and dried. Then, the GDLs are assembled to form the final MEA [28].

The CCS process is the common established MEA production way. However, the CCM process produces MEAs that offer significant benefits, such as improved contact between the membrane and the electrodes, reduced resistances and enhanced cell performance [31–34]. This is particularly the case when applying membrane direct coating. Additionally, the catalyst utilization is highly effective here, and also enables multilayer applications with additional layers that can be applied directly to the membrane (see Appendix 9.1). [35] The main challenges of this approach are membrane swelling and membrane handling in a roll-to-roll (R2R) process after coating, caused by ink solvents [36,37].[2] This topic is discussed in greater detail in Chapter 1.4. The respective advantages and disadvantages of all three process routes are presented in Appendix 9.1.

All MEA manufacturing routes are similar in that they require catalyst ink. Its formulation and processing is the subject of the next chapter.

1.3 Catalyst ink formulation and processing

The catalyst ink is the starting point for CCM production and is a complex material system. It is composed of catalyst nanoparticles, ionic polymer, and a variety of solvents. Additives, e.g. carbon nanotubes (CNT) or poly vinyl

[2] Membrane handling and swelling due to solvent contact is an issue in each manufacturing route. The membrane is very sensitive to the relative humidity of the ambient conditions (which changes several times within the process line). This was shown in a co-authored study [38]. In membrane direct coating (MDC), however, the effects are more pronounced when the membrane comes into contact with the ink solvents in addition to the ambient moisture.

alcohol, can also be supplemented [39,40]. Platinum doped on carbon carrier particles is usually used as catalyst with platinum loadings ranging from 10 up to 60 wt% platinum in the particles [41]. Typically, conductive carbon black is used as carrier particle, e.g. Vulcan XC-72. Additionally, there are high surface area (HSA) carbons with internal porosity, such as Ketjenblack. The carrier materials differ in their specific surface area and surface morphology [42–45]. The platinum content and the carrier material have an influence on the hydrophobicity of the particles and the interaction of the particles with each other, the ionomer, and the solvents [44–49]. For example, Chowdhury et al. [49] and Berlinger et al. [45] observed that with increasing platinum content the amount of absorbed ionomer on the catalyst particles decreases. The catalyst is usually in the form of an agglomerated powder. For example, the catalyst powder used in this work has an initial size of agglomerates of up to 100 µm. The agglomerates must be broken-up and stabilized during ink production. The particle size distribution (PSD) (ratio of primary particles and agglomerates) influences the ink properties and the later microstructure of the catalyst layers, e.g. the layer's pore diameter distribution [50].

Another essential component of both inks and films is the ionomer, an ionic polymer. It stabilizes dispersed particles in the ink and acts as proton conductor and binder in the coating [44,51]. During the catalyst grinding and ink mixing process, the ionomer forms an ultrathin film, measuring only a few nanometers in thickness, on the particles [52,53]. The resulting distribution and thickness of this film across the particle surface are heterogeneous [47,54–56]. It can be adsorbed on particles in the ink and additionally be present in the ink as free ionomer [57,58]. The ionomer acts as a binder between the particles during the solidification of the film [47,58–61]. Catalyst particles with higher surface area of the Carbon carrier require greater quantities of ionomer for stabilization, compared to their lower surface area counterparts, such as Vulcan XC-72 [42,44,61], with the consequence of reduced free ionomer [62]. Concurrently, the thickness of the ionomer film surrounding the particles diminishes as the particle size is reduced for a constant ionomer-to-carbon ratio [63].

The most widely used proton conducting ionomer class to date is the perfluorinated sulphonic acid (PFSA) copolymer. PFSA have a hydrophobic polytetrafluoroethylene backbone and a hydrophilic side chain, ending in a sulphonic acid group. By varying the side chain length or equivalent weight (EW), which is the ratio of ionomer weight per sulphonic acid group, the properties of the ionomer can be modified [35]. Commercial ionomers are for example most commonly Nafion (Chemours), 3M PFIA and 3M PFSA (both 3M), Aquivion (Solvay) or Fumion (Fumatech GmbH). In this work, Nafion is used as a state-of-the-art material.

Providing information about the ink formulation, the ionomer-to-carbon ratio (*I/C*) is often used in the literature. The *I/C* refers the gravimetric ionomer content of the ink to only the carbon content of the used catalyst. The ionomer is used to stabilize the particles from (re-)agglomeration by adsorbing onto the particle surface and increasing the repulsive forces between the particles [51]. In ink processing, agglomerates are broken up and then either re-agglomerate or remain as smaller particle fragments when stabilized against re-agglomeration by the ionomer. With higher *I/C*, the catalyst particles in the ink tend to be slightly smaller, since the particles are stabilized better [51,62] and the layer porosity decreases [64]. If the *I/C* is too high, pores and platinum particles can be blocked, resulting in performance losses due to water condensation and flooding during operation. The condensate water and the ionomer enrich the gas diffusion resistance [39,54]. An increased *I/C* also promotes the prevention of undesirable cracking in the catalyst layers. The absence of cracks, in turn, is beneficial for performance [62]. The *I/C* therefore has a direct effect on system performance [65,54,66,67]. The optimum *I/C* differs for different catalysts and is usually determined empirically [35]. Typical values are between 0.7 and 1.5 [54,68].

Catalyst particles and ionomer form the solids. The solid content of the inks depends on the coating method and is often between 8 and 20 wt% for slot die and doctor blade coating [42,62,69–74].

In addition to the solids that make up the final layer, solvents are used in the ink for manufacturing reasons. It is exceedingly challenging to produce

homogeneous, time-stable and coatable inks using a single solvent [51,75]. For this reason, a variety of solvent mixtures are used in catalyst inks and referenced in the literature, e.g. [76,58,77,78,72]. Water is mostly included and used to prevent carbon and organic solvents from igniting. Organic solvents, e.g. 1-propanol, 2-propanol, ethanol, ethylene glycol, propylene glycol and various more, enhance the dispersibility of the hydrophobic catalyst particles [68,74]. Furthermore, the ionomer is often dispersed in a solvent mixture. Notable examples include Nafion as D520 and D2020 (Chemours [79]) or 3M Ionomer 800EW (3M [80]). A commonly used solvent system in PEMFC is 1-propanol/water, e.g. in [42,44,57,58,60,72,74,76,81–85].

The solvent composition has a major influence on the ink properties, as it directly affects the ionomer, the catalyst particles and their interactions. The solvent mixture determines the permittivity and polarity of the system [57,86,87]. This in turn affects the ionomer morphology within the ink [88]. The main chain (hydrophobic and non-polar) and the side chain (hydrophilic and polar) of the ionomer have different properties. Therefore, solvents with different dielectric constants and solubility parameters are differently compatible, which leads to the formation of ionomer clumps with different morphology, size and conformation. For example, in organic solvents with different dielectric constants ε_r of the dispersing solvent (mixture), it has been reported that Nafion forms a solution ($\varepsilon_r > 10$), a colloid ($3 < \varepsilon_r < 10$) or a precipitate ($\varepsilon_r < 3$) [87]. In addition, different structures have been observed in various solvents: e.g. cylindrical ionomer agglomerates, less-defined and solvated ionomer agglomerates, random-coil ionomer agglomerates, or secondary ionomer agglomerates [35]. The ionomer's binding to the particles and the particles' size and re-agglomeration behavior are also influenced by the solvent composition [57,78,89,90]. In consequence, the microstructure of the catalyst layers varies depending on the solvent mixture [78,89,91–94].

In this thesis, 1-propanol and water are used as solvent system. This solvent system is commonly used in research. Furthermore, water and 1-propanol are the main solvents in the Nafion D2020 dispersion used (see Chapter 3.1). One

reason is that 1-propanol, water, and their mixtures exhibit $\varepsilon_r > 10$ [95], and thus Nafion in solution. Pure Nafion is reported to form cylindrical ionomer agglomerates in this solvent mixture [35]. With regard to the evaporation of a binary 1-propanol/water mixture, the two solvents have very similar boiling temperatures (1-propanol: 98 °C; water: 100 °C) and vapor pressure curves (see Appendix 9.3) but the solvent mixture forms an azeotrope (see Figure 6). A comprehensive review of the influence of different 1-propanol/water mixtures on catalyst layer properties can be found in Gong et al. [96].

Catalyst inks are produced in different processes and devices. The goals are to break up the catalyst agglomerates and to mix all components homogeneously. Methods used are ultra sonification [42,82,71,73,97–100], hydrodynamic cavitation [101], high-shear mixing [71,73,74], ball milling [42,44,73,102–107,100,44], and combinations of those. The manufacturing process affects the particle size distribution (PSD) of the inks, the viscosity and in consequence the properties of the resulting electrodes [73]. PSD and viscosity can therefore be used as quality characteristics.

Using a ball mill for mixing has the advantages of simultaneous particle comminution and component mixing, scalability for large quantities and the production of homogeneous inks with a suitable particle size distribution, sufficient time stability (low re-agglomeration and sedimentation of the particles), non-foaming and good coating properties of the ink (flow behavior, dosability, substrate wetting properties, ...) [103]. It also produces few unwanted air bubbles compared to ultra sonification [42]. To the best of the author's knowledge, ball milling does not remove platinum from the substrate to the extent reported for ultrasonic treatment [97]. Nevertheless, there are only few systematic studies on the process influences in the production of fuel cell inks using ball mills. This gap is addressed in this thesis. The principles of ball milling are outlined in Chapter 2.1 and will later be transferred from different material systems to fuel cell catalyst inks.

1.4 Membrane direct coating and membrane swelling

The catalyst ink produced is next applied to a substrate to form a thin catalyst film, which then dries to form the electrode. This thesis focuses on the membrane direct coating (MDC) as advanced processing method for CCM production. With directly applying the ink to the membrane, it comes into contact with the solvents from the ink during CCM production. The solvents penetrate the membrane, causing it to swell and then shrink again. These geometric deformations create stresses in the system (membrane and applied catalyst coatings resp. layers) [108].[3] The adsorbed solvent affects the membrane properties, including Young's modulus, stress relaxation and membrane handling [112,113].

The widely used membrane material for PEMFC is Nafion[4], or other perfluoro sulphonic acid (PFSA) materials. The solvent uptake and swelling behavior of these membrane materials depend on, among other things, the temperature, the equivalent weight of the membrane (EW) [36], and the solvents used [114,115]. When solvent mixtures are used, the solvent composition influences the swelling behavior. Mixtures swell the membrane much more than the pure solvents [37,114]. Solvent absorption and the resulting swelling are a dynamic processes. The duration of exposure influences the amount of swelling until an

[3] Literature focuses on the effects of membrane swelling and shrinking during fuel cell operation due to water from the pre-wetted educt gas flow and the resulting process water [108–110]. Repeated deformation occurring during operation results in material fatigue and (micro)cracks in the membrane, which can extend to the entire CCM [108]. However, for the water absorption of Nafion membranes throughout the whole CCM process, the results with vaporous water can be transferred to those with liquid water, present in MDC, under comparable conditions [111].

[4] This Nafion is essentially the same as the Nafion used in the catalyst ink, which enables proton conductivity during fuel cell operation. They may differ in the ratio of functional side chains to the main chain, which is expressed as the equivalent weight (EW). EW is defined as the mass of dry Nafion in grams per mole of sulfonic acid groups ($-SO_3H$). For example, this work uses Nafion in the membrane with an EW of 2.100 g mol^{-1} and 1,000 g mol^{-1} in the catalyst ink resp. layer. See Chapter 3.1 for more information.

equilibrium between the swollen membrane and the ambient solvent conditions is reached [37,116–118]. Due to different mass transport kinetics [119], selective solvent absorption may occur when using alcohol-water mixtures [114,120,121]. This means that one component is preferentially absorbed by the membrane compared to the other solvent(s). Although selective membrane swelling has so far received little interest, this effect is not to be underestimated in understanding and improving the MDC process.

Membrane direct coating (MDC) is no novel approach. However, to the author's knowledge, MDC is rarely carried out in the literature or on an industrial scale. Discussions during the preparation of this thesis indicate a high level of interest in membrane direct coating and a need for further development and understanding of (large-scale) implementation. Liu et al. [122] wrote about industrial MEA respectively CCM production: *"However, the swelling of PEM in the direct coating of ink onto the PEM is a snag, especially in the continuous coating process. […] Unfortunately, the detail information of these methods is a top grade secret. Most of the company adopt R2R process and slot die coating. […] There is no doubt that slot die coating and R2R manufacturing pose significant superiority than spray coating, such as higher efficiency and higher utilization of catalyst."*

For MDC, often spray coating [123–126,82,127–129,96,130] is used, but also applications via painting [33,131], screen [132] or ink jet printing [133], doctor blade coating [70], or slot die coating for roll-to-roll (R2R) processing [116] are utilized. The different coating processes have varying advantages and disadvantages. In addition, they have different requirements for the ink, such as solid content, and the physics of the processes involved differ (e.g. pressure and shear) [85].

In the spray coating process, several thin layers are applied in succession to a heated substrate, resulting in rapid (interim) drying. The final coating is a multilayer coating made up of several thin individual layers. The sequential ink application and subsequent drying process keeps the amount of solvent applied to the membrane manageable, making spray coating the preferred

method for MDC. However, the disadvantages are insufficient throughput, long process times and difficult scalability. [35,85]

Higher production rates and process scale-up are achieved with slot die or gravure coating in a R2R process [122]. The typical solid content of the ink is around 5 – 15 wt% [27,74,134], which is higher than for spray coating. The requirements for maximum particle sizes in the ink are not so restrictive. The entire ink application takes place once. As a result, the applied wet film is significantly higher and the amount of solvent in contact with the substrate after ink application is greater than with spray coating. In consequence, the interaction time between the ink solvents and the membrane until complete evaporation is longer [35,85]. This results in significant swelling of the membrane with this process route. This leads to the main process challenges including membrane deformation, wrinkling, inhomogeneous process conditions and difficult membrane handling.[5] [35,85] Vacuum fixation helps to manage membrane deformation after swelling at laboratory scale, but is impractical for scale-up [91]. So, a solution for membrane handling after large solvent contact must be found. For this purpose, it is important to understand mass transport phenomena involved and, in particular, the interactions of the ink solvents with the membrane. To counteract the deformation of the membrane caused by swelling, mechanically reinforced or composite membranes are often used. These membranes show reduced swelling behavior, increased mechanical stability and/or simplified handling [35,138–143]. Still, swelling occurs and needs to be addressed.

An alternative method to prevent swelling after ink application is pre-swelling the membrane prior to coating. It was reported that pre-swelling the membrane with specific solvents improves the coating pattern of the subsequent catalyst

[5] In slot die coating, the gap between nozzle and substrate and, in gravure coating, the uniform contact across the width of the substrate are critical process parameters [135–137]. If the membrane swells (irregularly) due to ink application, this affects these parameters and thus the ink application. This leads to inhomogeneous film thickness and platinum loading. In addition, previously stable coating windows can be left, leading to coating defects.

layer [70,144]. However, the addition of more solvent increases the complexity of the process. Moreover, the drying step prolongs and before device operation, it must be ensured that the used solvents are completely removed from the membrane.

1.5 Drying of catalyst layers and crack formation

After coating, the applied ink (and the swollen membrane) must be dried. The systematic description of drying parameters for catalyst inks for the production of fuel cell and electrolyzer electrodes is rarely the focus of literature. The ink coating is often dried for a specific time in an (convective) oven or under ambient conditions with unspecified drying parameters, e.g. [42,93,145–147]. In this case, the drying time is chosen much longer (sometimes hours and days) than is necessary and desirable from a process engineering point of view. While the drying time is generally not detrimental to the electrode result, it is not particularly time efficient, which suggests a potential area for improvement in terms of efficiency. In addition, important information on drying parameters is often missing or incomplete in literature. The literature dealing with the drying behavior of catalyst inks for fuel cells and electrolyzers is largely based on empirical studies, which mostly only examine individual specific drying effects. Convective drying is most commonly used.[6] The following is an overview on the state-of-the-art drying for fuel cell inks. A more detailed summary can be found in Appendix 9.3.

Catalyst inks are particulate-multi-solvent systems. During drying, the solvents evaporate, the film shrinks, the particles move closer together, solidify and form a particulate network of catalyst particles and ionomer.[7] During the solidification stage, the solvents evaporate from the pores of the particulate

[6] The comparison of different types of drying (convection, vacuum, and freeze drying) and their influence on microstructural properties, e.g. porosity, has been investigated [147,148]. A fair comparison in the sense of comparable drying rates or similar is not given in the studies.

[7] A more detailed description of the principles of convective particulate and multi-solvent film drying is given in chapter 2.3. The focus in this chapter is on giving an overview on fuel cell catalyst ink drying.

network. Cracks may form in the layers in this last part of the drying process. In the literature, fuel cell ink drying is often analyzed using drying curves. Hereby, the total mass of the dying ink film is measured over the drying time [62,64,76,81,94,149–151]. This enables statements on the influence of different drying conditions on the drying rate and time. For instance, the initial solvent composition [151], the particle material used, and the ionomer-to-carbon ratio have been demonstrated to exert an influence on the drying rate and duration [62]. Regarding the drying conditions, (water) preloading of the drying air prolongs the drying time, but higher volume flows of the drying air and higher temperatures shorten the drying time [64,81]. Thin films dry faster than thicker ones [76].

Since catalyst inks contain multiple solvents, a component-specific drying analysis is required for a more detailed understanding. Only a few studies have examined such component-specific analysis during the drying process, using either Fourier transform infrared (FTIR) or proton nuclear magnetic resonance (^{1}H NMR) spectroscopy. Hereby, it is observed that one solvent depletes faster than the other(s) and the solvent composition of the remaining film changes [76,81,94,149,151]. This effect is called selective evaporation and is affected by the solvents used and drying conditions applied. Experimentally it was shown that the selected solvents and their specific composition [76,81,94,151], the drying temperature [64,81], the overflow rate [81], and the preloading of the drying air with solvent [64,81] influence the selective solvent evaporation. A deeper look into the film in-situ during drying has not yet been feasible.

The applied drying conditions result in differences in crack patterns in the catalyst layers [76,81,94,151] and their pore size distribution or porosity [64,91,152]. The drying parameters also affect the distribution and accumulation of the ionomer in the dry catalyst layer [91]. Based on the knowledge of selective evaporation gained from the work of Scheepers et al. [76], later studies concluded that (quasi-)azeotropic solvent ratios should minimize uneven evaporation and specifically chose corresponding formulations in their inks [40,103].

Liu et al. [35] summarized the current state of research on processing influences on catalyst layers. They state that although the drying process is critical to the formation of the catalyst layer structure, research in this specific area is limited. More research on the drying process is needed to understand the causes of catalyst layer defects and to enable well-designed layer structures. This is where the present thesis aims to make a contribution.

Cracks have an unfavorable impact on the performance and lifetime of the CCM and thus the entire PEM system. They have some positive, but various negative effects on the mass transport properties during operation [109,153–156], on the mechanical properties of the CCM [108,156–161] and also on the chemical properties [162–165]. During operation, they facilitate the mass transport of the educts and products [153,154]. On the other hand, they can be flooded with product water, especially at high current densities [155,156] and cause interruptions in conductivity. In addition, cracks are mechanical weak spots in the CCM, which undergoes dimensional changes during operation, and carry the risk of defect enlargement. This includes crack growth, delamination of the layer from the membrane, and membrane destruction with even more serious consequences, such as fuel leakage, the formation of destructive hydroxide peroxide, loss of performance or functional failure [108,159–162]. In addition to affecting performance, cracks have a negative impact on the durability of a CCM [166]. More information on the influences of cracked catalyst layers is given in Appendix 9.1. In general, the literature states that cracking should be avoided. To achieve this, it is essential to comprehend the formation of cracks.

Ink formulation and drying conditions exert an influence on the formation of cracks. In fuel cell and electrolyzer catalyst inks, a higher *I/C*, irrespective of its impact on cell performance [167], results in a reduction of the number of cracks [62]. Furthermore, the particle morphology [62] and the solvent (mixtures) used with their respective interactions to the ionomer, have been identified as influencing factors for crack formation [58,94,131,168]. To increase the mechanical stability of the layer, additives like a polymeric binder [169,170] or carbon nanotubes (CNT) [39] are added.

Additionally, the manufacturing process has an influence on the cracking. However, there is less systematically investigation in this so far. In addition to the ink formulation, the processing of the ink and the resulting particle size distribution (PSD) also affect the formation of cracks [103]. Filtering out the largest agglomerates improves the crack pattern [58]. In general, higher layer thicknesses lead to more pronounced crack patterns in the catalyst layers [64]. Consequently, the product-related required or desired thickness of the catalyst layer is decisive. Another aspect is the coating substrate. There is no known comparison of the influence of the coating substrate in the literature. Furthermore, the drying method [148] and drying parameters [64] also exert an influence on the microstructure of the layers. The drying parameters, such as relative air humidity, are of great importance in this context [76,81,94]. The process-related influences on crack initiation are often determined only experimentally and are not fully understood. This thesis is intended to contribute in this direction. The fundamentals of crack formation and influencing parameters are given in Chapter 2.2.

1.6 Aim of this work

Building up on the state of knowledge, this thesis focuses on the fabrication of carbon-platinum (*Pt/C*) based catalyst inks and their application to the proton-conducting membrane to form the catalyst-coated membrane (CCM), which is the main component of a polymer electrolyte membrane fuel cell (PEMFC). The focus is on membrane direct coating (MDC) as an advanced and economical approach for manufacturing. This work investigates essential steps in CCM production: the ink formulation and production as well as challenges during MDC and the ink drying. The questions to be answered are: How has a catalyst ink for direct membrane coating to be formulated and processed? Furthermore, how can membrane direct coating be achieved using a doctor blade/slot die coating (dealing with large quantities of applied solvent)? Resp. what effects need to be understood and tailored to deal with the applied solvents (in contrast to decal coating on inert substrate)? What effects must be taken into account when drying the multi-component ink system on membranes (including membrane selectivity and selective solvent evaporation)? How do all these affect the quality of the CCMs?

Overall, it is hypothesized that major process challenges are caused by the mass transport processes involved in all mentioned process steps. Ink solvents, ink composition, and the solvent fluxes occurring during ink processing need to be thoroughly understood to enable efficient processing of CCMs. The guiding questions are addressed through three hypotheses.

Ink processing affecting layer quality via particle size and ionomer distribution

Essential properties of the catalyst ink and layer are specified during the ink processing (see Chapter 1.3). Thus, as first step of this thesis, process-related influences during the ink formulation on membrane direct coatings are investigated. To date, the influence of the process and the formulation of the ink have not been considered together. This leads to

Hypothesis 1: In order to reduce cracking in catalyst layers, the processing and formulation of the ink must be adjusted and balanced. The link is the particle size distribution (PSD) of the ink.

In order to verify this, catalyst inks with constant solid contents but different and similar PSD are produced and their effects on surface and structure properties (pore diameter distribution and crack formation) of the coatings are analyzed. A theoretical and empirical model is derived to describe the relationship between PSD, ionomer distribution and layer cracking. This is experimentally tested. To the best of the author's knowledge, there is no joint consideration of PSD and ionomer demand in the form of the ionomer-to-carbon ratio (*I/C*) in the literature. The study in the thesis addresses this gap.

Selective evaporation of multi-solvent ink formulation during drying

To better understand the entire manufacturing process, the drying stage is considered. Catalyst inks often consist of multiple solvents (see Chapter 1.3). During processing, selective evaporation of one solvent occurs, resulting in the preferential removal of that solvent (see Chapter 1.5). Changes in the solvent composition are believed to have a negative effect on crack-free film formation. It is therefore crucial to know the non-selective drying composition and to understand the influencing (drying) factors of the process. This leads to

Hypothesis 2: Selective drying influences microstructure formation during film consolidation of the fuel cell electrode.

First, the selective drying process must be better understood and quantified. In order to investigate the drying selectivity of multi-solvent inks, the ink system is simplified to a frequently used binary solvent mixture. This enables a comprehensive analysis of the fundamental influences and the formulation of predictive models. Experimentally, the drying of solvent mixtures with and without the influence of gas kinetics is investigated. The solvent composition of the drying film is determined by density measurements. Inverse micro Raman spectroscopy (IMRS) is used to transfer the results to thin films. First insights into concentration gradients within catalyst film are conducted. This information allows for initial statements on microstructure formation to be made.

Membrane-solvent-interactions in membrane direct coating (MDC)

Nafion membranes tend to swell in contact with solvent. This makes MDC a challenge. In addition to the aforementioned selective drying, selective solvent uptake from the membrane occurs, increasing process complexity (see Chapter 1.4). Coating the second side of the membrane presents further challenges. In this step, the stabilizing support film of the membrane is removed and the consequences regarding membrane stabilization and deformation have to be investigated. The aim here is to gain deeper understanding for developing a concept for (double-sided) CCM processing:

Hypothesis 3: Increased degrees of freedom of the membrane after ink coating and during drying result in fewer cracks in the directly coated catalyst layer.

The theoretical description of selective ink drying is supplemented by considering the effects of membrane swelling. The occurrence of solvent mass flows is examined. The deformation of the membrane is investigated experimentally with and without support. Different coating scenarios are then investigated experimentally and evaluated for their suitability for direct membrane coating. The influence of the removed support foil on tensile stresses is also investigated. The extent to which the second MDC affects the first layer on the back of the membrane and vice versa is also explored.

2 Theoretical basics

In order to validate the hypotheses, the study draws on a broad knowledge base in the relevant subject areas. This forms the starting point for the considerations and experiments that are to be carried out at a later point. In order to empirically validate Hypothesis 1, a ball mill is utilized in the production of the catalyst inks. The following section will provide a detailed exposition of the established fundamentals of this technology. In order to validate Hypotheses 1 and 3, the crack pattern of the manufactured catalyst layers is analyzed. The fundamental influences on the formation of cracks are therefore outlined as follows. The basis for considerations to clarify Hypothesis 2 is formed by known relationships between the drying technology of particulate systems and multi-component solvent mixtures.

2.1 Basics of the ball milling process

A ball mill is a type of grinder that consists of either a rotating hollow cylinder or a stationary hollow cylinder with a rotating grinding disc in the center. The cylinder is partially filled with grinding media, usually steel or ceramic balls. As the cylinder or the grinding disc rotates, the balls whirl around and strike the material inside, breaking it up and turning it into a finer powder. Ball mills are common grinding and mixing devices for various material systems, including fuel cell inks. The basic principles of particle size reduction are known for other materials and are outlined here. Within a ball mill, the particles are subjected to stress between two grinding media or between the grinding media and the vessel wall [171,172]. The most significant mechanism is identified to be the stress between the grinding media (GM) at different (tangential) speeds [173]. Several process parameters, such as milling time, rotational speed, the size, shape, and filling of the GM, and ink parameters, e.g. the solid content and viscosity of the ink, influence the result of ball milling [106,174,175]. Summarizing them, two main parameters for particle comminution are derived: the stress intensity *SI* (Eq. (2.1)) and the stress

number *SN* (Eq. (2.3)). They describe the impingement intensity required for particle break-up and the probability of an agglomerate being at the place of impact [176].

A specific minimum comminution energy is required for agglomerate break-up. This energy derives from the kinetic energy of the grinding media and is thus correlated to the stress intensity of the grinding process [176].

$$SI \propto SI_{GM} = {d_{GM}}^3 \cdot \rho_{GM} \cdot {v_{GM}}^2 \qquad (2.1)$$

SI	Stress intensity of the milling process in J
SI_{GM}	Stress intensity of the grinding media in J
d_{GM}	Diameter of the grinding media in mm
ρ_{GM}	Density of the grinding media in g cm^{-3}
v_{GM}	Velocity of the grinding media in cm min^{-1}

Simplifying assumptions are made for describing the energy input: The stress intensity due to centrifugal forces is negligibly small compared to the *SI* based on the kinetic energy of the grinding media (GM), only individual particles experience intense stress between the GM, meaning the stressed particle volume is independent of the GM size, and the elasticity of the feed material is much smaller than that of the GM. Furthermore, the velocity of the GM is assumed to depend on the rotational speed of the grinding disk (Eq. (2.2)). Increasing the *SI* (significantly) higher than the required value does not improve the break-up result of the agglomerates. [176]

$$v_{GM} = \pi \cdot d_{GD} \cdot n \qquad (2.2)$$

d_{GD}	Diameter of the grinding disk in cm
n	Rotational speed of the grinding disk in rpm

In addition, the number of stress events that lead to agglomerate break-up is important. The stress number *SN* quantifies those events and results from three critical parameters (Eq. (2.3)), and is defined in more detail in Eq. (2.4). Eq. (2.4) applies in the case of deagglomeration of agglomerates (non-crystalline

material). In this case, the shear stresses occurring between the surfaces of the grinding media are sufficient to break up the particles. [176]

$$SN = \frac{N_C \cdot P_S}{N_P} \tag{2.3}$$

SN	Stress number in m^{-1}
N_C	Number of grinding media contacts (dimensionless)
P_S	probability of impact in m^{-1}
N_P	number of particles in the system (dimensionless)

$$SN \propto \frac{\varphi_{GM} \cdot (1-\varepsilon)}{(1-\varphi_{GM} \cdot (1-\varepsilon)) \cdot \Phi_v} \cdot \frac{n \cdot t}{d_{GM}} \tag{2.4}$$

φ_{GM}	Volumetric filling ratio of grinding media (GM) to ink in ml ml^{-1}
ε	Porosity of the bulk of grinding media in vol%
Φ_v	Volumetric solid content of the product suspension in vol%
t	Milling time in h

The movement of the grinding media is described as a statistical variable, which means that certain deviations are expected [176]. The process parameters must be adapted and optimized for each individual material system to obtain the aimed properties [175]. Given the equation for *SN*, it is expected that a longer milling time and a higher rotational speed result in multiple stress events and, consequently, in smaller particle sizes. This correlation has also been demonstrated qualitatively for fuel cell inks by Lindermeir et al. [106], and simultaneously to the research in this work by Baez-Cotto et al. [103] and Liu et al. [100].

It is assumed that *SN*, as a measure of particle break-up, can specifically influence the particle size distribution (PSD) of the ink. Using the above-described correlations, different and comparable *SN* values are generated by adjusting the grinding time and speed to produce different or similar PSD values. The influence of the PSD on the formation of cracks in catalyst layers produced from the inks is then investigated. Chapter 4 discusses the relationship between the grinding process and ink formulation to clarify

Hypothesis 1. Therefore, a more grounded knowledge of the formation of cracks within catalyst layers is necessary, which is provided in the following.

2.2 Formation of cracks

An issue affecting (long-term) cell performance is cracks in catalyst layers. Although their influence is not fully understood, they cause more negative than positive effects (see Appendix 9.1). The consensus in the literature is to avoid cracking of the catalyst layers. Therefore, it is necessary to understand how they form. In this study, cracks are used to analyze the quality of the layer and evaluate the influence of different process parameters on its production, such as milling time and rotational speed during ink processing, the effect of the coated substrate, and the influence of temperature and relative humidity during drying. Cracking is a known phenomenon across a wide range of applications, e.g. fuel cell or battery electrodes, mud, blood droplets or paintings [76,177–179]. Fundamentals are outlined in the following.

Individual cracks occur in different forms. They are described by their shape as I-, U-, V-, Y-, or T-shaped cracks. I-shaped cracks are typically the result of isolated primary cracking. However, when material anisotropy dominates, primary cracks may also exhibit U- or V-shaped forms. Y- and T-shaped cracks are indicative of secondary crack formation. [58]

Cracks form during the drying of particulate films due to arising stresses during film solidification.[1] The solvents evaporate from the porous particle network, creating capillary pressures. This causes stresses in the pore network. If the film cannot compensate for these stresses, micro-cracking and, later, macro-cracking will occur. [181,182] Kumano et al. [58] defined three types of

[1] The author collaborated on studies to determine the drying time until crack formation. The results are published as peer-revied article: Zimmerer N, **Quarz P**, Janning L, Scharfer P, Schabel W. *In-situ investigation of crack formation during drying of catalyst layers for polymer electrolyte membrane (PEM) fuel cells and electrolyzer*. Colloids and Surfaces A: Physicochemical and Engineering Aspects 2026;728:138807. https://doi.org/10.1016/j.colsurfa.2025.138807, referred to as [180].

cracks: primary cracks, secondary cracks, and defect cracks caused by the presence of critical defects, which locally trigger higher stresses than the fracture toughness. Secondary cracks occur as extensions or junctions of primary cracks, especially in thicker films [183]. Primary cracks are cracks without detectable defects and depend, among other things, on the thickness of the drying film when solidifying. Therefore, the model of the critical crack thickness (CCT) was developed. It indicates the height above which cracks will occur. Basically, the CCT is a function of the drying-induced stress and the fracture resistance of the film, which is a function of several material specific parameters [169]. Based on the Griffith's criterion [184] for fracture mechanics, Tirumkudulu et al. [185] and Singh et al. [182,186] developed a semi-empirical model for calculating the CCT in aqueous (monomodal) particulate films. A distinction must be made between hard and soft, deformable particles. Eq. (2.5) shows the model for hard particles, like the catalyst particles investigated in this thesis.

For porous films with hard particles, one influencing factor for crack formation is the size of the involved particles. Smaller particles result in a lower CCT. This is caused by the smaller particle size leading to a smaller pore diameter and thus to an increase in capillary pressure and higher stresses in the porous system. [182,186]

$$h_{\mathrm{CCT}} = 0.64 \left(\frac{G M \phi_{\mathrm{rcp}} r^3}{2\gamma_{\mathrm{L}}} \right)^{\frac{1}{2}} \left(\frac{2\gamma_{\mathrm{L}}}{(-p_{\mathrm{max}}) r} \right)^{\frac{3}{2}} \tag{2.5}$$

h_{CCT}	Critical crack thickness in µm
G	Shear modulus of the particles in MPa
M	Coordination number (dimensionless)
ϕ_{rcp}	Particle volume fraction at random close packing in vol%
r	Particle radius in µm
γ_{L}	Surface tension of the solvents in N m^{-1}
p_{max}	Maximum capillary pressure in Pa

The CCT model is based on several assumptions and simplifications [182]. For example, a rigid substrate and no slip between substrate and film is assumed. This causes the film to consolidate vertically to the plane. Furthermore, particle

size distributions (PSD) and particulate films with binders are not addressed. It is known that the addition of polymeric binder improves crack resistance [170]. With respect to particle size distributions, Wu and Francis [187] reported an increasingly inhomogeneous stress development behavior within thin films. Wider particle size distributions exhibit higher stresses, which are attributed to increased particle packing density, smaller pores and higher capillary pressures. In addition, the pH can affect the repulsive forces of individual particles and polymers within the film and therefore the CCT [169,188]. With respect to the ionic ionomer, this may be particularly relevant for fuel cell inks. The influence of a flexible substrate that undergoes changes in volume, similar to the behavior of a fuel cell membrane, on the model equation that assumes a rigid substrate is still open.

The concept of CCT has been adopted for fuel cells and the CCT value has been determined experimentally for some catalyst ink formulations and process conditions. Kumano et al. [58] used the original definition and determined the CCT as the film thickness at which no spontaneous primary cracks occur. For this purpose, they filtered out large agglomerates from the ink that would otherwise cause defect cracks. In contrast, Hoffmann et al. [62] defined the CCT as the film thickness at which the total crack area exceeds 1 % of the entire layer area, as their films had a (basic) proportion of defect cracks that existed independently of the film thickness due to the non-existing removal of large agglomerates. The more pragmatic definition of CCT proposed by Hoffmann et al. and the fundamentals of crack formation, particularly with regard to particle size and distribution, are of central importance for the subsequent discussion of the test results. As cracks form during the drying of a catalyst layer, the focus of the next chapter is on this essential process step.

2.3 Drying of particulate films and solvent mixtures

Drying describes the removal of solvents from a product by the application of thermal energy. This process involves several steps: the liquid solvent must be converted to a vapor state and then it must be removed. In the case of porous

or polymeric materials and solvent mixtures, the transport of the solvent in the liquid phase to the liquid-gas interface must also be taken into account. In convection drying, solvent evaporation is caused by thermal energy input by tempered gas, often air, flowing through or over the material. Heat and mass transport are coupled (see Lewis analogy in Appendix 9.3). The important equations and correlations to understand this work are outlined in the following and in Appendix 9.3. [189]

The drying of thin films is described in multiple steps, which are shown schematically in Figure 5 for two evaporating solvents 1 and 2 ($\dot{m}_1$, $\dot{m}_2$). During the first drying phase, the solvent evaporates from the surface of the product and the mass of the sample decreases linearly with time (Figure 5 a). A constant wet-bulb temperature results in the film. During the evaporation of the solvent, the particles move closer together, forming a porous network.

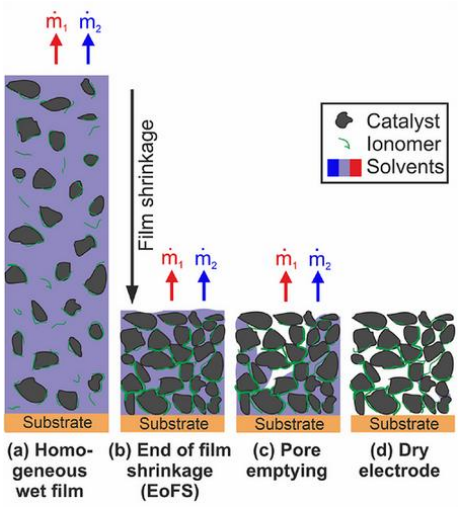

Figure 5: Schematic illustration of the drying steps of a catalyst ink (a–d) from a homogenous wet ink film to the dry electrode. The film shrinks due to solvent evaporation (shown as arrows) until the end of film shrinkage (EoFS). Afterwards, the solvents evaporate from the pores within the porous network. [190]

At the end of film shrinkage (EoFS), the resulting porous network is completely filled with the solvents (Figure 5 b). Given the initial solid content of 10 wt% in the inks examined in this study, most of the solvents evaporate during the first drying period before the EoFS. As the drying process continues, capillary forces in the thin pores transport the solvents to the film surface, where they still evaporate at a constant rate (Figure 5 c). Larger pores empty in favor of smaller ones. Towards the end of drying, remaining liquid clusters that are not accessible via capillary transport must evaporate from within the porous structure. This creates a transport resistance, which lowers the overall drying rate. Consequently, the film temperature rises towards the end of the drying process. As the film solidifies and the pores empty, tensile stresses are generated within the film, which can result in the formation of cracks and other defects [185,191]. When the evaporation of the solvents is finished, the drying process ends and a porous catalyst layer is present (Figure 5 d). Some solvents may still be present within the electrode due to hygroscopic equilibrium and ambient humidity. [189]

The drying is modeled by describing the evaporation of the solvents. For this purpose, the temperature-dependent vapor pressure curves are used. Studying mixtures, the interactions between the solvents during evaporation must also be taken into account (Eq. (2.6)) [189]. These are considered in the form of the component-dependent activity, which is described e.g. by the van Laar model [192]. During the first drying period, the effects of the solids are negligible due to their low concentration.

$$\tilde{y}_i^{\mathrm{Ph}} = \frac{p_{i,\mathrm{Ph}}^{*}(T_{\mathrm{film}})\,\gamma_i\left(\tilde{x}_i^{Ph}\right)\cdot\tilde{x}_i^{\mathrm{Ph}}}{p} \tag{2.6}$$

$\tilde{y}_i^{\mathrm{Ph}}$	Molar fraction of component *i* in the gas phase at the phase boundary in mol%
$p_{i,Ph}^{*}(T_{\mathrm{film}})$	Temperature-dependent vapor pressure of component *i* at the phase boundary in Pa
$\gamma_i(\tilde{x}_i^{\mathrm{Ph}})$	Composition-dependent activity coefficient of component *i*
$\tilde{x}_i^{\mathrm{Ph}}$	Molar fraction of component *i* in the liquid at the phase boundary in mol%
p	Ambient pressure in Pa

In this work, mixtures of 1-propanol and water are studied. In the range between 0 and 100 °C, the vapor pressure curves of these two solvents are very close to each other (see Appendix 9.3). The pure substances are almost equally volatile at each temperature [193]. Based on this, a vapor-liquid equilibrium (VLE) with nearly similar gas and liquid compositions can be derived for a hypothetical ideal liquid mixture (assuming all $\gamma_i(\tilde{x}_i) = 1$). For an exemplary temperature of 17.5 °C, this is shown in the orange line in the McCabe-Thiele diagram in Figure 6. The x-axis describes the mass fraction of 1-propanol in the liquid phase and the y-axis the mass fraction of 1-propanol in the binary vapor above.

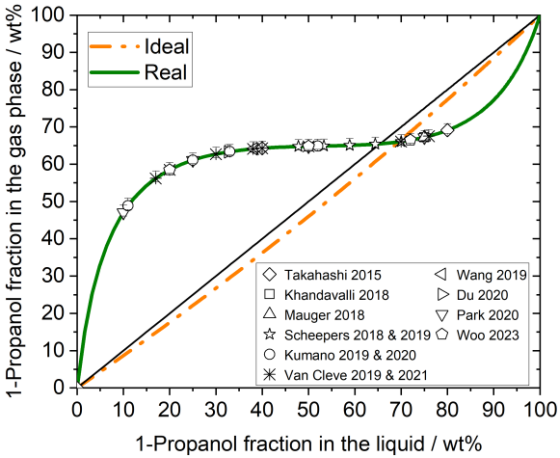

Figure 6: McCabe-Thiele diagram of 1-propanol/water mixtures at 17.5 °C. Assumed ideal (orange) and real (green) mixture behavior and ink compositions from literature [42,44,57,58,60,72,76,78,81–85]. If the vapor-liquid-equilibrium (VLE) curve is above the bisector, then 1-propanol will evaporate preferentially. Conversely, if the VLE curve lies below the bisector, water evaporates preferentially. The greater the distance from the bisector, the greater the difference in composition between the liquid and gas phases will be. An azeotrope is present at the intersection. *Data previously published in Quarz et al.* [190].

However, since 1-propanol/water mixtures do not show ideal behavior, the interactions between the two components need to be considered. In particular, the activity coefficients of the dilute component are high for mixtures with a highly enriched component (γ_i = f($\tilde{x}_i$), see Appendix 9.3) [192]. The thermodynamic equilibrium of the non-ideal mixture shows the typical S-shaped course of an azeotropic mixture (Figure 2: green line) with the azeotropic mass composition of $x_{1,\mathrm{az}}$ = 65.5 wt% (molar composition: $\tilde{x}_{1,\mathrm{az}}$ = 36.3 mol%) at 17.5 °C.[2] The liquid temperature of 17.5 °C shown here is the result of experiments on selective evaporation carried out later (see Chapter 6.1). The index 1 refers to 1-propanol, which is the lower-boiling point solvent in the mixture. At the azeotropic point (az), the solvent mixture has the same composition in the vapor and in the liquid phase (Eq. (2.7)).

$$y_{i,\mathrm{az}} = x_{i,\mathrm{az}} \quad \text{resp.} \quad \tilde{y}_{i,\mathrm{az}} = \tilde{x}_{i,\mathrm{az}} \tag{2.7}$$

$y_{i,\mathrm{az}}$ Mass fraction of component *i* in the gas phase at the azeotrope az in wt%

$x_{i,\mathrm{az}}$ Mass fraction of component *i* in the liquid at the azeotrope az in wt%

$\tilde{y}_{i,\mathrm{az}}$ Molar fraction of component *i* in the gas phase at the azeotrope az in mol%

$\tilde{x}_{i,\mathrm{az}}$ Molar fraction of component *i* in the liquid at the azeotrope az in mol%

When vaporizing the mixture at the azeotropic composition, the solvent composition remains constant during the solvent removal. For compositions below the azeotropic point ($x_1 < x_{1,\mathrm{az}}$), there is a selective accumulation of 1-propanol in the gas phase. If this vapor is removed, e.g. in a convective flow, a relatively larger amount of 1-propanol will be taken out. The composition of the remaining liquid changes according to a distillation process. Conversely, for $x_1 > x_{1,\mathrm{az}}$, water is selectively enriched in the vapor and thus the 1-propanol concentrates in the liquid. Evaporation at the azeotropic composition requires

[2] At isothermal equilibrium, the sum of the partial pressures of the solvent vapors depends on the solvent composition and is between 0.017 (pure 1-propanol) and 0.026 bar at the azeotrope at 17.5 °C. In a pure binary liquid system and its binary vapor, this equals the system pressure.

a high degree of control of the process parameters, since e.g. minimal temperature fluctuations will change the azeotropic composition.

The compositions of various 1-propanol/water inks from literature are shown in Figure 6. All of the points are located on the VLE line, accounting for the real vaporization behavior of the mixtures at 17.5 °C, which is the liquid temperature of the experiments conducted in this study. As this is not necessarily the relevant (drying) temperature in the literature experiments, the corresponding temperature-dependent y_1-values for a film temperature range of 10 – 35 °C are given in the form of error bars. Due to evaporative cooling, this range corresponds to drying air temperatures of approx. 20 – 120 °C for convection drying. As is evident from the different positions in the diagram, very different drying behaviors and selectivities are expected for each of the quoted inks. In particular, near the azeotropic composition, small changes in drying conditions (e.g. temperature change) can change the selectivity and lead to preferential 1-propanol or preferential water evaporation. This actually affects the drying path, the interaction between ionomer and particles during layer formation, and ultimately the microstructure of the layer [88,89].

So far, discussions in the fuel cell literature and what has been described above primarily focus on the thermodynamic state of the vaporization of the binary solvent mixture and its binary vapor at the boiling temperature and boiling pressure. However, drying does not take place under boiling conditions.

The term azeotrope (from the Greek *azeotropos* "boiling without change") originally defines the thermodynamic VLE, in which the vapor and liquid composition of the mixture are the same at boiling conditions (see Eq. (2.7)) [194,195]. However, in drying, an inert gas phase is normally present, e.g. in the form of the ambient or drying air. The solvent can pass into the gas phase at a given pressure below the boiling temperature, e.g. when drying laundry. The additional inert component converts vaporization into evaporation or drying when a dry good remains. In addition to thermodynamic equilibrium at the phase boundary, boundary layers form between the phase boundary and the bulk of the gas or liquid phase. The boundary layer and the kinetics within influence the composition of the non-selective drying composition [196].

In the fuel cell literature, if selective drying – i.e., the preferential evaporation of one solvent – is considered at all, the azeotropic composition (purely thermodynamic) is sometimes assumed to be the key composition for unselective drying [103]. No distinction is made between vaporization at boiling conditions and the actual evaporation that takes place below the boiling temperature, including the influence of the gas phase mass transport kinetics. With long interaction times between the liquid and gas phases, quasi-azeotropic conditions can indeed be achieved, e.g. in a saturator. In most cases, however, the residence times are not long enough to achieve equilibrium in the boundary layers, leading to the incorrect assumption of non-selective drying at the azeotropic composition. In any case, the use of the term azeotrope without boiling conditions is misleading. [196] For this reason, the (thermodynamic) azeotrope is substituted by the 'dynamic azeotrope' or 'pseudo azeotrope' as introduced by Riede and Schlünder [196], which takes into account the dynamic gas kinetics in solvent mixture drying.

To avoid confusion, Schlünder [195] proposed a new term, a-rheo-trope, in reference to the original Greek term for mass transfer-controlled processes, replacing the boiling *zeo* with the Greek word for flow *rheo*, which refers to the relative component evaporation flow. Schlünder's proposed name arheotrope means "flow without change". [197,198] This term is not yet widely referred to, but it describes the processes involved very well.

In general, E.-U. Schlünder (1929–2019) and his research group conducted pioneering work on mixture evaporation and the analytical description of binary solvent drying [195–208]. The considerations derived from this work form the essential basis for the descriptions of mixture evaporation presented in this thesis. Important definitions and equations are outlined below.

The difference between azeotrope and arheotrope in a nutshell: Azeotrope describes the state of an unchanging composition of a liquid mixture during vaporization (at boiling conditions) (see (2.7)). This process is essentially controlled purely thermodynamically. Arheotrope (ar), on the other hand, describes the state of unchanging composition of an evaporating liquid mixture. Thermodynamics and gas kinetics (in the boundary layer above the liquid

phase) must be considered. The composition of the evaporating material flux (from the liquid to the gas phase) is equal to the composition of the liquid. It is expressed with masses (Eq. (2.8)) or moles (Eq. (2.9)). [201]

$$\dot{r}_{i,\mathrm{ar}} = x_{i,\mathrm{ar}} \tag{2.8}$$

$\dot{r}_{i,\mathrm{ar}}$ Relative mass flux of component *i* at the arheotrope in $\frac{\mathrm{g\,s^{-1}}}{\mathrm{g\,s^{-1}}}$%

$x_{i,\mathrm{ar}}$ Mass fraction of component *i* in the liquid at the arheotrope in wt%

$$\tilde{\dot{r}}_{i,\mathrm{ar}} = \tilde{x}_{i,\mathrm{ar}} \tag{2.9}$$

$\tilde{\dot{r}}_{i,\mathrm{ar}}$ Relative molar flux of component *i* at the arheotrope in $\frac{\mathrm{mol\,s^{-1}}}{\mathrm{mol\,s^{-1}}}$%

$\tilde{x}_{i,\mathrm{ar}}$ Molar fraction of component *i* in the liquid at the arheotrope in mol%

The gravimetric reference $\dot{r}_i$ is more practical and intuitive (2.10). For this reason, it is defined and applied in this work. However, the relative mass flux is originally defined in relation to molar quantities (Eq. (2.11)) [201]. The following equations can be converted accordingly.

$$\dot{r}_i = \frac{\dot{m}_i}{\dot{m}_{\mathrm{total}}} \tag{2.10}$$

$\dot{r}_i$ Relative mass flux of component *i* at the arheotrope in $\frac{\mathrm{g\,s^{-1}}}{\mathrm{g\,s^{-1}}}$%

$\dot{m}_i$ Mass flux of an evaporating component *i* into the gas phase in g s^{-1}

$\dot{m}_{\mathrm{total}}$ Total evaporation mass flux in g s^{-1}

$$\tilde{\dot{r}}_i = \frac{\dot{N}_i}{\dot{N}_{\mathrm{total}}} \tag{2.11}$$

$\tilde{\dot{r}}_i$ Relative molar flux of component *i* in $\frac{\mathrm{mol\,s^{-1}}}{\mathrm{mol\,s^{-1}}}$%

$\dot{N}_i$ Molar flux of an evaporating component *i* into the gas phase in mol s^{-1}

$\dot{N}_{\mathrm{total}}$ Total molar evaporation flux in mol s^{-1}

In selective evaporation, one solvent evaporates in a greater proportion than it is in the liquid. If $\tilde{\dot{r}}_i$ resp. $\dot{r}_i$ is understood as the composition of the evaporation stream, the difference to the composition of the liquid is used to determine the selectivity of the drying process (Eqs. (2.12) and (2.13)). [201] As before, the

molar description comes from Schlünder, and the gravimetric redefinition was adapted for this work.

$$S_i = \dot{r}_i - x_i \tag{2.12}$$

S_i Gravimetric selectivity of the evaporation process in wt%
x_i Mass fraction of component *i* in the liquid in wt%

$$\tilde{S}_i = \tilde{\dot{r}}_i - \tilde{x}_i \tag{2.13}$$

$\tilde{S}_i$ Molar selectivity of the evaporation process in mol%
$\tilde{x}_i$ Molar fraction of component *i* in the liquid in mol%

For $\tilde{S}_i > 0$, component *i* evaporates preferentially and depletes relatively in the liquid phase, the composition of the (remaining) liquid changes. For $\tilde{S}_i < 0$, component *i* evaporates under-proportionally and accumulates relatively in the remaining solvent mixture. However, the total amount of component *i* in the mixture is always reduced in both cases as long as $\tilde{\dot{r}}_i > 0$. For $\tilde{S}_i = 0$, the composition of the outgoing evaporating flux is the same as the composition of the liquid. An arheotrope is present and Eq. (2.8) applies. The drying is non-selective and the compositions remain constant. [201]

To describe the mass transport processes, e.g. in form of $\tilde{\dot{r}}_i$ during the evaporation of solvent mixtures, the kinetics in the gas phase must be specified (Eq. 2.14). One important parameter is the mass transfer coefficient, which is proportional to the diffusion coefficient of component *i* in the gas phase. Using the Lewis analogy, it is related to the heat transfer coefficient of the drying process (see Appendix 9.3). The driving gradient is the molar composition at the phase boundary $\tilde{y}_i^{Ph}$ resulting from the thermodynamic equilibrium there (see Eq. (2.6)) and the bulk composition $\tilde{y}_i^{\infty}$. $\tilde{y}_i^{\infty}$ is defined by a potential preloading of the drying air, e.g. the relative air humidity. [202]

$$\dot{N}_i = \tilde{\dot{r}}_i \, \tilde{\rho}_{\mathrm{g}} \, A_{\mathrm{Ph}} \, \beta_{i,\mathrm{g}} \, \ln\left(\frac{\tilde{\dot{r}}_i - \tilde{y}_i^{Ph}}{\tilde{\dot{r}}_i - \tilde{y}_i^{\infty}}\right) \tag{2.14}$$

$\tilde{\rho}_{\mathrm{g}}$ Molar gas density in kg mol^{-1}
A_{Ph} Liquid-gas-interphase in m²
$\beta_{i,\mathrm{g}}$ Mass transfer coefficient of component *i* into the gas phase g in m s^{-1}

$\tilde{y}_i^{\infty}$ Molar fraction of component *i* in the bulk of the gas phase in mol%

The decreasing amount of solvent due to drying can be determined from the total and component molar balances of the liquid (see Eqs. (9.7) and (9.8) in Appendix 9.3). The mass and mass quantity ratios correlate, as does the volume ratio when excess volumes are neglected (see Appendix 9.2). Furthermore, under the assumption of a constant interfacial area, the height ratio also correlates. Assuming no film-side mass transport resistance, it is possible to compare height ratios calculated from heights of different magnitudes. [201] In this work, the experimental mass data will be plotted as height ratios and explained using the above-described molar considerations.

According to Schlünder [201], if the evaporation flow is set in relation to the drying gas flow, two extreme cases can be distinguished. This is done using the so-called number of transfer units (NTU). In the $NTU_{i,\mathrm{g}} \rightarrow \infty$ scenario, evaporation dominates and the drying process is thermodynamically controlled. For $NTU_{i,\mathrm{g}} \rightarrow 0$, the gas-side mass transport resistance is pivotal, and gas kinetics become significant (see Appendix 9.3). This differentiation is specifically investigated experimentally in the drying experiments (see Chapter 1). The effects on selective drying behavior and the non-selectively drying solvent composition are the main focus, dealing with Hypothesis 2, where the drying path is linked to the microstructure formation of the fuel cell electrode.

Before examining catalyst ink drying and investigating crack patterns and their causes, the materials and methods used to produce and characterize the inks and coatings will be reviewed. The choice of material and its processing influence crack formation, while characterization methods influence their analysis and are therefore described in detail.

3 Materials and Methods

Experiments, model development and simulation are required to address the hypotheses (see Chapter 1.6). This chapter lists the materials and test setups used to examine the hypotheses and research questions. A catalyst ink suitable for producing catalyst-coated membranes (CCM) is required, as well as subsequent coating and drying steps, described below. Reference is always made to the relevant hypothesis. The essential characterization methods for validating the hypotheses are also outlined.

Hypothesis 1 postulates that the particle size distribution (PSD) of the catalyst ink is a key factor in determining the appearance of layers produced using these inks. To obtain inks with different PSDs, the processing of the ink is varied specifically and its influence on the PSD is analyzed. To further proof the hypothesis, the ionomer-to-carbon ratio (*I/C*), and therefore the ink formulation, is varied in a targeted manner. The PSD is determined and a procedure for evaluating the layer image is developed. The latter is achieved through an optical analysis of the layers for cracks.

Hypothesis 2 addresses the drying behavior of the layers. The investigation is carried out using a solvent system that is relevant and frequently used: 1-propanol and water. To understand the occurring effects, the system is abstracted at various levels of complexity. Various experiments are conducted in different drying setups. A simulation is also used to generate understanding for Hypothesis 2.

Further experiments are necessary to evaluate Hypothesis 3, which focuses on the substrate and its interaction with the ink. Deformation of the membrane is investigated and also the role of a supporting layer and effects in the application of the second catalyst layer on the second side of the membrane to finally form the CCM. These are described below.

3.1 Materials

A wide range of materials can be used to produce catalyst-coated membranes (CCMs) for fuel cells. The materials used in this thesis were selected based on their frequent appearance in the literature to enable comparison. The coating inks use a catalyst commonly employed in industry, which, as is typical for catalysts, is supplied as an agglomerated powder. With regard to Hypothesis 1, the particle size distribution of the catalyst particles is postulated to be important. A common Nafion dispersion consisting of mainly two solvents is used. This means that the effects of mixture evaporation (regarding Hypothesis 2) and membrane solvent interactions (regarding Hypothesis 3) are relevant. The choice of solvents is based in particular on the selection of Nafion D2020 and its constituents, namely 1-propanol and water.

Catalyst: Tanaka TEC10EA50E

The catalyst (Tanaka Kikinzoku Kogyo K.K., Japan) consists of carbon support material doped with platinum, distributed on the surface of the carbon in the form of nanoparticles. The 50 in the name indicates the platinum group metal content in wt%. According to the manufacturer, the platinum content in the batches varies between approx. 46 – 47 wt%. The support material is graphitized carbon with a specific surface area of 150 $m^2\ g^{-1}$. The primary particles are in the order of 50 – 100 nm, but are initially present as agglomerated powder. The aim of the ink manufacturing process is to break up the agglomerates and to mix all ink components.

Ionomer: Nafion D2020

The ionomer used is Nafion (Chemours, USA). It is a copolymer of Teflon with sulphonic acid groups on the side chains and the chemical name 2-[1-[difluoro[(trifluoroethenyl)oxy]methyl]-1,2,2,2-tetrafluoroethoxy]-1,1,2,2-tetrafluoroethanesulfonic acid. It is hence a perfluoro sulphonic acid (PFSA),

which belongs to the family of per- and polyfluorinated alkyl substances (PFAS[1]). The structure of Nafion is shown in Figure 7.

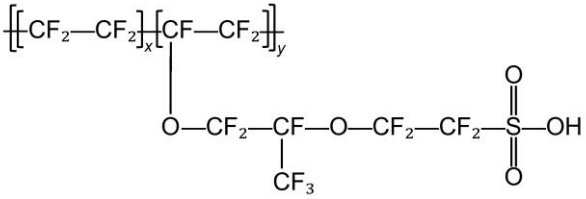

Figure 7: Chemical structure of Nafion ionomer. Adapted from [212].

The Nafion used is supplied as dispersion D2020 (distributor IonPower, USA). It contains 20 wt% Nafion with an equivalent weight (EW) of 1000 g mol^{-1} dispersed in a mixture of water (34 wt%), 1-propanol (44 wt%) and ethanol (< 2 wt%). The small amount of ethanol is neglected in the following because of its low content and high volatility, which is assumed to evaporate very quickly. According to the manufacturer's description, the dispersion has a density of 1.02 g cm^{-3}. [79] Nafion itself is colorless and is listed with CAS number 31175-20-9. The ionomer allows proton conduction in the catalyst layer. Due to the strongly acidic sulphonic acid group, Nafion can selectively conduct protons and other cations. Nafion binds to the catalyst particles in the ink, where it also acts as a binder during film solidification. When attached to the catalyst, it stabilizes dispersed particles and inhibits re-agglomeration due to steric and electrostatic repulsion. It is also used as proton conducting membranes, which will be discussed later in this chapter.

[1] Also known as "forever chemicals", PFAS are particularly stable, long-lasting molecules. They are difficult and costly to degrade and remove from the environment. During the preparation of this work, policies to reduce PFAS pollution and international bans on various PFAS chemicals have been and are being discussed and adopted [209–211]. PFAS for use in fuel cells and electrolyzers have so far been explicitly excluded from bans. Substitutes are being researched, but are not (yet) state of the art.

Solvents: 1-Propanol and water

The ink solvents used are 1-propanol (Carl Roth GmbH, Germany; > 99.5 %) and ultrapure water (Milli-Q® EQ 7000, Merck, Germany). 1-propanol has a terminal hydroxyl group and a molar mass of 60.1 g mol^{-1}. Water, on the other hand, is about 3.3 times lighter with a molar mass of 18.0 g mol^{-1}. This leads to large differences when considering quantity in mass or mol units.

The boiling temperatures at 1.013 bar of 1-propanol is 98 °C and for water 100 °C. For a wide range of temperatures, the vapor pressure curves are very close to each other (see Appendix 9.3). But, a clear difference can be seen when looking at the diffusion coefficients in air. According to Fuller [213], water diffuses with 2.50 10^{-5} m^2 s^{-1} in air about 2.5 times faster than 1-propanol with 1.02 10^{-5} m^2 s^{-1} (25 °C, 1.013 bar). The diffusion coefficient depends on the temperature. However, the ratio of the two diffusion coefficients is independent of temperature (see Appendix 9.3). Both volatility and diffusion properties are important when evaluating Hypothesis 2.

Substrate: Nafion 212 membrane

The Nafion membrane NR212 (Chemours, USA) used is approx. 50.8 µm thick and has an equivalent weight (EW) of 2100 g mol^{-1}. It is made of perfluoro sulfonic acids (PFSA). The membrane is supplied on a 75 µm thick mechanically stabilizing backing foil and a protective film. The protective film must be removed for coating while the backing film is used to increase the mechanical stability of the membrane during coating of the first catalyst layer on the membrane. The backing film must also be removed for coating the second side. Unless otherwise stated, the ink is always applied and dried on the membrane including the backing film.

The trend goes to use thinner or reinforced membranes to suppress membrane swelling when in contact with solvents and to decrease the proton conductivity resistance. However, Nafion 212 membrane was chosen, because swelling effects and challenges of membrane direct coating are obvious. Understanding and handling of this membrane and its effects are thought to be more difficult than with improved membranes. Results can be transferred.

Inert substrates: Decal substrate and PTFE substrate

Polytetrafluoroethylene (PTFE), trade name Teflon, serves as an inert substrate for the catalyst layers. Due to its low adhesion properties, it is suitable as a decal substrate in the electrode production. PTFE virginal substrates with a specified thickness of 50 µm and additionally a glass fiber-reinforced PTFE substrate with woven structure consisting of 64 % PTFE polymer were used (both: Hightechflon GmbH & Co. KG, Germany). Reinforced PTFE is also often used as decal substrate for PEM coatings. The decal substrates are used to enable comparison of decal coating to membrane direct coating.

3.2 Ink formulation and processing parameters

In-depth knowledge of the catalyst-containing coating ink is required for research into the effects of manufacturing catalyst-coated membranes (CCM). Hypothesis 1 addresses the influence of the ink's particle size distribution (PSD) on the resulting catalyst layers. Different ink processing methods are used to produce inks with different PSDs. First, a suitable ink production device must be identified, purchased and operationalized. Next, a suitable ink composition must be selected. The process parameters are then varied in a targeted manner to validate the hypothesis. Furthermore, based on the findings from Hypothesis 1, a standard procedure for ink production is defined. This then forms the basis for testing Hypotheses 2 and 3. This chapter lists the investigated ink compositions and process parameter variations.

A ball mill was identified as a suitable ink manufacturing device with the ability to set different PSDs via various process parameters. The advantages of breaking up the agglomerates of catalyst particles and simultaneously mixing all ink components in a scalable system are decisive here (see Chapter 1.3). A CN 10, APS 250 (VMA Getzmann GmbH, Germany) ball mill was then purchased and put into operation. The reproducibility of parameter variations and ink properties was confirmed in preliminary tests.

Two studies were carried out on the subject of ink production (see Chapter 0), one on the influence of the formulation (initial solvent composition) with

constant process parameters (see Appendix 9.2) and one on the influence of the process parameters (grinding time and speed) with a constant ink formulation (see Chapter 0). Based on the findings, a standard ink composition and processing were developed for further investigations (see Chapters 5 and 1).

For most experiments, 30 ml of ink were processed with 30 ml grinding media made of yttrium-stabilized zirconium oxide (d_{GM} = 0.6 – 0.8 mm). All inks were produced with a constant solid content of 10 ± 0.5 wt% (*Pt/C* catalyst and ionomer). The standard ionomer-to-carbon ratio (*I/C*) was 1.0. For selected trials, the *I/C* was increased to 1.2 and 1.5 (see Chapter 4.3).

In the study of the influence of the initial solvent composition, the 1-propanol content of the total solvent composition varies from 20 to 50 and 80 wt%. Table 1 shows the inks produced in the variation of the initial solvent content with constant process parameters. Except this study, all experiments have a total solvent composition of 20 wt% 1-propanol and 80 wt% water.

Table 1: Ink parameters in the study on the initial solvent composition: The ink formulation with varying solvent compositions, constant ionomer-to-carbon ratio *I/C* and solid content x_{solid} are given for each produced ink. The applied process parameters (milling time *t* = 3 h and rotational speed *n* = 1000 rpm) remain constant.

Ink	***t***	***n***	**Solvent composition**		***I/C***	x_{solid}
			1-propanol	**Water**		
	h	**rpm**	**wt%**	**wt%**	**g g^{-1}**	**wt%**
I	3	1000	20	80	1.0	10
II	3	1000	50	50	1.0	10
III	3	1000	80	20	1.0	10

In the study on the ink processing, two process parameters were investigated in detail: the milling time and the rotational speed of the grinding disk. First, the milling time was varied in a range from 1 h to 24 h at a constant rotational speed of 1000 rpm (Table 2). The applied ink processing times are much shorter than by Baez-Cotto et al. [103] or Liu et al. [100]. This is due to the higher rotational speed in the conducted experiments. As a second parameter,

the rotational speed was varied from 1000 to 2000 rpm. Hereby, two test series are distinguished. On the one hand, the milling time remained constant with 3 h. In a second series, the milling time was adapted to the rotational speed in order to obtain the same stress number (*SN*), calculated according to Eq. (2.4). Table 2 provides an overview of the process conditions for the different inks. The resulting *SN* and stress intensity (*SI*) are also given.

Table 2: Ink parameters in the study on the ink processing: With increasing grinding time *t* or increasing rotational speed *n* the stress number *SN* increases. The resulting stress intensities *SI* and, additionally, the ionomer-to-carbon ratio *I/C* are given for each produced ink. All other formulation parameters remain constant (10 wt% solid content, and 20 wt% 1-propanol, 80 wt% water in the residual 90 wt% solvent composition, referring to Ink I in Table 1).

Ink	***t***	***n***	***SN***	***SI***	***I/C***
	h	**rpm**	**10^8 m^{-1}**	**10^{-8} kg m^{2}s^{-2}**	**g g^{-1}**
A	1	1000	1.11	1.14	1.0
B	3	1000	3.34	1.14	1.0
C	6	1000	6.68	1.14	1.0
D	24	1000	26.7	1.14	1.0
E	24	1000	26.7	1.14	1.2
F	24	1000	26.7	1.14	1.5
G	4.5	1500	7.52	2.57	1.0
H	3	2000	6.68	4.57	1.0

Resulting from the investigations in Chapter 0, the experiments discussed in Chapters 5 and 1 used the ink formulation and process conditions of Ink I (Table 1) resp. Ink B (Table 2).

3.3 Analysis of ink properties

Investigating Hypothesis 1 requires knowledge of the particle size distribution (PSD) of the catalyst inks produced. To determine the PSD, a Mastersizer 3000 including a dispersion module Hydro MV (Malvern Panalytical, UK) was purchased. The dynamic light scattering of the two integrated laser beams (470 and 633 nm) in the measuring system enables measurements to be taken of the

ink sample particles in the size range from 10 nm to 3.5 mm. The ink is diluted about 1:10,000 in an ultrasonic-degassed solvent mixture. The dispersing solvent mixture has the same composition as the solvents of the investigated ink to not affect ionomer modification and particle size due to changed composition.[2] In order to calculate the particle size from the measured refracted light distribution, the software of the measuring device requires the refractive indices of the particle material and the dilution solvent. The refractive index chosen for the dilution media was n_{solvent} = 1.34 and for the particles was n_{CB} = 1.746 for carbon black [214], as it is the main solid component. Platinum, ionomer and other additives could affect the refractive index, resulting in a slight shift of the measured particle size curves. However, qualitative comparability is given at identical measure settings and the measured absolute values are within the expected range.

3.4 Manufacturing of the catalyst layers

To investigate the influence of the ink's particle size distribution (PSD) on the layer pattern in the context of Hypothesis 1, catalyst layers must be produced. These must be fabricated under consistent and defined coating and drying conditions to ensure that any changes to the layers can be clearly attributed to variations in the ink's properties, primarily in terms of PSD. Layers must also be produced to validate Hypothesis 3. The interactions between ink and membrane require some adjustments to the drying setup. Details are explained below.

The catalyst layers were applied with a doctor blade (ZUA 2000, Zehntner-Testing-Instruments, Switzerland), allowing sheet-to-sheet production with many variations of ink and process parameters with minimal ink consumption, little wastage and short cleaning times. The ink application and the amount of ink simultaneously applied to the substrate are comparable to slot die coating,

[2] In pure water as dilution medium, e.g. the particles agglomerate during the measurement. This leads to falsified measurement results and must be avoided. Therefore, in this work, the same solvent composition is used for the dilution medium as in the ink.

a well-scalable process. Slightly modified setups were used for the investigations. Throughout all experiments, the coating speed was 10 cm s^{-1}. The coating gap was varied from 75 – 225 µm to achieve different wet film heights and consequently dry film thicknesses.

Unless otherwise described, the membrane was always coated with the stabilizing backing foil underneath. For coating directly onto the membrane, the doctor blade was run on a Polyethylene terephthalate (PET) mask for even gliding. If the doctor blade is moved directly over the membrane, it will not slide. This results in non-uniform movement and therefore uneven ink application. The thickness of the PET mask was considered in the total gap height. No coating mask was necessary for the tests on the decal substrates.

Isothermal film drying

The conclusive verification of Hypothesis 1 requires defined drying conditions, which are implemented using the 'BatchCoater' established within the research group [215–227]. By moving the sample periodically back and forth on a heated plate under 20 slot nozzles, a set (quasi-)isothermal temperature is forced on the film and held constant by a combination of conductive and convection drying. Isothermal drying enables the targeted investigation of the influence of temperature on film drying and the resulting layer. This set (quasi-) isothermal temperature is comparable to the film temperature resulting from convective energy input and evaporative cooling in pure convective drying and should not be confused with the significantly higher air temperature in convective drying without additional contact drying. The (quasi-) isothermal drying temperature was set to 25 °C (heating plate and air temperature). All coatings were dried within 5 min. The heat transfer coefficient as a measure of the drying air flow was set to 35 W m^{-2} K^{-1}. The defined heat transfer coefficient is relevant to the coupled mass transport, rather than the energy input (see Appendix 9.3). The resulting calculated mass transfer coefficients are 0.018 m s^{-1} for 1-propanol and 0.030 m s^{-1} for water into the drying air. Since the drying air has no pre-conditioning, the preloading of the air with water is not adjustable and is predetermined by the weather and seasonal variations in relative humidity. It ranged between 20 and 65 % relative humidity at 25 °C. For the

experiments described in this study, however, this does not significantly affect the selectivity of drying, since 1-propanol evaporates preferentially under all of these water preloadings with an initial solvent composition of 20 wt% 1-propanol and 80 wt% water (see Chapters 2.3 and 1). There is no preloading of the air with 1-propanol.

Experimental setup to study the influence of tensile stresses during film drying

Hypothesis 3 concerns the interactions between the coating ink and the membrane during direct coating. This is specifically carried out in a roll-to-roll setup because this is relevant to industry. This setup also allows for coating on both sides of the membrane. To simulate a Roll-to-Roll (R2R) process, the membrane is clamped during coating and dying. This setup was constructed for coating the second side of the membrane. During this process, tensile stresses prevail in the form of a web tension. To study the effects of these stresses, a setup was developed in which the membrane was clamped horizontally on one side. The other side is deflected 90° by a non-adhesive roll and has weights attached (Figure 8). By varying these weights (70 and 570 g) on the vertically suspended membrane, different tensile stresses in the range from 6 to 116 N cm^{-2} are created. Further information on the conversions and resulting tensions can be found in Appendix 9.6.

The setup is located under a 'Comb-Nozzle Impingement Dryer' with honeycomb nozzle array and integrated air extraction [218,228]. The heat transfer coefficient was set to 35 W m^{-2} K^{-1}. A drying air temperature of 82 °C was chosen to result in a film's wet-bulb temperature of 25 °C due to evaporative cooling for the given solvent composition and relative humidity. This correlates to the film temperature in the isothermal drying. Towards the end of drying, the film temperature rises and converges to the air temperature. The drying time was set to 5 min, as in the previous experiments with isothermal drying, since each layer dried within this time.

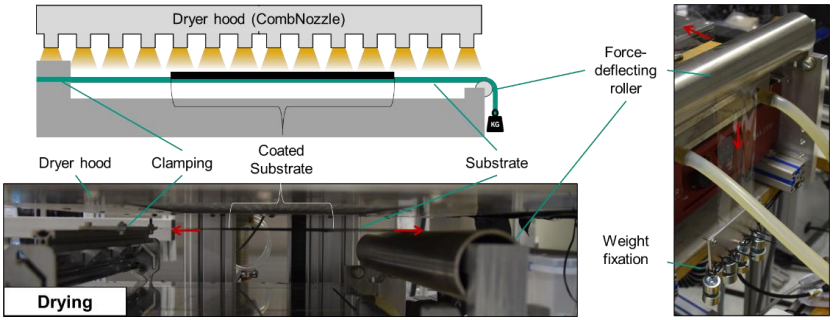

Figure 8: Experimental and schematic setup built here to study the influence of different tensile stress during drying. The substrate is tensioned horizontally. During drying, a web tension is applied to the substrate (shown in red arrows), caused by the weight of variable weights deflected in a horizontal direction by a roller.

3.5 Catalyst layer characterization

To validate the hypotheses of this work, it is necessary to analyze the manufactured catalyst layers in order to evaluate the correlations arising from the different processing parameters. The properties of the layers produced reflect the influences of the process conditions examined in Hypotheses 1 and 3. The layers are characterized optically, paying special attention to the appearance of cracks within the layers. To ensure comparability, the thickness of the dry layer is measured and kept constant. For analyses relating to Hypothesis 1, knowledge of the pore distribution within the layers is also required.

Surface images with top-light and back-light illumination

The layers are characterized using a camera (Nikon, Japan) and a VHX digital microscope (VH-Z100R objective, Keyence, Japan). Two distinct illumination techniques are employed to determine the crack pattern. The use of back-light facilitates the identification of cracks in the electrodes on a membrane since the light shining through the cracks causes them to appear white whereas the catalyst layer is black. Microscopic images of characteristic areas of the layer, approx. 1 x 1 cm², are taken by stitching. This involves placing and moving

the layer on a *xy*-table and taking successive images from different positions with 100x zoom, which are then combined to create an image with a larger recorded area. The evaluation is carried out using a machine-learning based image evaluation tool developed in a supervised Master's thesis[3]. Top-light illumination (200x zoom) is useful for obtaining information about the surface condition, e.g. occurrence of agglomerates, and when analyzing CCMs.

Measuring the dry layer thickness

Constant dry layer thickness (LT) enables an accurate comparison of the crack patterns in the catalyst layers. The LT is determined using a digital gauge (ID-H0530, Mitutoyo Japan) with a resolution of 0.5 µm. The LT is measured at 15 positions and an average value is calculated. In 3 different rows, 5 positions are measured perpendicular to the coating direction: approx. 2 cm after the start of the coating, in the middle and 2 cm before the end of the coating.

Determining the pore diameter distribution

Referring the pore size distributions of the produced layers to the particle size distributions of the respective catalyst inks helps to validate Hypothesis 1. The pore size distribution was analyzed by mercury intrusion (Poremaster GT33, Anton Paar, Austria). For this purpose, 3 cm x 3 cm samples from the catalyst layer (layer on membrane incl. backing foil) were measured. For the mass reference, the total sample weight (balance: Kern & Sohn GmbH, Germany, accuracy 0.1 mg) minus the substrate mass was determined via its weight per unit area. In a first low pressure analysis followed by a separate high pressure analysis, pressure levels from 0.2 to 50 psi (≙ 0.014 to 3.45 bar) corresponding to 1000 to 4 µm and 20 to 33000 psi (≙ 1.38 to 2275 bar) corresponding to 10 to 0.0064 µm were conducted and the amount of mercury infiltrated at each level

[3] The thesis was supervised jointly by Nadine Zimmerer and Philipp Quarz:
Nico Korell, *Software assisted methods for investigating influencing parameters on the structure of catalyst layers in PEM electrolysis*, Master's thesis, 05/2023.

was measured. The Washburn equation was used to assign the pore diameters to the pressure levels.

3.6 Investigations of solvent mixture evaporation

The selectivity of the ink solvents during drying was analyzed by simplifying the system. For this purpose, only the solvent mixtures without the solid components of the inks were considered. The effects were studied in different experimental setups: In a liquid column setup combined with density measurements, different drying parameter were investigated experimentally. In addition, micro Raman spectroscopy allows the analysis of thin films [229–232]. Further advantages of the specialized Raman measurement setup are that the film composition can be analyzed in-situ during the drying in real time and with spatial resolution using so-called in-situ and inverse micro Raman spectroscopy (IMRS) [231–234]. Moreover, a simulation model was also introduced and used to describe and complement the experiments.

Investigating solvent mixture evaporation using density analysis[4]

100 g of binary solvent mixtures of 1-propanol and water with varying solvent composition (1-propanol mass fraction of x_1 = 40.0; 60.0; 65.5; 72.0, and 81.5 wt%) were placed in a heated liquid column on a balance. The schematic design is shown in Figure 9. The mixtures were dried in two experimental setups differing in the air input, volume flow and air and liquid temperature, resulting in the two different limiting drying cases, described in Chapter 2.3: $NTU_{i,\mathrm{g}} \rightarrow \infty$ and $NTU_{i,\mathrm{g}} \rightarrow 0$ (see also Figure 30). The conditioned air had a dew point of -16.6 °C ($\triangleq \tilde{y}_2^{\infty}$ = 0.0014) and can be preloaded with water in a saturator at 11 °C ($\triangleq \tilde{y}_2^{\infty}$ = 0.013) for experiments with increased humidity.

[4] The experimental setup presented, with the adjustments made for the 1-propanol/water solvet system, was serving as a template for a new practical experiment in Prof. Schabel's "Angewandte Stoffübertragung / Applied mass transfer" new Master's course for chemical and process engineers since 2024/25 winter semester.

The initial temperature of the liquid always was 21 °C and decreased as the solvents evaporate.

In the first setup, the drying air is introduced into the liquid through a frit (Figure 9 I)). Many small bubbles with a large total phase interface area and relative long residence time are formed. The evaporation flow predominates over the applied gas flow. This leads to mainly thermodynamically controlled drying and Schlünder's [202] predicted limiting case of $NTU_{i,g} \rightarrow \infty$ (see also Figure 30 I)). Basically, this is a saturator. The drying air flew at a volumetric flow rate of $\dot{V}_g$ = 0.1 l s^{-1} and was tempered to 20 ± 1 °C. Unregulated evaporative cooling would reduce the liquid temperature to 11 °C. To provide comparable temperature conditions of the liquid in the different setups, the liquid was water-heated to 17.5 ± 0.5 °C.

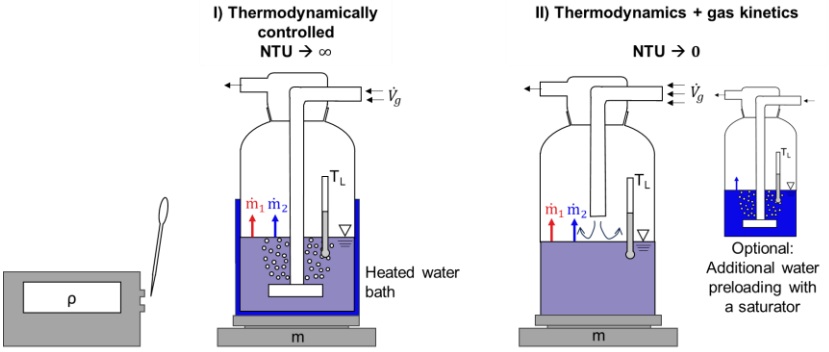

Figure 9: Schematic illustration of the experimental setup for the two different drying settings. 100 g of the solvent mixture is placed in a liquid column, which is placed on a balance. I) For realizing thermodynamically controlled drying, a frit is used, so many small air bubbles pass through the sample. The setup is additionally water heated. II) For gas-kinetics controlled drying, air is blown on the sample from an impingement nozzle. Optional the drying air can be preloaded using an additional saturator. In both cases, liquid temperature T_L and mass m are measured at regular intervals. To determine the solvent composition, approx. 2 ml samples are taken at a time and their density ρ is measured with a density meter (left). Air and liquid temperature, gas flow rate $\dot{V}_g$ and water preloading can be adjusted.

In the second setup, air at $\dot{V}_g$ = 0.4 l s^{-1} and 50 ± 2 °C is blown through an impingement nozzle onto the liquid (Figure 9 II)). The liquid-gas interface and the residence time are significantly lower than in the first setup. The evaporation flow is minor compared to the gas flow. This results in gas-side controlled drying with the theoretical limiting case $NTU_{i,g} \rightarrow 0$ [202] (see also Figure 30 II). The temperature of the liquid was not regulated and decreased from the initial temperature (21 °C) at the start to 18 °C at the second measuring point. As the drying process continued, the temperature decreased further to 17 °C. In this setup, experiments were also carried out with a preloading of the air. Therefore, a water saturator was placed upstream of the air supply. In this case, the liquid temperature was 20.5 ± 0.3 °C due to hindered evaporation and reduced evaporative cooling. The effect of different liquid temperatures on the selectivity is discussed alongside the results.

During the experiments, the solvents evaporated. The mass loss and the (potential) change in solvent composition due to selective evaporation were determined. At regular intervals, the amount of the residual solvents was measured using a balance (Satorius, Germany). Additionally, a sample of approx. 2 ml was extracted. From these samples the density was measured at 20 °C (DMA 4100 M, Anton Paar, Austria). For the binary solvent system, the previously conducted calibration curve (Eq. (3.1)) is used to calculate the solvent compositions from the density measurement. The calibration applies for the composition range 10 – 90 wt% at 20 °C. The drying progress is converted from the decrease in mass to a decrease in volume or height according to Eq. (9.8). Hereby, the time-dependent density of the mixture and the loss of weight due to sample extraction are taken into account.

$$x_1 = \frac{1008.55 \pm 1.20 - \frac{\rho_{mix}}{kg\ m^{-3}}}{2.01 \pm 0.02} \qquad (3.1)$$

x_1	Mass fraction of 1-propanol in wt%
ρ_{mix}	Density of the mixture in kg m^{-3}

In-situ and inverse micro Raman spectroscopy (IMRS) for thin film investigations

Catalyst layers are made from thin catalyst coatings. To investigate the selectivity of drying in thin films, inverse micro Raman spectroscopy (IMRS) was used. A suitable glass reservoir was developed for the existing experimental setup to hold the low-viscosity solvent mixtures. A special calibration method, first proposed by Schabel [231] for concentration measurements in polymer-solvent mixture films, was applied. The drying set-up essentially consists of a glass reservoir (24 mm x 24 mm) in which the sample is placed and which is located in a drying channel (Figure 10). Air with defined flow velocity (0.1 m s^{-1}), temperature (25 °C) and air humidity (1 %, corresponding dew point of -31.7 °C ($\triangleq \tilde{y}_2^{\infty} = 0.0003$)) flows laterally over the reservoir.

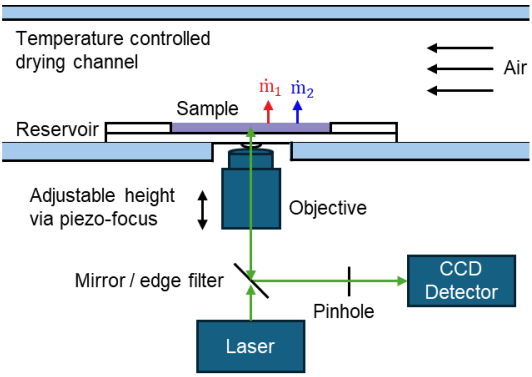

Figure 10: Schematic illustration of the setup of the Inverse Micro Raman spectroscopy (IMRS) of the thin liquid films within a temperature-controlled drying channel. The measuring position within the film is adjustable using a piezo-focus. Detailed information on the measuring device and the calibration method can be found in the original work of Schabel [231].

The sample is measured from the bottom through the glass plate of the reservoir and centered to the objective to avoid edge effects and the potential influence of the sample position within the air flow [235]. A 515 nm laser (Cobolt,

Sweden) is directed into the sample via edge filters and mirrors through the objective. The excited Raman signal returns and is detected by a CCD detector in a Raman unit (Jobin Yvon Labram, Horiba, France). Therefore, the Raman radiation is spatially filtered through a confocal pinhole. The piezo focus allows depth scans along the height of the film. The focus point is set successively at different measurement positions along the height of the film at discrete intervals. This makes it possible to measure at different positions in a short time. Due to the focal aperture of the microscope objective used, film thicknesses up to 180 µm can be measured. Due to refraction, the mechanically adjustable focus point can have a significantly shorter optical focal length depending on the liquid (composition). For the investigated 1-propanol/water mixtures this is around 110 µm. For thicker films, the upper film part, e.g. at the beginning of the drying process, cannot be measured. But due to film shrinkage, it becomes possible to measure the entire film towards the end of drying. The automated spectrometer software needs the exposure time and step size of the depth scans as input (here: ex-situ: 5 s, in-situ: 1 s, step size 20 µm). Longer exposure times increase the measured Raman intensity and the signal-to-noise-ratio. However, in dynamic drying experiments, there is a trade-off between achieving an acceptable level of intensity and achieving the desired level of time resolution in a short amount of time. The same applies to the step size. The measurement time is proportional to the number of measurement points (along the film height). If the intervals are too small, the time offset is no longer negligible. This is a particular problem when measuring gradients.

Binary solvent mixtures with compositions of 20, 50, 52, 54 and 66 wt% 1-propanol were prepared. 155 µl of each mixture was applied to the reservoir, resulting in an initial film thickness of 269 µm (assuming ideal wetting), and then dried in the drying channel. Thus, in the beginning of the experiments, the film is approx. 160 µm thicker than the measuring range (around 110 µm).

With measured spectra of the pure substances (Figure 11), the composition of a mixture is determined from its mixture spectrum by superposition (Eq. (3.2)). The weighting factors are determined by minimizing the squared errors between calculated and measured spectra [120,236,237]. Using the calibration method of Schabel [231] for polymeric films, the Raman intensity is converted

into a mass ratio of the solvents to each other. The calibration constant is found in a preliminary experiment with known sample composition and an evaluation range of 2500 – 3800 cm^{-1} (Eq. (3.3)).

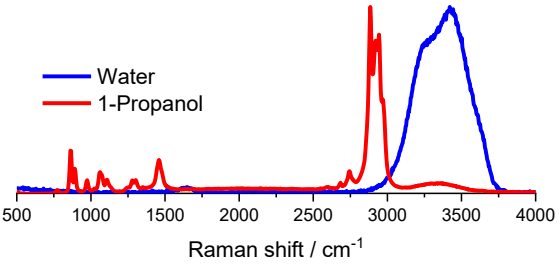

Figure 11: Measured Raman spectra of pure 1-propanol and pure water, normalized to maximum intensity.

$$I_{\text{mixture}} = \omega_1 \cdot I_1 + \omega_2 \cdot I_2 \tag{3.2}$$

I_{mixture}	Raman intensity of the mixture in a.u.
ω_1	Weighting factor of 1-propanol (dimensionless)
I_1	Raman intensity of 1-propanol in a.u.
ω_2	Weighting factor of water (dimensionless)
I_2	Raman intensity of water in a.u.

$$\frac{\omega_1}{\omega_2} = K_{1,2} \cdot X_{1,2} \tag{3.3}$$

$K_{1,2}$	Calibration constant in g g^{-1}
$X_{1,2}$	1-Propanol to water mass ratio in g g^{-1}

Raman spectroscopy has only been used to investigate pure solvent systems for quantitative determination of the solvent composition or diffusion experiments [229,230,238–241]. However, to the best of the author's knowledge, no such studies have been ever carried out on a drying process in which all components evaporate. In previous drying publications, a polymer or particles remained in the system and served as a constant reference [120,121,231–237,242–260]. In a new study by the author's research group, a high-boiling-point solvent was used as quasi-nonvolatile constant reference [261]. In

contrast, in the binary solvent system in this work, the two solvents being evaporated must be related to each other at each time step.

To further characterize the ink system, a measurement was performed with ionomer added to the solvent mixture. Therefore, a sample with 4 wt% Nafion ionomer and 52 wt% 1-propanol in terms of solvents was also prepared. The 4 wt% Nafion are equivalent to the ionomer mass fraction of a typical ink with 10 wt% solids and *I/C* = 1. The 52 wt% 1-propanol correspond to the arheotropic solvent composition found in Chapter 6.2 under the given experimental conditions. The aim is to examine ionomer influence on selectivity and drying kinetics. The same 1-propanol/water calibration was used for the analysis as for the binary solvent system. Since no Raman peak of Nafion is detected in the spectral region on which the calibration is based (2500 – 3800 cm^{-1}), Nafion does not interfere with the analytical routine.

Modelling the arheotropic composition

A simulation model was developed within two supervised Master's theses[5] for the interpretation of the experimental results and to make predictions about the selectivity of drying processes. The selectivity depends on the drying conditions such as drying temperature and preloading of the drying air and can be described as a function of the relative evaporation mass flow rate $\dot{r}_i$. $\dot{r}_i$ is modeled as a function of solvent composition in Python, using the initial value problem (IVP) solver from the SciPy library to solve the differential equations. The model is based on the considerations and equations of Riede and Schlünder [196] for the case $NTU_{i,g} \rightarrow 0$. The substance and mixture data are taken from the VDI Wärmeatlas [193] and from Jang and Chang [192]. The Wagner equation with parameter data from [193] is used for the vapor pressure curves (see Appendix 9.3). The mass transfer coefficients are determined using Lewis

[5] Both theses were supervised jointly by Nadine Zimmerer and Philipp Quarz:
Lukas Löttert, *Charakterisierung des Trocknungsverhaltens nanopartikel-basierter Beschichtungstinten für Brennstoffzellen CCMs (Catalyst Coated Membranes)*, Master's thesis, 12/2021.
Ellen Terhorst, *Untersuchung des Trocknungsverhaltens von Katalysatortinten für Brennstoffzellen- und Elektrolyseuranwendungen*, Master's thesis, 02/2024.

analogy with the diffusion coefficients according to Fuller (see Appendix 9.3). The temperature is isothermal for the gas phase and the liquid. At the phase boundary, the Raoult-Dalton law is used with van Laar activity coefficients according to [192] (see Eq. (2.6)). The gas kinetics are described by the logarithmic Stefan-Maxwell approach (see Eq. (2.14)). No film-side mass transport resistance is considered, hence assuming constant solvent composition in the liquid boundary layer. The input parameters of the simulation are the temperature, the preloading of the drying air and the ratio of the diffusion coefficients of the solvents in the drying air.

4 Process-related influences in catalyst ink manufacturing[1]

The prerequisite for high-quality catalyst layers[2] is a homogeneous, stable and reproducible catalyst ink. There are many studies on ink formulation in the literature. However, there are only a few studies focusing on the ink processing. This chapter identifies and discusses key correlations between catalyst ink and catalyst layer, taking into account the process parameters applied during ink production. This is based on research Hypothesis 1:

In order to reduce cracking in catalyst layers, the processing and formulation of the ink must be adjusted and balanced. The link is the particle size distribution (PSD) of the ink.

The correlations are relevant for all catalyst inks and layers, regardless of the subsequent manufacturing process for the catalyst-coated membrane (CCM) (see Chapter 1.2). In this study, the catalyst ink is applied directly to the membrane. This is in the context of research into the process of membrane direct coating (MDC), and serves as preparation for testing Hypothesis 3. Uniform inks are essential for subsequent measurements and causally analyses of the influence of coating and drying.

---

[1] Parts of the results and figures presented in this chapter have been previously published in a peer-reviewed article, available under a CC BY 4.0 license:
Quarz P, Zimmerer N, Janning L, Steck A-M, Scharfer P, Schabel W. *Ink processing and its influence on particle size distribution, ionomer requirements and electrode properties in polymer electrolyte membrane fuel cell and electrolyser catalyst coated membranes*. Energy Technol 2025. https://doi.org/10.1002/ente.202501844, referred to in this work as [262].

[2] 'High-quality catalyst layer' is defined here as a homogeneous layer with suitable microstructure in terms of porosity and pore size distribution, many triple-phase boundaries, desired Pt loading, no or at least less cracks and good membrane contact (no delamination). This work does not make comprehensive statements about the performance of a manufactured catalyst layer in operation. The focus is on the coating pattern and any cracks and coating defects that may occur. Pore size distributions are also determined but not evaluated in terms of performance.

Here, a ball mill is used to carry out a systematic investigation of ink processing. To this end, a suitable device was chosen, installed and brought into operation (see Chapter 3.2). The same applies to the particle size analysis device using dynamic light scattering. For more in-depth investigations into pore radius distribution, an existing measuring device was put into operation.

Next, a suitable ink composition for the investigations had to be found. To this end, preliminary tests were carried out to study the influence of the solvent (see Appendix 9.2). It was found that, for the selected catalyst and ionomer material and driven membrane direct coating, inks containing less 1-propanol produced layers with few cracks, whereas inks containing a high proportion of 1-propanol and a low proportion of water produced layers with pronounced crack networks. Based on these results, the solvent ratio for subsequent investigations was set to 20 wt% 1-propanol and 80 wt% water.

In order to validate the significance of PSD as a postulated central parameter, comparable conditions for the evaluation of different experiments must be ensured. After different ink processing, this applies to identical coating and drying conditions and uniform determination of the measured variables. Preliminary tests showed that, to ensure a valid comparison, the layers must all have the same thickness. This is because the proportion of the defect area increases significantly with increasing layer thickness (see Appendix 9.2).

To test the hypothesis, inks with different particle size distributions (PSDs) have to be produced. First, the influence of different process parameters (milling time and rotational speed) on the PSD and on layer quality (in form of cracks) is analyzed and correlated. Then, by adjusting the milling time and rotational speed, inks with similar PSDs are processed, and conclusions are drawn about their effect on electrode quality. One important question is, whether similar PSDs result in similar catalyst layer properties, regardless of how the PSD is achieved.

In a next step, a theoretical model is developed to describe the effects of PSD on the specific surface area of the catalyst particles and the ionomer distribution. These theoretical considerations are then correlated with experimental data on PSD and crack patterns. To further test this conclusion, inks and layers with higher ionomer content are produced and analyzed. To the best of the author's knowledge, the literature does not consider PSD and the ionomer

requirement in the form of the ionomer-to-carbon ratio (*I/C*) so far. This work addresses this gap.

4.1 Process parameters in the milling process affecting the ink and layer properties

The influence of process parameters on ink and layer properties during ball milling is investigated based on variations in grinding time and rotational speed. According to theory (see Chapter 2.1), the particle size distribution (PSD) should shift towards smaller particles as both parameters increase. With fewer large particles, which act as nucleation points for defect cracks, it is expected that less cracking will occur in the layers. Recording the PSD and subsequently correlating it with the resulting layer image are essential elements in clarifying Hypothesis 1.

Influence of the milling time on ink and layer properties

Investigating ink processing relates to catalyst particles and their sizes. First, important terms are defined. The catalyst raw material is present as agglomerates. An agglomerate consists of several aggregates of different but smaller sizes. In turn, an aggregate is made up of many small primary particles. Regardless of size, the term 'particle' is used as an umbrella term.

For investigating the influence of the milling time, the ink formulation and all other process parameters are kept constant (e.g. rotational speed n = 1000 rpm, volume ratio of grinding media to ink, grinding media size). The inks were

processed for 1, 3, 6 and 24 h.[3] The ink properties and milling effects are discussed in relation to the particle size distribution (PSD). It is expected that, as milling time increases, the particles will become smaller and fewer agglomerates will be formed, resulting in layers with fewer (defect introduced) cracks. Longer grinding times lead to more agglomerate break-up events and thus to smaller particles. This relationship is described in the literature in the stress number (see Eq. (2.4)). To determine the PSD, the inks were diluted ~ 1:10,000 in a solvent mixture with the same solvent composition as the ink[4] (20 wt% 1-propanol, 80 wt% water). Dilution influences the particle size distribution, with measured size values differing from those in the ink. For example, a 20 % reduction in carbon black particle size was observed at a 1:100 dilution [51]. Nevertheless, a qualitative comparison of the samples is warranted, since expected primary particle sizes have been measured and all the measurements were performed under the same conditions. While the overall order of magnitude should remain similar, dynamic light scattering is an established method for ink characterization [42,51]. However, pure ionomer aggregates cannot be detected here [88], as they are only a few nanometers in size, falling below the 10 nm detection threshold measurement device used. To minimize technical influences, the inks were always diluted and measured using the same procedure. This necessitates the unverified assumption that dilution does not affect

[3] In the literature [100,103], inks are processed at lower rotational speeds and for longer milling times. However, at higher speeds, the required grinding time for effective particle break-up is expected to decrease in line with the stress number. For scalability purposes, a process that can be completed within a few hours is preferable to grinding over several days. Preliminary tests with platinum-free carbon particles demonstrated that a suitable ink could be produced within 3 h at 1000 rpm. This approach was then transferred to platinum-containing catalyst particles, forming the basis for a detailed series of investigations. To demonstrate the effects of greater and lesser particle break-up and their consequences for layer microstructure, processing times of 1, 6 and 24 h were investigated. These times are feasible in daily laboratory operations, including subsequent characterization and further processing, and reveal different phenomena.

[4] Changing the solvent composition affects the ionomer and the particle size (see Chapter 1.3). Using a different composition would significantly alter the solvent composition of the sample in the measurement due to the high amount of solvent added.

the qualitative comparison between the inks. This limitation must be considered when discussing the results.

The inks milled for 1 to 6 h show a bimodal PSD, seen in the volume-weighted particle size distribution density (Figure 12). The fine fraction in the PSD shows particle diameters less than 0.1 µm resp. 100 nm and represents the primary particles and smallest aggregates (schematically shown in Figure 12). The coarse fraction with particle diameters larger than 100 nm refers to aggregates and bigger agglomerates (schematically shown in Figure 12). The largest agglomerates measured in the milled inks are significantly smaller than in the unmilled powder ($t = 0$ h).[5] The error bars are the result of taking measurements of different samples of the same ink.

With longer milling times, the peak in the coarse fraction shifts to smaller particle sizes and the peak in the fine fraction increases. Finally, in the ink ground for 24 h (green) the PSD is monomodal. The 24 h milling time is used here as an example of a significantly longer grinding time where there are no particles in the range of 1 µm or larger in the ink.[6] As expected, longer mixing and grinding in the ball mill result in a narrower PSD.

The expectation is fulfilled and explained theoretically by referring to the model of stress numbers *SN* and stress intensity *SI* in ball milling (see Chapter 2.1). Longer milling times rise the chance of agglomerate break-ups and thus increased SN (see Eq. (2.4)). Starting from large catalyst agglomerates, finely dispersed primary particles or small aggregates are produced. Under the

[5] The catalyst powder (without any ionomer) was not milled and just diluted in the solvent mixture for measuring the PSD. This was made to compare the 'pure and initial' powder with the milled inks and emphasize the large milling effect. In the relatively large error bars the inhomogeneity of the unprocessed powder becomes visible.

[6] The specific milling time of 24 h is both compatible with normal laboratory operations and has been chosen in previous studies [103]. The observed monomodal distribution may become apparent in less than 24 h. However, the aim of this study is not to determine an optimal grinding time, but rather to identify significant effects in clearly distinguishable PSDs.

applied process conditions, the resulting *SI* is high enough to break up the agglomerates and aggregates (see Table 2 and Eq. (2.1)).

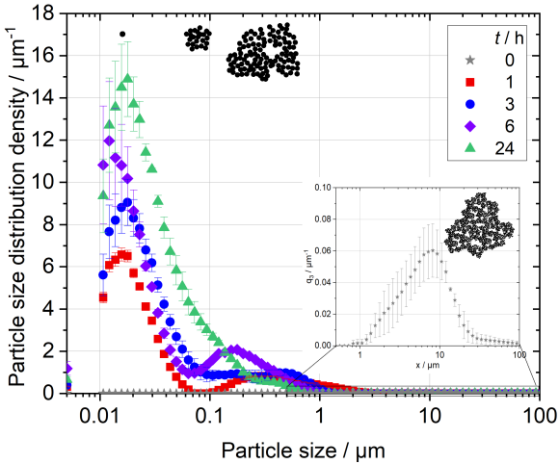

Figure 12: Volume-weighted particle size distribution density (PSD) q_3 depending on ink milling time from t = 1, 3, 6 and 24 h in a ball mill with constant rotational speed of 1000 rpm. The schematic representation above depicts primary particles, aggregates and larger agglomerates, anticipated for each size class. In addition, the PSD of the catalyst powder in the solvent mixture without further processing (t = 0 h) with large agglomerates is shown in a zoom[7] between 0.5 and 100 µm. [262]

For further analyzing the PSD, the cumulative particle size distribution is used.[8] Characteristic distribution parameters such as percentile values can be read from the cumulative plot. Figure 13 shows the cumulative PSD resulting

[7] The particle size distribution density is divided by the interval width. As the interval width increases with larger particle sizes, the q_3 value decreases and may be barely visible above the abscissa. Since the integral of q_3 is always 1, $q_3 > 1$ µm^{-1} is expected for $x < 1$ µm, and $q_3 < 1$ µm^{-1} is expected for $x > 1$ µm.

[8] The plot's advantage is that the curves are next to each other, not on top of each other, and are therefore easier to distinguish. The distribution and position of the unprocessed catalyst powder is also clearly visible in the diagram.

from Figure 12. In the cumulative diagram, the curves that have been milled for a longer time are positioned to the left at smaller particle sizes.

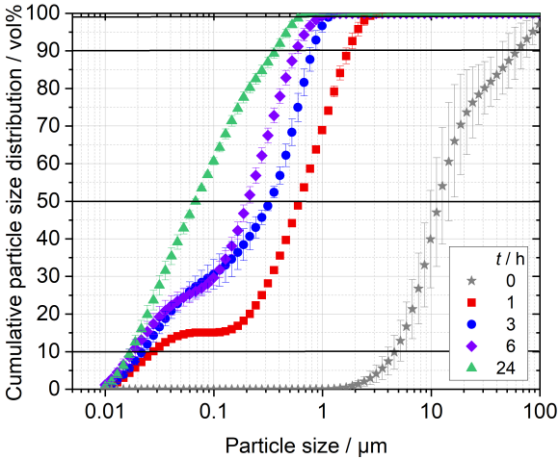

Figure 13: Cumulative volume-weighted particle size distribution (PSD) depending on the milling time t from t = 1, 3, 6 and 24 h in a ball mill. In addition, the PSD of the catalyst powder in the solvent mixture without further processing (t = 0 h) is shown.

For longer milling times, it is observed that the corresponding size values are smaller for all percentile values (see Figure 13). The d_{10} percentiles, representing the smallest size fractions, are within a narrow range for all curves. After 1 h of milling, d_{10} is 0.03 µm, for the longer milling times it is 0.02 µm. Larger differences can be seen in the d_{50}, ranging from 0.63 µm after 1 h to 0.07 µm after 24 h and d_{90}, ranging from 1.77 µm after 1 h to 0.37 µm after 24 h. Large particles are broken up first. When two grinding beads or a bead and a wall of the grinding chamber collide, large particles are initially captured, while smaller ones are 'protected'.

Table 3: Percentile values d_{10}, d_{50}, d_{90} and d_{99} of the particle size distributions of inks milled for varying milling times. *0 h represents catalyst particles in the solvent mixture without ionomer and without milling.

	0 h*	**1 h**	**3 h**	**6 h**	**24 h**
$\boldsymbol{d_{10}}$ **/ µm**	4.6	0.03	0.02	0.02	0.02
$\boldsymbol{d_{50}}$ **/ µm**	11.7	0.63	0.34	0.20	0.07
$\boldsymbol{d_{90}}$ **/ µm**	61.3	1.77	0.83	0.57	0.37
$\boldsymbol{d_{99}}$ **/ µm**	105	2.60	1.13	0.94	0.61

The maximal detected particle size also decreases with increasing milling time. Therefore, the d_{99} is interpreted as the maximal particle size detected. After 1 h of milling, d_{99} is 2.6 µm, after 3 h particles of 1.1 µm, after 6 h of 0.9 µm and after 24 h of 0.6 µm size exist. This is important to note regarding the potential for cracking in films produced with these inks, as larger agglomerates act as starting points for cracks and other defects [58,263]. However, the largest agglomerates are significantly reduced, particularly due to the longer milling time.

In the next step, the inks are directly coated onto a Nafion NR212 membrane and dried identically using isothermal drying. Differences in the layers must result from different properties of the inks and not from the further processing steps (coating and drying). Layers have comparable dry thicknesses of 7.4 ± 0.5 µm. The following nomenclature of the layers is related to the processing parameters of the ink on which they are based. The images show representative sections of the multiple layers produced.

It is expected that the appearance of the layer will improve in the form of fewer cracks with longer grinding times, as large agglomerates, which often cause cracks, will be less present. Taking images of the layers with back-light illumination identifies cracks and defects as white spots in the black catalyst layer (Figure 14). The layers of those inks that were processed for 1 to 6 h show some individual, small, short cracks. Crack shape and size are similar regardless of the milling time, in contrast to Baez-Cotto et al. [103]. Most cracks are classified as Y-shaped, randomly oriented cracks [58]. From 1 h to 6 h of ink

grinding, the number of cracks decreases continuously. Conversely, surprisingly, a pronounced and interconnected crack network is observed after 24 h of milling. The number of cracks is no longer meaningful here, as many individual cracks now form an entire network. The ratio of the crack area to the total layer area is therefore more meaningful than the number and individual crack size or width.

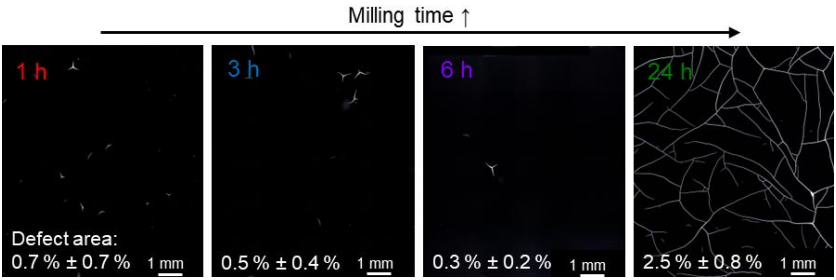

Figure 14: Observed crack pattern of catalyst layers after different ink milling times of 1, 3, 6 and 24 h. All inks were directly coated onto the membrane and dried under similar isothermal drying conditions. The dry layer thickness of all layers is tried to be constant at 7.4 ± 0.5 µm. The number of cracks and the relative cracked area to the total layer area observed in the dry layers initially decrease with longer milling times. However, if the milling time is too long, a crack network is formed. The defect area fraction compared to total area is given. [262]

The white areas are mainly due to cracks and, in some cases, by spalling resulting from cracking. Relating the white area to the total catalyst area gives the relative crack area. As the milling time increases, the crack area initially decreases slightly from 0.73 % (1 h) via 0.48 % (3 h) to 0.25 % (6 h). Contrary to this trend, the proportion of defects rises sharply at 24 h (2.5 %). The crack area is more than ten times greater than the relative defect area after 6 h of grinding. This increase is not surprising when looking at the crack pattern with the pronounced crack network (see Figure 14). Surprising is the general occurrence of the crack network and the strongly altered crack pattern after 24 h of milling. The reasons for the differences in the crack network are discussed in the following. At this point, it should be noted that there is obviously an

optimal grinding time with regard to the fracture pattern. However, the aim of this study was not to find this optimum, but to demonstrate the influence of extreme grinding conditions and the unexpected effects they cause, and to gain a better understanding of the relationships between process variables and layer properties.

The critical crack thickness (CCT), above which spontaneous cracking occurs (see Chapter 2.2), is not exceeded in layers where the ink was milled for 1, 3 or 6 h, with a layer height of approx. 7.4 µm. Many cracks start at inhomogeneities, such as agglomerates (see Appendix 9.4). Also a number of cracks occur without visible agglomerates in the immediate vicinity. Here, it seems that the cracks are caused by unknown inhomogeneities in the layer, e.g. due to the local component distribution, fluctuating layer heights, or other inhomogeneities in the coating and drying process. Hoffmann et al. [62] developed a more pragmatic definition, away from the strict physical definition of the CCT. They defined the CCT as the thickness at which more than 1 % of the surface area is covered by cracks (see Chapter 2.2). This definition is more practical for determining CCT in the layers observed, as it also accounts for cracks caused by agglomerates to some extent. According to this definition, the CCT is not exceeded at 7.4 µm in the layers after 1, 3 and 6 h of milling. For the precise value of the CCT, a more detailed study on different layer thicknesses for each milling period is necessary.

In order to avoid cracks induced by defects, these defects, e.g. large particle agglomerates, must be prevented. A filter step between ink production and coating would serve to separate the undesired large agglomerates from the ink. However, given the tiny size of the 'large' agglomerates in the coating inks on a µm scale (see Figure 13), a small mesh size needs to be used and a high filter resistance is anticipated. Due to its high catalyst content, the resulting filter cake should be recycled. This study did not use a filter, as the aim was to investigate the effects of different particle sizes and discuss the relationship between ink processing and layer properties without restriction.

There are also a few agglomerates in the layer for which the ink was processed for 24 h (see Appendix 9.4). However, the crack pattern is completely different

from the previously examined layers. According to Hoffmann et al., the CCT is now exceeded at the same dry film thickness of 7.4 µm due to 2.5 % of the catalyst layer area consisting of cracks. The differences in crack pattern cannot be attributed to large agglomerates as they are reduced here. Instead, other, additional factors must be found to explain this. This will be examined below. As interim conclusion it can be stated at this point that the ink processing has a huge impact on the crack pattern. The results show that the CCT depends on both, material properties (already known from literature) and ink processing parameters. The latter is reflected in particle size and distribution, which are key factors (see Figure 13 and Eq. (2.5)).

To further understand the impact of these two ink-processing-modified parameters, the pore diameter distribution, a critical microstructural parameter linked to ink particle size [50], is examined. Capillary pressure builds up within the pores of the layer during the drying process. This creates tension and is responsible for potential cracking. Capillary pressure and resulting tensions are determined by the pore size (distribution). The measurements are conducted using mercury intrusion (see Chapter 3.5). The resolution is limited to a minimum pore size of approx. 6 nm. Smaller pores (< 6 nm) would only be expected in the primary particles themselves. The smallest measurable pores are referred to as primary pores within individual agglomerates and aggregates. Larger pores are expected to be secondary pores between different agglomerates (see Appendix 9.4).

The pore diameter distribution of the layers after different ink processing is shown in Figure 15 (similar to the particle size distribution density). The volume of mercury intruded per pore size interval, relative to the catalyst layer sample mass, is plotted against pore size. Referring to the respective sample mass allows comparison of the intrusion volumes. The pore size is plotted logarithmically on the x-axis from 0.006 µm (= 6 nm) to 10 µm. This range corresponds to the minimum measurable pore size and the approximate layer thickness on the upper side.

The layers milled for 1, 3 and 6 h show a bimodal pore diameter distribution with two peaks: one at approx. 0.007 µm (all) and the other around 0.051 µm

(1 h, red) to 0.038 µm (6 h, purple). In the layer after 24 h of processing, only the peak at 0.007 µm remains. The maximum relevant pore size detected is < 0.1 µm. With increasing milling time, the distribution shifts towards smaller diameters. The volume of mercury introduced into the small pores, and consequently their number, increases slightly. Simultaneously, the number of large pores declines. Moreover, the largest significant pore size becomes smaller. Most of the very small pores (d_p < 0.02 µm) are present in the layer after 6 h of milling. Fewer of the smallest pores are present after 24 h than after 6 h.

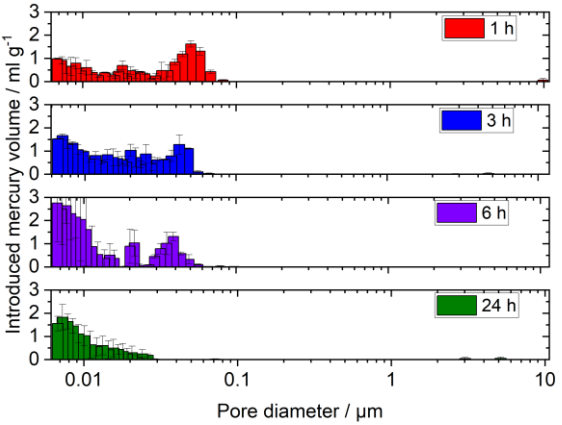

Figure 15: Influence of the ink milling time on the pore diameter distribution of the formed electrodes. With increasing milling time, the larger pores reduce. After 1, 3 and 6 h, a quasi-bimodal pore size distribution is observed. The cluster of 'large' pores measuring between 0.03 and 0.09 µm is absent from the layer whose ink was ground for 24 h. Most of the small pores appear after 6 h rather than 24 h. [262]

When the particle size distributions of the ink are compared with the pore diameter distributions of the layers, the similarity is apparent (see Appendix 9.4). There is a visible correlation. These investigations are a strong indication for the verification of Hypothesis 1, according to which the PSD is a key parameter for the layer properties. In order to investigate these findings further, after the influence of the grinding time in this chapter, the rotational speed will be varied as another essential process parameter in the next chapter. A detailed

discussion on the cause of the layer pattern with the ink with 24 h milling time is given in Chapter 4.2.

Influence of the stress number *SN* on ink and layer properties

In the previous chapter, the milling time at constant speed was varied. This resulted in different *SN* and different ink and layer properties. In order to test the PSD as key parameter and to test the assumption that *SN* is the key factor influencing ink and film properties, in this chapter inks are produced with different processing methods but comparable *SN*. The product of milling time and rotational speed is chosen to be constant.

First, the PSDs of the inks are examined (Figure 16). The curve for 6 h at 1000 rpm (purple) is already known from the previous analyses, with a calculated $SN = 6.68 \cdot 10^8$ m^{-1}. The same *SN* is generated by milling an ink for 3 h at 2000 rpm (yellow) and 4.5 h at 1500 rpm (orange) with a slightly higher *SN* ($7.52 \cdot 10^8$ m^{-1}). The targeted adjustment of milling time and rotational speed results in a very similar multiplication product. If the other process parameters (grinding media size and ratio to the ink as well as the ink's solid content) are kept constant, this results in the corresponding very similar *SN*. The three curves of the PSDs with very similar *SN* almost overlap over the entire investigated particle size range. Small differences between the PSDs are explained by inhomogeneities in the milling process or in the sampling and preparation for the PSD measurements. In fact, it seems that the PSD mainly depends on the product of the milling time and speed, with all other parameters remaining constant. Taking these additional process parameters into account, it is postulated that *SN* represents the relevant process function for the milling progress, at least in the varied parameter field. Limits regarding the rotational speed are set by the minimum stress intensity required for breakup, mainly dependent on the rotational speed, which must always exceed a certain level (see Eqs. (2.1) and (2.2)), and by a possible change in the flow pattern in the grinding chamber during grinding, and air intake at higher rotational speeds.

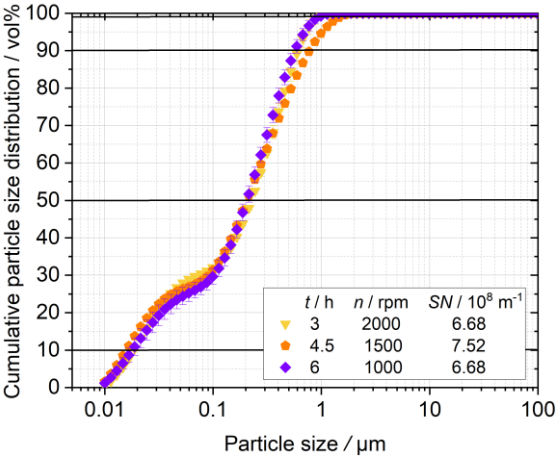

Figure 16: Cumulative particle size distribution (PSD) of inks processed with different milling times t and rotational speeds n, but similar stress numbers SN. Similar SN results in similar PSDs.

In comparison to the work of Baez-Cotto et al. [103] (24 – 96 h milling time on a jar mill roller at 60 rpm) the milling times in this study (1 – 24 h at 1000 rpm) are much shorter. This is due to the much higher rotational speeds used. The reason why they did not use higher rotational speeds is unknown. Perhaps it was beyond the scope of their study, or perhaps their jar mill was limited in some way. However, SN is in the same magnitude of order in both studies (see Appendix 9.4). Unfortunately, they do not specify particle size distributions. This significantly limits the comparison with this work.

In order to generate small particles in a time-efficient manner, a (further) increase in rotational speed is conceivable, considering limiting air entrainment. This leads to coating defects in further processing. It is possible to degas the ink prior to coating by using ultrasound or vacuum extraction. However, ultrasound affects the PSD and degassing under vacuum influences the ink composition through selective evaporation. The effects depend on the degassing duration. To rule out these influences, however, degassing is not used in this

study. In addition, speed-dependent changes in viscosity (shear thinning ink rheology), and therefore a change in the flow field during the milling process, may have an effect on agglomerate disintegration at a certain rotational speed. Furthermore, if the speed of the grinding disc is too high, slippage may also occur, preventing a complete power transfer. This does not appear to be an issue in the speed range studied here (1000 – 2000 rpm), but may be an issue at higher speeds. Lower rotational speeds appear to be disadvantageous as they increase milling time. It is also important to ensure that the *SI*, which is quadratically dependent on the rotational speed (see Eqs. (2.1) and (2.2)), remains high enough to enable particle breakup.

The next step is to examine the layer patterns produced by the inks processed with comparable *SN*. The hypothesis is that the PSD is the key parameter for the dried layer properties. With the same PSD, there is a strong expectation that the layers will be very similar. Indeed, this expectation is fulfilled (Figure 17). All layers show similar size and number of cracks. These are randomly oriented and mostly Y-shaped. The averaged relative defect area is 0.3 % in all layers.

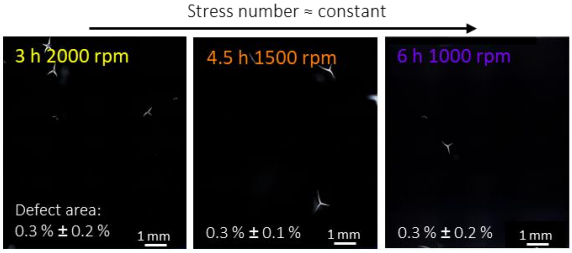

Figure 17: Observed crack pattern of catalyst layers from inks processed with different milling times and speeds, but similar stress numbers. All inks were directly coated onto the membrane and dried under similar drying conditions. The dry layer thickness of all layers is around 7.4 ± 0.5 µm. The number of cracks and the proportion of cracks observed in the dry layers are very similar.

With the same PSD, it is expected that the pore diameter distributions, which are related as already analyzed in Figure 67, are very similar here. Indeed, the

bar diagrams are similar regarding their form. A bimodal pore diameter distribution with two peaks is visible (Figure 18). The peak in the range of 0.04 – 0.05 µm varies slightly. However, compared to the distributions with different *SN* (due to the variation of the milling time at constant speed, see Figure 15), these curves are much closer to each other than to the others.

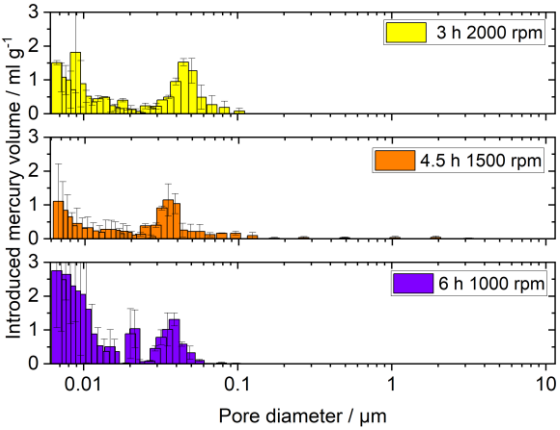

Figure 18: Pore diameter distribution of electrodes from inks processed with different milling times (3, 4.5 and 6 h) and rotational speeds (2000, 1500 and 1000 rpm), but similar stress numbers *SN* (6.68, 7.52 and 6.68 · 10^8 m^{-1}). The pore size distributions are quasi-bimodal, and the three distributions shown are very similar compared to layers of inks with significantly different *SN*.

The results for PSD, pore diameter distribution and crack pattern clearly show that the interaction of rotational speed and milling time has a significant effect on the product properties of the ink and consequently the coating. For milling processes, the stress number equation (see Eq. (2.4) from Kwade et al. [176]) is known from the literature as a process function. Here it is applied to the material system used. The product of speed and milling time is discussed in detail, while the other parameters of this model equation were kept constant. The calculated values for *SN* can be found in Table 2. The other parameters affecting the *SN* have also been taken into account in considerations or in separate studies. A brief overview is given in Appendix 9.4.

4.2 Influence of the particle size distribution on the ionomer distribution

From the previous results it is concluded that the *SN* is the process function for the PSD. Similar PSD results in similar layer properties. The question remains, as why there is an optimal PSD with respect to the film appearance in the form of cracks. As can be seen from Figure 14 and Figure 65, the crack pattern initially improves in form of less cracks with increasing *SN* and the associated smaller PSD (more small particles and fewer large ones), but then significantly worsens with further increasing the processing time.

There are two aspects to consider when looking at the formation or prevention of cracking. One is the forces that occur in the drying film that lead to cracking. The other is the inherent resistance and internal stability of the drying film to cracking. If the stresses exceed the mechanical stability of the film, cracking will occur. If the cracks can be handled by the internal stability, the film remains intact. This relationship seems to change for films made from inks with different PSD.

First, the occurring forces are considered. The theory states that cracks are caused by high capillary pressures and large agglomerates (see Chapter 2.2). As already mentioned in the analysis of Figure 14, fewer defect-induced cracks (due to large agglomerates) occur in the layers produced from inks with less large particle sizes. Although this explains the initial improvement in the crack pattern with decreasing PSD, it does not explain why the ink with the lowest PSD and the fewest large agglomerates (see Table 3) results in a layer with a pronounced crack network. Capillary pressure may help to explain this. The capillary pressure is high in small, narrow pores. With the many cracks in the layer with the smallest PSD (24 h milling), it is expected that this layer also has the most small pores. But this is not the case. Rather, after 6 h of milling and a larger PSD, the layer has the largest proportion of small pores. Since the highest proportion of smallest pores is found in this layer (see Figure 15), it is anticipated that the highest number of cracks would be found here. However, this layer shows the fewest cracks (see Figure 14). Furthermore, it is expected

that pores of a similar size will deplete more uniformly than pores of very different sizes [181]. This leads to fewer and more uniform stresses. Although the width of the PSD of the ink milled for 24 h is the narrowest, the expected superior lower and more uniform stress levels do not seem to prevent massive crack formation. Consequently, the capillary pressure is insufficient to provide a comprehensive explanation for the observed cracking behavior.

Since no consistent explanation for the observed behavior was found on the crack initiation side, the cohesion and mechanical stability of the layer to cracking is now discussed. If the cohesion between the particles is reduced, it is expected that the mechanical strength of the pore network is limited and cracks will appear at some point at (almost constant) capillary pressures. One explanation could be the ionomer distribution within the layer and on the particles. As large agglomerates are broken down into smaller primary particles, the specific surface area, i.e. the ratio of surface area to volume, increases. For spheres, this ratio is calculated from sphere geometry (Eq. (4.1)). When an agglomerate is broken up, many smaller particles are formed. The number ratio is linked to the particle size and is calculated for non-porous monomodal spheres from the sphere geometry (Eq. (4.2)). Splitting a large sphere into smaller ones keeps the total volume the same. This means the size ratio affects the number ratio cubically. Using this relationship, the ratio of the total particle surface area can then be calculated from the number of particles times the individual particle surface area (Eq. (4.3)). [264]

$$S_\mathrm{V} = \frac{6}{d} \tag{4.1}$$

S_V Specific surface area / µm^{-1}
d Particle size / µm

$$\frac{N_\mathrm{B}}{N_\mathrm{A}} = \left(\frac{d_\mathrm{A}}{d_\mathrm{B}}\right)^3 \tag{4.2}$$

N_A Number of particles in case A (dimensionless)
N_B Number of particles in case B (dimensionless)
d_A Particle size in case A in µm
d_B Particle size in case B in µm

$$\frac{S_{\mathrm{total,B}}}{S_{\mathrm{total,A}}} = \frac{N_{\mathrm{B}}}{N_A}\frac{4\pi d_{\mathrm{B}}^2}{4\pi d_{\mathrm{A}}^2} = \frac{d_{\mathrm{A}}}{d_{\mathrm{B}}} \tag{4.3}$$

$S_{\mathrm{total,A}}$ Total surface area of all particles in case A in µm²
$S_{\mathrm{total,B}}$ Total surface area of all particles in case B in µm²

The particles are crushed during the ink milling process. This increases the number of particles and the overall specific surface area. This becomes visible when Eq. (4.3) is applied to the examined inks. The measured x_{50} after 1, 3, 6 and 24 h grinding at 1000 rpm serve as data for the respective particle size (see Table 3). The agglomerates, aggregates, and primary particles are initially considered to be spheres. Assuming monomodal, non-porous particles, a single particle with a diameter of 0.63 µm after 1 h of milling becomes six particles with a diameter of 0.34 µm after 3 h of milling, 31 particles with a diameter of 0.20 µm after 6 h of milling, and 729 particles with a diameter of 0.07 µm after 24 h of milling. At the same time, the total surface area increases by factors of 1.9, 3.2 and 9.0 (Table 4).[9]

These considerations are relevant to crack formation when the effects of the particle surface on the ionomer in the ink are being considered. The ink contains the ionomer in different forms: bound to the particle or free in solution in the solvents [58]. The proportions of those two types is related to the overall particle surface area. It is differentiated into a part of ionomer which is bound to the particles and stabilizes them in the ink. When the layer solidifies, this bound ionomer acts as a stress-absorbing binder. The other portion of the ionomer is unbound and mobile, referred to as free ionomer. The amount of bound ionomer is related to the total surface area of the particles. The ionomer adheres to newly formed particle surfaces. Consequently, (a larger proportion of) free ionomer is only present once the particles have enough bound ionomer to saturate their surfaces. Therefore, the presence of free ionomer indicates an

[9] The values are an estimation considering non-porous spheres. In reality, the large particles are porous agglomerates and aggregates of primary particles and voids in between. The number of primary particles is reduced by the factor of the agglomerate's porosity. This also reduces the total surface area formed from the agglomerate in the same way. [264]

adequate supply of bound ionomer for the particle surfaces and also acts as a reserve for any newly created surfaces.

Table 4: Particle parameters of the inks milled for 1, 3, 6, and 24 h are presented in relation to each other. The d_{50} value from the particle size distributions (PSD) is provided. The particle size ratios $\frac{d_i}{d_A}$, the number ratio $\frac{N_i}{N_A}$ and the surface area ratio $\frac{S_{total,i}}{S_{total,A}}$, are calculated according to Eqs. (4.2) and (4.3) assuming monomodal and non-porous spheres.

Ink	t	d_{50}	$\frac{d_i}{d_A}$	$\frac{N_i}{N_A}$	$\frac{S_{total,i}}{S_{total,A}}$
	H	µm	µm µm^{-1}	-	µm^2 µm^{-2}
A	1	0.63	1	1	1
B	3	0.34	0.54	6.4	1.9
C	6	0.20	0.32	31.3	3.2
D	24	0.07	0.11	729	9

The discussion concerns primary cracks studied in classical fracture mechanics (see Chapter 2.2). The hypothesis is that the particles need to be adequately stabilized, and there must be enough ionomer present between them to offer sufficient internal resistance against crack formation. This necessary ionomer originates from a sufficiently thick shell of bound ionomer surrounding the particles, as well as from the additional free ionomer existing between them. It is suggested that a larger amount of free ionomer in the liquid ink ensures sufficient binder is available during layer solidification to dissipate stresses and consequently reduce cracking within the layers.

The link to the milling process is the total particle surface area. Different milling conditions result in different particle size distributions (PSDs) (see Figure 12). In turn, different PSDs result in different total surface areas (see Eq. (4.3)) and, therefore, different ratios of bound to free ionomer. The total amount of ionomer is determined during ink formulation and remains constant, regardless of subsequent ink processing or the particle sizes within the system. However, when new surface area is created during particle grinding, the ionomer attaches to or interacts with this new surface. Consequently, it's likely that the

proportions of bound and free ionomer in the ink will change. If the total particle surface area becomes too large, there won't be enough ionomer available to effectively stabilize the particles or the resulting layer (see Figure 20).

Figure 19 shows a schematic illustration of the model. For the same ink formulation but different processing, particles of different sizes (agglomerates, aggregates and primary particles) to which ionomer is bound and additional free ionomer are shown. The particle size and number as well as the ionomer distribution for the inks after 1, 3, 6 and 24 h of milling is presented. The measured d_{50} (see Table 3) serve as the respective particle size. An agglomerate with d_{50} = 0.63 µm present after 1 h of ink processing is broken down into multiple smaller agglomerates with a size of 0.2 µm after 3 h of ink processing. These, in turn, are broken into many even smaller aggregates and primary particles as the milling time continues. To cover the newly created surface by ionomer, the initially free ionomer (green) adsorbs onto the new surface. If the total particle surface area is too large, at some point there will no longer be any free ionomer in the liquid phase between the particles. Further adsorption of ionomer to the particles will not be possible.

The effects described apply to all types of particles: primary particles, aggregates and agglomerates with internal porosity formed from primary particles. The proportion of free ionomer in the ink is quantified in a next step. The total amount of ionomer $m_{\mathrm{I,total}}$ in an ink is defined by the ink formulation. However, the ionomer (I) is present in different forms in the ink [57,58]:

- free ionomer: free in solution and postulated to act as binder between particles during film solidification (index: binder);
- adsorbed and immobilized ionomer on the primary particle or agglomerate surface (index: surface);
- immobilized ionomer within porous agglomerates or porous primary particles (e.g. Ketjenblack) (index: porosity).

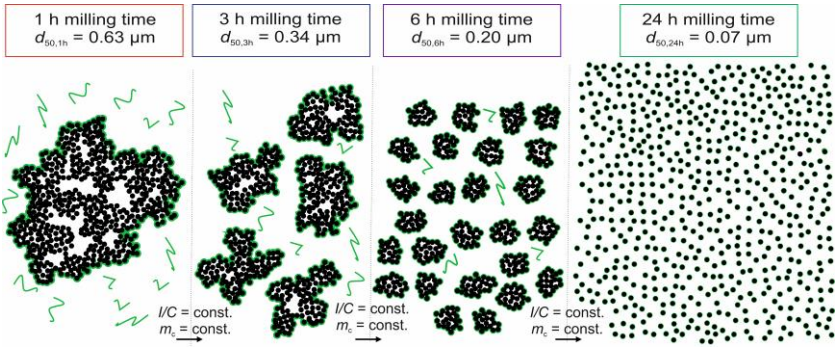

Figure 19: Schematic illustration of the influence of the milling time t on the number N_i and size d_{50} of agglomerates, aggregates and primary particles and their total surface area. The stated size per milling time corresponds to the d_{50} of the experimentally tested inks. Taking a constant ionomer-to-carbon ratio *I/C* and catalyst content m_C, with increasing milling time the size of particles decreases and their number and specific surface area increase. More ionomer adsorbs at the greater surface and the content of free ionomer in solution decreases. [262]

The individual proportions of ionomer forms vary depending on the way the ink is processed, but the total amount remains constant (Eq. (4.4)). The individual amounts of the different ionomer forms can be described by their volumes and the corresponding densities (Eq. (4.5)).

$$m_{\mathrm{I,total}} = const. = m_{\mathrm{I,binder}} + m_{\mathrm{I,surface}} + m_{\mathrm{I,porosity}} \qquad (4.4)$$

$m_{\mathrm{I,total}}$	Total amount of ionomer in mg
$m_{\mathrm{I,binder}}$	Amount of ionomer present as free ionomer in mg
$m_{\mathrm{I,surface}}$	Amount of adsorbed and immobilized ionomer on the primary particle or agglomerate surface in mg
$m_{\mathrm{I,porosity}}$	Amount of immobilized ionomer within porous agglomerates or porous primary particles in mg

$$m_{\mathrm{I,total}} = \rho_{\mathrm{I,binder}} \cdot V_{\mathrm{I,binder}} + \rho_{\mathrm{I,surface}} \cdot V_{\mathrm{I,surface}} + \rho_{\mathrm{I,porosity}} \cdot V_{\mathrm{I,porosity}} \qquad (4.5)$$

$V_{\mathrm{I,total}}$	Total volume of ionomer in cm³
$\rho_{\mathrm{I,binder}}$	Density of ionomer present as free ionomer in mg cm^{-3}

$V_{\mathrm{I,binder}}$	Volume of ionomer present as free ionomer in cm³
$\rho_{\mathrm{I,surface}}$	Density of adsorbed and immobilized ionomer on the primary particle or agglomerate surface in mg cm^{-3}
$V_{\mathrm{I,surface}}$	Volume of adsorbed and immobilized ionomer on the primary particle or agglomerate surface in cm³
$\rho_{\mathrm{I,porosity}}$	Density of immobilized ionomer within porous agglomerates or porous primary particles in mg cm^{-3}
$V_{\mathrm{I,porosity}}$	Volume of immobilized ionomer within porous agglomerates or porous primary particles in cm³

The densities of the ionomer modifications differ and depend on the interactions with the immediate environment. The density of the free ionomer is influenced by the properties and interactions with the ambient solvents [88]. Furthermore, the density of the adsorbed ionomer is influenced by the surrounding solvents and the particle surfaces (e.g. platinum content). The ionomer within agglomerates and porous primary particles is affected by the interactions within the agglomerate and the particle microstructure [44,265]. It is important to note that changing conditions during ink application and drying may change those interactions.

The proportion of the ionomer that is relevant to the analysis of crack formation is $V_{\mathrm{I,binder}}$. This is determined by the subtraction of the proportions of immobilized ionomer from the total mass of ionomer. In a first approximation, it is assumed that there is little to no ionomer in the agglomerates themselves due to the small pores within an aggregate or agglomerate ($V_{\mathrm{I,porosity}} \rightarrow 0$). The surface of the particles is relevant for the amount of the bound ionomer. This means that $V_{\mathrm{I,binder}}$ is dependent on $V_{\mathrm{I,surface}}$. $V_{\mathrm{I,surface}}$ in fact, can be estimated under the premises, that the (free) ionomer adsorbs onto (the newly formed) agglomerate or primary particle surface, and that the particles are spherical. Assuming the ionomer coverage as a shell around the particles, $V_{\mathrm{I,surface}}$ results then from the sum of all volumes of spherical shell of a shell thickness d around each of the N_i particles with size x_i of all size classes (Eq. (4.6)). Potential geometric deviations and incomplete surface coverage are taken into account in the factor ξ.

$$V_{\mathrm{I,surface}} = \sum N_i \cdot \xi \cdot \frac{\pi}{6} \cdot \left((d_i + 2\mathrm{s})^3 - {d_i}^3 \right) \qquad (4.6)$$

N_i	Number of particles in size class *i* (dimensionless)
ξ	Surface coverage and geometric factor (dimensionless)
d_i	Particle size in size class *i* in µm
s	Shell thickness of ionomer around particles in nm

When $d_i \gg s$, the term is simplified by using the first binomial formula for the third power and neglecting the terms with d in a higher power, resulting in the sphere surface multiplied by the shell thickness (Eq. (4.7)). If the shell thickness is constant and independent of the particle size, even an explicit conversion of Eqs. (4.5) and (4.7) to s would be possible. In summary, the free ionomer proportion of the ink is dependent on the particle size distribution (PSD) (Eq. (4.8)). With the hypothesis that free ionomer is necessary as a stress-resistant binder during film solidification to prevent cracking, it is hereby evident that the PSD of an ink has a strong influence on the crack pattern of a layer produced from this ink.

$$V_{\mathrm{I,surface}} \approx \sum N_i \cdot \xi \cdot \pi \cdot {d_i}^2 \cdot \mathrm{s} \qquad (4.7)$$

$$V_{\mathrm{I,binder}} = f(PSD) \qquad (4.8)$$

Kumano et al. [57,58] determined the free ionomer content experimentally by filtering out particles and adsorbed ionomer from the ink. The liquid residue (solvent and free ionomer) was then dried and weighed. The dry mass is defined as free ionomer and can be related to the total ionomer mass from the initial ink formulation. Unfortunately, similar experiments were unsuccessful here. It was not possible to separate all the particles, especially the smallest ones (around 10 nm in size), either by filtration or centrifugation. However, these would significantly distort the free ionomer mass result. Kumano et al. [58] also observed the highest adsorption rate of ionomer on *Pt*/Carbon and thus the lowest free ionomer content in the inks with the smallest particles. It should be added that the solvents (compositions) also changed in their ink series, which may have influenced the distribution somewhat (see Chapter 1.3).

Kumano et al. [58] consider free ionomer to be more causative of cracking (due to inhomogeneous ionomer clumping). This is in contrast to the previous assessment of free ionomer as beneficial for crack resistance, as presented in this study. They emphasize that for high crack resistance the particles must be sufficiently wetted with ionomer and thus stabilized, i.e. $V_{\mathrm{I,surface}}$ must be high. As a result, they would prefer to go for the particle-adsorbed ionomer over the free ionomer. At first glance, these two interpretations sound contradictory, but at second glance they fit well together and complement each other. Firstly, great amounts of free ionomer, resulting in the formation of substantial ionomer agglomerates, can act as a nucleation site for cracks. Furthermore, the explanations presented here also suggest that the ionomer preferentially wets the (new) particle surface and that this must be the case for stable inks and coatings. However, it is essential that free ionomer is present during particle breakup to ensure that newly formed surfaces (e.g. in the grinding process) can be adequately wetted with ionomer without the addition of further ionomer. The free ionomer can thus be considered as an ionomer reservoir in the ink. If the ionomer has already been distributed over the existing particle surface, new surfaces can no longer be covered. For the grinding process in particular, this means that the particles may become so small that its surface cannot be completely covered with ionomer because all free ionomer has been consumed. This seems to be the case for the particles in the ink after 24 h of milling, thus resulting in a pronounced crack network in the dried layer (see Figure 14). There are theoretically two possibilities to supply the new surface with ionomer when no free-ionomer is available:

- I) The shell thickness around the different particles will decrease (Figure 20 I)). This is also described in [63]. This might result in a reduction of particle stabilization which can lead to particle re-agglomeration.
- II) The coverage of the particle surface with ionomer is reduced (Figure 20 II)). As a result, particles which are not completely covered with ionomer are present. This decreases particle stabilization.

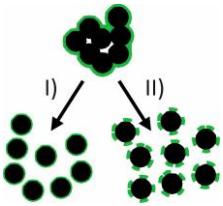

Figure 20: Effect of the particle surface area on the ionomer shell around particles. If no additional free ionomer is available from the ink, I) the ionomer shell thickness becomes thinner or II) the particles are only partially covered with increasing particle surface area. [262]

Beyond ink stability and the crack pattern, it is assumed that the distribution of the ionomer influences the electrochemistry in the operation of an electrode. These aspects are not discussed in more detail in this thesis, but should nevertheless be mentioned. Aspects to be considered are the proton conductivity and the coverage of the active catalyst sites under an ionomer shell which both is expected to negatively influence the fuel cell performance [54].

4.3 Adjusting the ionomer-to-carbon ratio to the particle size distribution for crack mitigation

The assumption is: The presence of free ionomer indicates that the particles are adequately covered with ionomer, which prevents cracking during film solidification. This is investigated for validity by increasing the *I/C* ratio. The addition of ionomer increases the amount of ionomer adsorbed on the particle surface where it was previously insufficient, and also increases the amount of free ionomer. Accordingly, if the *I/C* is sufficiently high, there should be enough (free) ionomer to produce a layer without cracks.

Since less cracks are obtained after a milling process for 6 h ($SN = 6.68 \cdot 10^8$ m^{-1}; $I/C = 1.0$), it is assumed that there is sufficient ionomer at the given PSD to prevent cracking. The *I/C* of 1.0 matches the present PSD in this ink. After 24 h ($SN = 26.7 \cdot 10^8$ m^{-1}; $I/C = 1.0$), many cracks occur in the layer and the *I/C* ratio is considered as too low for the given PSD. Following the assumption, the *I/C* of the ink is increased and then processed for 24 h. The additional

ionomer requirement is calculated from the ratio of the total particle surface area per gram of ink of the two inks milled for 24 h (*I/C* does not match PSD) and for 6 h (*I/C* matches PSD). Assuming all particles as spheres, the PSDs result in a surface area ratio of 1.37. Consequently, new ink formulations are tested with a slightly higher *I/C* than originally (*I/C* = 1.2) and one with a bit higher *I/C* than the calculated particle surface area ratio to compensate for ideal simplifications in the calculation (*I/C* = 1.5). The new inks are processed in the ball mill also for 24 h at 1000 rpm ($SN = 26.7 \cdot 10^8$ m^{-1}) to achieve the same or a similar PSD and particle surface area to the ink with 24 h and *I/C* = 1.0. With similar particle surface area, the additional amount of ionomer should compensate for eventually missing bound ionomer at the particle surface, and the residual should increase the free ionomer content.

All three inks which were milled for 24 h, but with different *I/C* ratios, exhibit a similar particle size distribution (Figure 21). In the *I/C*-range tested, as the *I/C* increases, the curves shift slightly to the right towards somewhat larger particle sizes. However, these differences are not large enough to be considered relevant, and it is concluded that the *I/C* has no significant effect on the resulting PSD. Similar observations were made by Hoffmann et al. [62]. From these results it is concluded that all three inks effectively have a similar particle surface areas in the inks. Therefore, the same amount of ionomer is needed to sufficiently cover the particle surface.

Next, the quality of the layers produced by the inks is analyzed. Comparing the pore diameter distribution, it was found that fewer pores were measured at higher *I/C*. The maximum detected pore diameter also decreases (see Appendix 9.4). The ionomer probably narrows and blocks the pores during film formation. This may be due to a thicker ionomer shell around the particles or to ionomer still present as free ionomer which forms ionomer-clusters during film solidification. Comparable findings were made by Yu et al. [67] and Carcadea et al. [66].

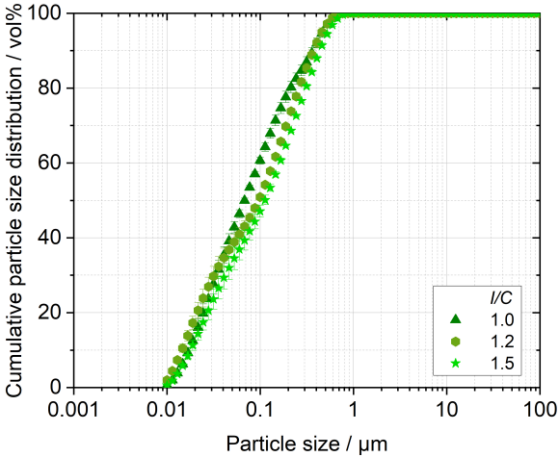

Figure 21: Cumulative particle size distribution (PSD) depending on the *I/C* ratio for inks milled for 24 h at 1000 rpm ($SN = 26.7 \cdot 10^8\ m^{-1}$). The *I/C* seems to have no significant influence on the PSD, when processed the same. In the context of the investigation, it is important that the particle distributions reveal similar total surface areas. [262]

In terms of crack patterns, as is already known from Figure 14, with *I/C* = 1.0, a pronounced crack pattern extends throughout the entire layer with a crack area of 2.5 % ± 0.8 %. Increasing the *I/C*, a crack network is also observed at *I/C* = 1.2 (Figure 22). Although the crack network is less pronounced, the improvement in the crack area is only slight (2.3 % ± 0.8 %). A small amount of additional ionomer strengthens the particles' cohesion slightly, thereby increasing their resistance to cracking slightly. Further increasing the *I/C* ratio beyond what is necessary to account for the large PSD based on the crack pattern of the layer which ink was milled for 6 h (calculated surface area ratio 1.42) results in the disappearance of the crack network at *I/C* = 1.5, and a reduced crack area with 0.3 % ± 0.6 %. This corresponds exactly to the proportion of cracks in the reference layer (see Figure 14). The *I/C* of I.5 used here allows for a slight margin of error in the amount of ionomer used, due to simplifications in the calculation of the factor. For example, the calculation assumes idealized spherical particles, which do not exist in reality.

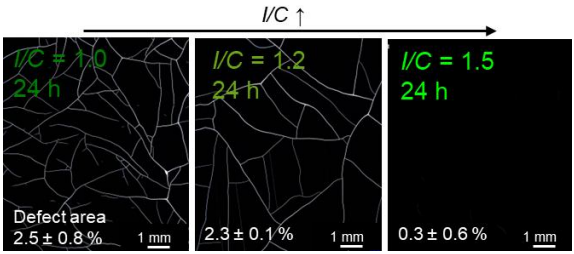

Figure 22: Crack pattern depending on the *I/C* ratio. The inks were all milled for 24 h, directly coated onto the membrane and dried under identical drying conditions. Layer thicknesses are comparable at 7.3 ± 0.6 µm. Increasing the *I/C* leads to less cracks. [262]

A reduced crack area was also observed within an *I/C* series with 3 h ball mill treatment and increased *I/C*. As the presence of cracks was not particularly prevalent at an *I/C* of 1.0, the enhancement is less perceptible at an *I/C* of 1.2, but still significant (see Appendix 9.4). In all conducted experiments, a significant improvement of the electrode quality in the form of a smaller total defect area is obtained when ionomer is added. This is due to the sufficient wetted particle surfaces and the free ionomer in the ink acting as a binder between the particles during solidification.

It should be noted that an *I/C* ratio that is too high compared to what is required for the particle surface can clog pores, thereby reducing the electrochemical performance of the electrode during operation (what was not investigated in this work). Excessive free ionomer and large agglomerates of ionomer could also cause defects [35]. However, the assumption that adding sufficient ionomer to the ink can compensate for the large surface area of the particles and stabilize the films against cracking is further confirmed. The beneficial amount of ionomer and the surface area of the particles are linked. To achieve a good result, *I/C* from the ink formulation and the processing must be coordinated.

4.4 Conclusion on ink processing

The objective of the chapter was to enhance comprehension of the ink processing. This investigation involved a systematic analysis of various process parameters during ball milling, in order to validate Hypothesis 1:

In order to reduce cracking in catalyst layers, the processing and formulation of the ink must be adjusted and balanced. The link is the particle size distribution (PSD) of the ink.

With longer milling times, as expected, the particle size distribution (PSD) shifts towards more small particles with longer milling times. In particular, the largest agglomerates are broken up. A similar effect is observed when the rotational speed in the milling process is increased under otherwise identical ink processing conditions. In a next step, milling time and speed were adjusted to provide a constant stress number ($SN \sim t \cdot n$). The *SN* is derived from ball milling considerations of different material systems and, to the best of the author's knowledge, has not yet been applied to the catalyst ink for PEM fuel cells. By adjusting *SN*, a very similar PSD is found. It is concluded that *SN* is the process function for the PSD of the catalyst inks and describes the relationship between the process parameters and the PSD (Figure 23). The process function links the diverse process parameters to the essential physicochemical properties, which determine the product properties.

In addition, membrane direct coatings were produced with the investigated inks. For reproducible process conditions, the coating and drying parameters where kept constant and the layer quality was analyzed via cracking pattern analysis and pore diameter distribution measurements. It is found that both properties are correlating with the PSD. Similar PSDs lead to very similar pore diameter distributions and also to very similar crack patterns. The PSD is therefore the key physicochemical parameter for the layer properties. For predictions in the manufacturing process of catalyst layers, the PSD of an ink is a valuable parameter.

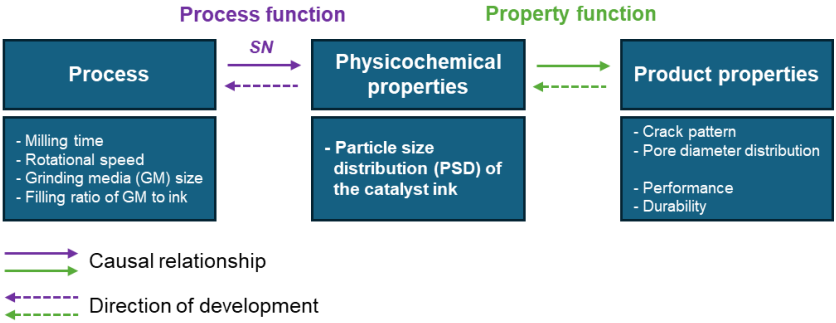

Figure 23: Process and property functions in ink processing.[10] Physicochemical properties and the process and property functions are the link between the desired product properties and the set process parameters. The particle size distribution (PSD) of the catalyst ink was found to be the essential physicochemical property that determines the specific product properties of the layers produced from the ink. The stress number (*SN*) describes the process function of the various process parameters.

An analysis of the crack pattern reveals an optimum for the milling process. On the one hand, the absence of large agglomerates, which function as nucleation points for cracks, is beneficial. This improves with higher *SN* during ink processing. Furthermore, an initially unexpected effect of a pronounced crack network occurs for an ink with a very small PSD. This phenomenon is found to be attributed to the extensive surface area requiring stabilization, which is associated with the numerous small particles. The amount of ionomer in the ink is predetermined by the formulation, and thus the amount of particle surface to be stabilized with the ionomer present varies depending on the PSD. Sufficient ionomer wetting of the particles is claimed to have a positive binding property and thus can dissipate occurring stresses in the solidification process of a drying film. A marker of sufficient ionomer wetting of the particles is the presence of free ionomer. This serves as a reservoir for further particle surface stabilization. However, an optimum balance must be struck between the

[10] The model of process and property functions was developed by Hans Rumpf (1911–1976). The model is widely used in process engineering product development [266–270].

provision of ionomer for new surfaces, binding activity, and supporting crack resistance and electrochemistry, before too much ionomer clogs pores or forms ionomer agglomerates that are either unnecessary or unfavorable.

A higher *I/C*, and thus more ionomer for the larger particle surface in inks with a smaller PSD, can compensate for the assumed lack of ionomer. With similar PSDs and thus approximately the same particle surfaces, layers with a higher *I/C* exhibit significantly less cracking. Consequently, the ionomer requirement is related to the PSD of the ink. To the best of the author's knowledge, this relationship has not yet been identified. In most cases, the formulation is set independently of the ink processing. However, it is recommended that the interaction between formulation and processing is considered holistically. In summary, Hypothesis 1 is completely confirmed at the end of the investigations: The PSD is a crucial factor in ink processing and must be taken into account when formulating inks. Ink processing resulting in an individual particle surface requires the appropriately adjusted amount of *I/C*. Or vice versa: given a specific *I/C*, the ink processing must be adjusted for this specific mixture.

In continuing this work, the ink processing was standardized to 3 h at 1000 rpm. However, better processing is found at 6 h at 1000 rpm or 3 h at 2000 rpm. Nevertheless, it seems useful for further optimization and understanding if some imperfections occur in the layer. This makes it easier to identify and understand effects of different process parameters on the layer quality in form of the crack pattern.

5 Solvent composition of the ink during processing in decal and membrane direct coating[1]

The next steps in the catalyst-coated membrane (CCM) production process – coating and drying – are now discussed. Challenges in the processing of the ink to form the electrode are the formation of cracks in the layers and, in the case of membrane direct coating (MDC), the pronounced swelling and shrinkage with deformation of the membrane. These effects affect both the manufacturing process itself and the subsequent performance and durability of the CCM. The investigations carried out in this thesis are based on the overriding hypothesis that membrane swelling and different crack formation behavior are essentially due to the ink solvents, their composition and the solvent fluxes occurring during ink processing and can be specifically addressed with an adequate understanding of the mass transport processes taking place.

First, the interactions of the ink with different substrates from different CCM production processes (decal or MDC) are examined. The same ink is applied to two decal substrates: a glass-fiber reinforced polytetrafluoroethylene (PTFE) foil (Decal) and a virgin PTFE foil (Teflon), and to a Nafion NR212 membrane (M w/ S).[2] The isothermal drying conditions remain constant.

[1] Parts of the results and figures presented in this chapter were presented at the Fuel Cell Conference Chemnitz 2024 and have been published in a conference paper, available under a CC BY 4.0 license:
Quarz P, Zimmerer N, Janning L, Mannes F, Scharfer P, Schabel W. *From Decal coating to membrane direct coating in catalyst coated membrane (CCM) production*. Wasserstofftechnologien Effizient Produziert, vol. 1, Chemnitz, Germany: Verlag Wissenschaftliche Scripten; 2024, p. 135–44. https://doi.org/10.60687/2025-0065, referred to in this work as [30].

[2] The Nafion N212 membrane is supplied on a mechanically stabilizing backing foil (see Chapter 3.2). In the course of the investigations, the membrane is considered with (M w/ S) and without (M w/o S) support. Unless otherwise stated, M w/ S is used, e.g. in Chapter 4.

Under otherwise identical conditions, there are significantly more defects on the membrane than on the decal substrates (Figure 24). The crack area rises.

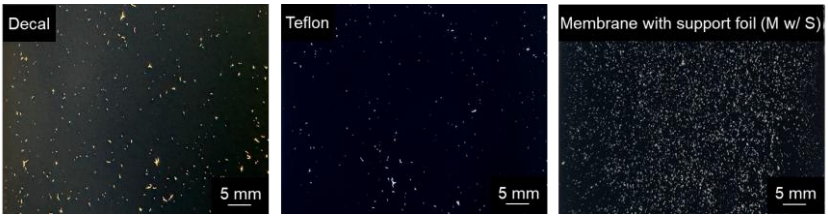

Figure 24: Influence of the substrate on the crack pattern in catalyst layers. An identical ink was applied to a decal foil, a Teflon foil and the membrane (M w/ S) and the catalyst films were dried with the same drying conditions (T = 25 °C, α = 35 W m^{-2} K^{-1}). The dry film thickness is approx. 8.6 ± 0.5 µm. Cracks are visible as white spots. [30]

The different crack pattern between the PTFE substrates and the membrane is attributed to the pronounced swelling behavior of the membrane in contact with the catalyst ink. Membrane swelling due to water contact is well documented (see Chapter 1.4). The interactions between the substrates and the ink solvents are investigated by applying the pure solvent mixture (20 wt% 1-propanol, 80 wt% water) to the different substrates (Figure 25).

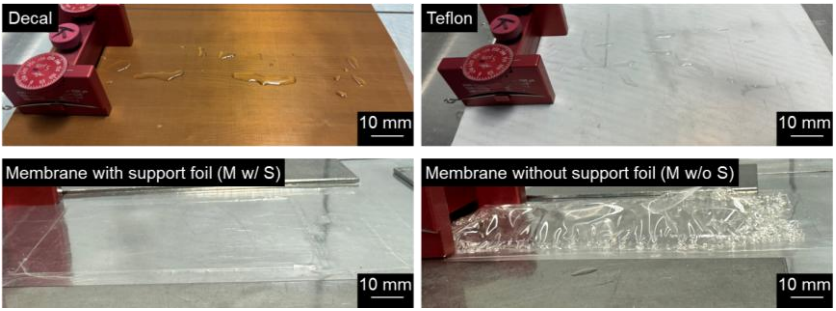

Figure 25: Interaction behavior of the inert Decal and the Teflon foil as well as the membrane with (M w/ S) and without (M w/o S) supporting backing foil in contact with an applied thin film of the solvent mixture (20 wt% 1-propanol; 80 wt% water). [30]

The solvent does not interact or even wet the Decal and the Teflon foil. Conversely, the membrane swells. This is barely noticeable without magnification for the membrane with a mechanically supporting backing foil (M w/ S). The situation is more obvious when the backing foil is removed (M w/o S). In this case, the membrane swells and deforms significantly. Due to the huge deformation, it is assumed that the membrane is unsuitable for adequate substrate handling and low-crack coating, which is why the backing foil is initially always used. However, the removal of the backing foil is necessary for the coating of the second electrode and is discussed in Chapter 1.

In order for the membrane to swell to this extent, a significant amount of ink solvent must flow into it. This solvent is removed from the ink. If this happens selectively, i.e. preferably for one specific solvent, this changes the solvent composition in the remaining ink film. The effects of solvent composition on the microstructure and crack pattern of a fuel cell electrode are often directly attributed to the initial composition. However, given the significant swelling behavior observed, compositional changes must be considered in the process steps between ink mixing and the final layer. These changes occur after the ink is applied to the substrate and during drying and result from selective membrane swelling (see Chapter 1.4) and selective evaporation (see Chapter 2.3) with all the associated consequences (see Chapter 1.3). The actual solvent composition significantly impacts the ionomer's conformation and how particles interact together. These solvent-particle interactions, in turn, dictate the final structure of the solidifying catalyst coating, making the actual solvent composition a crucial factor. However, the process-related influences on the compositional changes after ink application are still largely unknown or insufficiently investigated. The following investigations therefore deal with the changing composition of the solvents in the ink $x_i(t)$ after coating and during drying.

In MDC, drying and membrane swelling occur simultaneously. Thereby, different solvent mass flows occur into the drying air and into the membrane. In order to understand the entire (mass transport) process after ink application, it is important to consider the two phenomena step by step. For simplification, a schematic illustration of a drying film on a membrane is given in Figure 26.

Two phenomena are distinguished and the component material flows leaving the ink (shown as arrows) are considered in each case. Firstly, only selective drying is considered (Figure 26 I)). This phenomenon occurs in both the decal and MDC processes. The description of selective drying is sufficient to describe the change in ink composition in the decal process. In MDC, it does not fully describe the compositional change, since the flow of solvents into the membrane must also be considered. However, it is an essential part that must be considered separately to gain a deep understanding of the overall coating and drying process. Chapter 1 discusses selective evaporation in catalyst inks in great detail.

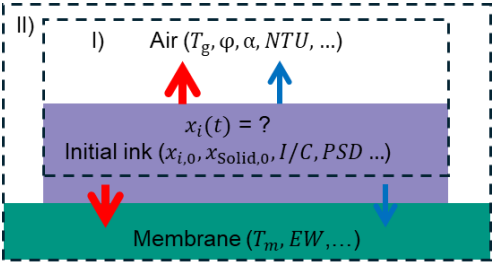

Figure 26: System boundaries and solvent mass flows (shown as arrows) occurring after coating and during drying of a catalyst ink. The solvent composition $x_i(t)$ in the ink changes after the ink application on the substrate during the subsequent drying process. This is influenced by several parameters. In order to work out the effects step by step: I) first only the selective drying is analyzed only accounting for the ink and the drying air (without interactions to the substrate). II) For membrane direct coating, the selectively swelling membrane is added in a second step.

In a second step, the MDC, including both the selective drying and the swelling membrane, is discussed (Figure 26 II)). Here, there are additional material flows, first from the ink into the membrane during swelling and then from the membrane during subsequent membrane drying and thus shrinking. This is content of Chapter 1.

The component-specific mass flows can be balanced depending on the components which are accounted for. Eq. (5.1) applies solely to the time-resolved

selective drying into the air (see Figure 26 I)). For MDC (see Figure 26 II)), this equation is extended by the membrane swelling term (Eq. (5.2)). As the membrane shrinks, the mass flow, and therefore the last term in Eq. (5.2), may reverse. In a first step, it is postulated: Regarding the compositional change during ink drying, it is initially irrelevant whether the solvents deplete into the drying air or the membrane. The decisive factor is the component-specific total solvent release.[3]

$$\frac{\partial m_{i,\mathrm{air}}}{\partial t} = -\dot{m}_{i,\mathrm{air}} \tag{5.1}$$

$m_{i,\mathrm{air}}$	Mass of component *i* in the ink at time *t* regarding only drying into the air in g
t	Time in s
$\dot{m}_{i,\mathrm{air}}$	Mass flow of component *i* induced by drying into the air in g s^{-1}

$$\frac{\partial m_{i,\mathrm{MDC}}}{\partial t} = -\dot{m}_{i,\mathrm{air}} - \dot{m}_{i,\mathrm{membrane}} \tag{5.2}$$

$m_{i,\mathrm{MDC}}$	Mass of component *i* in the ink at time *t* after membrane direct coating (MDC) in g
$\dot{m}_{i,\mathrm{membrane}}$	Mass flow of component *i* induced by membrane swelling and shrinkage in g s^{-1}

The total mass flows alone are not sufficient to describe the possible change in composition. Rather, the solvent composition of the outgoing total mass flow must be considered in relation to the current ink solvent composition. In fact, this is the definition of the selectivity (see Chapter 2.3 and Eq. (2.13)). For example, for an ink with 20 wt% 1-propanol and 80 wt% water, the outgoing water mass flow must be 4 times greater than the 1-propanol mass flow to keep the solvent composition constant. As the relative mass flow is defined as the mass flow of the observed component divided by the sum of all component

[3] Drag currents may vary depending on mass flows, entrain free ionomer and influence ionomer distribution in the film. Such variation in the ionomer distribution was observed by Mauger et al. [91] due to different drying conditions, which can be explained by these effects. To understand all effects, it is crucial to account for material transport in all directions – in the drying air and into the membrane itself.

mass flows, it is interpreted as the necessary composition of the outgoing mass flows. The relative component mass flow and the corresponding selectivity that describe membrane direct coating, balance space II, are defined in Eqs. (5.3) and (5.4), based on Schlünder's definitions [196,200,201].

$$\dot{r}_{i,\mathrm{MDC}} = \frac{\dot{m}_{i,\mathrm{air}} + \dot{m}_{i,\mathrm{membrane}}}{\dot{m}_{\mathrm{total,air}} + \dot{m}_{\mathrm{total,membrane}}} \tag{5.3}$$

$\dot{r}_{i,\mathrm{MDC}}$ Relative mass flow of component *i* during membrane direct coating (MDC) in g s^{-1} g s^{-1} %

$\dot{m}_{\mathrm{total,air}}$ Total evaporating mass flow into the air in g m^{-2} s^{-1}

$\dot{m}_{\mathrm{total,membrane}}$ Total mass flow induced by membrane swelling and shrinking in g m^{-2} s^{-1}

$$S_{i,\mathrm{MDC}} = \dot{r}_{i,\mathrm{MDC}} - x_i \tag{5.4}$$

$S_{i,\mathrm{MDC}}$ Selectivity of component *i* during membrane direct coating (MDC) in wt%

x_i Solvent mass fraction of component *i* in the ink in wt%

When making statements about changes in ink-solvent composition, the overall selectivity must be considered. The mass fluxes that occur depend on the actual composition of the ink [37,190]. Drying and swelling are coupled via the present composition and influence each other. However, for step-by-step consideration, the system can be divided into the two subprocesses: the evaporation flow from drying into the air and the mass flow into the membrane. The selectivity and relative mass flow are described separately because both can be simulated and described by specific experiments and model considerations for each subprocess. This allows for a deeper understanding of the process to be developed. First, the relative mass flow and selectivity are defined solely with respect to the selective drying into air (Eqs. (5.5) and (5.6)), equivalent to balance space I.

$$\dot{r}_{i,\mathrm{air}} = \frac{\dot{m}_{i,\mathrm{air}}}{\dot{m}_{\mathrm{total,air}}} \tag{5.5}$$

$\dot{r}_{i,\mathrm{air}}$ Relative evaporation flow of component *i* into the air in g s^{-1} g s^{-1} %

$$S_{i,\mathrm{air}} = \dot{r}_{i,\mathrm{air}} - x_i \tag{5.6}$$

$S_{i,\mathrm{air}}$ Selectivity for component *i* drying into the air in wt%

Second, the relative mass flow and selectivity are defined solely with respect to the membrane swelling and subsequent shrinking (Eqs. (5.7) and (5.8)).

$$\dot{r}_{i,\mathrm{membrane}} = \frac{\dot{m}_{i,\mathrm{membrane}}}{\dot{m}_{\mathrm{total,membrane}}} \tag{5.7}$$

$\dot{r}_{i,\mathrm{membrane}}$ Relative mass flow of component *i* induced by membrane swelling and shrinking in g s^{-1} g s^{-1} %

$$S_{i,\mathrm{membrane}} = \dot{r}_{i,\mathrm{membrane}} - x_i \tag{5.8}$$

$S_{i,\mathrm{membrane}}$ Selectivity of membrane swelling and shrinking for component *i* in wt%

Referring back to the distinction between the two balance spaces mentioned above, balance space I is considered first with regard to only air drying (see Eqs. (5.5) and (5.6)). There are three cases to be distinguished regarding selectivity for inks with binary solvent mixtures (*i* and *j*) (cases (5.9) – (5.11)).

Balance space I: regarding only the drying into the air:

$S_{i,\mathrm{air}} > 0$ → Solvent *j* accumulates relatively in the ink. (5.9)

$S_{i,\mathrm{air}} = 0$ → Solvent composition remains constant. (5.10)

$S_{i,\mathrm{air}} < 0$ → Solvent *i* accumulates relatively in the ink. (5.11)

The three cases are applied to the 1-propanol/water solvent system used in this study. The change in film composition is illustrated in Figure 27. The initial ink is presented purple as a mixture of the two solvents (blue: water, red: 1-propanol). With the identical initial composition, depending on the selective drying (cases Eq. (5.9) or (5.11)) the composition of the film changes. A bluer color indicates a higher proportion of water in the remaining ink during drying, a redder color indicates a higher proportion of 1-propanol. The thickness of the arrows indicates the magnitude of the evaporation mass flows (red: 1-propanol, blue: water). To simplify the model and for showcasing the effect of selectivity, the initial composition is 50:50. This allows that the selectivity can be inferred directly from the indicated strength of the mass flows or the relative

mass flows derived from them. (For all other compositions, the relative mass flux is not sufficient (see Eq. (5.6)).

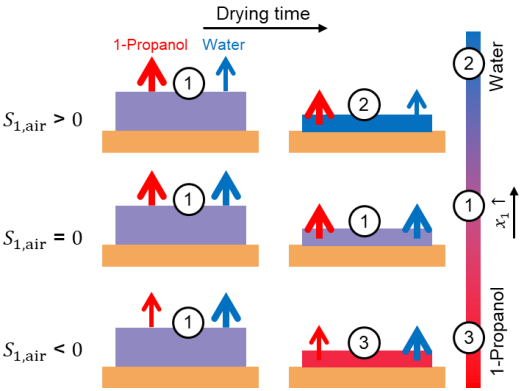

Figure 27: Influence of the 1-propanol selectivity $S_{1,air}$ due to drying into the air on the ink composition, color-coded. The arrows symbolize the relative fluxes of 1-propanol (red) and water (blue) of different strengths (arrow thickness). A transfer to drying selectivity should be given here directly. If 1-propanol preferentially escapes from the ink ($S_{1,air} > 0$), the proportion of water in the remaining ink rises, shown in a more blue color ①→②. When drying non-selectively ($S_{1,air} = 0$), the initial composition stays the same ①→①. If water preferentially evaporates ($S_{1,air} < 0$), the proportion of 1-propanol in the remaining ink rises and is colored redder ①→③.

Considering balance space II and describing the membrane direct coating while accounting for all mass fluxes occurring during drying and membrane swelling increases the complexity. For each of the three cases above, the additional solvent flows into the membrane (and out of the membrane during membrane shrinking) can increase, neutralize or reverse the overall selectivity. For the first approximation, only the solvent fluxes from the ink into the membrane during swelling (without reverse fluxes during membrane shrinking) are considered. Based on the aforementioned three cases for $S_{i,air}$, a further conclusions can be drawn: For $S_{i,air} = 0$, the total selectivity is determined solely by $S_{i,membrane}$. In the case of $S_{i,air} < 0$, there are 5 possibilities regarding the total selectivity. The same is true for $S_{i,air} > 0$, but vice versa (cases (5.12) – (5.16)).

The decisive factor here is whether drying or membrane swelling predominates. The individual selectivities ($S_{i,\mathrm{air}}$ resp. $S_{i,\mathrm{membrane}}$) alone are not sufficient. Instead, the mass flows must be added together and considered together (see Eqs. (5.3) and (5.4)). A high membrane selectivity combined with a low solvent mass flow into the membrane and a simultaneous high drying rate into the air with less pronounced selectivity may not be as significant. This emphasizes the complexity of membrane direct coating.

Balance space II: Solvent fluxes into the air and the membrane in the case of $S_{i,\mathrm{air}} > 0$ and different $S_{i,\mathrm{membrane}}$

$S_{i,\mathrm{MDC}} >>> 0$ → Solvent *j* accumulates relatively in the ink. (5.12)

$S_{i,\mathrm{MDC}} >> 0$ → Solvent *j* accumulates relatively in the ink. (5.13)

$S_{i,\mathrm{MDC}} > 0$ → Solvent *j* accumulates relatively in the ink. (5.14)

$S_{i,\mathrm{MDC}} = 0$ → Solvent composition remains constant. (5.15)

$S_{i,\mathrm{MDC}} < 0$ → Solvent *i* accumulates relatively in the ink. (5.16)

The overall selectivity resulting from the selective drying and membrane swelling are shown schematically in Figure 28. The thickness of the arrows is again intended to symbolize the magnitude of the relative material fluxes into the drying air and into the swelling membrane (1-propanol red and water blue). Color scheme and initial composition are identical to Figure 27. The overall selectivity and solvent compositions can be deducted from the color palette. The selectivity of drying and membrane swelling can reinforce or counteract and weaken each other. In a very special case, they cancel each other out ($S_{i,\mathrm{MDC}} = 0$), and the ink solvent composition does not change. However, if the membrane is swollen and this flux is reduced or even reversed during membrane drying, $S_{i,\mathrm{MDC}} = 0$ no longer applies.

The situations described provide an overview of the selectivities that occur, when only observing the drying into the air (which applies to the decal process) and observing MDC and how they affect qualitatively the ink composition. The individual effects influence each other. The next step is to examine the material flows and selectivities in more detail. Selectivity and the various factors influencing it in the drying process will be examined first.

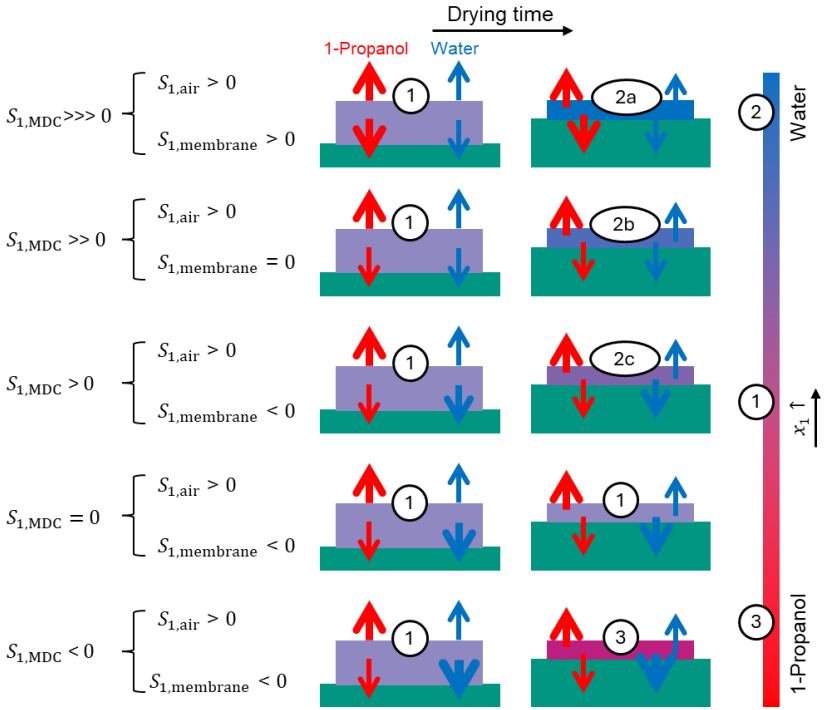

Figure 28: Influence of solvent selectivity due to drying and membrane swelling on ink composition, color-coded. The arrows symbolize the relative fluxes of 1-propanol (red) and water (blue) of different strengths (arrow thickness). A transfer to selectivity should be given here directly. If 1-propanol preferentially escapes from the ink, the proportion of water in the remaining ink increases, shown in a more blue color ①→②. In the special case $S_{1,MDC} = 0$, the composition stays the same ①→①. If water escapes preferentially overall, the proportion of 1-propanol in the residual ink increases and is colored redder ①→③. For $S_{1,membrane} < 0$, three different cases arise for $S_{1,MDC}$.

6 Selective solvent evaporation in catalyst ink drying

This chapter provides a systematic analysis of the drying of fuel cell inks. Previous work on this subject in the literature has mainly been empirical. This chapter aims to improve the understanding of the drying process and the effects that occur during it, with a focus on the solvent composition, based on Hypothesis 2:

Selective drying influences microstructure formation during film consolidation of the fuel cell electrode.

The drying selectivity describes the preferential evaporation of one solvent compared to another. In order to determine under which conditions selective evaporation occurs and how it influences the microstructure of a fuel cell electrode, it is necessary to identify the factors influencing selective evaporation and the extent of their influence. To investigate ink drying selectivity, the ink system is simplified to its solvents (Figure 29). This approach is feasible at the beginning of drying because the influence of ionomer and particles is negligible. Without solids, the correct term for describing solvent mixtures is evaporation instead of drying. However, since this work refers to inks including solids, evaporation in experiments involving only solvents is also called drying.

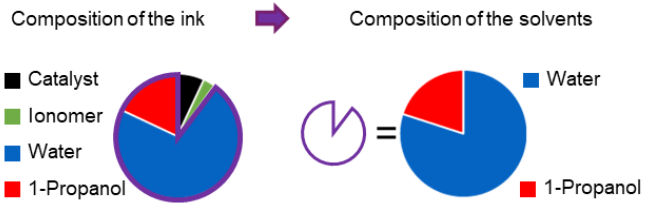

Figure 29: Mass composition of a catalyst ink (left) and the solvent mixture it contains (right).

The drying behavior of the binary solvent mixtures is analyzed in different experimental setups. A setup with a saturator is used to study thermodynamic

influences on drying (see Chapter 2.3). The flow of drying air through the liquid enables a large liquid-gas interface and relatively long residence times. However, it requires a liquid column of a certain height (cm scale) in the experimental setup used (Figure 30 I)). It is assumed that there are no gradients in the gas and liquid phases due to liquid mixing through the rising air bubbles and the long residence times, which are sufficient for thermodynamic equilibrium to be reached. At the phase boundary, there is a thermodynamically induced equilibrium.

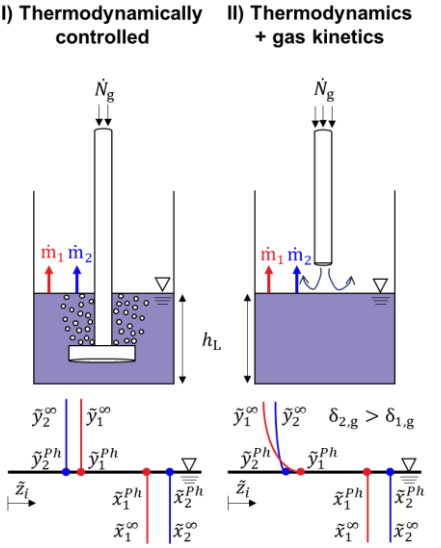

Figure 30: Limiting case considerations of mixture drying: I) thermodynamically controlled and II) gas-side-limited drying. Depending on the drying setup, the solvent fraction gradients in the boundary layer in the drying air are affected due to different gas kinetics, expressed by different diffusion coefficients. [190]

Flowing air over the liquid is closer to catalyst film drying. The first setup is slightly modified (Figure 30 II)) and allows the investigation of the selectivity in a gas-side controlled drying regime (see Chapter 2.3). Furthermore, experiments with preloading of the drying air were carried out in this setup, as this further influences the selectivity. As a first assumption from the theoretical

background, it is assumed that there are no concentration gradients in the liquid phase. For the gas phase, gradients of solvent fractions are expected in the predicted mass transfer boundary layer. This is caused by different gas kinetics, expressed in different diffusion coefficients. The ratio of solvent fractions directly at the phase boundary to those in the ambient air is expected to change with increasing distance from the phase boundary.

It is hypothesised that the results obtained can be transferred to thin films (Figure 31). For this purpose, the experiment and the analysis method have to be modified. Based on an existing experimental setup with a drying channel and inverse micro Raman spectrometry (IMRS) as a quantitative measurement method, an experiment on drying a thin film of the solvent mixture is performed. Previous works have only investigated drying with at least one non-volatile component as a reference substance e.g. [231–234,256]. Thus, a proof of concept of measuring and analyzing only solvent drying without non-volatile reference component and a quantitative accuracy assessment of the results are required. The selective evaporation of thin binary solvent films is then investigated. The film's height is scanned in so called depth scans in order to draw conclusions about the possible occurrence of concentration gradients and mass transport resistances in the liquid film (Figure 31 I)).

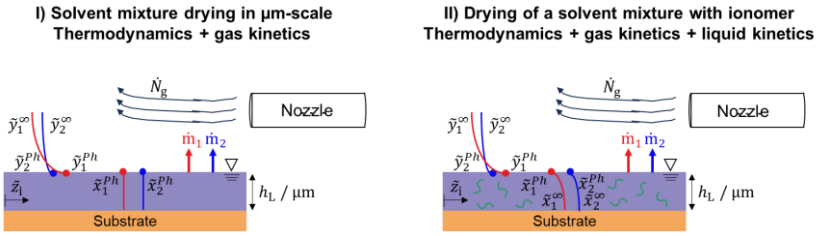

Figure 31: Assumed concentration profiles of the solvents in a thin drying film. I) The assumption is that the thin film drying of the solvent mixture is mainly affected by thermodynamics and gas kinetics and less by liquid-sided solvent composition gradients. II) With ionomer in the solvent mixture, liquid-side solvent fraction gradients may form in consequence of selective drying.

In a next step, the complexity of the investigated system is increased. Additionally to the solvents, an ionomer is added to investigate its influence on the

drying selectivity. With the ionomer, it is possible that concentration gradients occur on the film side (Figure 31 II)). Finally, a roadmap for future analyses of the entire ink system is outlined.

6.1 Gas-side influences on selective drying[1]

First, the influence of the gas side on selective drying is investigated and quantified. The aim is to highlight the importance of drying conditions by comparing two different drying scenarios. Next, the impact of air humidity and the preloading of air with water are examined.

Selectivity in thermodynamically controlled drying

First, the case of thermodynamically controlled drying (number of transfer units $NTU_{i,\mathrm{g}} \rightarrow \infty$) described by Thurner and Schlünder [201] is experimentally realized (see Chapter 3.6 and Appendix 9.3). The experimental setup is functionally analogous to a gas saturator. It is expected that the evaporation of the solvents is mainly determined by thermodynamic factors, such as the vapor pressure curves and the composition-dependent activities of the solvent mixture (see Chapter 2.3). It is expected that the azeotropic composition of the mixture dries unselectively. With a lower content of 1-propanol than the azeotropic composition, $x_1 < x_{1,\mathrm{az}}$, a preferential evaporation of 1-propanol is anticipated, and for $x_1 > x_{1,\mathrm{az}}$, a preferential evaporation of water. In the experiments, the liquid temperature is 17.5 ± 0.5 °C. At this temperature, the azeotropic composition is calculated to be $x_{1,\mathrm{az}}$ = 65.5 wt%.

The analysis of the solvent mixture drying measurements is shown by normalizing the (changing) film height to the initial film height. This is plotted versus

[1] Parts of the results and figures presented in this chapter have been previously published in a peer-reviewed article, available under a CC BY 4.0 license:
Quarz P, Zimmerer N, Scharfer P, Schabel W, *About drying phenomena of fuel cell and electrolyzer CCM inks: selectivity of the evaporation of 1-propanol/water mixtures*, Fuel Cells, 2024. 10.1002/fuce.202300252, referred to in this work as [190].

the mass fraction of 1-propanol for mixtures with an initial solvent composition of $x_{1,0}$ = 60.0, 65.5, 72.0, and 81.5 wt% (Figure 32). Accordingly, all experiments start at 100 % normalized film height and decrease from top to bottom. The dashed lines mark the assumed non-selective drying process with a constant solvent to solvent composition.

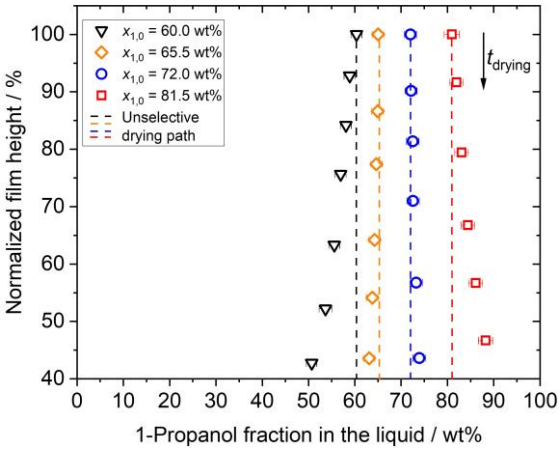

Figure 32: Plot of the normalized film height versus the mass fraction of 1-propanol x_1 of four mixtures of different initial composition $x_{1,0}$ = 60.0, 65.5, 72.0 and 81.5 wt% at low air flow ratios ($NTU_{i,g} \rightarrow \infty$, thermodynamically controlled) and ~17.5 °C. Drying proceeds from top to bottom, whereby the composition may change. Dashed lines symbolize assumed unselective drying paths (no change in composition). At the experimental temperature, the thermodynamic azeotrope is calculated to be $x_{1,az}$ = 65.5 wt%. [190]

For $x_{1,0}$ = 60 wt% (black), and thus $< x_{1,az}$, the 1-propanol fraction decreases during drying. As expected, the 1-propanol evaporates preferentially. At the azeotropic composition with $x_{1,0}$ = 65.5 wt% (orange), a slight relative accumulation of water is seen in the shift to the left, so the actual azeotrope appears to be slightly smaller under these experimental conditions. This is explained by a slightly varying temperature between 18 and 17 °C, which affects the position of the azeotrope minimal. More relevant, the air used for drying was not completely dry, with a relative humidity of 7.1 % at 17.5 °C, resp.

$\tilde{y}_2^{\infty}$ = 0.0014. This preloading shifts the azeotrope slightly to the right. These examples show how sensitive the system is to process influences and how difficult it is to achieve non-selective drying on a laboratory/production scale. Although the changes in composition may not appear dramatic, they are likely to be much more significant towards the end of the drying process. Unfortunately, this cannot be measured here due to limitations in the experimental saturation setup. In order for air bubbles to flow through the liquid, the liquid level must be high enough to ensure the air supply is within the liquid (see Chapter 3.6).

To the right of the calculated azeotrope (blue and red), the 1-propanol content increases during drying. As expected, water evaporates preferentially. The selectivity or gradient in composition between two measuring points initially increases with increasing distance from the azeotropic composition (initial composition or also during drying) as the distance between the boiling curve and the bisector (equal liquid and gaseous composition) in the relative-mass-flow-versus-liquid-composition-diagram increases (see Figure 6). If the vertical distance of the boiling curve and the bisector is large, the difference between the liquid and the gaseous composition is large.

In order to represent the drying progress as a normalized film height, the density of the mixture must be taken into account for each composition during evaporation. With a density of 0.803 g cm^{-3} (1-propanol) to 0.998 g cm^{-3} (water) at 20 °C [193], 1-propanol is approx. 20 % less dense than water. Thus, mass evaporation rate of 1-propanol causes a greater change in volume and height than the comparable gravimetric quantity of water. This effect is not very pronounced in the compositional changes observed. In a catalyst ink system, however, the magnitude of the volume change in the ink solidification step could possibly have an influence. It is noted that the selectivity affects the time-resolved volumetric film shrinkage.

Selectivity in gas-side controlled drying

In a drying process, the interaction time is relatively short and not long enough to reach thermodynamic equilibrium. This results in the limiting case $NTU_{i,\mathrm{g}}$

→ 0 (see Appendix 9.3). A mass boundary layer develops above the liquid surface, where concentration profiles of the evaporating solvents form. Corresponding considerations and effects are verified here in a modified experimental setup (see Chapter 3.6). The drying air (relative humidity φ = 7.1% at 17.5 °C, $\tilde{y}_2^{\infty}$ = 0.0014) at a temperature of 50 ± 2 °C is blown onto the liquid with an impingement jet round nozzle. Evaporative cooling results in a wet-bulb liquid temperature between 17 and 18 °C, like in the experiment before. The calculated azeotrope is again at 65.5 wt% 1-propanol.

In Figure 33, the composition of the residual liquid of different binary solvent mixtures with $x_{1,0}$ = 40.0, 60.0, 65.5, 72.0 and 81.5 wt% is plotted as normalized film height during the drying process. As the mixtures dry, the (normalized) film height decreases and the composition of the remaining solvent mixture may change due to selective evaporation.

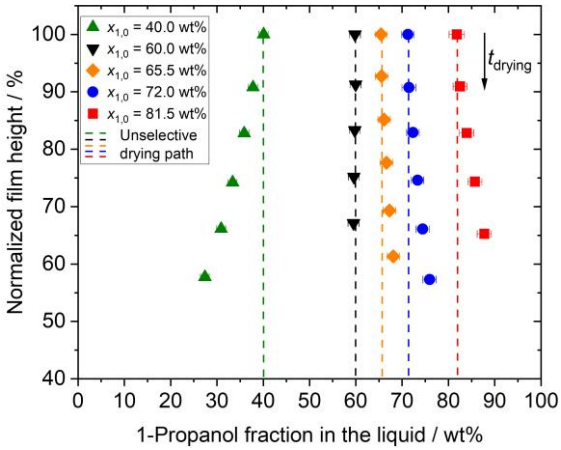

Figure 33: Composition (change) of the residual solvent mixture in the form of the 1-propanol mass fraction x_1 in the course of gas-side controlled film drying shown above the decreasing normalized film height for binary mixtures with initial compositions $x_{1,0}$ = 40.0, 60.0, 65.5, 72.0 and 81.5 wt% at 17.5 °C ($x_{1,az}$ = 65.5 wt%). Dashed lines symbolize unselective drying paths. [190]

For compositions with $x_{1,0} > x_{1,az}$ (red and blue), the 1-propanol content increases during drying. A different result to what might be expected can be seen when looking at the film with $x_{1,0}$ = 65.5 wt% (orange), which is the azeotropic composition at the given temperature. Here, the 1-propanol content increases due to water evaporating preferentially. Instead, the composition at $x_{1,0}$ = 60 wt% dries with an almost constant composition and therefore non-selectively. This can be attributed to the influence of the gas-phase kinetics on evaporation (see Chapter 2.3). For lower initial 1-propanol fractions ($x_{1,0}$ = 40 wt%, green), the curve shifts towards the left side, where 1-propanol evaporates preferentially.

The non-selectively drying composition is shifted to lower compositions compared to the thermodynamically controlled case (Figure 34). In general, the curse of the curves representing the data with short interaction times ($NTU_{i,g} \rightarrow 0$) are shifted to the left in comparison to those with long interaction times ($NTU_{i,g} \rightarrow \infty$). The drift to the right is either less pronounced or in some cases the selectivity is even inversed. This is explained considering the gas kinetics. Additionally to the thermodynamics, the diffusion coefficients of the evaporated solvents in the gas phase and the gradient between the solvent concentration at the phase boundary and the bulk for each solvent come into play (see Eq. (2.14)). For illustration purposes, a simplified example is chosen: Water diffuses faster in air than 1-propanol ($\delta_{2,g} > \delta_{1,g}$) and the thermodynamically favored evaporation of 1-propanol at $x_1 < x_{1,az}$ is partially or even over compensated. (A complete description must also consider the partial pressures of the solvents.)

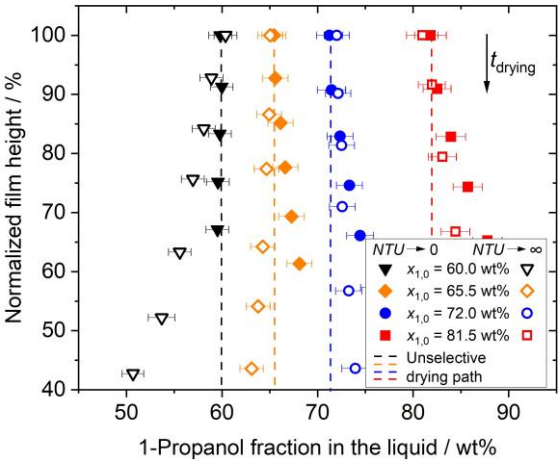

Figure 34: Comparison of the drying with thermodynamically (unfilled symbols) and additionally gas-sided (filled symbols) controlled drying (T_L = 17.5 ± 0.5 °C, $x_{1,az}$ = 65.5 wt%). Dashed lines symbolize unselective drying paths. [190]

The evaporation, resp. drying, conditions influence the position of the tipping point for preferential solvent evaporation. Depending on the air flow conditions, the azeotropic composition may not evaporate non-selectively. Where interaction times of the air and the solvent mixture are short, gas kinetics must be taken into account. This shifts the location of the non-selective drying composition (arheotropic composition).

Influence of the relative humidity of the drying air on the selectivity

Another important factor influencing the selective evaporation of the solvent mixture is the preloading of the drying air. The preloading of the drying air is represented by $\tilde{y}_i^{\infty}$ in Eq. (2.14). In consequence, the driving gradient of the solvent component concerned $\tilde{y}_i^{Ph} - \tilde{y}_i^{\infty}$ will be lower with preloading. This will inhibit its specific evaporation rate. The selectivity shifts towards the component that continues to evaporate unhindered, respectively the non-selectively drying composition is shifted. This is investigated experimentally by saturating the drying air with water at 11 °C, which leads to a water preloading of

$\tilde{y}_2^{\infty} = 0.013$, and heating the air subsequently to 50 ± 2 °C. The corresponding results are compared in Figure 35 with those of the air not specifically preloaded ($\tilde{y}_2^{\infty} = 0.0014$, one order of magnitude less). All the curves for air preloaded with water bent to the left, which is explained by the hindered evaporation of water. Under the given conditions, the arheotropic point is at slightly higher 1-propanol fractions than 81.5 wt% and will be calculated in the next step (see Figure 36). The preloading has a decisive influence on the selectivity.

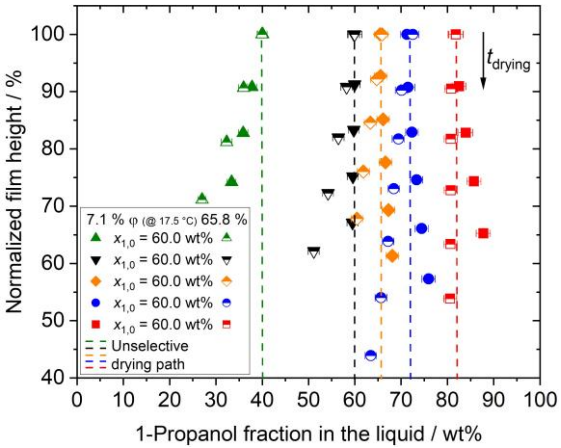

Figure 35: Influence of the water preloading of the drying air on the selective drying behavior in gas-side controlled drying. Filled symbols describe drying with a relative humidity of φ = 7.1 % at 17.5 °C ($\tilde{y}_2^{\infty} = 0.0014$). Half-filled symbols derive from a preloading of φ = 65.8 % at 17.5 °C ($\tilde{y}_2^{\infty} = 0.013$) but a thus resulting higher liquid temperature of 20.5 °C. [190]

The hindered water evaporation reduces the total evaporation rate and therefore the evaporative cooling. The experiments with $\tilde{y}_2^{\infty} = 0.013$ result in a liquid temperature of approx. 20.5 °C under the given conditions. This higher temperature compared to the experiments without active preloading has a negligible effect on the selectivity due to the almost parallel temperature-dependent vapor pressure curves of 1-propanol and water. The temperature increase of 3 °C would shift the calculated position of the arheotrope by only 0.3 wt%

(see Figure 36). The influence of humidity is clearly noticeable. The calculated gradients (see Eq. (2.6) and Appendix 9.3) of the components between the phase boundary and the bulk of the gas phase are given in Table 5 for the different 1-propanol/water mixtures investigated. The reduced total evaporation rate, and thus increased liquid temperature, results in higher partial pressures and gaseous molar fractions at the phase boundary for both solvents. Consequently, the 1-propanol gradient increases, while the water gradient decreases due to the initial impact of the higher subtrahend.

Table 5: Influence of the water preloading of the drying air $\tilde{y}_2^\infty$ on the concentration gradients for 1-propanol (index 1) and water (index 2) between the phase boundary $\tilde{y}_i^{Ph}$ and the bulk of the gas phase $\tilde{y}_i^\infty$ for different solvent mixtures, specified in the gravimetrical 1-propanol fraction in the liquid x_1. First two rows describe drying with a relative humidity of φ = 7.1 % at 17.5 °C ($\tilde{y}_2^\infty$ = 0.0014). Last two rows derive from a preloading of φ = 65.8 % at 17.5 °C ($\tilde{y}_2^\infty$ = 0.013), but thus a resulting higher liquid temperature of 20.5 °C. 1-propanol preloading is $\tilde{y}_1^\infty = 0$ in both cases. With higher water preloading, the temperature is increased, leading to higher $\tilde{y}_i^{Ph}$. The 1-propanol gradients increase with higher liquid temperature for all solvent liquid compositions. On the other side, the overall water gradient is significantly smaller due to the water preloading.

Conditions	**Gradients**	x_1 / wt%				
		40	**60**	**65.5**	**72**	**81.5**
T = 17.5 °C $\tilde{y}_1^\infty = 0$	$\tilde{y}_1^{Ph} - \tilde{y}_1^\infty$	0.010	0.010	0.010	0.011	0.011
$\tilde{y}_2^\infty = 0.0014$	$\tilde{y}_2^{Ph} - \tilde{y}_2^\infty$	0.017	0.017	0.017	0.016	0.015
T = 20.5 °C $\tilde{y}_1^\infty = 0$	$\tilde{y}_1^{Ph} - \tilde{y}_1^\infty$	0.012	0.012	0.013	0.013	0.014
$\tilde{y}_2^\infty = 0.013$	$\tilde{y}_2^{Ph} - \tilde{y}_2^\infty$	0.009	0.009	0.009	0.008	0.007

This finding is significant, as the humidity of unconditioned drying air can exhibit substantial variability due to seasonal and meteorological fluctuations. For example, in Karlsruhe, Germany, there are fluctuations of 15 – 75 % relative humidity at 25 °C (corresponding dew points between approx. -3 (≙ $\tilde{y}_2^\infty$ = 0.004) and 20 °C (≙ $\tilde{y}_2^\infty$ = 0.019)) between summer and winter. In this context, it should be noted that relative humidity is temperature-dependent, which is why comparative values are given here at a constant temperature or alternatively in form of the temperature-independent $\tilde{y}_2^\infty$.

The influence of humidity, also in combination with different temperatures (isotherms for liquid and gas phase), is now analyzed by simulations, assuming $NTU_{i,g} \rightarrow 0$ and no film-side resistance (see Chapter 3.6). For preloadings $\tilde{y}_2^{\infty}$ = 0.000; 0.0014 and 0.013 that were also investigated experimentally earlier, corresponding to relative humidities of φ = 0.0 % (green); 7.1 % (blue) and 65.8 % (red) at 17.5 °C and relative humidities of 0.0 % (light green); 5.8 % (light blue) and 54.4 % (pink) at 20.5 °C, the relative mass flow of 1-propanol $\dot{r}_1$ in $\frac{g \cdot s^{-1}}{g \cdot s^{-1}}$% is plotted against the liquid composition.

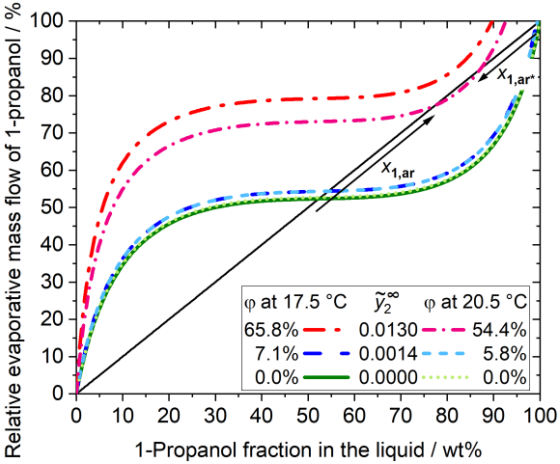

Figure 36: Simulated influence of water preloading of the drying air on the relative 1-propanol evaporation flux $\dot{r}_1$ in $\frac{g \cdot s^{-1}}{g \cdot s^{-1}}$% versus the mass fraction of 1-propanol in the liquid x_1. The air flow conditions (gas-side controlled drying), the isothermal temperatures in gas and liquid and the pressure of 1.013 bar are set. The experimentally prevailing humidities $\tilde{y}_2^{\infty}$ of 0.0014 and 0.013 and dry air (0.000) are varied for the experimental liquid temperatures of 17.5 and 20.5 °C. Different temperatures correspond to different relative humidity values for the same amount of liquid. Points of intersection with the bisector are arheotropes, which are described as 'unstable' $x_{1,ar}$, and 'stable' $x_{1,ar*}$. [190]

Similar to the McCabe-Thile diagram, 1-propanol evaporates preferentially when $\dot{r}_1 > x_1$ and the curve lies above the bisector. Water evaporates

preferentially when $\dot{r}_1 < x_1$. An arheotrope is present when the actual liquid composition is equal to the composition of the outgoing evaporation stream (see Eq. (2.8)) and lies on the bisector.

A water preloading shifts the curves upwards to a larger $\dot{r}_1$ and thus the position of the arheotrope to the right to a higher x_1. This is due to the inhibited water evaporation rate. As the 1-propanpol continues to evaporate, the bisector is intersected a second time. Thus, with preloaded air, a second arheotrope can exist. This additional arheotrope is stable $x_{1,\mathrm{ar}*}$ [196]. The attribute 'stable' comes from the fact that the driving gradients show towards this point and small deviations will end up again at this composition. For $x_{1,\mathrm{ar}} < x_1 < x_{1,\mathrm{ar}*}$ water evaporates preferred, leading to an increase in x_1. For $x_1 > x_{1,\mathrm{ar}*}$, 1-propanol evaporates preferred, leading to an decrease in x_1. With preloaded air, three cases are distinguished. For $x_1 < x_{1,\mathrm{ar}}$, x_1 tends to diverge against 0 during the drying process. For $x_1 = x_{1,\mathrm{ar}}$, it remains constant and for $x_1 > x_{1,\mathrm{ar}*}$, it tends towards $x_{1,\mathrm{ar}*}$. Consequently, tailored preloading of the drying air enables a stable and non-selective operating state for a desired initial solvent composition.

Without preloading ($\tilde{y}_2^{\infty} = 0.000$), the exact position of $x_{1,\mathrm{ar}}$ depends slightly on temperature (light and dark green, 0.4 wt%). However, with increasing water preloading, the shift becomes more pronounced. Moreover, $x_{1,\mathrm{ar}*}$ is dependent on both temperature and preloading.

With water preloading, $\dot{r}_1$ becomes > 100 % for high x_1. Here, $\tilde{y}_2^{\infty}$ becomes greater than $\tilde{y}_2^{Ph}$ and water no longer evaporates but condenses from the air, while the remaining 1-propanol continues to evaporate. To enable complete drying here, it is necessary to increase $\tilde{y}_2^{Ph}$ over $\tilde{y}_2^{\infty}$ again (either by the self-induced change in x_1 or, if necessary, via a higher temperature (see Eq. (2.6)).

As the humidity of the drying air increases, the inhibition of water evaporation growths and consequently the range of preferential water evaporation between the two arheotropes becomes smaller. For $\tilde{y}_2^{\infty} > 0.011$ at 17.5 °C and for $\tilde{y}_2^{\infty} > 0.015$ at 20.5 °C, water evaporation is restricted to such an extent that 1-

propanol evaporates preferentially across the entire composition range. There is no intersection with the bisector, i.e. no arheotropic composition. Drying always ends with pure water in the residual liquid.

As described above, the impact of the preloading is temperature-dependent. This is because the concentration gradients between the phase boundary and the bulk $\tilde{y}_i^{Ph} - \tilde{y}_i^{\infty}$ have a decisive influence on the selectivity (see Eq. (2.14)). Small changes in temperature lead to changes in $\tilde{y}_i^{Ph}$. Without preloading, the gradients are relatively large and the effects of changes in $\tilde{y}_i^{Ph}$ on them are negligible. With increasing preloading, the gradient becomes smaller and even small changes in $\tilde{y}_i^{Ph}$ lead to relatively large changes in the resulting gradient. The temperature-dependence of the selectivity therefore increases with the preloading. Vice versa, preloading has a greater effect at lower temperatures due to the lower $\tilde{y}_i^{Ph}$. Therefore, preloading and temperature should always be considered interconnected in the evaporation process.

6.2 Solvent mixture evaporation analysis in thinner films[2]

The initial film height, respectively mass, affects the drying time. Less solvent requires less drying time for a given power input. Assuming that there is no mass transport resistance on the film side and thus no gradients, the film height is expected to have no influence on the selectivity (Eqs. (9.7) and (9.8)). Experiments with half the initial amount of solvent, and therefore half the initial film height, were examined using the same experimental setup as in Chapter 6.1. The initial film height showed no influence. Minor deviations are within the margin of measurement error (see Appendix 9.5). Nevertheless, the

[2] Parts of the results and figures presented in this chapter have been previously published in a peer-reviewed article, available under a CC BY-NC 4.0 license, reproduced in accordance with the author rights granted by Taylor & Francis:
Quarz P, Janning L, Zimmerer N, Scharfer P, Schabel W. *Selective evaporation of solvent mixtures in thin films for fuel cell and electrolyser catalyst coatings.* Dry. Technol., 44(3), 346–355. https://doi.org/10.1080/07373937.2026.2616748, referred to in this work as [271].

statement and the assumption of no mass transport resistance (or concentration gradients) on the liquid side need to be investigated. The next step is to validate whether the knowledge gained in the previous chapter can be applied to thin films as the real ink drying system.

In order to measure the composition of drying films of solvent mixtures that are only a few 100 µm thick, the measurement setup has to be changed. For this purpose, the research group's test facility, which features a drying channel and in-situ sample analysis using inverse micro Raman spectroscopy (IMRS), has been modified. Binary solvent mixtures of 1-propanol and water were investigated. To the best of the author's knowledge, this is the first time that drying tests using IMRS were performed without a non-volatile component, e.g. a polymer, remaining in the analysis area during the measurement and serving as a reference substance for the composition analysis.[3] Therefore, the applicability of the measurement and analytical methods must first be evaluated. This is described in Appendix 9.5 and shows a highly accurate quantitative determination of the composition under the relevant drying conditions, with deviations of less than 0.5 wt%.

To enable transfer and comparability with the experiments in the previous subsection, a few details need to be addressed. The mechanical measuring range from the bottom into the film is 140 µm in height. Optically corrected with the refractive index of the solvent mixture, the real measurement height is approx. 100 µm (x_1 = 0 wt%) to 110 µm (x_1 = 100 wt%), depending on the solvent composition. This is less than the thickness of the films to be analyzed at the beginning of the drying process. Consequently, only the lower part of the sample can be measured in the thicker films at the beginning of the experiment. Film shrinkage causes the film to become thinner with drying time. Towards the end of the drying process, the entire film is within the measuring range.

[3] In parallel with the experiments conducted for this thesis, the author's colleague Lukas Lödige carried out similar fundamental experiments on the evaporation of pure solvent mixtures in the context of battery recycling. He used a high-boiling-point solvent as quasi-non-volatile reference component [261]. Both are pioneers of this particular type of experiment.

In the IMRS drying experiments, it is not possible to determine the total solvent amount. Also the current film height can only be determined if the entire film is not thicker than the measuring range. Therefore, it is not possible to plot the composition with decreasing normalized film height as shown in Figure 32 – Figure 34. However, the composition can be visualized over time. This is sufficient to analyze the selectivity. Towards the end of the drying process, the solvent films dewet from the glass bottom of the reservoir. This results in different end-of-measurement data. However, in order to make a statement about the selectivity, it is sufficient to detect the beginning of the shift in the solvent composition, since the driving gradients point away from the 'unstable' arheotrope (see Chapter 6.1) [190,196].

The drying conditions during the thin film evaporation experiments remain constant. However, they differ in some aspects from the conditions in the experiments with the liquid column (see Chapters 6.1): different air overflow (lateral overflow instead of impingement jet), temperature and different preconditioned air. Qualitative comparisons between the two setups are possible, but quantitative comparisons are limited.

Selective drying in thinner films

Thin films of binary solvent mixtures of different compositions are dried at a liquid temperature of 25 °C. The azeotropic composition is calculated to be 66 wt%. For each experiment, a series of depth scans is measured along the height of the film. The integral composition of the residual liquid is shown in the form of the 1-propanol fraction over the course of the drying process. At the experimental conditions, the azeotropic composition (orange) dries selectively (Figure 37). During drying, the 1-propanol fraction in the liquid increases. Water evaporates preferentially.

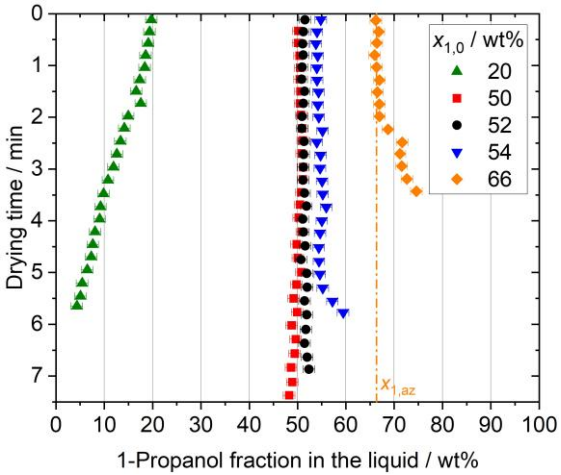

Figure 37: Drying paths in form of the mass fraction of 1-propanol x_1 in the residual solvent mixture over the drying time, measured with IMRS. Different solvent mixtures of initial composition $x_{1,0}$ = 20; 50; 52; 54 and 66 wt% at 25 °C in gas-side controlled drying are investigated. The azeotropic composition ($x_{1,az}$ = 66 wt%) dries selectively and a non-selective drying is found at $x_{1,ar}$ = 52 wt% (experimental arheotropic composition). For $x_{1,0}$ < 52 wt%, the 1-propanol fraction decreases. For $x_{1,0}$ > 52 wt%, it increases. [271]

A drift towards a relative 1-propanol enrichment can still be observed at 54 wt%. Drying with a constant composition occurs only at 52 wt%. With regard to the process parameters, an arheotropic composition of $x_{1,ar}$ = 52 wt% is previously predicted for the 1-propanol/water mixtures at a drying temperature of 25 °C and dry air (see Chapter 6.1), calculated according to Riede and Schlünder [196]. This evidence justifies the theory of the arheotrope and the use of their model for future drying path calculations for the investigated solvent system.

For solvent mixtures with $x_{1,0} < x_{1,ar}$, the curse of the curves shift to the left towards lower 1-propanol contents in the residual liquid during drying. The 1-propanol evaporates preferentially. The change is less pronounced for a

composition close to the arheotrope and more pronounced further away from it. The reason for this is the distance between the effective relative evaporation mass flow curve and the bisector (see Figure 36). The tipping point for relative component depletion or enrichment is the arheotropic composition.

Solvent concentration gradients within the drying film

In the previous experiments, it was assumed that the liquid composition is constant along the film height and there are no mass concentration gradients present in the liquid phase. This assumption is now being investigated. For this purpose, the measurements from Figure 37 are analyzed as depth scans, providing insights into the film along its height. The composition of the film is shown at different heights of the film at different times of drying. In non-selective drying, where the overall solvent composition remains constant, no concentration gradients are expected along the film height (see Appendix 9.5).

At the beginning of the drying process, only the lower part of the film can be detected due to the limited depth of focus. But by the end of drying, the entire film can be measured. The maximum measurable height depends slightly on the solvent composition. This is because, although the piezo focus is set to various fixed positions, the refractive index of the solvent mixture, which depends on its composition, influences the exact position of the laser focus and thus the measurement point. It is expected that possible concentration gradients will start directly below the surface of the film and extend into it without any external mixing. This is due to convective mass transport, which is described by Stefan diffusion. Once the film has been detected over its entire height, it is possible to reliably identify any gradients that may have formed.

First, an overall decreasing 1-propanol composition (initially $x_{1,0}$ = 20 wt%) is examined (Figure 38). The integral composition changes with time, but is almost uniform along the height of the film. The same applies to the lower part of the film at the beginning of the drying, as well as for the entire film observed at the end of drying. The time offset between the lowest and highest measurement point of one height scan, connected by a line, is approx. 11 s. The

composition changes slightly during this time. A narrow gradient in the direction of the overall shift from bottom to top can be explained by this.

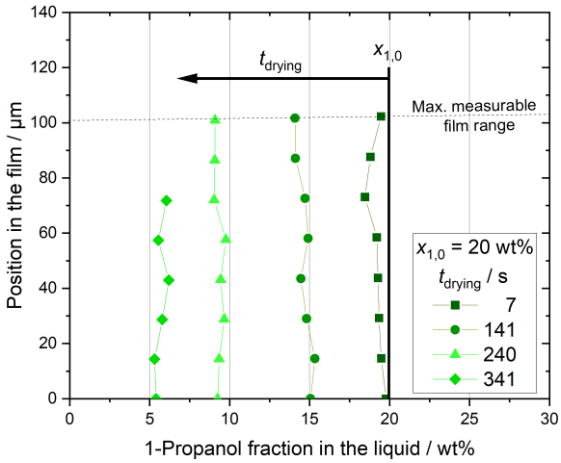

Figure 38: Liquid compositions in the film along the film height for a mixture with overall decreasing 1-propanol fraction ($x_{1,0}$ = 20 wt%) at different drying times t_{drying}. With increasing drying time the overall composition changes, but there are no significant changes of composition along the film height. The wet film height shrinks during drying. [271]

There are two possible explanations. Firstly, no concentration gradients are formed. In the second scenario, due to selective evaporation, there is a slight local concentration gradient directly at the surface. This would grow into the film, but the effect is directly neutralized by self-induced convective mixing. For $x_{1,0} < x_{1,ar}$, 1-propanol preferentially evaporates. This increases the water fraction directly at the surface. Since water and thus more water-rich mixtures have a higher density and a higher surface tension than 1-propanol or mixtures containing more 1-propanol [193], this would lead to unstable stratifications. This could induce e.g. Marangoni convection, and thus equalize the resulting gradients by mixing.

A different behavior is expected for $x_{1,0} > x_{1,ar}$. If the water evaporates preferentially, the 1-propanol fraction at the surface increases. Density and surface stratification are now stable and self-induced mixing is not expected. This hypothesis is tested by analyzing depth scans of a measurement with an integrally relative enrichment of the 1-propanol fraction during drying (Figure 39).

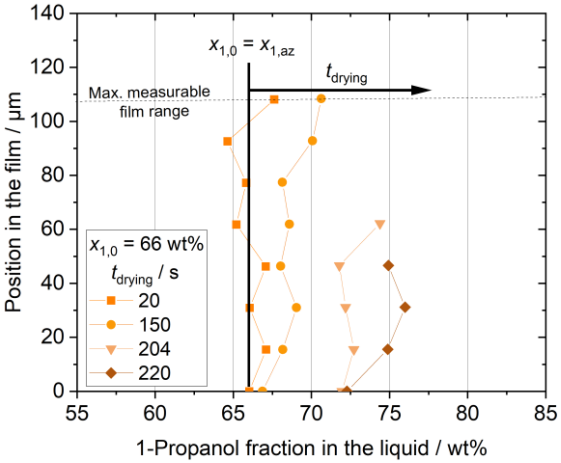

Figure 39: Liquid compositions in the film along the film height for a mixture with overall increasing 1-propanol fraction ($x_{1,0}$ = 66 wt%) at different drying times t_{drying}. With increasing drying time the integral composition changes to higher 1-propanol fractions. The film height shrinks during drying and a shift in the fractions becomes visible at the top of the film. [271]

The composition along the film height is not as uniform as in the previous example. Especially at lower film thicknesses (where the entire film is within the measuring range) a change in composition along the film height is visible. A relative accumulation of 1-propanol is observed towards the phase boundary. These measurements suggest that selective drying results in the development of weak concentration gradients along the film height. To confirm these first findings, further measurements are required. For example, three-dimensional flow field measurements using micro particle tracking velocimetry (3D-µPTV)

[272–274] with tracer nanoparticles in the 1-propanol/water system with different compositions are an option to detect and quantify convection flows in thin films during drying.

Influence of Nafion on the solvent selectivity during drying

After evaluating the selective drying of a binary solvent mixture, the influence of the ink ionomer is examined. The same drying parameters used for the binary solvent mixture were employed to dry and compare the drying of the arheotropic mixture composition (52 wt% 1-propanol with respect to the solvents), both with and without 4 wt% Nafion. The goal is to gain a deeper understanding of real catalyst inks containing ionomer (Figure 40).

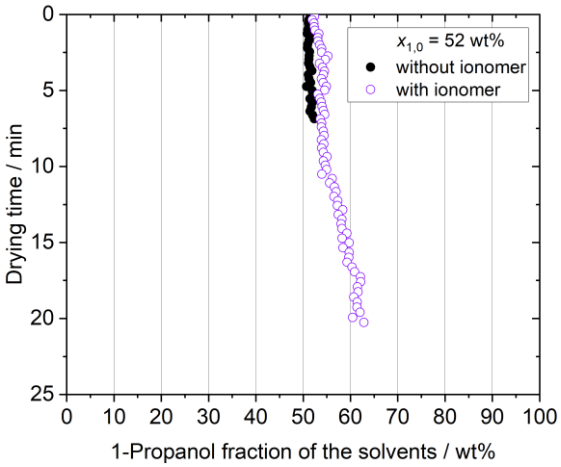

Figure 40: Influence of Nafion on the selectivity of a drying solvent mixture. The plotted 1-propanol mass fraction refers (only) to the solvents. Nafion transforms the previously unselective drying process into a selective one. [271]

The drying with ionomer is measured significantly longer. Without ionomer, no sample is measured after about 7 min due to dewetting over the measuring position. With Nafion, a signal of the solvent is still measured after more than 21 min, which is at least 3 times longer than without ionomer. The experiment

was stopped at this point. The film would have taken even longer to dry. The Nafion ensures film formation and prevents dewetting.

With Nafion, the previously unselective drying process is now selective. Water evaporates preferred. The Nafion seems to shift the position of the arheotropic point (in this case towards lower 1-propanol fractions), triggering selective evaporation at the given solvent composition. Interactions between the ionomer and the solvents may affect the activity of the solvents within the mixture and thus the partial pressures of the solvents at the phase boundary (see (2.6)). Additionally, the Nafion could cause a mass transport resistance within the film towards the surface. During the drying process, the Nafion fraction increases, as probably do its effects on the solvents. Moreover, the *pH* value of the ionic polymer, which changes constantly during drying, and thus the film properties may affect the interactions between the solvents and the ionomer. It is also known from other solvent-polymer film drying experiments that the diffusion coefficient of the solvent decreases with increasing polymer content in the film [247,251,275,276]. The dependence of the diffusion coefficient could be different for the two solvents. This means that changes in the polymer fraction could have different effects on the diffusion coefficient for 1-propanol and that of water in the liquid.

Solvent compositions along the film height are investigated (Figure 41). No profiles are observed in the lower part of the film at the outset of the drying process, as the overall composition remains nearly constant. As the drying time increases and the Nafion concentration rises, the 1-propanol shows a gradient along the film height. E.g., at 18 min, the 1-propanol solvent fraction (without Nafion) is observed to be 57 wt% at the bottom of the film and 67 wt% at the top. The pronounced profiles will influence the overall drying process as the liquid solvent composition is not constant at all along the film height. This must be taken into account when describing the actual ink drying process, especially towards the end of the drying.

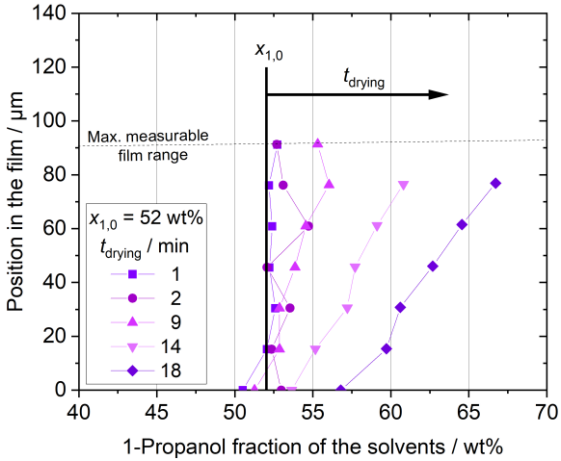

Figure 41: Solvent composition along the film height for a ternary mixture ($x_{1,0}$ = 52 wt% of the solvent composition) with Nafion at different drying times. The x-axis represents the 1-propanol mass fraction regarding solely the solvents (1-propanol and water) in the ternary mixture with Nafion. With increasing drying time the integral solvent fraction first stays nearly constant without a gradient along the measured film height. As drying proceeds, the overall composition changes towards purer 1-propanol (see Figure 40) and pronounced concentration gradients become visible. The film shrinks during drying. [271]

The initial Raman studies revealed the impact of Nafion on selectivity and film-side concentration gradients. In further studies, it is recommended that the fraction of Nafion is also determined during the experiments and systematically correlated. This will require re-calibrating the ternary system. Additionally, the low signal-to-noise ratio of the characteristic Raman peaks of Nafion needs to be improved, especially at the beginning of drying when these peaks are particularly low. In further studies, it should be investigated whether concentration profiles are formed in the polymer film right from the start, and which component is diffusion-limited in the polymer film.

6.3 Effects of selective drying on the catalyst layer formation

After discussing the influencing parameters and effects of selective evaporation, the transfer and effects of the change in (binary) solvent composition in the ink and thus on the electrode to be produced will be addressed. For this purpose, the results are theoretically applied to an ink with an initial solid content (catalyst and ionomer) of $x_{\mathrm{solid},0}$ = 10 wt%. The compositions and relative film heights from the binary drying experiments with short interaction times in the liquid column (see Chapter 6.1) are used as input data for these investigations.[4] The decrease in solvent measured is converted to an increase in solid content. The transfer is based on simplifications: In a catalyst ink, the polymer will affect the selectivity, especially at higher solid fractions towards the end of drying. In addition, towards the end of drying, when evaporating from a porous particle network, an additional film-side resistance must be considered. [219,277]. This affects the selective evaporation [278].

However, the majority of the solvents is evaporating during the first drying period, i.e., until the end of film shrinkage (EoFS) is reached. In this drying phase, the evaporation is not or only slightly affected by film-side parameters. In addition, a study [279] was co-authored in parallel with this thesis to investigate this effect.[5] For this purpose, gravimetric drying curves of a thin film of a fuel cell ink consisting of 1-propanol, water, Nafion as ionomer and catalyst

[4] Although the thin films in the Raman measurements are closer to the actual ink system, ideally also with ionomer, it was not possible to quantify the decrease in solvent and thus not possible to calculate an according solid fraction. With further development of the experiments and a more extensive multi-component calibration, this may be possible in the future with reference to a polymer and then will be sufficient as input data for the considerations made here.

[5] The author collaborated on studies on the influence of drying parameters and solvent composition on ink composition evolution. The results are published as peer-revied article:
Zimmerer N, **Quarz P**, Terhorst E, Janning L, Scharfer P, Schabel W. *Influence of Ink Formulation and Drying Parameters on Component Composition during Drying of Catalyst Layers for Polymer Electrolyte Membrane Fuel Cells and Electrolyzers*. Energy Tech 2025:2500516. https://doi.org/10.1002/ente.202500516, referred to here as [279].

particles were determined. In parallel, a simulation was carried out to model the selective drying of a binary solvent mixture of 1-propanol and water without mass transfer effects on the film side under the test conditions. In comparison, both drying curves (gravimetrically measured and simplified simulated) show good agreement until the EoFS[6]. This indicates that film-side effects related to the increasing polymer and particle fractions are likely negligible for this system, at least until the EoFS.

The theoretical transfer of the experimental binary mixture experiments to an ink is shown in a triangular plot of 1-propanol, water and solid content (Figure 42). By definition, drying starts at $x_{\mathrm{solid},0}$ = 10 wt% and ends at the top of the triangle at $x_{\mathrm{solid,end}}$ = 100 wt%. The assumed non-selective drying paths are shown as dashed lines, connecting the starting points directly to the end point. Until $x_{\mathrm{solid}} \approx 60$ wt%, the first drying period is expected, for which the transfer is expected to have good validity. This area is highlighted in yellow. At higher solid contents, the polymer and particle fractions could affect the drying process. In addition, microstructure formation and cracking may occur during this subsequent drying period. The solvent-to-solvent ratio, which depends on the drying conditions, plays a decisive role here.

[6] Assuming a porosity of the layer of 65 vol%, and the standard solid composition of the ink in this work. With only pure 1-propanol as solvent, $x_{\mathrm{solid,EoFS}}$ would be 67 wt% calculated according to [277]. With pure water as solvent, it would be 62 wt%. Higher porosities mean lower $x_{\mathrm{solid,EoFS}}$.

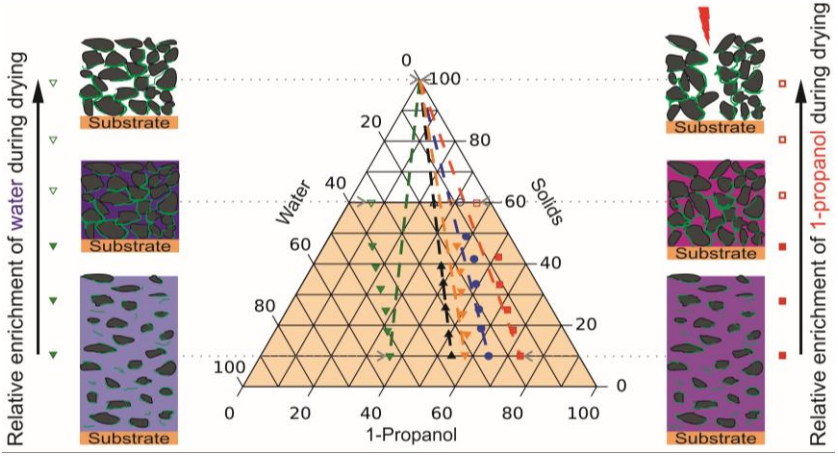

Figure 42: Drying paths of catalyst inks with an initial solid content of 10 wt% and different initial solvent compositions in the course of gas-side controlled film drying. During drying, the solid content increases continuously (bottom to top). Dashed lines symbolize unselective drying paths. From the end of film shrinkage (EoFS, $x_{\mathrm{solid,EoFS}} \approx 60$ wt%), further factors influence the drying process, the microstructure forms and cracks may appear. The current solvent-solvent ratio plays a decisive role here. [190]

The drying paths for five different starting compositions are plotted. Only drying of the ink with $x_{1,0}$ = 60 wt% 1-propanol of the solvents (black) is non-selective. The solid content increases in the course of drying, while the solvent-solvent ratio remains constant. This is different for a composition with initially less 1-propanol (green). The measuring points deviate to the left from the straight line representing non-selectivity. 1-propanol evaporates preferentially, which is why its proportion is reduced. To the left of the triangular diagram, this is shown schematically by a shrinking film. The film is shown at three different stages of the drying process, with decreasing solvent content and film height. The solvent composition is color-coded: blue for water, red for 1-propanol, and purple for mixtures. As the 1-propanol evaporates preferentially and the water fraction increases, the color of the solvent becomes increasingly blue during the drying process, also affecting the conformation of ionomer (green)

and particles (grey) and the overall microstructure of the solidifying film. Once all the solvents have evaporated, the particulate network remains.

Conversely, for inks with an initial higher concentration of 1-propanol than the arheotropic composition (orange, blue, red), the relative 1-propanol content (affecting the solvents) in the ink increases. This behavior is represented schematically on the right-hand side, where the solvent becomes less and more red. Consequently, alterations in the solvent composition influence particles, ionomer and microstructure formation. In the red example, a crack forms in the drying catalyst layer, as observed for real inks with high initial 1-propanol content (see Figure 57).

The microstructure of the dry film is formed towards the end of the drying process as the film solidifies. In Figure 42, this corresponds to the white are at the top of the triangular plot. The graph clearly shows that the solvent composition at the EoFS (unfilled symbols) is significantly different from the initial formulation. Changing the solvent composition also changes important solvent mixture properties that influence cracking, like surface tension, liquid-solid contact angle, Nafion conformation, evaporation rate and, indirectly, pore size. Direct conclusions between the initial solvent composition and the cracking behavior do not appear to be conclusive. Different compositions passed during the drying process may result in different ionomer and particle states and interactions [280]. A comprehensive investigation into the interactions between particles and the ionomer, as well as interparticle interactions, must be conducted as a function of varying solvent compositions. This approach is essential for elucidating the impact of the drying pathway on the resulting electrode microstructure. In addition to the absolute compositions, the kinetics, e.g. how fast changes occur or how long a certain state is maintained, may also be relevant. This should be addressed in further studies. It is concluded that the composition of the drying catalyst layer during the critical time period of layer solidification is important for a thorough understanding of catalyst layer properties and effects such as cracking. Film formation is strongly influenced by the initial ink formulation and drying parameters.

6.4 Conclusion on catalyst ink drying

In the literature on fuel cell catalyst ink drying, azeotropic compositions are sometimes deliberately chosen. The idea is that this solvent composition will not change during drying. The results in this chapter demonstrate that this approach is insufficient for ink drying in most cases. Other effects shift the non-selective drying composition. This chapter was based on the Hypothesis 2:

Selective drying influences microstructure formation during film consolidation of the fuel cell electrode.

The first step was to understand selective drying and how drying parameters influence specific characteristics, such as the composition, which dries non-selectively. Several parameters affect the selectivity of the evaporation of a binary 1-propanol/water solvent mixture. It was shown experimentally that the solvent-specific vapor pressure curves and the composition-dependent activities significantly influence the position of the azeotrope. Temperature has only a minor effect, because the vapor pressure curves of 1-propanol and water are similar over a wide temperature range, and the change in their ratio is negligible within the relevant temperature range (10 – 50 °C).

It was shown in this work that for catalyst ink drying, the gas-side mass transfer is an important factor which needs to be considered. The composition of the unselective drying process changes from the azeotrope to the so-called "arheotrope". This change is influenced by the diffusion coefficients of the solvents in air and, especially, the preloading (or air humidity). When the air is preloaded with one solvent, there is a certain range in which multiple arheotropes exist. Drying in a lab oven without knowing the exact drying parameters, like accumulation of solvents, is not sufficient to achieve a reproducible drying path. The same applies to determining the causal correlations to the resulting layer properties when drying real systems.

During drying binary 1-propanol/water mixtures, the most important factors influencing the selectivity are the (initial) composition, the temperature and the preloading of the drying air. Preloading reduces the drying rate by reducing the driving concentration gradients between the phase boundary and the ambient

air. Increased temperature in turn increases the drying rate due to higher vapor pressure and thus higher solvent concentrations at the phase boundary and larger (gas) diffusion coefficients ($\delta_{i,j} \sim T^{1,75}$, see Appendix 9.3).

These fundamental factors and insights were developed experimentally in tests with large volumes of liquid in cm-scale. In a next step, Raman spectroscopy was used to transfer the results to the µm-scale relevant for catalyst-coated membranes: thin films. The method enabled the experimental investigation of composition gradients developing within the film during drying. There is a good agreement with the arheotropic composition determined by simulation under the given experimental conditions. The experiments with the thin liquid films provide a first insight into the mass transport resistances in the liquid film. To the left of the arheotrope, at lower 1-propanol fractions, there are no concentration gradients along the film height. The situation is different to the right of the arheotrope, at higher 1-propanol fractions, where slight concentration profiles are observed. This could be due to different unstable and stable stratifications, depending on the evaporation component that is preferred. This results in changes in local surface tension (and density), which can induce (Marangoni) convection within the film, equalizing concentration differences.

In the initial Raman investigations, it was also possible to add Nafion as ink ionomer to the system. Initial tests showed that Nafion influences the selectivity. Conversely, selective drying results in pronounced differences in film composition along the film's height may affecting the forming film's resp. layer's microstructure. Further and more in-depth research in this area is needed. In particular to the following questions: How exactly does the Nafion affect both solvents in terms of absorption, activity and diffusion coefficients in the film, and how does it interact with solids as they are present in a real ink? What about assumed self-induced mixing due to unstable stratification along the film height to the left of the arheotrope? Does this affect ionomer and particle distribution and shape? This could have an impact on the ionomer distribution in the resulting electrode observed by Mauger et al. [91].

The drying paths derived from experiments show significant changes in composition during selective drying. Due to the strong influence of the solvent

composition on particles, ionomers, and their interaction, a change in composition consequently has a major impact on crack and microstructure formation. The concentration gradients of Nafion along the film height are further evidence of the influence of selective evaporation on the formation of the microstructure of the layers. Hypothesis 2 can therefore be confirmed.

The basis for this is a deeper understanding of selective drying. Figure 43 schematically summarizes the previous steps of understanding the drying process in membrane direct coating. The composition of binary solvent mixtures was investigated using density measurements during the drying process. Then, Raman spectroscopy was applied to examine the time- and spatially resolved properties within thin films, as these are the relevant format in membrane direct coating (MDC). Next, the complexity was increased by adding an ionomer to the solvent mixture. The next step will be to investigate an even more complex system containing particles, and finally the drying on a membrane.

These findings comprehensively describe the selectivity in balance scope I, shown in Figure 26 in Chapter 5. However, the question of the consequences of selective membrane swelling remains unresolved. Investigations regarding the membrane-solvent interactions will be addressed in the next chapter.

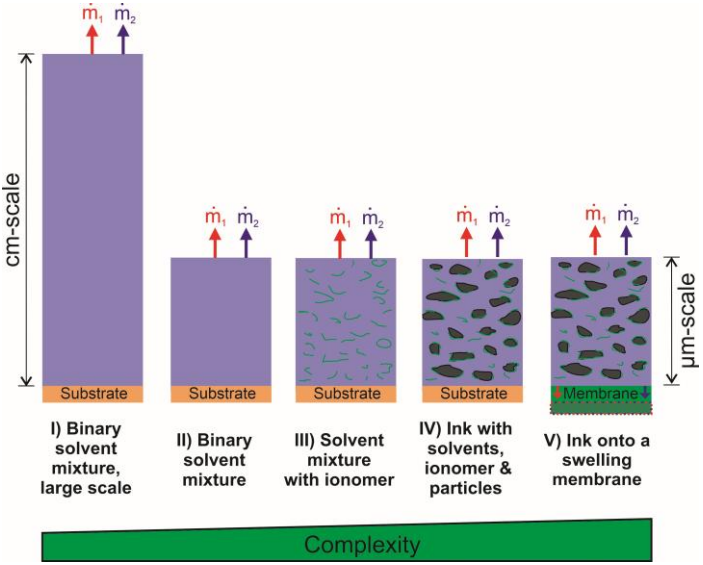

Figure 43: Roadmap towards comprehension of mass transport processes and the ink composition during (selective) drying of catalyst inks. The complexity of the system increases as the number of materials involved increases. The system is simplified to abstraction levels: I) a binary solvent mixture on a large scale, II) a solvent mixture on the relevant micrometer-scale, III) a solvent mixture with ionomer (all: this chapter), IV) with additional catalyst particles, and V) an ink on a non-inert membrane (next chapter). [271]

7 Challenges in membrane direct coating[1]

The focus of this investigation is on the interaction of the catalyst ink with the membrane. For production scale-up and roll-to-roll (R2R) coating, it is beneficial to apply the ink to the membrane using a slot die. Here, the wet film of catalyst ink is applied to the membrane. Interactions of the ink solvents with the membrane are therefore more extensive and more concentrated than e.g. in sequential spray coating. The membrane direct coating (MDC) divides into different steps: First, coating the first layer (hereafter referred to as the cathode), and secondly, coating the back of the membrane. The second coating is referred to as the anode here. The membrane is supplied on a mechanically stabilizing backing foil. For the coating of the second side, however, the backing foil must be removed. The deformation of the membrane due to swelling is expected to be more pronounced. Disturbances in intended movement and deformation could introduce additional stress to the system. This leads to

Hypothesis 3: Increased degrees of freedom of the membrane after ink coating and during drying result in fewer cracks in the directly coated catalyst layer.

During coating the anode, the cathode is already on the reverse side. This means that, unlike the cathode coating, two things change simultaneously when the anode is coated: the backing foil is gone and therefore the cathode is present on the back of the membrane. In order to isolate the influence of the (missing) backing film, the coating of the membrane without the backing film was investigated.

[1] The underlying data and raw illustrations presented in this chapter originate from the Master's thesis titled '*Development of a coating concept for the direct coating of Catalyst-coated membranes (CCM)*' by Frank Michael Mannes (2024), which was supervised and structurally conceptualized by the author of this work. The integration into the broader scientific context, the joint discussion of the results, and the subsequent further development and reorganization of the figures and results represent the author's own independent scientific contribution.

If different processes and process steps or above mentioned cases are considered, different material flows of the ink solvent occur. In consequence, the ink composition changes after the application to the substrate and during drying. Drying and membrane swelling, as well as subsequent drying of the membrane, take place simultaneously. This corresponds to balance scope II, shown in Figure 26 in Chapter 5. The expected material flows of the solvents for the interconnected process of MDC are abstracted and shown in Figure 44. As reference, the decal process is considered first. In the decal process, the solvents evaporate from the ink into the drying air. Due to selective drying, the individual component-specific evaporation flows differ. Figure 44 I) illustrates the solvent flows, indicated by arrows (red for 1-propanol and blue for water) pointing into the drying air. The inert decal substrate is not affected by the ink.

In membrane direct coating, the solvent fluxes of evaporation also occur, but there are additional solvent fluxes into the membrane due to its solvent affinity. The membrane swells by absorbing the solvent from the ink. Accordingly, two additional solvent flows into the membrane are illustrated in Figure 44 II a, b) and III) (see also Figure 26 II). Different solvent-specific fluxes can result from the selective membrane affinity. During drying, the solvents from the ink that have been absorbed by the membrane must also be evaporated. If the membrane is supported by a backing foil that is impermeable for the solvents, they must pass through the (partially dried) catalyst layer and subsequently into the drying air (Figure 44 II a)). This again influences the time-dependent solvent concentration in the film. In addition, as mentioned in Chapter 5, the distribution of the free, unbound ionomer can be influenced by the different solvent flows, while it is still mobile and the film is not fully solidified.

It is possible to coat the first side (cathode) without the backing layer underneath the membrane (Figure 44 II b). This was done in this study to better understand the effects of coating the second side, where the backing foil has to be removed. However, this is a topic in itself. First, the ink solvents penetrate the membrane. Then, due to the absence of a backing foil, the membrane dries from both the top and bottom. The same solvent fluxes occur when coating the second layer (the anode) on the membrane (Figure 44 III)) as when coating the

cathode without a backing foil. It is possible that the membrane exhibits different swelling behavior due to the first coated catalyst layer.

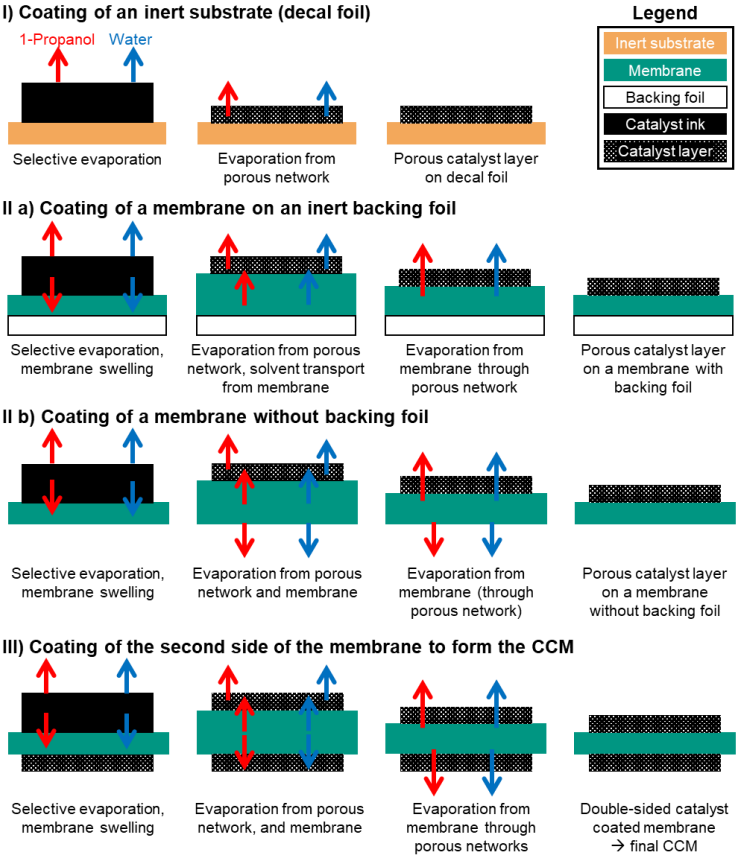

Figure 44: Comparison of the decal coating (I) and membrane direct coating (II-III) process. The membrane direct coating (MDC) is divided in MDC on membrane with (II a) and without an inert backing foil (II b) and MDC of the second side of the membrane to form the final CCM (III). Possible solvent mass flows after coating are indicated with arrows (red: 1-propanol, blue: water). This involves selective evaporation and, in the case of MDC, additional selective solvent absorption (swelling) and release (shrinkage) of the membrane. Swelling and shrinkage of the membrane is indicated by varying thicknesses of the green membrane.

Looking at the membrane deformation, the swelling is assumed to behave rather differently in the cases with or without a lower restriction, among others present in form of the backing foil. It is anticipated that the membrane exhibits only one-dimensional swelling when in contact with a backing foil or positioned on a coating plate, with lateral expansion being constrained by the adhesion to the underground. Similarly, the subsequent shrinkage is also influenced by these boundary conditions (Figure 45 II a)). Conversely, without a supporting boundary, the membrane possesses the freedom to deform and contract in all spatial orientation (Figure 45 II b)).

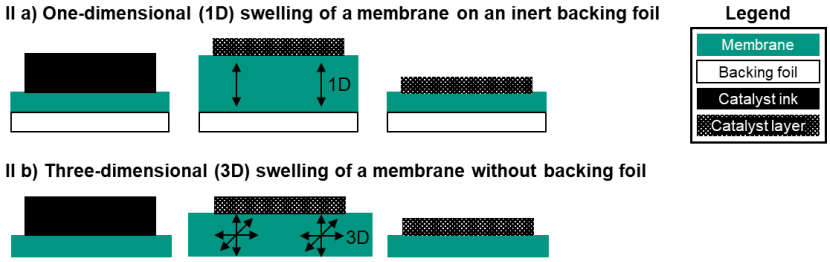

Figure 45: Membrane swelling and shrinking after coating and during drying on a membrane with (II a) and without a backing foil (II b). With support, the deformation is limited in one dimension (1D); without support, it is free in all three dimensions (3D).

In the following, the considerations are tested experimentally. In order to demonstrate the fundamental importance of the solvent absorption, the membrane is exposed to different solvent mixtures and the swelling is examined. In the next step, the ink is applied directly to the membrane and various effects are evaluated. The ink is applied with a doctor blade in this study. The advantage of this method is the smaller amount of ink and membrane required and a greater possibility of variation in the layer production compared to slot die coating. However, the effects found can be transferred to slot die coating for R2R production.

In R2R processes, the membrane undergoes a specific web tension. When the web tension is kept constant, deformation of the membrane due to swelling and

shrinkage after contact with the ink leads to different web speeds. This makes processing more difficult. Furthermore, the material's elasticity changes with different solvent loads. So far, all experiments in this work have been conducted on a membrane without external tensions. However, the influence of different tensile stresses in the membrane is discussed in initial experiments.

7.1 Membrane deformation due to swelling

The significance of membrane swelling is examined in a relatively simple experiment. The theoretical considerations suggest that the membrane is constrained in its movement by the lower fixation and only swells in its thickness rather than laterally (see Figure 45). The considerations are validated experimentally by placing membrane pieces of the same size (initial diameter 13 mm) with and without backing foil in the ink solvents for less than 2 s (Table 6 and Table 7). It should be noted that the contact area without backing foil is twice as large as with the backing foil.

After 2 s of solvent exposure, the area of the membrane sample with support (M w/ S) remains unchanged (Table 6). Without support (M w/o S), the membrane expands laterally. The membrane has the greatest spatial change due to swelling in 1-propanol. Without backing foil, the membrane in 1-propanol exhibits a nearly twofold increase in sample area. In water, the sample area increases by 16 % compared to the initial area. The membrane exhibits swelling behavior similar to that observed in pure 1-propanol when immersed in the solvent mixture, despite the fact that the 1-propanol mass fraction in the mixture is only 20 wt%.

A similar trend is evident when examining the increase in membrane thickness (Table 7). In 1-propanol, the change in membrane thickness from originally 51 µm with the backing foil is more than 7 times greater at 58 % to 8 % in water. Without the backing foil, the change in thickness is also significantly greater in 1-propanol (39 %) than in water (7 %). In the solvent mixture, the membrane exhibits a degree of swelling comparable to that observed in pure

1-propanol, regardless of the presence of the backing foil. These simple experiments cannot provide a final conclusion about the component-specific swelling behavior in the mixture.

Table 6: Spatial expansion of the membrane samples with (M w/ S) and without (M w/o S) supporting backing foil when completely immersed in the solvents water, 1-propanol and a solvent mixture of 80 wt% water and 20 wt% 1-propanol for 2 s.

	1-Propanol	Water	Water:1-propanol (80:20 wt%)
Membrane with support foil (M w/ S)	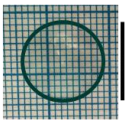 13 *mm*	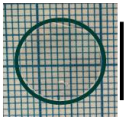 13 *mm*	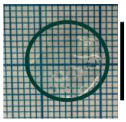 13 *mm*
Membrane without support foil (M w/o S)	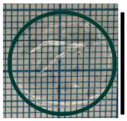 18 *mm*	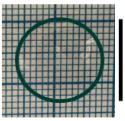 14 *mm*	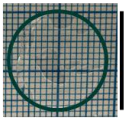 16 *mm*

Table 7: Thickness expansion of the membrane with (M w/ S) and without (M w/o S) supporting backing foil when completely immersed in the solvents water, 1-propanol and a solvent mixture of 80 wt% water and 20 wt% 1-propanol for 2 s.

	Water	**Water:1-propanol (80:20 wt%)**	**1-Propanol**
Membrane with support foil (M w/ S)	~ 8 %	~ 56 %	~ 58 %
Membrane without support foil (M w/o S)	~ 7 %	~ 34 %	~ 39 %

The change in thickness of the membrane with backing foil is greater in all solvents than without. In pure 1-propanol and the solvent mixture, the increase in thickness is 50 % higher when a membrane with backing foil is used (56 %) in comparison to the membrane without (34 %).

Without the backing foil, the changes in both lateral directions and in thickness in water and 1-propanol are nearly identical. The pure NR212 membrane exhibits isotropic swelling, as already observed for Nafion membranes without backing foil, e.g. N115 and N117 [281]. With backing, it swells only in the axial direction, but slightly more. The membrane is held in place by the backing foil. However, the pronounced swelling in the thickness also indicates that, despite the fact that the contact surface of the membrane to the solvent is only half as large for M w/ S than for M w/o S, the solvent absorption is pronounced and must be taken into account in the process. The experiments clearly show that the membrane is strongly deformed by contact with the solvent. The backing foil has a major influence on the degree of deformation of the membrane. Consequently, different swelling behaviors are expected for the coating of firstly the anode and subsequently the cathode on the membrane. It was shown that an exposure time of 2 s already leads to dimensional changes, suggesting that swelling is a phenomenon with a short timescale. Indeed, a large excess of solvent was used here. However, when ink is applied with a slot die or doctor blade, also a relatively large amount of solvent comes into contact with the membrane at one time. This means that immediately after ink application, a large proportion of the solvents migrate into the membrane and deform it. Additionally, changes in ink composition due to membrane penetration are expected to occur within a very short timescale.

These changes in composition may lead to modifications in the selective drying. Further studies on membrane swelling, especially on the component-specific quantitative solvent fluxes, are important for understanding the membrane selectivity (see Eq. (5.8)) and the overall selectivity (see Eq. (5.4)). Thus, inverse micro Raman spectroscopy can be applied in further studies on solvent uptake and subsequent release in (transparent) membranes with spatial and temporal resolution. However, the challenge will be to ensure that the deforming membrane remains continuously within the measuring range of the spectrometer during the experiment.

After the solvent contact, the membrane shrinks due to the solvent evaporation. This is observed to be reversible (regarding geometrics). For a R2R process,

however, this also means that changes in the dimensions of the membrane must be considered during the process.

7.2 Influence of the backing foil on the crack pattern

The effects of the different swelling behavior and the different deformation of the membrane with and without backing foil are now investigated with the ink. For this purpose, the ink is applied as a wet film and the resulting crack pattern is qualitatively analyzed as a criterion for the electrode quality. Isothermal drying with a combination of convective and conductive drying is applied (see Chapter 3.4). The focus here is on the entire layer image rather than individual cracks. For this reason, the images are shown with less zoom and cover a larger area than in Chapter 0, however they are similar to Figure 24 in Chapter 5. The crack pattern of the layer on the membrane with the supporting backing foil shows the crack pattern known from Figure 24: a black layer with individual white spots, which are known as cracks. (Figure 46 M w/ S).

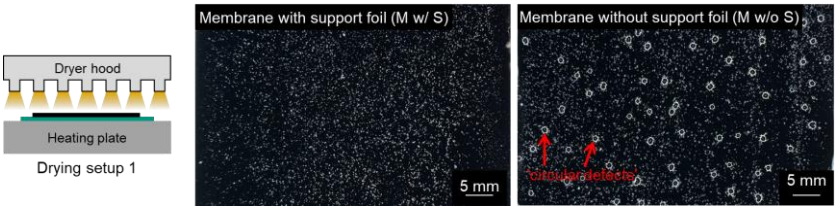

Figure 46: Crack pattern photographed in back-light after membrane direct coating on a membrane with (M w/ S) and without supporting backing foil (M w/o S), both dried isothermally ($T = 25$ °C, $\alpha = 35$ W m^{-2} K^{-1}). White spots are cracks. In the sample of the membrane without the supporting foil, 'circular' defects appear, most probably caused by 'dust particles'. The dry layer thicknesses are 8.9 ± 0.5 µm. Additional schematic illustration of drying setup 1 (left).

The comparison to the membrane without the backing foil (M w/o S), imitating the membrane coating of the second side, is interesting. The membrane without backing foil shows good mechanical integrity and adheres uniformly to the

surface of the heating plate in the isothermal drying setup, which facilitates the handling during sheet to sheet processing. However, the crack pattern of the dried catalyst layer on the membrane without support shows many small cracks and circular defects (Figure 46 M w/o S). These circular defects are probably caused by dust particles between the plate and the membrane leading to deformation and inhomogeneities introducing additional stresses within the catalyst layer. The backing foil prevents the dust from adhering to the membrane and can level out the unevenness to a certain extend. This assumption can be verified in future studies in a more 'clean room atmosphere'.

M w/o S crack pattern is similar to M w/ S crack pattern except for the circular defects. The similarity could be due to the fact that in both cases the membrane is effectively fixed at the bottom by the contact with the heating plate or by the backing foil. This presumably leads in both cases to the lateral swelling behavior already observed with M w/ S and to a generally similar crack pattern.

For a R2R process, it seems unfavorable to coat and dry the membrane permanently fixed on a heating plate. In order to better reproduce the intended R2R process, the drying setup is now varied. The membrane is no longer placed on the heating plate, but is clamped to hang freely under a drying hood. Thus, the membrane is not resticted in any movement or swelling (see Chapter 3.4).[1] In this setup, the presence of the backing foil fundamentally changes the crack pattern (Figure 47). Firstly, the cracking in the catalyst layer on the M w/ S is consistent with the results of the test conducted using the isothermal heating plate setup (see Figure 46). This leads to the conclusion that clamping and the different drying setup are not significant factors in crack formation here. In contrast, the unsupported membrane (M w/o S) displays remarkably little cracking after drying. Almost no cracks are visible.

[1] Isothermal drying conditions by contact and convection drying are not possible in drying setup 2. Only convection drying is used. However, the air temperature is chosen to achieve a comparable film temperature (due to evaporative cooling) for the most of the drying time. For more information on the different drying setups, refer to Chapter 3.4.

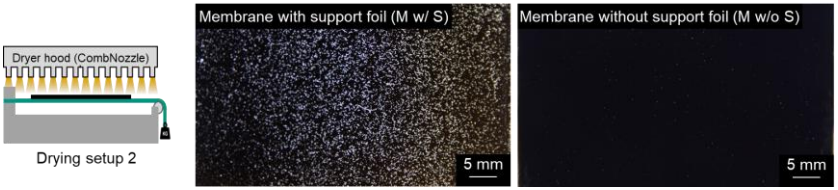

Figure 47: Crack pattern photographed in back-light after membrane direct coating onto a membrane with (M w/ S) and without a supporting backing foil (M w/o S) after drying in a 'free hanging' membrane setup. White spots are cracks. The membrane without the supporting foil imitates the second coating on the reverse side of the membrane, whereby the backing foil has to be removed. Dry layer thicknesses are around 9.0 ± 0.5 µm. Additional schematic illustration of drying setup 2 (left).

This is surprising, because without the support, the layer dried on the heating plate shows a large number of cracks, even when the 'circular' defects are neglected (see Figure 46). It was also expected that there would be more swelling and deformation after the ink application (see Chapter 7.1), which might lead to more cracks. In fact, extended membrane deformation was observed when the clamped membrane was examined during the drying process. Immediately after coating, the membrane without backing foil expands and forms a wave-like shape (Figure 48). However, it returns to its original shape towards the end of the drying process (Figure 49). The deformation results from the expansion of the membrane due to solvent absorption. At the end of the drying process, the solvents are removed from the membrane and it returns to its original shape. Surprisingly, the lack of restraint for deformation of the membrane appears to be beneficial for the quality of the electrode measured with the crack pattern. Restraining the movement of the membrane could lead to tension in the membrane that induces stress in the coated catalyst layer. This causes cracks.

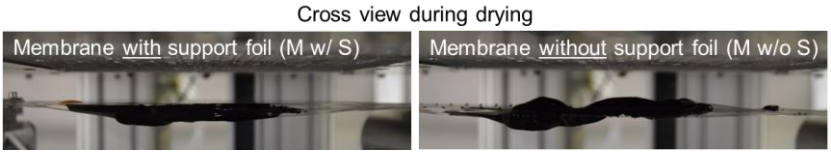

Figure 48: Cross view on catalyst layer (black) and membrane with (M w/ S) and without (M w/o S) supporting backing foil during drying in drying setup 2. Without support, the membrane deforms much more.

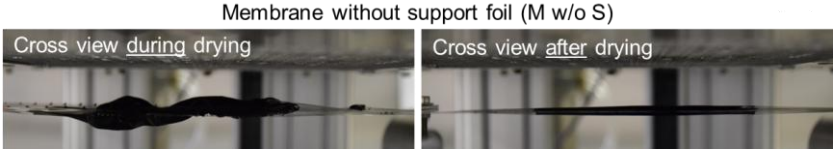

Figure 49: Cross view on catalyst layer (black) and membrane without (M w/o S) supporting backing foil during and after drying in drying setup 2. The membrane deformation during drying due to the solvent contact after ink application is reversible.

In summary, the backing foil has a significant influence on the crack pattern. This must be taken into account when coating (the second side of) the membrane. In initial trials on this topic, it was observed that the first layer was unaffected by the second coating and drying process (see Appendix 9.6). Furthermore, the second coated layer, which was free to move during drying, behaved like the first layer on the membrane without support and showed nearly no cracking. These initial tests suggest that if the membrane can be handled without support in the R2R process (mechanically with regard to the change in mechanical properties and the length expansion), crack-reduced catalyst layers can be produced. Further investigation is recommended, especially with regard to membrane reinforcements.

7.3 Influence of tensile stress on the crack pattern

Removal of the backing film in the free-hanging setup changes the tensile stress on the membrane. This is because less material experiences the same web tension as the substrate's thickness decreases. Increasing web tension could influence the crack pattern. Moreover, given the significance of tensile stress in R2R processes, where it is unavoidable, this parameter is examined by varying the substrate tension. Removing the backing foil from the membrane reduces the overall thickness by about 60 % (from 126 µm to 51 µm). For a constant web tension (per unit width), this leads to an increase in tensile stress of 2.4 times (based on cross-sectional area). To investigate the effect of increased stress from a lower web tension (LWT), the web tension was increased by a factor of 8.1 during ink drying for both supported and unsupported membranes. This higher web tension (HWT) is representative for industrial roll-to-roll systems [282] and results in an equivalent eightfold increase in cross-sectional area-related tensile stress for the two investigated membranes. An overview of the applied tensions and stresses and an outline of the calculations are given in Appendix 9.6.

The tensile stress, in this experiments up to 116 N cm^{-2}, is in the elastic range of a (dry) NR212 membrane, which is up to around 1400 N cm^{-2} [283]. Unfortunately, no data were found for a wetted 212 membrane. However, there is data for a Nafion 117 membrane in the literature, which loses more than 50 % of its strength when wetted with water [141]. When this is extrapolated to the 212 membrane, the tensile stress is still expected to be within the elastic deformation range.

With the web tensions tested, no significant increased crack formation is visible, whether support was present or absent (Figure 50). Notably, the tensile stress of the unsupported membrane at lower tension ($\sigma_{M\ w/o\ S\text{-}LWT}$ = 14 N cm^{-2}) lies between the two tension levels of the supported membrane ($\sigma_{M\ w/\ S\text{-}LWT}$ = 6 N cm^{-2} and $\sigma_{M\ w/\ S\text{-}HWT}$ = 48 N cm^{-2}). This means that the backing foil has a significant impact on the crack pattern, which is not caused by increased tensile

stress within the substrate. Higher applied stress in the substrate does not result in poorer coating quality, i.e. a larger crack area. This is considered favorable for establishing a R2R process.

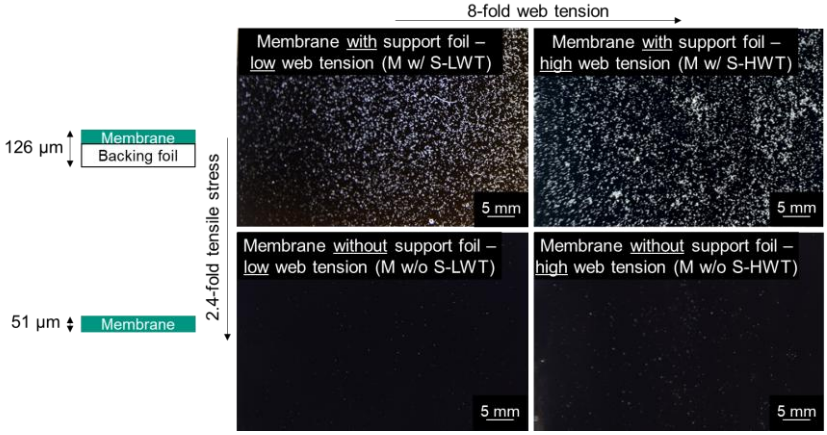

Figure 50: Influence of the web tension on crack pattern in catalyst layers of membrane coatings with (M w/ S) and without (M w/o S) backing foil. Identical ink and drying conditions were used. Removing the backing foil reduces the substrate thickness and increases the tensile stress by a factor of 2.4. Higher web tension (HWT) is eight times greater than the lower web tension (LWT). Dry layer thicknesses are 8.8 ± 0.5 µm. Defects are shown white in back-light illumination. The backing foil significantly impacts the crack pattern, which does not result from increased tensile stress within the substrate.

7.4 Conclusion on membrane direct coating

The main challenge in membrane direct coating is the swelling of the membrane. Especially when the catalyst ink is applied via slot die or doctor blade coating for roll-to-roll (R2R) processing of catalyst-coated membranes (CCMs). Membrane swelling could change the ink solvent composition and deform the membrane. These issues were examined under Hypothesis 3:

Increased degrees of freedom of the membrane after ink coating and during drying result in fewer cracks in the directly coated catalyst layer.

In order to understand the complex processes taking place after ink applying, the solvent flows that occur were elaborated. The membrane is supplied with a backing foil for mechanical support. However, this additional foil must be removed in order to coat the second side. Both cases were examined. As the backing foil is inert to the ink solvents, it acts as a barrier to them. As a result, the solvent fluxes with and without the liner are directed differently, especially when the membrane is drying towards the end of the process.

The membrane absorbs a large amount of solvent within a short period of time. As a result, the membrane begins to deform immediately after solvent contact, e.g. after ink application. With backing foil, the membrane swells mainly in the axial direction; without backing foil, it swells isotropically in all directions. A strong affinity for 1-propanol is observed in excessive swelling. Quantitative and component-resolved measurements were not possible in this work. However, this can be further investigated, e.g. using in-situ micro Raman spectroscopy.

Theoretical considerations deal with selective membrane swelling and selective drying from the previous chapters. With the investigated ink formulation and drying conditions, and according to the results from Chapter 6, 1-propanol evaporates preferentially in the drying process. Combined with the assumption from the experiments in Chapter 7.1 that the membrane also preferentially absorbs 1-propanol, the 1-propanol is preferentially removed from the drying catalyst layer, both by drying and membrane absorption. Overall, the total selectivity within the membrane direct coating (MDC) under these conditions is clearly in favor of 1-propanol, resulting in a reduction in its fraction in the ink.

Cracks appear in the catalyst layer on the membrane with the backing foil. The same applies for a catalyst layer coated on the membrane without backing foil, and fixed on the coating plate. In a clamped setup, where the membrane hangs freely, a similar crack pattern results for the catalyst layer on the membrane with support. In contrast to this, the catalyst layer shows significantly fewer cracks without the backing foil. The unfixed membrane deforms strongly under the influence of the solvent from the coating. However, the deformation is reversible and the reduced restraint of the membrane seems to be advantageous

to avoid cracks in the catalyst layer. Presumably, this results in less induced stress, which is a cause of cracking. The free movement in the deformation of the membrane without restraint seems to be beneficial for electrode quality, e.g., by reducing cracking. The issue of the layer's dryness and solidification status upon the membrane's shrinkage remains an open question. Once the catalyst layer has partially dried and solidified, it can be susceptible to tensile stress caused by lateral membrane shrinkage. However, this does not seem to be an issue.

Removing the backing foil for the second coating changes the tensile stress in the substrate, when coated again. This is due to the smaller cross-sectional area of the substrate at constant web tension. However, tests with different web tensions and tensile stresses showed that this parameter was not decisive for the crack pattern.

Back-light illumination is not suitable for the analyzing cracks in (double-side) CCM, particularly with regard to the detection of coatings. Therefore, the analytical approach was modified to employ top-light illumination. It was found that the second layer is produced almost crack-free on the membrane with coated cathode. The first catalyst layer does not provide significant restraint for the membrane, which would lead to cracking as shown above. Hypothesis 3 can therefore be verified in this case for the NR212 Nafion membrane. Free movement of the membrane as a form of a higher degree of membrane freedom is beneficial for preventing crack formation in the coated layer.

It is concluded that it is advantageous to apply and dry the catalyst ink directly onto the membrane without a backing foil or other fixation. The prerequisite is that the membrane is mechanically stable enough to pass through the process without support and that deformation changes in the belt can be handled. Otherwise, this can perhaps be achieved from a mechanical engineering point of view by sensitive re-adjusting and re-tensioning the drive rollers in the coating and drying system. First results indicate that the second side coating of a CCM does not affect the first layer. More comprehensive investigations are needed to better understand the underlying mechanisms.

8 Summary and Outlook

The aim of the thesis was to gain a deeper understanding of the processing of catalyst-coated membranes (CCM) for fuel cells by membrane direct coating (MDC) and the main phenomena that occur. A comprehensive examination was conducted, encompassing the processing of the catalyst ink, the subsequent coating on the membrane, and the drying process. The decisive characterization parameter for electrode quality was the crack pattern of the different layers produced.

Ink processing was systematically investigated using a ball mill. Not surprisingly, longer milling times and higher rotational speeds during ink processing lead to a particle size distribution (PSD) with more small particles and the break-up of larger agglomerates. The stress number (*SN*), which is influenced by milling time and rotational speed of the grinding disk, is derived from ball milling considerations and identified as the process function for PSD in catalyst inks. Similar *SN* values result in very similar PSDs. Furthermore, a strong correlation between the ink PSD and the properties of the resulting membrane direct coatings, especially their crack patterns and pore diameter distributions, is demonstrated in this study. Similar PSDs result in similar layer properties, making the PSD a key parameter for predicting layer properties, as hypothesized. This allows the potential prediction of layer properties through simple PSD determination for different catalyst ink formulations, provided that coating and drying conditions remain consistent.

Most interestingly, analysis of the crack pattern reveals an optimum milling process. Although the absence of large agglomerates (achieved with higher SN) is beneficial for reducing crack nucleation, a very small PSD with many small particles results in an interconnected crack network. The suggested explanation is that the large particle surface area must be stabilized with a limited amount of ionomer. The presence of free ionomer indicates adequate wetting of the particle surface by ionomer, which is critical for stabilizing the particles within the ink. The ionomer acts as a binder during layer formation and

increases crack resistance when distributed properly. A higher ionomer-to-carbon ratio (*I/C*) compensates for the lack of ionomer in inks with a small PSD, resulting in improved crack patterns for similar PSD. To the best of the author's knowledge, it is shown for the first time that the ionomer requirement for crack-free layers is a function of the ink PSD. This interaction between ink formulation and processing must be taken into account when optimizing inks and their coatings.

Regarding the drying process of catalyst inks, a major knowledge gap has been identified in the literature. Selective evaporation occurs during the drying process. This means that one solvent evaporates preferentially over the other, which changes the composition of the remaining solvents and affects the properties of the coating. Solvent mixtures of 1-propanol and water, often used in catalyst inks, were analyzed to simplify the system and investigate fundamental phenomena. The solvent composition was determined during the drying process by measuring the density of the binary mixture, which required a relatively large amount of liquid. 1-Propanol/water mixtures show a non-selectively drying solvent composition that depends on the drying parameter (e.g. temperature, preloading like relative humidity). This is known as an arheotropic composition and differs from the more common thermodynamic azeotrope by taking into account gas kinetics. It was shown experimentally that for 1-propanol compositions lower than the arheotropic composition, 1-propanol evaporates preferentially. Water evaporates preferentially when the concentration of 1-propanol in the solvent mixture is higher than the azeotropic composition. The arheotropic composition's position is little affected by the mass transfer coefficient, which is determined by the heat transfer coefficient, and in dry air by the drying temperature. However, these factors impact the solvents' drying rate. The most significant influence is preloading the drying air with solvent. This is demonstrated here using water as an example. With preloading, the temperature's influence on the azeotropic composition increases. This means that if the drying air is not pre-conditioned, the (relative) humidity, and therefore the weather, season and production site location, have a significant influence on the drying process. However, the large influence of drying

air preloading also offers the possibility to specifically adjust the non-selectively evaporating solvent composition via the drying conditions.

The results can be transferred to thin films, more closely resembling coated catalyst layers. Using inverse micro Raman spectroscopy (IMRS), it was possible to experimentally observe the selectivity in thin solvent mixtures, even without a non-volatile reference component. In addition to the integral compositional change, a spatially and temporally resolved quantitative determination of the composition could be performed with high accuracy during drying. There were small concentration gradients observable along the film height with preferential water evaporation. With preferential 1-propanol evaporation, these gradients were not observed, possibly due to unstable stratification inducing convection within the drying film. With regard to the catalyst film drying, this convection could affect the ionomer distribution during film solidification.

Initial tests showed that adding ionomer (Nafion) to the solvent mixture affects the arheotropic composition. Strong concentration gradients form in the film during drying and as the Nafion mass fraction increases. This is indicative of resistance occurring on the film side. The local and dynamic differences in solvent composition may influence microstructure formation, when particles and ionomer are exposed to different solvent compositions at different times, affecting their interactions and modifications.

Selective drying comprehensively describes the material transport processes on inert substrates, e.g. used in the decal process. However, membrane direct coating (MDC) is different. Here, selective membrane swelling also occurs. In initial swelling tests with a Nafion NR212 membrane, there appears to be a preferential uptake of 1-propanol, at least there is a greater deformation of the membrane. To describe the compositional change of the ink in fuel cell processing, all material flows of membrane swelling and drying must be taken into account. The presumably preferential absorption of 1-propanol by the membrane, combined with the preferential evaporation of 1-propanol from the drying ink with the used ink formulation and drying conditions, will lead to a depletion of 1-propanol in the applied catalyst film and a shift in the overall arheotropic composition.

The main challenge in MDC is the amount of solvent applied to the membrane and the resulting swelling and deformation of the membrane. The analyzed Nafion NR212 membrane without embedded reinforcement is supplied on a supporting backing foil. Removal of the backing foil is necessary for the second side coating and optional for the first side coating. The hypothesis investigated is that a higher degree of freedom in the deformation of the membrane due to swelling and shrinkage after ink contact and during drying is beneficial for preventing cracking in the catalyst coatings. It has been shown that the membrane swells axially when supported by a backing foil. Without the support it swells significantly more and isotropically in all directions. The cracking pattern of the catalyst coatings without this support or any other fixation showed significantly fewer cracks. The free movement of the membrane during deformation appears to reduce the induced stress within the catalyst layer, thus minimizing cracking. Investigations into the influence of web tension on electrode quality during R2R processing showed that, within the investigated range, this has no significant effect on coating quality in terms of cracks.

Coating the second layer on a membrane with the fist catalyst layer resulted in almost crack-free layers, suggesting the advantageous freedom of movement during deformation. Studies indicate that, for both initial and later coatings, directly applying and drying the catalyst ink onto the membrane without a backing foil or fixation proves beneficial. This advantage holds as long as the membrane's structural integrity and process control can accommodate shifts in its mechanical membrane properties. Preliminary results indicate that applying the second coating does not affect the first.

The ink composition impacts the formation of the microstructure. Therefore, the ink composition and solvent fluxes that occur during catalyst layer processing are key factors in producing high-quality catalyst layers in the MDC. Various influencing parameters have been identified stepwise through literature review and own investigations regarding the ink solvent composition after the ink is applied onto the membrane (Figure 51). These parameters originate from three sources: the ink itself (considering its formulation and processing); the membrane (as the swelling substrate); and the drying conditions. It was

identified that for the ink, the important parameters are the initial solvent composition, solid content, ionomer-to-carbon ratio (*I/C*), particle size distribution (PSD) and ionomer distribution. Regarding the drying conditions, the temperature, air flow and especially preloading of the air affect the ink composition during the drying process. The selective membrane swelling is determined by the freedom of movement during deformation.

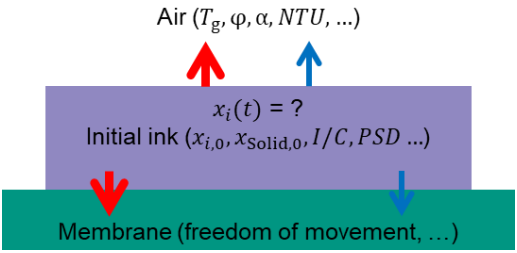

Figure 51: Influence parameters on the solvent composition of a catalyst coating during membrane direct coating. The solvent mass flows (shown as arrows) occurring after coating and during drying of a catalyst ink result in a compositional change in the ink which affects the microstructure of the produced layer. The solvent composition $x_i(t)$ in the ink and the resulting crack pattern of the dried layer depend on several parameters resulting from the ink properties themselves, the drying conditions, and the conditions of selective membrane swelling, all of which are interdependent.

In summary, the process parameters throughout the entire process chain, from ink to CCM via ink processing and membrane direct coating to subsequent drying, influence the overall properties of the individual catalyst layers and, consequently, the total CCM. The different process steps are interconnected and affect each other. This work has revealed and explained many of these interactions. Therefore, this work contributes to a deeper understanding of the CCM and fuel cell manufacturing process, enabling the production of higher-quality, more cost-effective systems. Open and further aspects are outlined in the following.

Due to the large influence of ink processing and the resulting significant particle size distribution (PSD), the stress number (*SN*) parameters should be

further tested and optimized. An interesting focus could be the further investigation of the influence of the solid content. Especially in the context of different coating processes that require different solid contents.

The IMRS measurement technique in the experimental setup used in this work is a powerful tool for further characterization of film-side mass transfer effects. The proof of concept for the quantitative determination of solvent mixture compositions during drying, without the presence of non-volatile components, paves the way for its application to various other solvent mixtures for fuel cell purposes, and even to completely different application fields. It is also possible to extend the measurement technique to multiple solvents and to study film-side gradients and kinetics. Supplementary microparticle tracing velocity (μPTV) measurements can also be made to investigate convection in the thin films induced by solvent gradients along the film height due to selective evaporation. With regard to the production of fuel cell electrodes, the ionomer content during the drying process can be quantitatively determined from the IMRS measurements with low signal-to-noise ratio. This will allow the drying process to be described in even more detail. Using transparent dummy particles, the drying of a real catalyst ink could also be imaged and quantitatively studied using IMRS.

In the future, selective membrane swelling should be investigated in more detail. IMRS can help here. The focus should be on the kinetics of solvent uptake and subsequent release. Key questions may be: Is there a solvent composition for unselective membrane swelling? How much solvent is absorbed by the membrane, and when is it released in the drying step? How fast do these processes take place? What solvent composition exposes the (dry) layer during membrane drying? Moreover, selective film drying and selective membrane swelling may be quantitatively determined and studied simultaneously in the drying process with spatial and temporal resolution.

A phase diagram of ionomer and particle conformations along the ink drying process would be useful. This could be used in the future to analyze the drying path from the initial composition of the ink through the coating and drying steps. Or, conversely, the drying path could be selected by targeting the drying

conditions to pass through or avoid certain areas of the phase diagram. This may help prevent cracking and promote achieving the desired microstructure.

The exact factors influencing crack formation during CCM production should be investigated in the future. Some process influences have been identified in this work. However, a more detailed investigation of this topic is useful in the long term. The theory behind crack formation is currently limited to simple model systems, containing of one solvent and particles. Many factors and assumptions of the widely used models only apply to complex, multi-component catalyst ink systems, either with restrictions or not at all. The ionic polymer, which can change its *pH* during drying and, thus, its interactions, and the flexible and self-deforming membrane are still underrepresented in the research. In addition, the influence of the solvent change during the layer solidification process and the associated changes in its properties (surface tension, contact angle, (volumetric) drying rate, interaction with ionomer and particles, ...) on crack formation in multi-solvent systems is not fully understood.

Performance tests with the layers under different manufacturing conditions are of course of interest. Polarization curves, relating to current-voltage curves which represent the overall performance of a fuel cell under certain operating conditions, as well as electrochemical impedance spectroscopy and ageing tests, help to improve the understanding of the consequences of processing. Especially with regard to the influence of cracks on performance and lifetime of the fuel cell system. The promising approach of carbon nanotubes (CNT) as a coating additive should also be investigated further.

References

[1] EU-Commission. Communication COM/2020/299. 2020.

[2] Bundesministerium für Wirtschaft und Energie (BMWi) Öffentlichkeitsarbeit. Die Nationale Wasserstoffstrategie 2020.

[3] Hebeling C, Ragwitz T, Fleiter T, Groos U, Härle D, Held A, et al. Eine Wasserstoff-Roadmap für Deutschland 2019.

[4] Jaroni MS. Mit Wasserstoff zur klimaneutralen Stahlproduktion 2021;2021:6–9.

[5] Lopez G, Farfan J, Breyer C. Trends in the global steel industry: Evolutionary projections and defossilisation pathways through power-to-steel. J Clean Prod 2022;375:134182. https://doi.org/10.1016/j.jclepro.2022.134182.

[6] Bockelmann M, Becker M, Stypka S, Bauer S, Minke C, Turek T. Erzeugung von Wasserstoff durch Elektrolyse: Grüner Wasserstoff. Chem Unserer Zeit 2024;58:29–45. https://doi.org/10.1002/ciuz.202300024.

[7] Ehsani M, Gao Y, Longo S, Ebrahimi K. Modern Electric, Hybrid Electric, and Fuel Cell Vehicles, Third Edition. 3rd ed. Milton: CRC Press; 2018.

[8] Gesetz über die Errichtung einer Bundesanstalt für den Digitalfunk der Behörden und Organisationen mit Sicherheitsaufgaben (BDBOS-Gesetz - BDBOSG). 2006.

[9] NOW GmbH. Fünf Bundesländer setzen im BOS-Digitalfunk auf die Brennstoffzelle. Berlin, Germany: 2019.

[10] Schœnbein CF. X. On the voltaic polarization of certain solid and fluid substances: To the editors of the Philosophical Magazine and Journal. Lond Edinb Dublin Philos Mag J Sci 1839;14:43–5. https://doi.org/10.1080/14786443908649658.

[11] Grove WR. XXIV. On voltaic series and the combination of gases by platinum. Lond Edinb Dublin Philos Mag J Sci 1839;14:127–30. https://doi.org/10.1080/14786443908649684.

[12] Wallace HD. Fuel Cells: A Challenging History. Substantia 2019:83-97 Pages. https://doi.org/10.13128/SUBSTANTIA-277.

[13] Mekhilef S, Saidur R, Safari A. Comparative study of different fuel cell technologies. Renew Sustain Energy Rev 2012;16:981–9. https://doi.org/10.1016/j.rser.2011.09.020.
[14] Sazali N, Wan Salleh WN, Jamaludin AS, Mhd Razali MN. New Perspectives on Fuel Cell Technology: A Brief Review. Membranes 2020;10:99. https://doi.org/10.3390/membranes10050099.
[15] TÜV Nord. Wirkungsgrad - Die Nutzbarkeit der Energie 2025. https://www.tuev-nord.de/de/privatkunden/verkehr/auto-motorrad-caravan/elektromobilitaet/wirkungsgrad/.
[16] Agora Energiewende. Frontier Economics (2018): Die zukünftigen Kosten strombasierter synthetischer Brennstoffe. Studie im Auftrag von Agora Verkehrswende und Agora Energiewende. In: Agora Verkehrswende, Agora Energiewende und Frontier Economics (2018): Die zukünftigen Kosten strombasierter synthetischer Brennstoffe. Berlin: 2018.
[17] Rodrigues JPDS, Nunes WT, Brunoro M, Nunes RB. Comparison of Well-to-Wheel energy efficiency between combustion vehicles and electric vehicles. 2022 Int. Conf. Electr. Comput. Energy Technol. ICECET, Prague, Czech Republic: IEEE; 2022, p. 1–4. https://doi.org/10.1109/ICECET55527.2022.9872658.
[18] Tashie-Lewis BC, Nnabuife SG. Hydrogen Production, Distribution, Storage and Power Conversion in a Hydrogen Economy - A Technology Review. Chem Eng J Adv 2021;8:100172. https://doi.org/10.1016/j.ceja.2021.100172.
[19] Schelling U. Brennstoffzellen. In: Zahoransky R, editor. Energietechnik Syst. Zur Konv. Erneuerbaren Energieumwandlung Kompaktwiss. Für Stud. Beruf, Wiesbaden: Springer Fachmedien Wiesbaden; 2019, p. 273308. https://doi.org/10.1007/978-3-658-21847-8_9.
[20] Töpler J, Lehmann J, editors. Wasserstoff und Brennstoffzelle: Technologien und Marktperspektiven. Berlin, Heidelberg: Springer Berlin Heidelberg; 2017. https://doi.org/10.1007/978-3-662-53360-4.
[21] Klingele M, Breitwieser M, Zengerle R, Thiele S. Direct deposition of proton exchange membranes enabling high performance hydrogen fuel cells. J Mater Chem A 2015;3:11239–45. https://doi.org/10.1039/C5TA01341K.
[22] Breitwieser M, Klingele M, Britton B, Holdcroft S, Zengerle R, Thiele S. Improved Pt-utilization efficiency of low Pt-loading PEM fuel cell

electrodes using direct membrane deposition. Electrochem Commun 2015;60:168–71. https://doi.org/10.1016/j.elecom.2015.09.006.

[23] Breitwieser M, Moroni R, Schock J, Schulz M, Schillinger B, Pfeiffer F, et al. Water management in novel direct membrane deposition fuel cells under low humidification. Int J Hydrog Energy 2016;41:11412–7. https://doi.org/10.1016/j.ijhydene.2016.05.018.

[24] Klingele M, Vierrath S, Breitwieser M, Klose C, Thiele S. (Invited) Direct Membrane Deposition – A Fast and Simple Technique for Membrane Electrode Assembly Manufacturing. ECS Trans 2017;80:571–6. https://doi.org/10.1149/08008.0571ecst.

[25] Alkayyali T, Zeraati AS, Mar H, Arabyarmohammadi F, Saber S, Miao RK, et al. Direct Membrane Deposition for CO_2 Electrolysis. ACS Energy Lett 2023;8:4674–83. https://doi.org/10.1021/acsenergylett.3c01716.

[26] Holzapfel P, Bühler M, Van Pham C, Hegge F, Böhm T, McLaughlin D, et al. Directly coated membrane electrode assemblies for proton exchange membrane water electrolysis. Electrochem Commun 2020;110:106640. https://doi.org/10.1016/j.elecom.2019.106640.

[27] Stähler M, Stähler A, Scheepers F, Carmo M, Stolten D. A completely slot die coated membrane electrode assembly. Int J Hydrog Energy 2019;44:7053–8. https://doi.org/10.1016/j.ijhydene.2019.02.016.

[28] Frölich K. Der Decal-Prozess zur Herstellung katalysatorbeschichteter Membranen für PEM-Brennstoffzellen. KIT Scientific Publishing; 2015.

[29] Hack J, Heenan TMM, Iacoviello F, Mansor N, Meyer Q, Shearing P, et al. A Structure and Durability Comparison of Membrane Electrode Assembly Fabrication Methods: Self-Assembled Versus Hot-Pressed. J Electrochem Soc 2018;165:F3045–52. https://doi.org/10.1149/2.0051806jes.

[30] Quarz P, Zimmerer N, Janning L, Mannes F, Scharfer P, Schabel W. From Decal coating to membrane direct coating in catalyst coated membrane (CCM) production. Wasserstofftechnologien Effizient Produziert, vol. 1, Chemnitz, Germany: Verlag Wissenschaftliche Scripten; 2024, p. 135–44. https://doi.org/10.60687/2025-0065.

[31] Shahgaldi S, Alaefour I, Li X. Impact of manufacturing processes on proton exchange membrane fuel cell performance. Appl Energy 2018;225:1022–32. https://doi.org/10.1016/j.apenergy.2018.05.086.

[32] Chun Y-G, Kim C-S, Peck D-H, Shin D-R. Performance of a polymer electrolyte membrane fuel cell with thin film catalyst electrodes. J Power

Sources 1998;71:174–8. https://doi.org/10.1016/S0378-7753(97)02792-4.

[33] Xiong L, Manthiram A. High performance membrane-electrode assemblies with ultra-low Pt loading for proton exchange membrane fuel cells. Electrochimica Acta 2005;50:3200–4. https://doi.org/10.1016/j.electacta.2004.11.049.

[34] Tang H, Wang S, Jiang SP, Pan M. A comparative study of CCM and hot-pressed MEAs for PEM fuel cells. J Power Sources 2007;170:140–4. https://doi.org/10.1016/j.jpowsour.2007.03.062.

[35] Liu H, Ney L, Zamel N, Li X. Effect of Catalyst Ink and Formation Process on the Multiscale Structure of Catalyst Layers in PEM Fuel Cells. Appl Sci 2022;12:3776. https://doi.org/10.3390/app12083776.

[36] Maier M, Abbas D, Komma M, Mu'min MS, Thiele S, Böhm T. A comprehensive study on the ionomer properties of PFSA membranes with confocal Raman microscopy. J Membr Sci 2023;669:121244. https://doi.org/10.1016/j.memsci.2022.121244.

[37] Park J, Ulsh M, Mauger SA. Solvent absorption rate of perfluorosulphonic acid membranes towards understanding direct coating processes. Int J Hydrog Energy 2021;46:30239–45. https://doi.org/10.1016/j.ijhydene.2021.06.168.

[38] Ma L, Zimmerer N, Schäfer J, Quarz P, Heckmann T, Scharfer P, et al. Investigation on a micro-environment concept for MEA production process supported by numerical simulations 2022. https://nbn-resolving.org/urn:nbn:de:bsz:ch1-qucosa2-764450.

[39] Suzuki T, Hashizume R, Hayase M. Effect of blending carbon nanoparticles and nanotubes on the formation of porous structure and the performance of proton exchange membrane fuel cell …. J Power Sources 2015:109–17. https://doi.org/10.1016/j.jpowsour.2015.03.119.

[40] Baez-Cotto CM, Pfeilsticker JR, Yu H, Van Cleve T, De Villers BT, Cetinbas CF, et al. Impact of polymer additives on crack mitigation of rod-coated fuel cell cathode catalyst layers. J Power Sources 2024;592:233852. https://doi.org/10.1016/j.jpowsour.2023.233852.

[41] Bonifácio RN, Neto AO, Linardi M. Influence of the relative volumes between catalyst and Nafion ionomer in the catalyst layer efficiency. Int J Hydrog Energy 2014;39:14680–9. https://doi.org/10.1016/j.ijhydene.2014.07.004.

[42] Du S, Guan S, Mehrazi S, Zhou F, Pan M, Zhang R, et al. Effect of Dispersion Method and Catalyst on the Crack Morphology and

Performance of Catalyst Layer of PEMFC. J Electrochem Soc 2021;168:114506. https://doi.org/10.1149/1945-7111/ac3598.

[43] Kim M, Park J-N, Kim H, Song S, Lee W-H. The preparation of Pt/C catalysts using various carbon materials for the cathode of PEMFC. J Power Sources 2006;163:93–7. https://doi.org/10.1016/j.jpowsour.2006.05.057.

[44] Khandavalli S, Park JH, Kariuki NN, Myers DJ, Stickel JJ, Hurst K, et al. Rheological Investigation on the Microstructure of Fuel Cell Catalyst Inks. ACS Appl Mater Interfaces 2018;10:43610–22. https://doi.org/10.1021/acsami.8b15039.

[45] Berlinger SA, Chowdhury A, Van Cleve T, He A, Dagan N, Neyerlin KC, et al. Impact of Platinum Primary Particle Loading on Fuel Cell Performance: Insights from Catalyst/Ionomer Ink Interactions. ACS Appl Mater Interfaces 2022;14:36731–40. https://doi.org/10.1021/acsami.2c10499.

[46] Khandavalli S, Park JH, Kariuki NN, Myers DJ, Stickel JJ, Hurst K, et al. Rheological Investigation of Catalyst Inks for Roll-to-Roll Processing of Fuel Cell Electrodes 2018.

[47] Holdcroft S. Fuel Cell Catalyst Layers: A Polymer Science Perspective. Chem Mater 2014;26:381–93. https://doi.org/10.1021/cm401445h.

[48] Malek K, Mashio T, Eikerling M. Microstructure of Catalyst Layers in PEM Fuel Cells Redefined: A Computational Approach. Electrocatalysis 2011;2:141–57. https://doi.org/10.1007/s12678-011-0047-0.

[49] Chowdhury A, Bird A, Liu J, Zenyuk IV, Kusoglu A, Radke CJ, et al. Linking Perfluorosulfonic Acid Ionomer Chemistry and High-Current Density Performance in Fuel-Cell Electrodes. ACS Appl Mater Interfaces 2021;13:42579–89. https://doi.org/10.1021/acsami.1c07611.

[50] Arya LM, Heitman JL. A Non-Empirical Method for Computing Pore Radii and Soil Water Characteristics from Particle-Size Distribution. Soil Sci Soc Am J 2015;79:1537–44. https://doi.org/10.2136/sssaj2015.04.0145.

[51] S. Shukla, S. Bhattacharjee, A. Z. Weber, M. Secanell. Experimental and Theoretical Analysis of Ink Dispersion Stability for Polymer Electrolyte Fuel Cell Applications. J Electrochem Soc 2017;164:600609. https://doi.org/10.1149/2.0961706jes.

[52] Ohma A, Mashio T, Sato K, Iden H, Ono Y, Sakai K, et al. Analysis of proton exchange membrane fuel cell catalyst layers for reduction of

platinum loading at Nissan. Electrochimica Acta 2011;56:10832–41. https://doi.org/10.1016/j.electacta.2011.04.058.

[53] Morawietz T, Handl M, Oldani C, Gazdzicki P, Hunger J, Wilhelm F, et al. High-Resolution Analysis of Ionomer Loss in Catalytic Layers after Operation. J Electrochem Soc 2018;165:F3139–47. https://doi.org/10.1149/2.0151806jes.

[54] Lee M, Uchida M, Yano H, Tryk DA, Uchida H, Watanabe M. New evaluation method for the effectiveness of platinum/carbon electrocatalysts under operating conditions. Electrochimica Acta 2010;55:8504–12. https://doi.org/10.1016/j.electacta.2010.07.071.

[55] Berejnov V, Susac D, Stumper J, Hitchcock AP. 3D Chemical Mapping of PEM Fuel Cell Cathodes by Scanning Transmission Soft X-ray SpectroTomography. ECS Trans 2013;50:361–8. https://doi.org/10.1149/05002.0361ecst.

[56] Lopez-Haro M, Guétaz L, Printemps T, Morin A, Escribano S, Jouneau P-H, et al. Three-dimensional analysis of Nafion layers in fuel cell electrodes. Nat Commun 2014;5:5229. https://doi.org/10.1038/ncomms6229.

[57] Kumano N, Kudo K, Akimoto Y, Ishii M, Nakamura H. Influence of ionomer adsorption on agglomerate structures in high-solid catalyst inks. Carbon 2020;169:429–39. https://doi.org/10.1016/j.carbon.2020.07.047.

[58] Kumano N, Kudo K, Suda A, Akimoto Y, Ishii M, Nakamura H. Controlling cracking formation in fuel cell catalyst layers. J Power Sources 2019;419:219–28. https://doi.org/10.1016/j.jpowsour.2019.02.058.

[59] Middelman E. Improved PEM fuel cell electrodes by controlled self-assembly. Fuel Cells Bull 2002;2002:9–12. https://doi.org/10.1016/S1464-2859(02)11028-5.

[60] Takahashi S, Mashio T, Horibe N, Akizuki K, Ohma A. Analysis of the Microstructure Formation Process and Its Influence on the Performance of Polymer Electrolyte Fuel-Cell Catalyst Layers. ChemElectroChem 2015;2:1560–7. https://doi.org/10.1002/celc.201500131.

[61] Lee S-H, Woo SH, Pak BJ, Kim S, Kang YS, Woo S, et al. Ink droplet drying analysis for understanding the ink-catalyst layer transition in proton exchange membrane fuel cells. J Power Sources 2023;585:233644. https://doi.org/10.1016/j.jpowsour.2023.233644.

[62] Hoffmann E, Zhang S, Thoma M, Damm C, Peukert W. Formulation of carbon black-ionomer dispersions for thin film formation in fuel cells.

Particuology 2019;44:7–21. https://doi.org/10.1016/j.partic.2018.08.001.
[63] Li S, Yuan J, Xie G, Sundén B. Effects of agglomerate model parameters on transport characterization and performance of PEM fuel cells. Int J Hydrog Energy 2018;43:8451–63. https://doi.org/10.1016/j.ijhydene.2018.03.106.
[64] Suzuki T, Tanaka H, Hayase M, Tsushima S, Hirai S. Investigation of porous structure formation of catalyst layers for proton exchange membrane fuel cells and their effect on cell performance. Int J Hydrog Energy 2016;41:20326–35. https://doi.org/10.1016/j.ijhydene.2016.09.078.
[65] Xie J, Xu F, Wood DL, More KL, Zawodzinski TA, Smith WH. Influence of ionomer content on the structure and performance of PEFC membrane electrode assemblies. Electrochimica Acta 2010;55:7404–12. https://doi.org/10.1016/j.electacta.2010.06.067.
[66] Carcadea E, Varlam M, Marinoiu A, Raceanu M, Ismail MS, Ingham DB. Influence of catalyst structure on PEM fuel cell performance – A numerical investigation. Int J Hydrog Energy 2019;44:12829–41. https://doi.org/10.1016/j.ijhydene.2018.12.155.
[67] Yu H, Roller JM, Mustain WE, Maric R. Influence of the ionomer/carbon ratio for low-Pt loading catalyst layer prepared by reactive spray deposition technology. J Power Sources 2015;283:84–94. https://doi.org/10.1016/j.jpowsour.2015.02.101.
[68] Kamiya A, Tsutsushima Y, Ishii M, Nagao S. Catalyst ink. JP2021190402A, 2020.
[69] Komoda Y, Okabayashi K, Nishimura H, Hiromitsu M, Oboshi T, Usui H. Dependence of polymer electrolyte fuel cell performance on preparation conditions of slurry for catalyst layers. J Power Sources 2009;193:488–94. https://doi.org/10.1016/j.jpowsour.2009.04.015.
[70] Park I-S, Li W, Manthiram A. Fabrication of catalyst-coated membrane-electrode assemblies by doctor blade method and their performance in fuel cells. J Power Sources 2010;195:7078–82. https://doi.org/10.1016/j.jpowsour.2010.05.004.
[71] Stoll J, Jeong J, Huynh P, Kjeang E. Impacts of Catalyst Ink Composition and Wet Film Thickness on Fuel Cell Catalyst Layers Fabricated by Direct Film Coating Method. J Electrochem Soc 2024;171:054520. https://doi.org/10.1149/1945-7111/ad4c11.
[72] Park J, Kang Z, Bender G, Ulsh M, Mauger SA. Roll-to-roll production of catalyst coated membranes for low-temperature electrolyzers. J

Power Sources 2020;479:228819. https://doi.org/10.1016/j.jpowsour.2020.228819.

[73] Yang D, Guo Y, Tang H, Yang D, Ming P, Zhang C, et al. Effect of rheological properties of catalyst slurry on the structure of catalyst layer in PEMFC. Int J Hydrog Energy 2022;47:8956–64. https://doi.org/10.1016/j.ijhydene.2021.12.227.

[74] Creel EB, Tjiptowidjojo K, Alex Lee J, Livingston KM, Randall Schunk P, Bell NS, et al. Slot-die-coating operability windows for polymer electrolyte membrane fuel cell cathode catalyst layers. J Colloid Interface Sci 2022;610:474–85. https://doi.org/10.1016/j.jcis.2021.11.047.

[75] Choi M, Kim JK, Kim J, Yang S, Park J-E, Kim O-H, et al. PtRu/C catalyst slurry preparation for large-scale decal transfer with high performance of proton exchange membrane fuel cells. RSC Adv 2018;8:36313–22. https://doi.org/10.1039/c8ra07754a.

[76] Scheepers F, Stähler A, Stähler M, Carmo M, Lehnert W, Stolten D. Layer Formation from Polymer Carbon-Black Dispersions. Coatings 2018;8:450. https://doi.org/10.3390/coatings8120450.

[77] Dixit MB, Harkey BA, Shen F, Hatzell KB. Catalyst Layer Ink Interactions That Affect Coatability. J Electrochem Soc 2018;165:264–71. https://doi.org/10.1149/2.0191805jes.

[78] Woo SH, Kim S, Woo S, Park S-H, Kang YS, Jung N, et al. Investigating the effect of solvent composition on ink structure and crack formation in polymer electrolyte membrane fuel cell catalyst layers. Korean J Chem Eng 2023;40:2455–62. https://doi.org/10.1007/s11814-023-1474-3.

[79] Ion Exchange Materials n.d. https://www.fuelcellearth.com/wp-content/uploads/converted_files/pdf/D520-D521-D1021-D2020-D2021-Product-Bulletin-Chemours.pdf.

[80] 3MTM Ionomers n.d. https://www.fuelcellearth.com/wp-content/uploads/converted_files/pdf/D520-D521-D1021-D2020-D2021-Product-Bulletin-Chemours.pdf.

[81] Scheepers F, Stähler A, Stähler M, Carmo M, Lehnert W, Stolten D. Steering and in situ monitoring of drying phenomena during film fabrication. J Coat Technol Res 2019;16:1213–21. https://doi.org/10.1007/s11998-019-00206-5.

[82] Wang M, Park JH, Kabir S, Neyerlin KC, Kariuki NN, Lv H, et al. Impact of Catalyst Ink Dispersing Methodology on Fuel Cell

Performance Using in-Situ X-ray Scattering. ACS Appl Energy Mater 2019;2:6417–27. https://doi.org/10.1021/acsaem.9b01037.

[83] van Cleve T, Wang G, Mooney M, Cetinbas CF, Kariuki N, Park J, et al. Tailoring electrode microstructure via ink content to enable improved rated power performance for platinum cobalt/high surface area carbon based polymer electrolyte fuel cells. J Power Sources 2021;482:228889. https://doi.org/10.1016/j.jpowsour.2020.228889.

[84] van Cleve T, Khandavalli S, Chowdhury A, Medina S, Pylypenko S, Wang M, et al. Dictating Pt-Based Electrocatalyst Performance in Polymer Electrolyte Fuel Cells, from Formulation to Application. ACS Appl Mater Interfaces 2019;11:46953–64. https://doi.org/10.1021/acsami.9b17614.

[85] Mauger SA, Neyerlin KC, Yang-Neyerlin AC, More KL, Ulsh M. Gravure Coating for Roll-to-Roll Manufacturing of Proton-Exchange-Membrane Fuel Cell Catalyst Layers. J Electrochem Soc 2018;165:1012–8. https://doi.org/10.1149/2.0091813jes.

[86] Akerlof G. Dielectric constants of some organic solvent-water mixtures at various temperatures. J Am Chem Soc 1932;54:4125–39. https://doi.org/10.1021/ja01350a001.

[87] Uchida M, Aoyama Y, Eda N, Ohta A. New Preparation Method for Polymer-Electrolyte Fuel Cells. J Electrochem Soc 1995;142:463–8. https://doi.org/10.1149/1.2044068.

[88] Mabuchi T, Huang S-F, Tokumasu T. Dispersion of Nafion Ionomer Aggregates in 1-Propanol/Water Solutions: Effects of Ionomer Concentration, Alcohol Content, and Salt Addition. Macromolecules 2020;53:3273–83. https://doi.org/10.1021/acs.macromol.9b02725.

[89] Ngo TT, Yu TL, Lin H-L. Influence of the composition of isopropyl alcohol/water mixture solvents in catalyst ink solutions on proton exchange membrane fuel cell performance. J Power Sources 2013;225:293–303. https://doi.org/10.1016/j.jpowsour.2012.10.055.

[90] Ngo TT, Yu TL, Lin H-L. Nafion-based membrane electrode assemblies prepared from catalyst inks containing alcohol/water solvent mixtures. J Power Sources 2013;238:1–10. https://doi.org/10.1016/j.jpowsour.2013.03.055.

[91] Mauger SA, Wang M, Cetinbas CF, Dzara MJ, Park JH, Myers DJ, et al. Development of high-performance roll-to-roll-coated gas-diffusion-

electrode-based fuel cells. J Power Sources 2021;506:230039. https://doi.org/10.1016/j.jpowsour.2021.230039.

[92] Song C-H, Park J-S. Effect of Dispersion Solvents in Catalyst Inks on the Performance and Durability of Catalyst Layers in Proton Exchange Membrane Fuel Cells. Energies 2019;12:549. https://doi.org/10.3390/en12030549.

[93] Lei C, Yang F, Macauley N, Spinetta M, Purdy G, Jankovic J, et al. Impact of Catalyst Ink Dispersing Solvent on PEM Fuel Cell Performance and Durability. J Electrochem Soc 2021;168:044517. https://doi.org/10.1149/1945-7111/abf2b0.

[94] Hasegawa N, Kamiya A, Matsunaga T, Kitano N, Harada M. Analysis of crack formation during fuel cell catalyst ink drying process. Reduction of catalyst layer cracking by addition of high boiling point solvent. Colloids Surf A 2021;628:127153. https://doi.org/10.1016/j.colsurfa.2021.127153.

[95] Méndez-Bermúdez JG, Dominguez H, Pusztai L, Guba S, Horváth B, Szalai I. Composition and temperature dependence of the dielectric constant of 1-propanol/water mixtures: Experiment and molecular dynamics simulations. J Mol Liq 2016;219:354–8. https://doi.org/10.1016/j.molliq.2016.02.053.

[96] Gong Q, Li C, Liu Y, Ilavsky J, Guo F, Cheng X, et al. Effects of Ink Formulation on Construction of Catalyst Layers for High-Performance Polymer Electrolyte Membrane Fuel Cells. ACS Appl Mater Interfaces 2021;13:37004–13. https://doi.org/10.1021/acsami.1c06711.

[97] Pollet BG. Let's Not Ignore the Ultrasonic Effects on the Preparation of Fuel Cell Materials. Electrocatalysis 2014;5:330–43. https://doi.org/10.1007/s12678-014-0211-4.

[98] Pollet B. The Use of Power Ultrasound for the Production of PEMFC and PEMWE Catalysts and Low-Pt Loading and High-Performing Electrodes. Catalysts 2019;9:246. https://doi.org/10.3390/catal9030246.

[99] Pollet BG, Goh JTE. The importance of ultrasonic parameters in the preparation of fuel cell catalyst inks. Electrochimica Acta 2014;128:292–303. https://doi.org/10.1016/j.electacta.2013.09.160.

[100] Liu C, Luo M, Zeis R, Abel Chuang P-Y, Zhang R, Du S, et al. Fabrication of catalyst layer for proton exchange membrane water electrolyzer: I. Effects of dispersion on particle size distribution and

rheological behavior. Int J Hydrog Energy 2024;52:1143–54. https://doi.org/10.1016/j.ijhydene.2023.08.154.
[101] Kuroki H, Onishi K, Asami K, Yamaguchi T. Catalyst Slurry Preparation Using a Hydrodynamic Cavitation Dispersion Method for Polymer Electrolyte Fuel Cells. Ind Eng Chem Res 2019;58:19545–50. https://doi.org/10.1021/acs.iecr.9b02111.
[102] Orfanidi A, Rheinländer PJ, Schulte N, Gasteiger HA. Ink solvent dependence of the ionomer distribution in the catalyst layer of a PEMFC. J Electrochem Soc 2018;165:1254.
[103] Baez-Cotto CM, Pfeilsticker JP, Godoy AO, Batool M, Zaccarine S, Wang M, et al. The effect of ink ball milling time on interparticle interactions and ink microstructure and their influence on crack formation in rod-coated catalyst layers. J Power Sources 2023;583:233567. https://doi.org/10.1016/j.jpowsour.2023.233567.
[104] Park Y-C, Tokiwa H, Kakinuma K, Watanabe M, Uchida M. Effects of carbon supports on Pt distribution, ionomer coverage and cathode performance for polymer electrolyte fuel cells. J Power Sources 2016;315:179–91. https://doi.org/10.1016/j.jpowsour.2016.02.091.
[105] Hashimasa Y, Numata T. Comparison of test results on load cycle durability of polymer electrolyte fuel cell cathode catalysts. Int J Hydrog Energy 2015;40:11543–9. https://doi.org/10.1016/j.ijhydene.2015.04.031.
[106] Lindermeir A, Rosenthal G, Kunz U, Hoffmann U. On the question of MEA preparation for DMFCs. J Power Sources 2004;129:180–7. https://doi.org/10.1016/j.jpowsour.2003.11.002.
[107] Bernt M, Gasteiger HA. Influence of Ionomer Content in IrO_2 /TiO_2 Electrodes on PEM Water Electrolyzer Performance. J Electrochem Soc 2016;163:F3179–89. https://doi.org/10.1149/2.0231611jes.
[108] Alavijeh AS, Khorasany RMH, Nunn Z, Habisch A, Lauritzen M, Rogers E, et al. Microstructural and Mechanical Characterization of Catalyst Coated Membranes Subjected to In Situ Hygrothermal Fatigue. J Electrochem Soc 2015;162:1461–9. https://doi.org/10.1149/2.0471514jes.
[109] Sadeghi Alavijeh A, Bhattacharya S, Thomas O, Chuy C, Yang Y, Zhang H, et al. Effect of hygral swelling and shrinkage on mechanical durability of fuel cell membranes. J Power Sources 2019;427:207–14. https://doi.org/10.1016/j.jpowsour.2019.04.081.
[110] Goulet M-A, Arbour S, Lauritzen M, Kjeang E. Water sorption and expansion of an ionomer membrane constrained by fuel cell electrodes.

J Power Sources 2015;274:94–100. https://doi.org/10.1016/j.jpowsour.2014.10.040.
[111] Jeck S, Scharfer P, Kind M. Absence of Schroeder's paradox: Experimental evidence for water-swollen Nafion® membranes. J Membr Sci 2011;373:74–9. https://doi.org/10.1016/j.memsci.2011.02.036.
[112] Tang Y, Karlsson AM, Santare MH, Gilbert M, Cleghorn S, Johnson WB. An experimental investigation of humidity and temperature effects on the mechanical properties of perfluorosulfonic acid membrane. Mater Sci Eng A 2006;425:297–304. https://doi.org/10.1016/j.msea.2006.03.055.
[113] Satterfield MB, Benziger JB. Non-Fickian Water Vapor Sorption Dynamics by Nafion Membranes. J Phys Chem B 2008;112:3693–704. https://doi.org/10.1021/jp7103243.
[114] Saarinen V, Kreuer K, Schuster M, Merkle R, Maier J. On the swelling properties of proton conducting membranes for direct methanol fuel cells. Solid State Ion 2007;178:533–7. https://doi.org/10.1016/j.ssi.2006.12.001.
[115] Li Y, Nguyen QT, Buquet CL, Langevin D, Legras M, Marais S. Water sorption in Nafion® membranes analyzed with an improved dual-mode sorption model—Structure/property relationships. J Membr Sci 2013;439:1–11. https://doi.org/10.1016/j.memsci.2013.03.040.
[116] Park J. Roll-to-Roll Direct Coating of Catalyst Inks on Membrane Films: Progress and Challenges 2020.
[117] Soniat M, Houle FA. Swelling and Diffusion during Methanol Sorption into Hydrated Nafion. J Phys Chem B 2018;122:8255–68. https://doi.org/10.1021/acs.jpcb.8b03169.
[118] Goswami S, Klaus S, Benziger J. Wetting and Absorption of Water Drops on Nafion Films. Langmuir 2008;24:8627–33. https://doi.org/10.1021/la800799a.
[119] Rivin D, Kendrick CE, Gibson PW, Schneider NS. Solubility and transport behavior of water and alcohols in Nafion™. Polymer 2001;42:623–35. https://doi.org/10.1016/S0032-3861(00)00350-5.
[120] Scharfer P, Schabel W, Kind M. Mass transport measurements in membranes by means of in situ Raman spectroscopy—First results of methanol and water profiles in fuel cell membranes. J Membr Sci 2007;303:37–42. https://doi.org/10.1016/j.memsci.2007.06.051.
[121] Scharfer P, Schabel W, Kind M. Modelling of alcohol and water diffusion in fuel cell membranes—Experimental validation by means of

in situ Raman spectroscopy. Chem Eng Sci 2008;63:4676–84. https://doi.org/10.1016/j.ces.2008.03.014.
[122] Liu P, Yang D, Li B, Zhang C, Ming P. Recent progress of catalyst ink for roll-to-roll manufacturing paired with slot die coating for proton exchange membrane fuel cells. Int J Hydrog Energy 2023;48:19666–85. https://doi.org/10.1016/j.ijhydene.2023.02.022.
[123] Prasanna M, Ha HY, Cho EA, Hong S-A, Oh I-H. Investigation of oxygen gain in polymer electrolyte membrane fuel cells. J Power Sources 2004;137:1–8. https://doi.org/10.1016/j.jpowsour.2004.05.034.
[124] Frey Th, Linardi M. Effects of membrane electrode assembly preparation on the polymer electrolyte membrane fuel cell performance. Electrochimica Acta 2004;50:99–105. https://doi.org/10.1016/j.electacta.2004.07.017.
[125] Kim K-H, Lee K-Y, Kim H-J, Cho E, Lee S-Y, Lim T-H, et al. The effects of Nafion® ionomer content in PEMFC MEAs prepared by a catalyst-coated membrane (CCM) spraying method. Int J Hydrog Energy 2010;35:2119–26. https://doi.org/10.1016/j.ijhydene.2009.11.058.
[126] Umap VM, Ugwekar RP. Performance of Catalyst Coated Membrane (CCM) at different operating conditions in Proton Exchange Membrane (PEM) fuel cell. IOP Conf Ser Mater Sci Eng 2019;561:012016. https://doi.org/10.1088/1757-899X/561/1/012016.
[127] Song S, Zhang H, Ma X, Shao Z-G, Zhang Y, Yi B. Bifunctional oxygen electrode with corrosion-resistive gas diffusion layer for unitized regenerative fuel cell. Electrochem Commun 2006;8:399–405. https://doi.org/10.1016/j.elecom.2006.01.001.
[128] Su H, Bladergroen BJ, Linkov V, Pasupathi S, Ji S. Study of catalyst sprayed membrane under irradiation method to prepare high performance membrane electrode assemblies for solid polymer electrolyte water electrolysis. Int J Hydrog Energy 2011;36:15081–8. https://doi.org/10.1016/j.ijhydene.2011.08.057.
[129] Su H, Linkov V, Bladergroen BJ. Membrane electrode assemblies with low noble metal loadings for hydrogen production from solid polymer electrolyte water electrolysis. Int J Hydrog Energy 2013;38:9601–8. https://doi.org/10.1016/j.ijhydene.2013.05.099.
[130] Mauger SA, Neyerlin KC, Alia SM, Ngo C, Babu SK, Hurst KE, et al. Fuel Cell Performance Implications of Membrane Electrode Assembly

Fabrication with Platinum-Nickel Nanowire Catalysts. J Electrochem Soc 2018;165:F238–45. https://doi.org/10.1149/2.1061803jes.

[131] Therdthianwong A, Ekdharmasuit P, Therdthianwong S. Fabrication and Performance of Membrane Electrode Assembly Prepared by a Catalyst-Coated Membrane Method: Effect of Solvents Used in a Catalyst Ink Mixture. Energy Fuels 2010;24:1191–6. https://doi.org/10.1021/ef901105k.

[132] Wang W, Chen S, Li J, Wang W. Fabrication of catalyst coated membrane with screen printing method in a proton exchange membrane fuel cell. Int J Hydrog Energy 2015;40:4649–58. https://doi.org/10.1016/j.ijhydene.2015.02.027.

[133] Willert A, Zeiner C, Zubkova T, Zichner R. Inkjet printing processes as an innovative manufacturing method for the production of catalytically coated membranes (CCM) for fuel cells as well as electrolyzers. Chemnitz. Brennst. Saubere Antriebe Effizient Produziert, Chemnitz, Germany: 2022.

[134] Mauger S, Ulsh M. Material-Process-Performance Relationships in PEM Catalyst Inks and Coated Layers. National Renewable Energy Laboratory; 2019.

[135] Schmitt M, Baunach M, Wengeler L, Peters K, Junges P, Scharfer P, et al. Slot-die processing of lithium-ion battery electrodes—Coating window characterization. Chem Eng Process Process Intensif 2013;68:32–7. https://doi.org/10.1016/j.cep.2012.10.011.

[136] Spiegel S, Hoffmann A, Klemens J, Scharfer P, Schabel W. High-speed slot-die coating of primer layers for Li-ion battery electrodes: model calculations and experimental validation of the extended coating window depending on coating speed, coating gap and viscosity. J Coat Technol Res 2024;21:493–505. https://doi.org/10.1007/s11998-023-00877-1.

[137] Benkreira H, Cohu O. Direct forward gravure coating on unsupported web. Chem Eng Sci 1998;53:1223–31. https://doi.org/10.1016/S0009-2509(97)00446-6.

[138] Shi S, Weber AZ, Kusoglu A. Structure/property relationship of Nafion XL composite membranes. J Membr Sci 2016;516:123–34. https://doi.org/10.1016/j.memsci.2016.06.004.

[139] Ahmad S, Nawaz T, Ali A, Orhan MF, Samreen A, Kannan AM. An overview of proton exchange membranes for fuel cells: Materials and

manufacturing. Int J Hydrog Energy 2022;47:19086–131. https://doi.org/10.1016/j.ijhydene.2022.04.099.
[140] Liu L, Li H, Avgouropoulos G. A review of porous polytetrafluoroethylene reinforced sulfonic acid-based proton exchange membranes for fuel cells. Int J Hydrog Energy 2024;50:501–27. https://doi.org/10.1016/j.ijhydene.2023.08.270.
[141] Kolde JA. Advanced Composite Polymer Electrolyte Fuel Cell Membranes. ECS Proc Vol 1995;1995–23:193–201. https://doi.org/10.1149/199523.0193PV.
[142] Zhu X-B, Zhang H-M, Liang Y-M, Zhang Y, Yi B-L. A Novel PTFE-Reinforced Multilayer Self-Humidifying Composite Membrane for PEM Fuel Cells. Electrochem Solid-State Lett 2006;9:A49–52. https://doi.org/10.1149/1.2142154.
[143] Gao J, Dong X, Tian Q, He Y. Carbon nanotubes reinforced proton exchange membranes in fuel cells: An overview. Int J Hydrog Energy 2023;48:3216–31. https://doi.org/10.1016/j.ijhydene.2022.10.173.
[144] Hsu C. An innovative process for PEMFC electrodes using the expansion of Nafion film. J Power Sources 2003;115:268–73. https://doi.org/10.1016/S0378-7753(03)00005-3.
[145] Akella SH, D. E, R. S. SS, Ahire A, Mal NK. Studies on structure property relations of efficient decal substrates for industrial grade membrane electrode assembly development in pemfc. Sci Rep 2018;8:12082. https://doi.org/10.1038/s41598-018-30215-0.
[146] Doo G, Lee JH, Yuk S, Choi S, Lee D-H, Lee DW, et al. Tuning the Ionomer Distribution in the Fuel Cell Catalyst Layer with Scaling the Ionomer Aggregate Size in Dispersion. ACS Appl Mater Interfaces 2018;10:17835–41. https://doi.org/10.1021/acsami.8b01751.
[147] Talukdar K, Ripan MA, Jahnke T, Gazdzicki P, Morawietz T, Friedrich KA. Experimental and numerical study on catalyst layer of polymer electrolyte membrane fuel cell prepared with diverse drying methods. J Power Sources 2020;461:228169. https://doi.org/10.1016/j.jpowsour.2020.228169.
[148] Talukdar K, Delgado S, Lagarteira T, Gazdzicki P, Friedrich KA. Minimizing mass-transport loss in proton exchange membrane fuel cell by freeze-drying of cathode catalyst layers. J Power Sources 2019;427:309–17. https://doi.org/10.1016/j.jpowsour.2019.04.094.
[149] Koga M, Matsumoto H, Tokita M, Masunaga H, Hikima T, Sugimori H, et al. Investigation of Drying Process of Catalyst Ink for Polymer

Electrolyte Fuel Cells by Grazing-Incidence X-Ray Scattering. ECS Trans 2018;86:157–61. https://doi.org/10.1149/08613.0157ecst.

[150] Santangelo PE, Romagnoli M, Puglia M. An experimental approach to evaluate drying kinetics and foam formation in inks for inkjet printing of fuel-cell layers. Exp Therm Fluid Sci 2022;135:110631. https://doi.org/10.1016/j.expthermflusci.2022.110631.

[151] Chen Z, Pan W, Yao D, Gao M, Gao Y, Chen X, et al. Crack evolution during the film drying process of fuel cell microporous layer ink. Colloids Surf Physicochem Eng Asp 2022;650:129283. https://doi.org/10.1016/j.colsurfa.2022.129283.

[152] Yang P, Huang J, Li J, Luo K, Zhang L, Fu Q, et al. Insights into the effect of drying temperature on catalyst layer structure and PEM water electrolysis performance. Int J Hydrog Energy 2024;52:170–6. https://doi.org/10.1016/j.ijhydene.2023.10.108.

[153] Manahan MP, Kim S, Kumbur EC, Mench MM. Effects of Surface Irregularities and Interfacial Cracks on Polymer Electrolyte Fuel Cell Performance. ECS Trans 2009;25:1745–54. https://doi.org/10.1149/1.3210730.

[154] Markötter H, Haußmann J, Alink R, Tötzke C, Arlt T, Klages M, et al. Influence of cracks in the microporous layer on the water distribution in a PEM fuel cell investigated by synchrotron radiography. Electrochem Commun 2013;34:22–4. https://doi.org/10.1016/j.elecom.2013.04.006.

[155] Schmittinger W, Vahidi A. A review of the main parameters influencing long-term performance and durability of PEM fuel cells. J Power Sources 2008;180:1–14. https://doi.org/10.1016/j.jpowsour.2008.01.070.

[156] Kundu S, Fowler MW, Simon LC, Grot S. Morphological features (defects) in fuel cell membrane electrode assemblies. J Power Sources 2006;157:650–6. https://doi.org/10.1016/j.jpowsour.2005.12.027.

[157] Ding G, Santare MH, Karlsson AM, Kusoglu A. Numerical evaluation of crack growth in polymer electrolyte fuel cell membranes based on plastically dissipated energy. J Power Sources 2016;316:114–23. https://doi.org/10.1016/j.jpowsour.2016.03.031.

[158] Singh Y, Khorasany RMH, Kim WHJ, Alavijeh AS, Kjeang E, Rajapakse RKND, et al. Ex situ characterization and modelling of fatigue crack propagation in catalyst coated membrane composites for

fuel cell applications. Int J Hydrog Energy 2019;44:12057–72. https://doi.org/10.1016/j.ijhydene.2019.03.108.
[159] Qin Y, Ma S, Chang Y, Liu Y, Yin Y, Zhang J, et al. Modeling the membrane/CL delamination with the existence of CL crack under RH cycling conditions of PEM fuel cell. Int J Hydrog Energy 2021;46:8722–35. https://doi.org/10.1016/j.ijhydene.2020.12.043.
[160] Ma S, Qin Y, Liu Y, Sun L, Guo Q, Yin Y. Delamination evolution of PEM fuel cell membrane/CL interface under asymmetric RH cycling and CL crack location. Appl Energy 2022;310:118551. https://doi.org/10.1016/j.apenergy.2022.118551.
[161] McIlroy D, Pauchard L. Evolution of the crack patterns in nanostructured films with subsequent wetting and drying cycles. Europhys Lett 2024;147:56002. https://doi.org/10.1209/0295-5075/ad6478.
[162] Arcot MP, Cronin M, Fowler M, Pritzker M. Morphological Characteristics of Catalyst Layer Defects in Catalyst-Coated Membranes in PEM Fuel Cells. Electrochem 2023;4:1–20. https://doi.org/10.3390/electrochem4010001.
[163] Weber AZ. Gas-Crossover and Membrane-Pinhole Effects in Polymer-Electrolyte Fuel Cells. J Electrochem Soc 2008;155:521. https://doi.org/10.1149/1.2898130.
[164] Halter J, Marone F, Schmidt TJ, Büchi FN. Breaking through the Cracks: On the Mechanism of Phosphoric Acid Migration in High Temperature Polymer Electrolyte Fuel Cells. J Electrochem Soc 2018;165:1176–83. https://doi.org/10.1149/2.0501814jes.
[165] N. Bevilacqua, M.G. George, S. Galbiati, A. Bazylak, R. Zeis. Phosphoric Acid Invasion in High Temperature PEM Fuel Cell Gas Diffusion Layers. Electrochimica Acta 2017;257:89–98. https://doi.org/10.1016/j.electacta.2017.10.054.
[166] Phillips A, Ulsh M, Neyerlin KC, Porter J, Bender G. Impacts of electrode coating irregularities on polymer electrolyte membrane fuel cell lifetime using quasi in-situ infrared thermography and accelerated stress testing. Int J Hydrog Energy 2018;43:6390–9. https://doi.org/10.1016/j.ijhydene.2018.02.050.
[167] Xu W, Scott K. The effects of ionomer content on PEM water electrolyser membrane electrode assembly performance. Int J Hydrog

Energy 2010;35:12029–37. https://doi.org/10.1016/j.ijhydene.2010.08.055.
[168] Huang D-C, Yu P-J, Liu F-J, Huang S-L, Hsueh K-L, Chen Y-C, et al. Effect of dispersion solvent in catalyst ink on proton exchange membrane fuel cell performance. Int J Electrochem Sci 2011;6:2551–65.
[169] Chiu RC, Garino TJ, Cima MJ. Drying of Granular Ceramic Films: I, Effect of Processing Variables on Cracking Behavior. J Am Ceram Soc 1993;76:2257–64. https://doi.org/10.1111/j.1151-2916.1993.tb07762.x.
[170] Kanai T, Sawada T. New Route to Produce Dry Colloidal Crystals without Cracks. Langmuir 2009;25:13315–7. https://doi.org/10.1021/la9033854.
[171] Mende G. Das Einfangen von Mahlgutpartikeln durch Mahlkugeln. 1st ed. Göttingen: Cuvillier Verlag; 2006.
[172] Kwade A. Determination of the most important grinding mechanism in stirred media mills by calculating stress intensity and stress number. Powder Technol 1999;105:382–8. https://doi.org/10.1016/S0032-5910(99)00162-X.
[173] Kwade A. Autogenzerkleinerung von Kalkstein in Rührwerkmühlen. Als Ms. gedr. Aachen, Germany: Shaker; 1997.
[174] Jankovic A. Variables affecting the fine grinding of minerals using stirred mills. Miner Eng 2003;16:337–45. https://doi.org/10.1016/S0892-6875(03)00007-4.
[175] Shin H, Lee S, Suk Jung H, Kim J-B. Effect of ball size and powder loading on the milling efficiency of a laboratory-scale wet ball mill. Ceram Int 2013;39:8963–8. https://doi.org/10.1016/j.ceramint.2013.04.093.
[176] Kwade A, Schwedes J. Breaking characteristics of different materials and their effect on stress intensity and stress number in stirred media mills. Powder Technol 2002;122:109–21. https://doi.org/10.1016/S0032-5910(01)00406-5.
[177] Hertaeg MJ, Tabor RF, Routh AF, Garnier G. Pattern formation in drying blood drops. Philos Trans R Soc Math Phys Eng Sci 2021;379:20200391. https://doi.org/10.1098/rsta.2020.0391.
[178] Giorgiutti-Dauphiné F, Pauchard L. Painting cracks: A way to investigate the pictorial matter. J Appl Phys 2016;120:065107. https://doi.org/10.1063/1.4960438.

[179] Goehring L, Conroy R, Akhter A, Clegg WJ, Routh AF. Evolution of mud-crack patterns during repeated drying cycles. Soft Matter 2010;6:3562. https://doi.org/10.1039/b922206e.
[180] Zimmerer N, Quarz P, Janning L, Scharfer P, Schabel W. In-situ investigation of crack formation during drying of catalyst layers for polymer electrolyte membrane (PEM) fuel cells and electrolyzer. Colloids Surf Physicochem Eng Asp 2026;728:138807. https://doi.org/10.1016/j.colsurfa.2025.138807.
[181] Scherer GW. Theory of Drying. J Am Ceram Soc 1990;73:3–14. https://doi.org/10.1111/j.1151-2916.1990.tb05082.x.
[182] Singh KB, Tirumkudulu MS. Cracking in drying colloidal films. Phys Rev Lett 2007;98:218302. https://doi.org/10.1103/PhysRevLett.98.218302.
[183] Yamamura M, Ono H, Uchinomiya T, Mawatari Y, Kage H. Multiple crack nucleation in drying nanoparticle-polymer coatings. Colloids Surf Physicochem Eng Asp 2009;342:65–9. https://doi.org/10.1016/j.colsurfa.2009.04.008.
[184] Griffith AA. VI. The phenomena of rupture and flow in solids. Philos Trans R Soc Lond Ser Contain Pap Math Phys Character 1921;221:163–98. https://doi.org/10.1098/rsta.1921.0006.
[185] Tirumkudulu MS, Russel WB. Cracking in drying latex films. Langmuir ACS J Surf Colloids 2005;21:4938–48. https://doi.org/10.1021/la048298k.
[186] Singh KB, Deoghare G, Tirumkudulu MS. Cracking in soft-hard latex blends: theory and experiments. Langmuir ACS J Surf Colloids 2009;25:751–60. https://doi.org/10.1021/la802857q.
[187] Wu Y, Francis LF. Effect of particle size distribution on stress development and microstructure of particulate coatings. J Coat Technol Res 2017;14:455–65. https://doi.org/10.1007/s11998-016-9866-5.
[188] Singh KB, Bhosale LR, Tirumkudulu MS. Cracking in Drying Colloidal Films of Flocculated Dispersions. Langmuir 2009;25:4284–7. https://doi.org/10.1021/la804331c.
[189] Gnielinski V, Mersmann A, Thurner F. Verdampfung, Kristallisation, Trocknung mit 30 Übungsbeispielen. Braunschweig, Germany: Vieweg; 1993.
[190] Quarz P, Zimmerer N, Scharfer P, Schabel W. About drying phenomena of fuel cell and electrolyzer CCM inks: selectivity of the evaporation of

1-propanol/water mixtures. Wiley Fuel Cells 2024;24:108–21. https://doi.org/10.1002/fuce.202300252.
[191] Routh AF. Drying of thin colloidal films. Rep Prog Phys 2013;76:046603. https://doi.org/10.1088/0034-4885/76/4/046603.
[192] Jang LK, Chang Y. Prediction of Vapor-Liquid Equilibrium for a Non-Ideal Binary Mixture Based on the Azeotropic Condition 2017;2017.
[193] Stephan P, Kabelac S, Kind M, Mewes D, Schaber K, Wetzel T. VDI-Wärmeatlas. Berlin, Heidelberg, Germany: Springer Berlin Heidelberg; 2019. https://doi.org/10.1007/978-3-662-52989-8.
[194] Wade J, Merriman RW. CIV.—Influence of water on the boiling point of ethyl alcohol at pressures above and below the atmospheric pressure. J Chem Soc Trans 1911;99:997–1011.
[195] Sundmacher K, Qi Z, Huang Y, Schlünder E-U. Thermodynamic and Kinetic Effects on the Feasible Products of Reactive Distillation: A-zeotropes and A-rheo-tropes. In: Sundmacher K, Kienle A, Seidel-Morgenstern A, editors. Integr. Chem. Process. 1st ed., Weinheim, Germany: Wiley; 2005, p. 85–148. https://doi.org/10.1002/3527605738.ch4.
[196] Riede T, Schlünder E-U. Selective evaporation of a binary mixture into dry or humidified air. Chem Eng Process 1990;27:83–93. https://doi.org/10.1016/0255-2701(90)85012-S.
[197] Schlünder E-U. Selective Drying 2013.
[198] Huang Y-S, Schlünder E-U, Sundmacher K. Feasibility analysis of membrane reactors – discovery of reactive arheotropes. Catal Today 2005;104:360–71. https://doi.org/10.1016/j.cattod.2005.03.076.
[199] Schlünder E-U. Über der Einfluss der Stoffübertragung auf die Selektivität der thermischen Trennverfahren - dargestellt am Beispiel der Schleppmitteldestillation. VERFAHR-TECH 1977;11:682–6.
[200] Thurner F, Schlünder E-U. Wet-bulb temperature of binary mixtures. Chem Eng Process 1985;19:337–43. https://doi.org/10.1016/0255-2701(85)85006-6.
[201] Thurner F, Schlünder E-U. Progress towards understanding the drying of porous materials wetted with binary mixtures. Chem Eng Process 1986;20:33–41. https://doi.org/10.1016/0255-2701(86)85004-8.
[202] Schlünder E-U. Einführung in die Stoffübertragung. [2. Aufl.]. Braunschweig, Germany: Vieweg; 1996.
[203] Schlünder E. Selektives Trocknen gemischhaltiger Produkte. Chem Ing Tech 1987;59:823–33. https://doi.org/10.1002/cite.330591103.

[204] Riede Th, Schlünder E-U. Selective evaporation of a ternary mixture containing one nonvolatile component with regard to drying processes. Chem Eng Process Process Intensif 1990;28:151–63. https://doi.org/10.1016/0255-2701(90)80016-X.
[205] Riede T, Schlünder E-U. Selective through-drying in fixed beds. Chem Eng Process Process Intensif 1991;29:9–26. https://doi.org/10.1016/0255-2701(91)87002-K.
[206] Knebel T, Schlünder E-U. Retention of volatiles in contact drying combined with membrane separation. Chem Eng Process Process Intensif 1995;34:219–27. https://doi.org/10.1016/0255-2701(94)04007-9.
[207] Steinbeck MJ, Schlünder E-U. Convective drying of porous material containing a partially miscible mixture. Chem Eng Process Process Intensif 1998;37:79–88. https://doi.org/10.1016/S0255-2701(97)00039-1.
[208] Schabel W. In memory of Professor Ernst-Ulrich Schlünder: An outstanding scientist in drying technology. Dry Technol 2022;40:1027–8. https://doi.org/10.1080/07373937.2022.2043642.
[209] European Commission - Press release. Commission restricts use of a sub-group of PFAS chemicals to protect human health and the environment. Brussels, Belgium: 2024.
[210] EPA United States Environmental Protection Agency. EPA's PFAS Strategic Roadmap: Three Years of Progress 2024.
[211] California Legislative Information. AB-1817 Product safety: textile articles: perfluoroalkyl and polyfluoroalkyl substances (PFAS). 2022.
[212] Mauritz, KA, Moore, RB. State of understanding of Nafion. Chem. Rev. 2004, 104, 10, 4535–4586. https://doi.org/10.1021/cr0207123.
[213] Fuller EN, Ensley K, Giddings JC. Diffusion of halogenated hydrocarbons in helium. The effect of structure on collision cross sections. J Phys Chem 1969;73:3679–85. https://doi.org/10.1021/j100845a020.
[214] Stagg BJ, Charalampopoulos TT. Refractive indices of pyrolytic graphite, amorphous carbon, and flame soot in the temperature range 25° to 600°C. Combust Flame 1993;94:381–96. https://doi.org/10.1016/0010-2180(93)90121-I.
[215] Klemens J, Schneider L, Burger D, Zimmerer N, Müller M, Bauer W, et al. Process and Drying Behavior Toward Higher Drying Rates of Hard Carbon Anodes for Sodium-Ion Batteries with Different Particle Sizes: An Experimental Study in Comparison to Graphite for Lithium-Ion-

Batteries. Energy Technol 2023;11. https://doi.org/10.1002/ente.202300338.

[216] Klemens J, Schneider L, Herbst EC, Bohn N, Müller M, Bauer W, et al. Drying of NCM Cathode Electrodes with Porous, Nanostructured Particles Versus Compact Solid Particles: Comparative Study of Binder Migration as a Function of Drying Conditions. Energy Technol 2022;10:2100985. https://doi.org/10.1002/ente.202100985.

[217] Kumberg J, Bauer W, Schmatz J, Diehm R, Tönsmann M, Müller M, et al. Reduced Drying Time of Anodes for Lithium-Ion Batteries through Simultaneous Multilayer Coating. Energy Technol 2021;9:2100367. https://doi.org/10.1002/ente.202100367.

[218] Kumberg J, Baunach M, Eser JC, Altvater A, Scharfer P, Schabel W. Investigation of Drying Curves of Lithium-Ion Battery Electrodes with a New Gravimetrical Double-Side Batch Dryer Concept Including Setup Characterization and Model Simulations. Energy Technol 2021;9:2000889. https://doi.org/10.1002/ente.202000889.

[219] Kumberg J, Müller M, Diehm R, Spiegel S, Wachsmann C, Bauer W, et al. Drying of Lithium-Ion Battery Anodes for Use in High-Energy Cells: Influence of Electrode Thickness on Drying Time, Adhesion, and Crack Formation. Energy Technol 2019;7:1900722. https://doi.org/10.1002/ente.201900722.

[220] Jaiser S, Friske A, Baunach M, Scharfer P, Schabel W. Development of a three-stage drying profile based on characteristic drying stages for lithium-ion battery anodes. Dry Technol 2017;35:1266–75. https://doi.org/10.1080/07373937.2016.1248975.

[221] Jaiser S, Sanchez Salach N, Baunach M, Scharfer P, Schabel W. Impact of drying conditions and wet film properties on adhesion and film solidification of lithium-ion battery anodes. Dry Technol 2017;35:1807–17. https://doi.org/10.1080/07373937.2016.1276584.

[222] Jaiser S, Müller M, Baunach M, Bauer W, Scharfer P, Schabel W. Investigation of film solidification and binder migration during drying of Li-Ion battery anodes. J Power Sources 2016;318:210–9. https://doi.org/10.1016/j.jpowsour.2016.04.018.

[223] Jaiser S, Funk L, Baunach M, Scharfer P, Schabel W. Experimental investigation into battery electrode surfaces: The distribution of liquid at the surface and the emptying of pores during drying. J Colloid

Interface Sci 2017;494:22–31. https://doi.org/10.1016/j.jcis.2017.01.063.
[224] Baunach M, Jaiser S, Schmelzle S, Nirschl H, Scharfer P, Schabel W. Delamination behavior of lithium-ion battery anodes: Influence of drying temperature during electrode processing. Dry Technol 2016;34:462–73. https://doi.org/10.1080/07373937.2015.1060497.
[225] Baunach M, Jaiser S, Cavadini P, Scharfer P, Schabel W. Local heat transfer characteristics of a slot nozzle array for batch drying of thin films under industrial process conditions. J Coat Technol Res 2015;12:915–20. https://doi.org/10.1007/s11998-015-9712-1.
[226] Schneider L, Klemens J, Herbst EC, Müller M, Scharfer P, Schabel W, et al. Transport Properties in Electrodes for Lithium-Ion Batteries: Comparison of Compact versus Porous NCM Particles. J Electrochem Soc 2022;169:100553. https://doi.org/10.1149/1945-7111/ac9c37.
[227] Klemens J, Burger D, Schneider L, Spiegel S, Müller M, Bohn N, et al. Drying of Compact and Porous NCM Cathode Electrodes in Different Multilayer Architectures: Influence of Layer Configuration and Drying Rate on Electrode Properties. Energy Technol 2023;11. https://doi.org/10.1002/ente.202300267.
[228] Altvater A, Heckmann T, Eser JC, Spiegel S, Scharfer P, Schabel W. (Near-) Infrared Drying of Lithium-Ion Battery Electrodes: Influence of Energy Input on Process Speed and Electrode Adhesion. Energy Technol 2022:2200785. https://doi.org/10.1002/ente.202200785.
[229] Bardow A, Marquardt W, Göke V, Koss H, Lucas K. Model-based measurement of diffusion using Raman spectroscopy. AIChE J 2003;49:323–34. https://doi.org/10.1002/aic.690490205.
[230] Bardow A, Göke V, Koß H-J, Lucas K, Marquardt W. Concentration-dependent diffusion coefficients from a single experiment using model-based Raman spectroscopy. Fluid Phase Equilibria 2005;228–229:357–66. https://doi.org/10.1016/j.fluid.2004.08.017.
[231] Schabel W. Trocknung von Polymerfilmen Messung von Konzentrationsprofilen mit der Inversen-Mikro-Raman-Spektroskopie. Karlsruher Institut für Technologie (KIT), 2004.

[232] Siebel D, Schabel W, Scharfer P. Diffusion in quaternary polymer solutions—Model development and validation. Prog Org Coat 2017;110:187–94. https://doi.org/10.1016/j.porgcoat.2017.05.002.
[233] Raupp SM, Siebel DK, Kitz PG, Scharfer P, Schabel W. Interdiffusion in Polymeric Multilayer Systems Studied by Inverse Micro-Raman Spectroscopy. Macromolecules 2017;50:6819–28. https://doi.org/10.1021/acs.macromol.7b01037.
[234] Merklein L, Eser JC, Börnhorst T, Könnecke N, Scharfer P, Schabel W. Different dominating mass transport mechanisms for drying and sorption of toluene-PMMA films – Visualized with Raman spectroscopy. Polymer 2021;222:123640. https://doi.org/10.1016/j.polymer.2021.123640.
[235] Schmidt-Hansberg B, Baunach M, Krenn J, Walheim S, Lemmer U, Scharfer P, et al. Spatially resolved drying kinetics of multi-component solution cast films for organic electronics. Chem Eng Process Process Intensif 2011;50:509–15. https://doi.org/10.1016/j.cep.2010.12.012.
[236] Schabel W. Inverse Mikro-Raman-Spektroskopie - Eine neue Messmethode zur Untersuchung lokaler Stofftransportvorgänge in dünnen Filmen, Folien und Membranen. Chem Ing Tech 2005;77:1915–26. https://doi.org/10.1002/cite.200500060.
[237] Gracia-Medrano-Bravo V, Merklein L, Oberle N, Batora M, Scharfer P, Schabel W. Determination of Binary Interaction Parameters for Ternary Polymer–Polymer–Solvent Systems Using Raman Spectroscopy. Adv Mater Technol 2021;6:2000149. https://doi.org/10.1002/admt.202000149.
[238] De Paepe ATG, Dyke JM, Hendra PJ, Langkilde FW. The use of reference materials in quantitative analyses based on FT-Raman spectroscopy. Spectrochim Acta A Mol Biomol Spectrosc 1997;53:2267–73. https://doi.org/10.1016/S1386-1425(97)00166-2.
[239] Sato-Berrú RY, Medina-Valtierra J, Medina-Gutiérrez C, Frausto-Reyes C. Quantitative NIR Raman analysis in liquid mixtures. Spectrochim Acta A Mol Biomol Spectrosc 2004;60:2225–9. https://doi.org/10.1016/j.saa.2003.11.020.
[240] Berg RW, Hansen SB, Shapiro AA, Stenby EH. Diffusion measurements in binary liquid mixtures by Raman spectroscopy. Applied spectroscopy 2007;61:367–73.

[241] Numata Y, Iida Y, Tanaka H. Quantitative analysis of alcohol–water binary solutions using Raman spectroscopy. J Quant Spectrosc Radiat Transf 2011;112:1043–9. https://doi.org/10.1016/j.jqsrt.2011.01.005.
[242] Baesch S, Scharfer P, Schabel W, Francis L. Influence of the drying conditions on the particle distribution in particle-filled polymer films: Predictive simulation of the particle distribution during drying. J Compos Mater 2017;51:3391–403. https://doi.org/10.1177/0021998316687144.
[243] Zheng Z, Bi Y, Zhao X, Wang J, Nie J. Effects of drying conditions on the solvent diffusion process during coated fabrics curing. Dry Technol 2022;40:1845–55. https://doi.org/10.1080/07373937.2021.1884568.
[244] Schabel W, Scharfer P, Müller M, Ludwig I, Kind M. Messung und Simulation von Konzentrationsprofilen bei der Trocknung binärer Polymerlösungen. Chem Ing Tech 2003;75:1336–44. https://doi.org/10.1002/cite.200300055.
[245] Raupp SM, Kitz PG, Siebel DK, Wunsch A, Merklein L, Scharfer P, et al. Modeling of interdiffusion in poly(vinyl acetate)–poly(methyl methacrylate)–toluene multicomponent systems. J Appl Polym Sci 2019;136:47092. https://doi.org/10.1002/app.47092.
[246] Schabel W, Ludwig I, Kind M. Measurements of Concentration Profiles in Polymeric Solvent Coatings by Means of an Inverse Confocal Micro Raman Spectrometer—Initial Results. Dry Technol 2004;22:285–94. https://doi.org/10.1081/DRT-120028234.
[247] Schabel W, Scharfer P, Kind M, Mamaliga I. Sorption and diffusion measurements in ternary polymer–solvent–solvent systems by means of a magnetic suspension balance—Experimental methods and correlations with a modified Flory–Huggins and free-volume theory. Chem Eng Sci 2007;62:2254–66. https://doi.org/10.1016/j.ces.2006.12.062.
[248] Krenn J, Scharfer P, Kind M, Schabel W. Drying of solvent-borne coatings with pre-loaded drying gas: Diffusion controlled skinning – solvent-solvent-interaction. Eur Phys J Spec Top 2009;166:45–8. https://doi.org/10.1140/epjst/e2009-00876-0.
[249] Müller M, Scharfer P, Kind M, Schabel W. Determination of Diffusion Coefficients of Non-volatile Additives in Polymeric Coatings by Means of Inverse Micro Raman Spectroscopy. Chem Ing Tech 2010;82:2097–102. https://doi.org/10.1002/cite.201000085.
[250] Nijdam J, Trouillet V, Kachel S, Scharfer P, Schabel W, Kind M. Coat formation of surface-active proteins on aqueous surfaces during drying.

Colloids Surf B Biointerfaces 2014;123:53–60. https://doi.org/10.1016/j.colsurfb.2014.07.050.

[251] Siebel D, Scharfer P, Schabel W. Determination of Concentration-Dependent Diffusion Coefficients in Polymer–Solvent Systems: Analysis of Concentration Profiles Measured by Raman Spectroscopy during Single Drying Experiments Excluding Boundary Conditions and Phase Equilibrium. Macromolecules 2015;48:8608–14. https://doi.org/10.1021/acs.macromol.5b02144.

[252] Nijdam J, Kachel S, Scharfer P, Schabel W, Kind M. Effect of Diffusion on Component Segregation During Drying of Aqueous Solutions Containing Protein and Sugar. Dry Technol 2015;33:288–300. https://doi.org/10.1080/07373937.2014.948962.

[253] Siebel D, Scharfer P, Schabel W. Prediction of diffusion in a ternary solvent–solvent–polymer blend by means of binary diffusion data: Comparison of experimental data and simulative results. J Appl Polym Sci 2016;133:app.43899. https://doi.org/10.1002/app.43899.

[254] Baesch S, Siebel D, Schmidt-Hansberg B, Eichholz C, Gerst M, Scharfer P, et al. Comparison of Surfactant Distributions in Pressure-Sensitive Adhesive Films Dried from Dispersion under Lab-Scale and Industrial Drying Conditions. ACS Appl Mater Interfaces 2016;8:8118–28. https://doi.org/10.1021/acsami.6b00830.

[255] Kachel S, Scharfer P, Schabel W. Measurements and predictive modeling of water diffusion coefficients in bovine serum albumin/polymer blends for biosensors. J Appl Polym Sci 2017;134:45368. https://doi.org/10.1002/app.45368.

[256] Gracia-Medrano-Bravo VC-A, Gröne J, Baesch S, Scharfer P, Schabel W. Influence of Particle Shape on the Drying Regime Maps for Platelike Particle-Polymer Composites. Langmuir 2020;36:6245–53. https://doi.org/10.1021/acs.langmuir.0c00942.

[257] Hamilton P, Littlejohn D, Nordon A, Sefcik J, Slavin P, Dallin P, et al. Studies of particle drying using non-invasive Raman spectrometry and particle size analysis. The Analyst 2011;136:2168. https://doi.org/10.1039/c0an00893a.

[258] Arya RK, Vinjamur M. Measurement of concentration profiles using confocal Raman spectroscopy in multicomponent polymeric coatings—model validation. J Appl Polym Sci 2013;128:3906–18. https://doi.org/10.1002/app.38589.

[259] Arya RK. Measurement of Concentration Profiles in Thin Film Binary Polymer-Solvent Coatings Using Confocal Raman Spectroscopy: Free

Volume Model Validation. Dry Technol 2014;32:992–1002. https://doi.org/10.1080/07373937.2014.880714.
[260] Sharma J, Arya RK, Ahuja S, Bhargava CK. Residual solvent study in polymer − polymer — solvent coatings: Poly(styrene) — poly(methyl methacrylate) — tetrahydrofuran coatings. Prog Org Coat 2017;113:200–6. https://doi.org/10.1016/j.porgcoat.2017.09.010.
[261] Lödige L, Heckmann T, Scharfer P, Schabel W. Thermal Drying in the Recycling Process of Lithium-Ion Batteries—Kinetics and Selectivity Aspects for the Evaporation of Electrolyte–Solvent Mixtures. Batteries 2025;11:436. https://doi.org/10.3390/batteries11120436.
[262] Quarz P, Zimmerer N, Janning L, Steck A-M, Scharfer P, Schabel W. Ink Processing and its Influence on Particle Size Distribution, Ionomer Requirements and Electrode Properties in Polymer Electrolyte Membrane Fuel Cell and Electrolyzer Catalyst Coated Membranes. Energy Technol 2025:e202501844. https://doi.org/10.1002/ente.202501844.
[263] Quarz P, Zimmerer N, Steck A-M, Scharfer P, Schabel W. Carbon Nanotubes (CNT) as an additive towards crack-free catalyst coated membranes (CCM). Int J Hydrog Energy 2024;57:789–97. https://doi.org/10.1016/j.ijhydene.2024.01.049.
[264] Löffler F, Raasch J. Grundlagen der mechanischen Verfahrenstechnik. Braunschweig Wiesbaden: Vieweg; 1992.
[265] Andersen SM, Borghei M, Dhiman R, Ruiz V, Kauppinen E, Skou E. Adsorption Behavior of Perfluorinated Sulfonic Acid Ionomer on Highly Graphitized Carbon Nanofibers and Their Thermal Stabilities. J Phys Chem C 2014;118:10814–23. https://doi.org/10.1021/jp501088d.
[266] Rumpf H. Über die Eigenschaften von Nutzstauben 1967;27:3–13.
[267] Polke R. Qualitätssicherung in der Feststoffverfahrenstechnik. Chem Ing Tech 1990;62:813–21. https://doi.org/10.1002/cite.330621008.
[268] Borho K, Polke R, Wintermantel K, Schubert H, Sommer K. Produkteigenschaften und Verfahrenstechnik. Chem Ing Tech 1991;63:792–808. https://doi.org/10.1002/cite.330630805.
[269] Krekel J, Polke R. Qualitätssicherung bei der Verfahrensentwicklung. Chem Ing Tech 1992;64:528–35. https://doi.org/10.1002/cite.330640609.
[270] Schuchmann HP, Danner T. Emulgieren: Mehr als nur Zerkleinern. Chem Ing Tech 2004;76:364–75. https://doi.org/10.1002/cite.200406163.

[271] Quarz P, Janning L, Zimmerer N, Scharfer P, Schabel W. Selective evaporation of solvent mixtures in thin films for fuel cell and electrolyser catalyst coatings. Dry. Technol., 44(3), 346–355. https://doi.org/10.1080/07373937.2026.2616748.

[272] Cavadini P, Weinhold H, Tönsmann M, Chilingaryan S, Kopmann A, Lewkowicz A, et al. Investigation of the flow structure in thin polymer films using 3D µPTV enhanced by GPU. Exp Fluids 2018;59:61. https://doi.org/10.1007/s00348-017-2482-z.

[273] Tönsmann M, Scharfer P, Schabel W. Transient Three-Dimensional Flow Field Measurements by Means of 3D µPTV in Drying Poly(Vinyl Acetate)-Methanol Thin Films Subject to Short-Scale Marangoni Instabilities. Polymers 2021;13:1223. https://doi.org/10.3390/polym13081223.

[274] Tönsmann M, Scharfer P, Schabel W. Critical Solutal Marangoni Number Correlation for Short-Scale Convective Instabilities in Drying Poly(vinyl acetate)-Methanol Thin Films. Polymers 2021;13:2955. https://doi.org/10.3390/polym13172955.

[275] Buss F, Göcke J, Scharfer P, Schabel W. From Micro to Nano Thin Polymer Layers: Thickness and Concentration Dependence of Sorption and the Solvent Diffusion Coefficient. Macromolecules 2015;48:8285–93. https://doi.org/10.1021/acs.macromol.5b01648.

[276] Börnhorst T, Scharfer P, Schabel W. Drying Kinetics from Micrometer- to Nanometer-Scale Polymer Films: A Study on Solvent Diffusion, Polymer Relaxation, and Substrate Interaction Effects. Langmuir 2021;37:6022–31. https://doi.org/10.1021/acs.langmuir.1c00641.

[277] Jaiser S, Kumberg J, Klaver J, Urai JL, Schabel W, Schmatz J, et al. Microstructure formation of lithium-ion battery electrodes during drying – An ex-situ study using cryogenic broad ion beam slope-cutting and scanning electron microscopy (Cryo-BIB-SEM). J Power Sources 2017;345:97–107. https://doi.org/10.1016/j.jpowsour.2017.01.117.

[278] Post S, Urukova I, Tsotsas E. Interfacial convection during evaporation of binary mixtures from porous obstacles. AIChE J 2005;51:3257–74. https://doi.org/10.1002/aic.10557.

[279] Zimmerer N, Quarz P, Terhorst E, Janning L, Scharfer P, Schabel W. Influence of Ink Formulation and Drying Parameters on Component Composition during Drying of Catalyst Layers for Polymer Electrolyte Membrane Fuel Cells and Electrolyzers. Energy Technol 2025:2500516. https://doi.org/10.1002/ente.202500516.

[280] Yamamura M. Drying paths of phase-separating solution coatings exposed to humidity. J Coat Technol Res 2022;19:15–23. https://doi.org/10.1007/s11998-021-00483-z.
[281] Scharfer P. Zum Stofftransport in Brennstoffzellenmembranen Untersuchungen mit Hilfe der konfokalen Mikro-Raman-Spektroskopie. Karlsruhe Institute of Technology (KIT), 2009.
[282] Fraunhofer-Institut für Produktionstechnik und Automatisierung IPA. Rolle zu Rolle Beschichtungsanlage - Schlitzdüsenbeschichtung im Technikumsmaßstab 2017.
[283] Kim SM, Ahn C-Y, Cho Y-H, Kim S, Hwang W, Jang S, et al. High-performance Fuel Cell with Stretched Catalyst-Coated Membrane: One-step Formation of Cracked Electrode. Sci Rep 2016;6:26503. https://doi.org/10.1038/srep26503.
[284] Kusoglu A. Chalkboard 1 - The Many Colors of Hydrogen. Electrochem Soc Interface 2021;30:44–8. https://doi.org/10.1149/2.F12214IF.
[285] Panić I, Cuculić A, Ćelić J. Color-Coded Hydrogen: Production and Storage in Maritime Sector. J Mar Sci Eng 2022;10:1995. https://doi.org/10.3390/jmse10121995.
[286] Jolaoso L, Zaman SF. Catalytic Ammonia Decomposition for Hydrogen Production: Utilization of Ammonia in a Fuel Cell. In: Inamuddin, Boddula R, Asiri AM, editors. Sustain. Ammon. Prod., Cham: Springer International Publishing; 2020, p. 81–105. https://doi.org/10.1007/978-3-030-35106-9_5.
[287] Carmo M, Fritz DL, Mergel J, Stolten D. A comprehensive review on PEM water electrolysis. Int J Hydrog Energy 2013;38:4901–34. https://doi.org/10.1016/j.ijhydene.2013.01.151.
[288] Böhm D, Beetz M, Schuster M, Peters K, Hufnagel AG, Döblinger M, et al. Efficient OER Catalyst with Low Ir Volume Density Obtained by Homogeneous Deposition of Iridium Oxide Nanoparticles on Macroporous Antimony-Doped Tin Oxide Support. Adv Funct Mater 2020;30:1906670. https://doi.org/10.1002/adfm.201906670.
[289] Wang S, Shang Y, Wang Y, Wang J. Fabrication and electrochemical performance of Poly (2,5-benzimidazole) (ABPBI)-based MEA by catalyst coated membrane (CCM) method for high-temperature polymer electrolyte fuel cells. Int J Hydrog Energy 2013;38:11060–6. https://doi.org/10.1016/j.ijhydene.2013.01.102.
[290] Morris DRP, Liu SP, Villegas Gonzalez D, Gostick JT. Effect of Water Sorption on the Electronic Conductivity of Porous Polymer Electrolyte

Membrane Fuel Cell Catalyst Layers. ACS Appl Mater Interfaces 2014;6:18609–18. https://doi.org/10.1021/am503509j.

[291] Wilson MS, Gottesfeld S. Thin-film catalyst layers for polymer electrolyte fuel cell electrodes. J Appl Electrochem 1992;22:1–7. https://doi.org/10.1007/BF01093004.

[292] Eccarius S, Garcia BL, Hebling C, Weidner JW. Experimental validation of a methanol crossover model in DMFC applications. J Power Sources 2008;179:723–33. https://doi.org/10.1016/j.jpowsour.2007.11.102.

[293] Cho HJ, Jang H, Lim S, Cho E, Lim T-H, Oh I-H, et al. Development of a novel decal transfer process for fabrication of high-performance and reliable membrane electrode assemblies for PEMFCs. Int J Hydrog Energy 2011;36:12465–73. https://doi.org/10.1016/j.ijhydene.2011.06.113.

[294] Jung C-Y, Kim W-J, Yi S-C. Optimization of catalyst ink composition for the preparation of a membrane electrode assembly in a proton exchange membrane fuel cell using the decal transfer. Int J Hydrog Energy 2012;37:18446–54. https://doi.org/10.1016/j.ijhydene.2012.09.013.

[295] Burdzik A, Stähler M, Friedrich I, Carmo M, Stolten D. Homogeneity analysis of square meter-sized electrodes for PEM electrolysis and PEM fuel cells. J Coat Technol Res 2018;15:1423–32. https://doi.org/10.1007/s11998-018-0074-3.

[296] Stähler A, Stähler M, Scheepers F, Carmo M, Stolten D. Reusability of decal substrates for the fabrication of catalyst coated membranes. Int J Adhes Adhes 2020;98:102473. https://doi.org/10.1016/j.ijadhadh.2019.102473.

[297] Suzuki T, Okada S, TSUSHIMA S. Analysis of Ionomer Distribution and Pt/C Agglomerate Size in Catalyst Layers by Two-Stage Ion-Beam Processing. J Electrochem Soc 2020;167:124513. https://doi.org/10.1149/1945-7111/abad6a.

[298] Mo S, Du L, Huang Z, Chen J, Zhou Y, Wu P, et al. Recent Advances on PEM Fuel Cells: From Key Materials to Membrane Electrode Assembly. Electrochem Energy Rev 2023;6:28. https://doi.org/10.1007/s41918-023-00190-w.

[299] Ney L, Hog J, Singh R, Göttlicher N, Schneider P, Tepner S, et al. Challenges of fabricating catalyst layers for PEM fuel cells using flatbed

screen printing. J Coat Technol Res 2023;20:73–86. https://doi.org/10.1007/s11998-022-00710-1.
[300] Liu P, Yang D, Li B, Kang J, Zhang C, Ming P, et al. Benzoic acid as additive: A route to inhibit the formation of cracks in catalyst layer of proton exchange membrane fuel cells. J Power Sources 2024;591:233817. https://doi.org/10.1016/j.jpowsour.2023.233817.
[301] Cellcentric. Conversation at the hy-fcell trade fair. Stuttgart, Germany: 2024.
[302] Audi. Conversation at the hy-fcell trade fair. Stuttgart, Germany: 2024.
[303] Laufenberg GmbH. Conversation at the hy-fcell trade fair. Stuttgart, Germany: 2024.
[304] Lim BH, Majlan EH, Tajuddin A, Husaini T, Wan Daud WR, Mohd Radzuan NA, et al. Comparison of catalyst-coated membranes and catalyst-coated substrate for PEMFC membrane electrode assembly: A review. Chin J Chem Eng 2021;33:1–16. https://doi.org/10.1016/j.cjche.2020.07.044.
[305] Kampker A, Heimes H, Kehrer M, Hagedorn S, Reims P, Kaul O. Fuel cell system production cost modeling and analysis. Energy Rep 2023;9:248–55. https://doi.org/10.1016/j.egyr.2022.10.364.
[306] Pak C, Jong D, Hwan K, Chang H. High Performance Membrane Electrode Assemblies by Optimization of Processes and Supported Catalysts. In: Minic D, editor. Hydrog. Energy - Chall. Perspect., InTech; 2012. https://doi.org/10.5772/53683.
[307] Shi J, Zhan Z, Di Zhang, Yu Y, Yang X, He L, et al. Effects of Cracks on the Mass Transfer of Polymer Electrolyte Membrane Fuel Cell with High Performance Membrane Electrode Assembly. J Wuhan Univ Technol-Mater Sci Ed 2021;36:318–30. https://doi.org/10.1007/s11595-021-2412-z.
[308] Rojas-Núñez C, Quarz P, Gracia-Medrano-Bravo VA, Kapp J, Käufer F, Sommer T, et al. Novel In-Liquid-Plasma Synthesis and Coating Process for Graphene-Coated Perfluorosulfonic Acid-Based Membranes for Application in High-Performance Direct Methanol Fuel Cells. Energy Technol 2025:e202501447. https://doi.org/10.1002/ente.202501447.
[309] Gartner P, Lanza G, Rudat J, Bilger M, Grünert T, Nesterov-Mueller A, et al. Self-healing Fuel Cells by Biological Actuators. Procedia CIRP 2023;116:161–6. https://doi.org/10.1016/j.procir.2023.02.028.

[310] Li X, Miao Z, Marten L, Blankenau I. Experimental measurements of fuel and water crossover in an active DMFC. Int J Hydrog Energy 2021;46:4437–46. https://doi.org/10.1016/j.ijhydene.2020.11.027.
[311] Yujing W, Hongxiu Z, Ao Z, Leqing Z. Numerical simulation of methanol crossover in flowing electrolyte-direct methanol fuel cell. J Power Sources 2022;519:230801. https://doi.org/10.1016/j.jpowsour.2021.230801.
[312] Zimmerer N, Quarz P, Janning L, Risinger J, Scharfer P, Schabel W. Processing of hierarchically structured electrodes with varying catalysts for PEM fuel cells. Wasserstofftechnologien Effizient Produziert, vol. 1, Chemnitz, Germany: Verlag Wissenschaftliche Scripten; 2024, p. 204–21. https://doi.org/10.60687/2025-0067.
[313] Zhao Q, Morawietz T, Gazdzicki P, Friedrich KA. Effect of high-boiling point solvents on inkjet printing of catalyst layers for proton exchange membrane fuel cells. Electrochimica Acta 2024;508:145273. https://doi.org/10.1016/j.electacta.2024.145273.
[314] Antoine O, Bultel Y, Ozil P, Durand R. Catalyst gradient for cathode active layer of proton exchange membrane fuel cell. Electrochimica Acta 2000;45:4493–500. https://doi.org/10.1016/S0013-4686(00)00505-3.
[315] Breitwieser M, Klingele M, Vierrath S, Zengerle R, Thiele S. Tailoring the Membrane-Electrode Interface in PEM Fuel Cells: A Review and Perspective on Novel Engineering Approaches. Adv Energy Mater 2018;8:1701257. https://doi.org/10.1002/aenm.201701257.
[316] Ye L, Gao Y, Zhu S, Zheng J, Li P, Zheng JP. A Pt content and pore structure gradient distributed catalyst layer to improve the PEMFC performance. Int J Hydrog Energy 2017;42:7241–5. https://doi.org/10.1016/j.ijhydene.2016.11.002.
[317] Xu Y, Chang G, Fan R, Cai T. Multi-objective optimization of temperature uniformity in cathode catalyst layer and performance of PEMFC with an ionomer-gradient design. Int J Energy Res 2022;46:21028–44. https://doi.org/10.1002/er.8527.
[318] Saleh MA, Akhtar S, Nessa M, Uddin MS, Bhuiyan MMH. Excess Molar Volumes of Aqueous Solutions of 1-Propanol, 2-Propanol, Allyl Alcohol and Propargyl Alcohol. Phys Chem Liq 1998;36:53–65. https://doi.org/10.1080/00319109808035920.
[319] Kusano T, Hiroi T, Amemiya K, Ando M, Takahashi T, Shibayama M. Structural evolution of a catalyst ink for fuel cells during the drying

process investigated by CV-SANS. Polym J 2015;47:546–55. https://doi.org/10.1038/pj.2015.36.
[320] Soboleva T, Malek K, Xie Z, Navessin T, Holdcroft S. PEMFC Catalyst Layers: The Role of Micropores and Mesopores on Water Sorption and Fuel Cell Activity. ACS Appl Mater Interfaces 2011;3:1827–37. https://doi.org/10.1021/am200590w.
[321] Shi C, Liu T, Chen W, Cui F, Liu L, Cai Y, et al. Interaction, structure and tensile property of swollen Nafion® membranes. Polymer 2021;213:123224. https://doi.org/10.1016/j.polymer.2020.123224.

Declaration of Generative AI and AI-assisted Technologies in the Writing Process

During the preparation of this work, the authors used DeepL (DeepL SE, Germany) and Google Gemini (Google LLC, USA) to improve readability and clarity. The authors reviewed and edited the content after usage and take full responsibility for the content of the publication.

List of Figures

List of Tables

9 Appendix

The appendix contains additional explanations, considerations and diagrams to help understanding the work better. Including them in the main text would distract from its central message. The chapters are organized into sections of general information and additional information related to the different hypotheses.

9.1 Contextualization and application of the results

The colors of hydrogen

Hydrogen is classified according to its origin: Green hydrogen is produced by electrolysis with renewable energy and is considered to be the main resource of a sustainable circular hydrogen economy with applications such as steel reduction [4,5], ammoniac synthesis or direct electrical energy conversion in fuel cells [6]. Hydrogen from other sources is labeled with different colors (Figure 52). The source is given in brackets. The types rich in carbon emissions are: black (hard coal gasification), brown (lignite gasification) and grey (natural gas steam reforming) hydrogen. Types of hydrogen defined as having poor carbon emissions are: blue (natural gas with carbon capture, utilization and storage (CCUS)), turquoise (methane pyrolysis), white (rare naturally occurring hydrogen), yellow (electrolysis with grid electricity) and violet, pink or red (electrolysis with nuclear power) hydrogen. Green hydrogen remains the sole renewable option without carbon emissions [284,285].

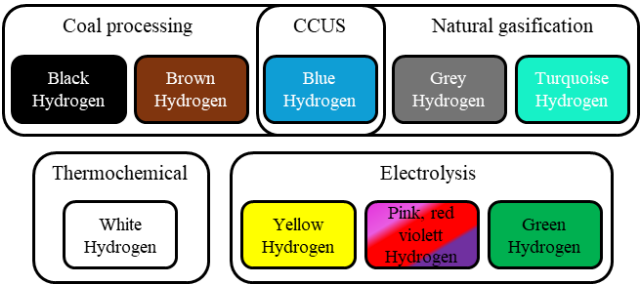

Figure 52: Colors of hydrogen and classification of how and from what it is produced. Adopted from [285].

Energy density of hydrogen and efficiency of a PEM fuel cell

One advantage of using hydrogen as an energy carrier is its high gravimetric energy density, which is significantly higher than that of diesel or gasoline. However, volumetrically, even when compressed and liquefied, its energy density is relatively low and lower than that of gasoline and diesel. Therefore, the focus of applications is on areas where weight is particularly relevant. [286]

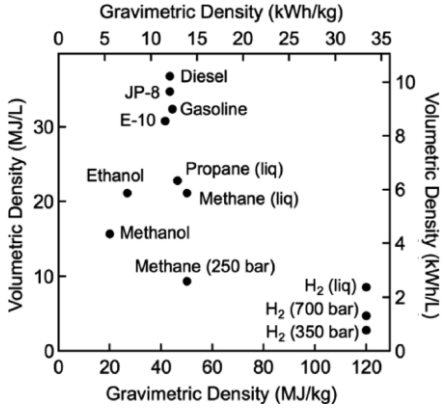

Figure 53: Gravimetric and volumetric densities of different energy carrier. Hydrogen has a low volumetric, but high gravimetric energy density (lower heating value). With permission from [286].

Fuel cells are highly efficient combined heat and power (CHP) systems, with reported efficiencies of up to 90 % [13]. Even without using the exhaust heat, the electrical efficiency of a polymer electrolyte membrane fuel cell (PEMFC) is higher than that of a conventional combustion engine (Table 8). When considering the entire process, from producing green hydrogen in an electrolyser using renewable energy sources, to storage and conversion losses, the efficiency of a fuel cell is comparable to that of a well-to-wheel diesel engine. However, fuel cells have the added benefit of being CO_2-free. [13,16,17] Compared to battery electric vehicles (BEVs), BEVs are more efficient, but batteries are much heavier than fuel cell systems and take longer to charge [17,20]. Ultimately, the specific application determines which system is most suitable.

Table 8: Engine and overall efficiencies (well-to-wheel) for cars with different drive types: fuel cell electric vehicle (FCEV) with green hydrogen, internal combustion engine (ICE) with gasoline or diesel drive, and battery electric vehicle (BEV) with electricity from renewable energies.

Vehicle / fuel	Powertrain	Well-to-wheel	Reference
FCEV	53 – 58 %	~ 26 %	[13,16]
ICE gasoline	14 – 33 %	11 – 26 %	[17]
ICE diesel	28 – 42 %	24 – 36 %	[17]
BEV	64 – 86 %	46 – 72 %	[17]

PEM water electrolysis and carbon based electrodes

In a polymer electrolyte membrane water electrolyzer (PEMWE) the reactions from a PEM fuel cell (see Eq. (1.1) – (1.3)) are reversed to produce hydrogen H_2 and oxygen O_2 from water H_2O and electricity (Eqs. (9.1) – (9.3)). Therefore, the components and production ways [287] of an electrolyzer and a fuel cell are comparable. The components and their fundamental functions are essentially similar with some modifications (Figure 54).

Anode:	$2\,H_2O$	$\rightleftarrows$	$O_2 + 4\,H^+ + 4\,e^-$	(9.1)
Cathode:	$4\,H^+ + 4\,e^-$	$\rightleftarrows$	$2\,H_2$	(9.2)
Redox:	$2\,H_2O$	$\rightleftarrows$	$2\,H_2 + O_2$	(9.3)

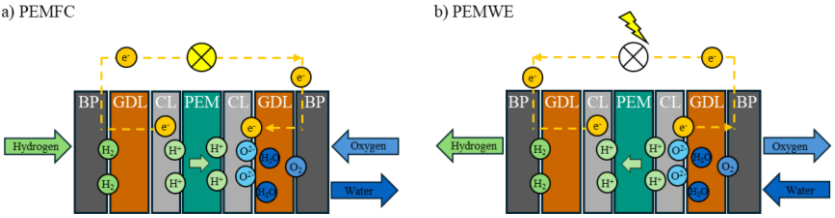

Figure 54: Structure of a) PEMFC and b) PEMWE unit consisting of bipolar plates (BP), gas diffusion layers (GDL), catalyst layers (CL) and proton electrolyte membrane (PEM) and the occurring educt and product flows.

Because of the higher pressures involved in electrolysis, the same membrane materials are used, but they are generally thicker and therefore more stable than those used in fuel cells. The thickness of the catalyst layers and the precious metal loadings are also adjusted [6]. Due to the different chemical reactions, other catalysts are more efficient. Iridium or iridium oxide is usually used on the anode side. Otherwise, the carbon in the *Pt/C* catalyst would decompose during the anode reaction [287]. Since iridium is one of the rarest elements in the earth's crust, research is being done to reduce iridium consumption in electrolyzers [6]. One possibility, is the development of highly porous electrodes achieving excellent results with minimal amounts of iridium [288].

On the cathode side, platinum on carbon is also commonly used in electrolysis [287]. If the cathode is first applied to the membrane, the production of the carbon-based electrode comes close to the manufacturing conditions and requirements of fuel cells. Developments and findings from the fuel cell manufacturing process can be used and transferred to this process.

Advantages and disadvantages of different MEA manufacturing routes

All membrane electrode assembly (MEA) manufacturing processes (see Chapter 1.2) have specific advantages and disadvantages. The following provides a brief overview.

In the process route via the catalyst-coated substrate (CCS), the process steps are relatively straightforward and membrane handling is generally not a major challenge. The roll-to-roll (R2R) ink application is established and large-scale production has been realized [35]. The disadvantages of the CCS process are that valuable catalyst is deposited in the porous gas diffusion layer (GDL) during coating and is not available for electrochemical reactions, and the porosity of the GDL is reduced [123]. In addition, it offers only limited interfacial contact between membrane and catalyst layer resulting in a lower cell performance [28,289]. Hot-pressing of the CCSs with the membrane improves the contacting and increases the performance, but is not mandatory [29]. However, with the goal of reducing the precious metal loadings in the catalyst layers, the MEAs produced in this way show relatively large losses in performance, if the platinum content is reduced [31].

On the other side, a great advantage of the catalyst-coated membrane (CCM) approaches is the beneficial contact between the membrane and the electrode, resulting in lower conduction resistances and improved cell performance [31–34]. The decal process is state of the art, widely used in the literature, e.g. [42,58,62,64,65,69,75,76,81,162,109,290–300], and established on an industrial scale [301–303]. The advantages of this process are that the decal substrate is mechanically flexible, easier to handle e.g. in R2R production and is inert to the catalyst ink and its solvents [304]. However, the major disadvantage of this process compared to the CCS and MDC processes is that it requires a process step to transfer the catalyst layer from the decal substrate to the membrane. This additional step is associated with higher costs for an additional machine, longer production time and material costs for the decal substrate [305]. There is also a loss of expensive product material in this step due to incomplete electrode transfer [31,296,306]. Other disadvantages of the transfer step from a product perspective are that the membrane and ionomer in the catalyst layers are exposed to unfavorably high temperatures during necessary hot-pressing [31,145]. In addition, the contact between the electrodes and the membrane after the electrode transfer is better than in CCS-processed MEAs, but only moderately good, resulting in a higher contact

resistance and restricted performance in operation compared to MDC-processed MEAs [296,306]. Higher pressure during the transfer step may help, but excessive pressure also reduces layer porosity and thus performance [64].

The advantages of MDC are a good performance and durability due to a high catalyst utilization and the improved interfacial contact between the catalyst layers and the membrane [35]. In addition, MDC enables the manufacture of multilayer applications with additional functional layers that require direct application to the membrane. However, the most significant challenges associated with this route are the excessive membrane swelling and membrane handling in a R2R process caused by the ink solvents after coating [36,37].

The advantages and disadvantages of different manufacturing routes are compared. Comparing MDC and CCS manufacturing, advantages and disadvantages are basically inverted. In comparison to the decal process, in MDC, the transfer step with the potential for incomplete transfer and the decal substrate can be eliminated, resulting in material, cost and production time reduction [91,305]. The contact between electrodes and membrane is also superior, resulting in a smaller contact resistance, which is beneficial for system performance [31]. Consequently, compared to the decal or the CCS process, the MDC allows the same performance to be achieved with less catalyst. This in turn reduces catalyst costs and addresses the limited worldwide availability of the precious metal. Hot-pressing is essential in the decal process and is also required in the CCS process to achieve acceptable contact between the electrodes and the membrane. However, hot-pressing reduces the porosity of the electrodes and therefore negatively affects the performance of the system in operation. In MDC, hot-pressing is not absolutely necessary, as hot-pressing of the GDL does not significantly improve performance [31].

Influence of cracks on performance and durability

Cracks in the catalyst layers of a catalyst-coated membrane (CCM) affect the occurring mass transport during operation. In a beneficial manner, cracks enhance the frequently limiting properties of gaseous mass transport during operation. The diffusion of reactants through the cracked structure is facilitated,

with water in particular being more effectively removed, thereby enabling higher current densities on the cathode side [153,154]. Conversely, product water may accumulate within the cracks, resulting in flooding of the cell and a reduction in ionic and electrical conductivity [155,156]. Moreover, cracks impede the conduction of electrons and protons by extending the diffusion paths around the crack and reducing the rate of electron and proton transfer [156]. To a certain extent, this should have no significant influence, as the electron and proton material transports are not limiting during operation. However, with a pronounced or even complete crack network, lateral conduction within the electrode is not possible anymore.

Additionally, cracks impact the mechanical properties of a system. During the production process and operation, the membrane undergoes continuous swelling and shrinkage, resulting in tensile stresses within the system [109]. Due to defects in the catalyst layer, these catalyst-free areas of the CCM react differently to moisture-induced dimensional changes than the catalyst-covered areas. The capacity to handle these differences in tension can lead to pinholes and cracks not only in the catalyst layer but also in the membrane itself [156–158]. These defects tend to intensify over time, potentially giving rise to more significant defects such as cracks and delamination between the membrane and catalyst layer [108,159–162].

Further consequences of occurring cracks are on a chemical perspective. Around catalyst layer defects, localized gas crossover is increased, which can result in further damage through the potential formation of hydrogen peroxide [162]. This results in mixing potentials and fuel loss, which in turn lead to a decline in performance. This phenomenon has been demonstrated to reduce the operational lifetime of the devices [162,163]. As a digression to high-temperature fuel cells: phosphoric acid has the potential to migrate through cracks in the material. Cracks in the catalyst layer act as injection points for the flooding of the microporous layer and the gas diffusion layer [164,165].

The desired electrochemical reactions do not take place at the cracks themselves. However, the catalyst has not disappeared and is present at their edges and is in principle functional. Stoll et al. [71] found only minimal effects on

performance in up to 4 % of defects. Note, however, that they did not examine classic cracks, but deliberately left the membrane without a catalyst layer at certain points. Basically, and especially with regard to lifetime, it also seems to have a dramatic effect on where the irregularities occur [166]. As cracks have a dual effect on cell performance, with both positive and negative consequences, it is postulated that an optimal ratio of cracks to the total catalytic area exists [307]. However, evidence suggests that the negative effects of cracks are more pronounced, in particular regarding the CCM lifetime. Therefore, the objective is to prevent cracking in catalyst layers.

Membrane direct coating for functional layers[1]

In addition to process and cost optimization, there are also applications where membrane direct coating (MDC) is the only pragmatic production method. As part of this thesis, two use cases were worked on in interdisciplinary teams, for which MDC was the only or best manufacturing route. These approaches were investigated, developed further and researched.

In direct methanol fuel cell operation, undesirable crossover of methanol through the membrane occurs. This leads to an inefficient fuel yield and reduces the performance of the system [292,310,311]. One approach to solve this problem is to apply a blocker layer between the membrane and the catalyst layer, which is only permeable to the protons generated in the electrode and retains the methanol. The position of this blocker layer requires direct

[1] Research into various fields of application resulted in two peer-reviewed publications: Rojas-Núñez C, **Quarz P**, Gracia-Medrano-Bravo VA, Kapp J, Käufer F, Sommer T, Kreyschenulte C, Lukassek V, Scharfer P, Wartmann J, Schabel W, Kuth *Novel In-Liquid-Plasma Synthesis and Coating Process for Graphene-Coated Perfluorosulfonic Acid-Based Membranes for Application in High-Performance Direct Methanol Fuel Cells*. Energy Technol 2025:e202501447. https://doi.org/10.1002/ente.202501447, referred to here as [308]; and Gartner P, Lanza G, Rudat J, Bilger M, Grünert T, Nesterov-Mueller A, Zimmerer N, **Quarz P**, Scharfer P, Schabel W, Jung A, Stahlberger M, Bräse S. *Self-healing Fuel Cells by Biological Actuators*. Procedia CIRP 2023;116:161–6. https://doi.org/10.1016/j.procir.2023.02.028, available under a CC BY-NC-ND 4.0 license, referred to here as [309].

application to the membrane. Here, the swelling of the membrane after contact with the solvent has to be managed. [308]

Another use case is the application of a functional enzyme layer on the membrane. Pinholes in the membrane are a failure mode in fuel cells and electrolyzers. They occur during operation and reduce performance and lifetime. Instead of disposing of these damaged systems, the idea is to repair them through enzymatic maintenance and continue to use them. This requires the enzyme layer to be applied directly to the membrane under the electrode. Enzymes are very expensive and temperature sensitive. They must therefore be applied very efficiently where they are needed and must not be subjected to excessive thermal stress. Thus, the hot-pressing step in the decal process must be avoided. The enzyme layer must be applied directly to the membrane, followed by the catalyst layer. [309]

Approaches for crack-free layers[2]

There are various approaches to further improve the manufacturing process, ink composition and structural optimization approaches. In addition to the quest for optimal mixing ratios of the individual ink components, there are approaches using ink additives. These include high-boiling-point solvents (HBPS) such as ethylene glycol or propylene glycol [94,168,313]. These have a high boiling point and remain in the solidifying layer throughout the drying

[2] Parts of the results and figures presented in this chapter have been previously published in a peer-reviewed article:
Quarz P, Zimmerer N, Steck A-M, Scharfer P, Schabel W. *Carbon Nanotubes (CNT) as an additive towards crack-free catalyst coated membranes (CCM)*. Int. J. Hydrogen Energy 2024, 57 789,797. https://doi.org/10.1016/j.ijhydene.2024.01.049, referred to in this work as [263], figures are reprinted with permission from Elsevier Ltd;
and were presented at the Fuel Cell Conference Chemnitz 2024 and have been published in a conference paper:
Zimmerer N, **Quarz P**, Janning L, Risinger J, Scharfer P, Schabel W. *Processing of hierarchically structured electrodes with varying catalysts for PEM fuel cells*, In: Wasserstofftechnologien Effizient produziert, Verlag Wiss. Scripten, Auerbach, Germany, 2024, https://doi.org/10.60687/2025-0067 referred to in this work as [312].

process. This significantly influences the microstructure of the resulting electrode. The description of the selective drying behavior of these inks is of particular interest. The influence of HBPS on the selectivity of other solvents and the behavior of concentration gradients within the film must be investigated. Building on the explanations of the selectivity of binary 1-propanol/water mixtures in this thesis, the complexity is increased by a third solvent. Solvent-solvent interactions and process influences such as drying temperature can lead to interesting observations. Distinct concentration gradients could form in the film with the quasi-inert HBPS. Raman spectroscopy in particular can be used here as quantitative measurement method. Furthermore, for example, in initial trials involving an additional HBPS, cell structures formed. This could be due to surface tension-driven effects during selective film drying. This can be investigated using micro particle tracking velocity (µPTV) in future research.

Another current approach to optimizing electrodes is to design hierarchical multilayer structures to archive an advantageous distribution of the platinum catalyst and ionomer as well as an optimized porosity within the layer [312,314–317]. Investigations into the topic of hierarchically structured catalyst layers were carried out in the context of this present work in collaboration with the parallel thesis by Nadine Zimmerer and are published in [312]. The multilayer structure requires a high level of process knowledge. Of interest here is the re-wetting of the already applied catalyst layers and the membrane by the subsequent multilayer coating. The effects on membrane swelling and on the already coated layers need to be further investigated.

Another ink additive is carbon nanotubes (CNT) [39]. The addition of CNTs improves the crack pattern of the catalyst layers. In the investigations carried out in the framework of this thesis [263], inks with different CNT contents were applied directly to a Nafion NR212 membrane under the same coating and drying conditions. The addition of CNTs significantly increases the resistance of coatings to cracking. For the same coating thickness, the number and total area of cracks in the catalyst layers decreases significantly with increasing CNT content from 0 (A8) via 1 (B8), 3 (C8), und 5 wt% (D8) (Figure 55).

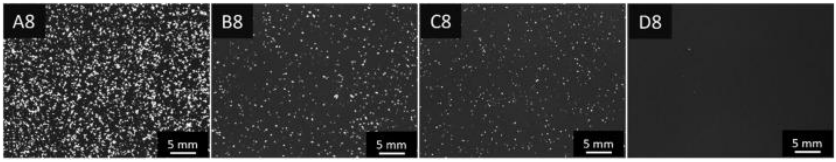

Figure 55: Influence of carbon nanotubes (CNT) on the crack pattern of membrane direct coatings. The CNT-fraction increases from 0 (A), 1 (B), 3 (C) to 5 wt% (D). All layers are around 8 µm thick. Defects are shown white. An increase in the CNT content reduces the defect content for the same film thickness. [263]

With 5 wt% CNT in the layers, virtually crack-free direct membrane coatings are possible. The reason for the low defect percentage is the low number of cracks. Even in membrane direct coatings over 20 µm thickness, only a few individual cracks occur. In contrast, under the same conditions without CNTs, a pronounced crack network appears at a layer thickness of only 10 µm. Initial investigations into the influence of the CNT on the functionality and performance of the layers are promising. Open questions should be pursued in the future and this approach should be further developed. [263]

9.2 Preliminary experiments for studies on the crack pattern of catalyst layers

Solvent composition and volumetric solid content

The solvent composition affects several mixing and ink parameters. The solvent mixture of 1-propanol and water shows less excess volume. The largest excess volume is less than 2.2 ($cm^3\ g^{-1}$)% for a mixture with an 1-propanol fraction of x_1 = 93 wt% [318]. This is important for the experiments on solvent composition determined with a density calibration (see Eq. (3.1) in Chapter 3.6) in the solvent mixture drying experiments in Chapter 6.1.

The ink components are always weighed by mass during ink formulation. If inks with different *I/C* and solvent ratios are produced, this will result in

slightly different volumetric solid contents in the ink due to the different densities of the components (Figure 56). Inks with a higher 1-propanol and lower water content have a lower volumetric solid content for a constant gravimetric solid content. A constant blade gap during coating results in thinner dry film thicknesses. To achieve comparable dry film thicknesses, larger blade gaps must be set. As the *I/C* ratio increases, the volumetric solid content increases as the gravimetric solid content remains constant. The films become slightly thicker for the same coating parameters. As the dry film thickness is relevant and therefore comparable for the evaluation of crack patterns, comparable film thicknesses are produced and the doctor blade gap is adjusted if necessary. Moreover, same adjustments are necessary for constant platinum loadings, as the layer thickness (LT) correlates with it.

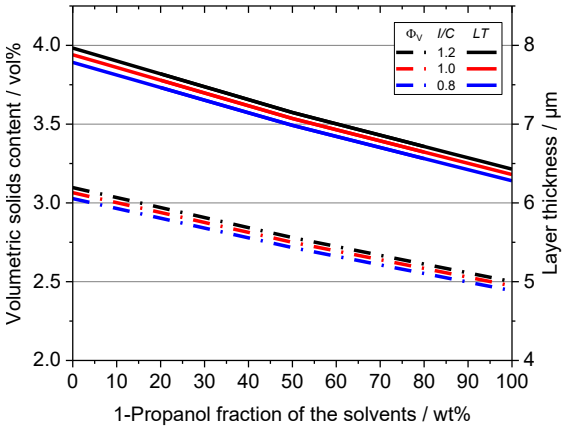

Figure 56: Influence of solvent composition and ionomer-to-carbon ratio (*I/C*) on the volumetric solid content Φ_v (dashed lines) and the dry layer thickness *LT* (solid lines) at a constant gravimetric solid content of 10 wt%. The 1-propanol fraction x_1 refers to the total amount of solvent (1-propanol and water), which makes up 90 wt% of the ink. For calculation, a constant ionomer density regardless the solvent composition and an electrode porosity of 65 vol% are assumed.

Influence of the ink solvent composition on the electrode quality

In preliminary tests, a suitable ink for membrane direct coating (MDC) and testing the hypotheses must be found. The focus is on the ink's solvent composition. It is well known from the literature that the solvent composition has a major influence on the catalyst particles, the ionomer and the way they are interacting. There are several overlapping effects, some of which reinforce each other and some of which work in opposite directions (see Chapter 1.3). As a starting point, all inks were produced with a solid content of 10 wt% and an *I/C* of 1.0. The composition of the remaining 90 wt% solvent were varied between 20, 50 and 80 wt% 1-propanol and the rest of water. This composition is based on primary research using references from literature [54,76,81].

All inks were processed in the same way during production, coating and drying. However, the different solvent composition results in different crack patterns after drying (Figure 57). This is shown in different scales in camera overviews (middle) and microscopic (bottom) images. Cracks appear white. With the catalyst-ionomer system chosen in this work, few individual cracks can be observed with 20 wt% 1-propanol and 80 wt% water at the composition of the initial 90 wt% solvent fraction. With increasing 1-propanol content, the proportion of cracks increases and a pronounced crack network is formed in the catalyst layers. For crack pattern analysis, it is important that the layer thicknesses are similar since the formation and morphology of cracks depend greatly on the film thickness (see Appendix 9.2).

Interestingly, Scheepers et al. [76] observed the opposite trend: fewer cracks in layers with higher proportions of 1-propanol in the ink. They argue on a higher surface tension in water-rich inks. Additionally, it is thought that hydrophobic carbon particles aggregate more in water-rich solvent compositions, creating larger agglomerates that cause cracking. Unfortunately, no particle sizes were measured in this study. However, the comparison with Scheepers et al. is not accurate because they used pure carbon, which is more hydrophobic and agglomerates more strongly in water rich-inks. It is possible that with a higher water content the particles form larger agglomerates which are then nucleation point of the cracks. Here, a *Pt/C* catalyst is used, to which Nafion

adsorbs differently [45]. Scheepers et al. coated PTFE and kept the wet film thickness constant. Here, the coating is applied directly onto the membrane, and the dry film thickness is kept constant. As the solvent composition varies, the density of the solvent mixture and thus the volumetric solid content changes. For a constant wet film thickness and gravimetric solid content, this results in a slightly thinner dry film thickness with more 1-propanol (see Appendix 9.2). The reduction of dry film thickness in turn contributes to a reduction of cracking (see Appendix 9.2).

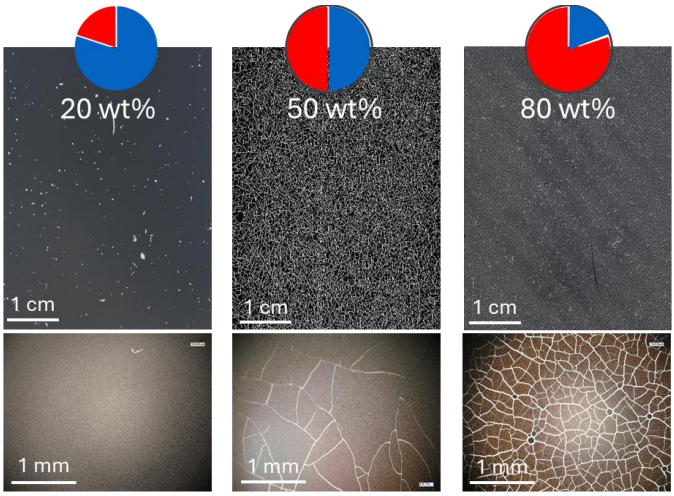

Figure 57: Influence of the initial solvent composition on the layer pattern of fuel cell electrodes. Top: Initial solvent composition and its 1-propanol mass fraction (red) of the inks. The solvents make initially 90 wt% of the ink. The solids composition (catalyst and ionomer) is the same. All membrane direct coatings have a dry film thickness of 7.6 ± 0.7 µm and were processed, coated and dried under constant conditions (T = 25 °C, α = 35 W m^{-2} K^{-1}). Cracks are visible in white in the camera (middle) and microscope (bottom) images due to the illumination setup. With increasing 1-propanol fraction more cracks occur.

Gong et al. [96] examined the surface of spray-coated membrane direct coatings of inks with different 1-propanol/water mixtures using SEM images. They observed a rather compact and uniform appearance of the layers with 80 and

50 wt% 1-propanol. With more water, the surface of the layers was rougher and voids in the layer become detectable. However, the water-rich ink showed the best electrochemical performance.

The different layer patterns observed here are due to the varying interactions between the catalyst particles and the ionomer, which depend on the solvent composition of the ink (see Chapter 1.3). In inks with a lower proportion of 1-propanol and a higher proportion of water, the particles tend to be smaller (Figure 58). With fewer large agglomerates present, fewer defects are initiated within the drying layer. The membrane also interacts differently with the various solvent compositions (see Chapter 7.1).

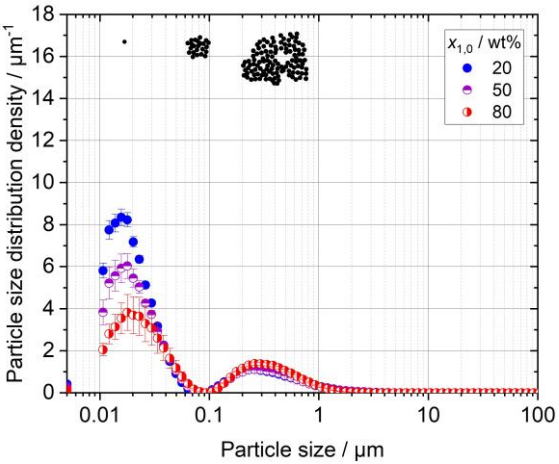

Figure 58: Volume-weighted particle size distribution density (PSD) q_3 depending on the solvent composition of the ink with 1-propanol mass fractions of the solvents of $x_{1,0}$ = 20, 50, and 80 wt%. All inks were processed in a ball mill under constant processing parameters (3 h and 1000 rpm). The schematic representation above depicts primary particles, aggregates and larger agglomerates, anticipated for each size class. With less 1-propanol and more water, more smaller particles are observed.

The discussion on different effects above, illustrates the complexity of the issue. The influence of the PSD on the crack pattern is already visible.

Consequently, the ink formulation is held constant in the following investigations. The solvent composition, comprising 20 wt% 1-propanol and 80 wt% water, is selected because, with this composition, the layer exhibits the fewest and smallest cracks on the membrane with the catalyst and ionomer used.

Influence of the layer thickness on crack pattern[3]

An influence of layer thickness (LT) on cracking is known from the literature [62,76]. However, the influence is of such relevance that it is explicitly highlighted for the catalyst inks used (Figure 59). Therefore, ink (Ink I, see Chapter 3.2) was applied with DMC on a Nafion membrane and dried with identical, isothermal drying conditions changing the height of the doctor blade gap. The resulting layers with different dry film thicknesses (4, 8, and 10 µm) show large differences in the crack pattern. Cracks appear as white spots, whereas the catalyst layer is black.

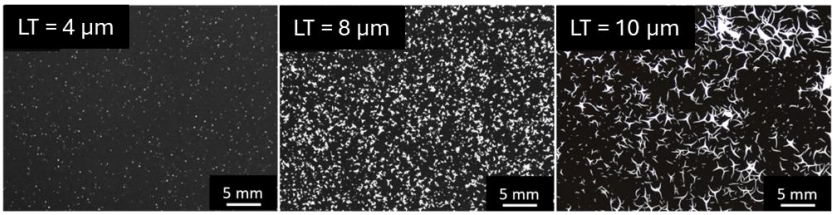

Figure 59: Influence of the layer thickness (LT) on the crack pattern in catalyst layers, as seen in camera images. Cracks appear white. The defect fraction increases with increasing LT. [263]

Typical crack shapes in catalyst layers can be observed depending on the LT. Microscopic images identify the point-like defects in Figure 59 as short cracks in thin layers, often around agglomerates and other inhomogeneities (Figure

[3] Results presented in this chapter are published as peer-reviewed article: **Quarz P**, Zimmerer N, Steck A-M, Scharfer P, Schabel W. *Carbon Nanotubes (CNT) as an additive towards crack-free catalyst coated membranes (CCM)*. Int. J. Hydrogen Energy 2024, 57 789,797. https://doi.org/10.1016/j.ijhydene.2024.01.049, referred to in this work as [263].
Figures have been reprinted with permission from Elsevier Ltd.

60, 4 µm; and see also Appendix 9.4). Kumano et al. [58] defined those cracks nearby critical defects as defect cracks. As the LT increases, additional cracks appear that are not in the immediate vicinity of agglomerates, so called primary cracks. The cracks become longer, branch out into secondary cracks (8 µm) and may grow together (10 µm). In thick layers this leads to the formation of a continuous network of cracks and thus delamination of the layer from the substrate and spalling.

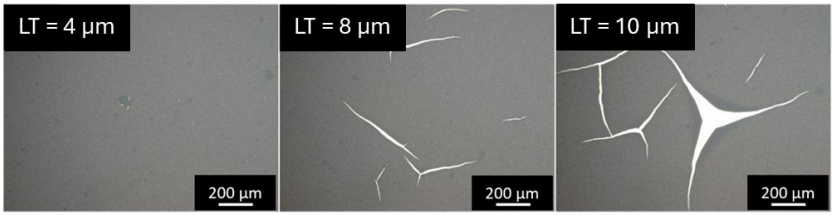

Figure 60: Influence of the layer thickness (LT) on the crack pattern in catalyst layers, as seen under a microscope. With increasing LT defect areas become larger. Secondary cracks are formed and when cracks are converging delamination can occur. [263]

The influence of LT on crack formation is quantified as defect area (cracks, spalling, etc.) relative to the total layer area analyzed and the number of defects in Figure 61. The defect area increases significantly while the number of defects decreases with increasing LT. This is due to crack coalescence. Consequently, the average defect size rises.

The derived conclusion is that the LT has a significant impact on layer quality. When investigating different process parameters along the process chain for CCM production, it is crucial to compare layers of similar LT to ensure an equitable comparison of different coatings.

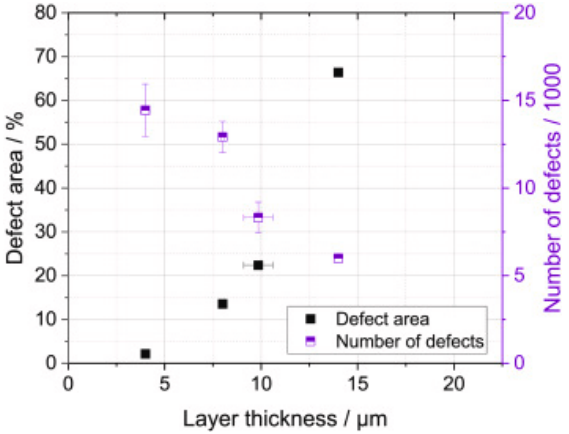

Figure 61: Percentage of defect area (cracks, resulting spalling, etc.) relative to the total area of the membrane direct coatings (black) and number of defects (purple) vs. the dry layer thickness. The layers were dried at an isothermal film temperature of 25 °C and with a heat transfer coefficient of 35 W $m^{-2} K^{-1}$. With increasing thickness, the defect fraction increases and the number of defects decreases. This results from crack coalescence. [263]

9.3 Further fundamentals of drying solvent mixtures

Calculation of gas-side mass transport

It is essential to remove the evaporating solvent from the liquid-gas interface. A high mass transfer coefficient increases the drying rate. Heat and mass transfer are coupled in convective drying. The Lewis analogy shows the relationship between the mass transfer coefficient and the convective heat transfer coefficient (Eq. (9.4))). The exponent n_{Lewis} assumes a value of 1/3 for laminar flows and a value of 0.42 for turbulent flows. Le_i is subsequently determined from the quotient of the dimensionless Schmidt and Prandtl numbers (Eq. (9.5)). The Schmidt number is defined as the ratio of the flow boundary layer thickness to the mass transfer boundary layer thickness. It is used to characterize the ratio of flow boundary layer thickness to mass transfer boundary layer

thickness. The Prandtl number is used to describe the relationship between momentum diffusivity and heat transfer. [189]

$$\beta_{\mathrm{Sol,g}} = \frac{\alpha}{\tilde{\rho}_{\mathrm{g}}\, \tilde{c}_{\mathrm{p,g}}\, Le_i^{\,1-n_{\mathrm{Lewis}}}} \tag{9.4}$$

$\beta_{\mathrm{Sol,g}}$	Mass transfer coefficient of the solvent sol into the gas g in m s^{-1}
α	Heat transfer coefficient in W m^{-2} K^{-1}
$\tilde{\rho}_{\mathrm{g}}$	Molar gas density in mol m^{-3}
$\tilde{c}_{\mathrm{p,g}}$	Molar heat capacity of the gas in J mol^{-1} K^{-1}
Le_i	Lewis number for component *i* (dimensionless)
n_{Lewis}	Lewis Flow parameter (dimensionless)

$$Le_i = \frac{Sc_i}{Pr} = \frac{\lambda_{\mathrm{g}}}{\tilde{\rho}_{\mathrm{g}}\, \tilde{c}_{\mathrm{p,g}}\, \delta_{\mathrm{Sol,g}}} \tag{9.5}$$

Sc_i	Schmidt number (dimensionless)
Pr	Prandtl number (dimensionless)
λ_{g}	Thermal conductivity of the gas in W m^{-1}K^{-1}
$\delta_{\mathrm{Sol,g}}$	Diffusion coefficient of the solvent in the gas in m² s^{-1}

The diffusion coefficient is determined by the Fuller equation (9.6) [213]. In air, diffusion coefficients of $2.50 \cdot 10^{-5}$ m²/s for water and $1.02 \cdot 10^{-5}$ m²/s for 1-propanol are obtained at an exemplary 25 °C and 1.013 bar. The small water molecule diffuses around 2.5 times faster than 1-propanol. Higher temperature and lower pressure increase the diffusion coefficients in each case. However, the ratio of two diffusion coefficients of different solvents to each other remains constant regardless of temperature and pressure.

$$\delta_{i,j} = \frac{0{,}00143\, T^{1{,}75} \left(\tilde{M}_i^{-1} + \tilde{M}_j^{-1}\right)^{0{,}5}}{p\, \sqrt{2} \left(\Delta v_i^{\frac{1}{3}} + \Delta v_j^{\frac{1}{3}}\right)^2} \tag{9.6}$$

$\delta_{i,j}$	Diffusion coefficient of component *i* in component *j* in cm² s^{-1}
T	Air temperature in K
$\tilde{M}_i$	Molar weight of component *i* in g mol^{-1}
$\tilde{M}_{\mathrm{g}}$	Molar weight of the gas in g mol^{-1}
p	Ambient pressure in bar
Δv_i	Structural diffusion volume increment of component *i* in cm³ mol^{-1}
Δv_j	Structural diffusion volume increment of component *j* in cm³ mol^{-1}

Calculating the decrease in liquid and the number of transfer units

Drying results in a reduction in the amount of solvent. This can be calculated using total and component molar balance equations for the liquid (Eq. (9.7)). [201] The experiments in this study measure the mass ratios of evaporating solvent mixtures. The current mass at time t is set in relation to the initial (index: 0) mass. Other ratios can be derived from this, which forms the basis for the results presented in Chapter 6.1 (Eq. (9.8)). Assuming negligible excess volumes (see Appendix 9.2), the mass ratio can be converted into the volume ratio via the density (see Eq. (3.1)). The density depends on the composition. Assuming the cross-sectional area of the beaker remains constant, the next step is to calculate the height ratio. Without film-side mass transport resistance occurring, height ratios resulting from different absolute heights can be compared, and results from liquid columns in the cm-scale can be transferred to the µm-scale. If the partial masses of the components are determined using the current composition, the molar masses can be used to calculate the amount of substance and the molar ratio. This provides the link to the kinetics described in Chapter 2.3.

$$\frac{N_\mathrm{L}}{N_\mathrm{L,0}} = \exp \int_{\tilde{x}_{1,0}}^{\tilde{x}_1} \frac{d\tilde{x}_1}{\tilde{r}_1(\tilde{x}_1) - \tilde{x}_1} \tag{9.7}$$

N_L	(Current) amount of substance in the liquid (L) in mol
$N_\mathrm{L,0}$	Initial (0) amount of substance in the liquid in mol
$\tilde{x}_1$	(Current) molar fraction of component 1 in the liquid in mol%
$\tilde{x}_{1,0}$	Initial molar fraction of component 1 in the liquid in mol%
$\tilde{r}_i$	Relative molar flux of component *i* in $\frac{\mathrm{mol\,s^{-1}}}{\mathrm{mol\,s^{-1}}}$%

$$\frac{h_\mathrm{L}(t)}{h_\mathrm{L,0}} = \frac{V_\mathrm{L}(t)}{V_\mathrm{L,0}} = \frac{\rho_\mathrm{L,0}}{\rho_\mathrm{L}(t)} \frac{m_\mathrm{L}(t)}{m_\mathrm{L,0}} \sim \frac{N_\mathrm{L}(t)}{N_\mathrm{L,0}} \tag{9.8}$$

$h_\mathrm{L}(t)$	Film height at the time *t* in cm
$h_\mathrm{L,0}$	Initial film height in cm
$V_\mathrm{L}(t)$	Volume of the liquid at the time *t* in mL
$V_\mathrm{L,0}$	Initial volume of the liquid in mL
$m_\mathrm{L}(t)$	Mass of the liquid at time *t* in g
$m_\mathrm{L,0}$	Initial mass of the liquid in g

A drying process can be characterized using the number of transfer units, understood as a dimensionless 'number of time units' (Eq. (9.9)). Here, the evaporation flow (numerator) is compared to the drying gas flux (denominator). This allows two limiting cases to be distinguished. For $NTU_{i,\mathrm{g}} \rightarrow \infty$, the evaporation flow strongly dominates and a quasi-thermodynamic equilibrium is reached. One could also argue that there is enough interaction time to reach thermodynamic equilibrium. The drying process is thermodynamically controlled. For $NTU_{i,\mathrm{g}} \rightarrow 0$, the convective gas flux dominates the evaporation flow and interaction times are too short to achieve the thermodynamic equilibrium. The gas-side mass transport resistance is decisive and the gas kinetics becomes relevant. [201]

$$NTU_{i,\mathrm{g}} = \frac{\tilde{\rho}_{\mathrm{g}}\, A_{\mathrm{Ph}}\, \beta_{i,\mathrm{g}}}{\dot{N}_{\mathrm{g}}} \tag{9.9}$$

$NTU_{i,\mathrm{g}}$ Number of transfer units (dimensionless)
$\dot{N}_{\mathrm{g}}$ Molar flux of the drying gas in mol s^{-1}

In the literature on fuel cells, the specific characteristics and processes of mixture evaporation are usually not considered, even though this phenomenon was already observed experimentally [76,81,94]. This work will fill this gap by systematic investigations with the commonly used 1-propanol/water solvent mixtures, which will serve as a model material system.

Vapor pressure curves and activity coefficients of the ink solvents

The vapor pressure curves of the pure solvents, 1-propanol and water, are fundamental material properties of the two solvents and are relevant for all drying processes involving them [193]. In the temperature range from 0 to 100 °C, the curves exhibit minimal discrepancy (Figure 62). For temperatures below 55 °C, the water curve exhibits a slight elevation in comparison to that of 1-propanol, indicating a slightly higher degree of volatility. Conversely, above 55 °C, the 1-propanol curve exceeds that of water, resulting in the known boiling temperatures at atmospheric pressure of 98 °C for 1-propanol and 100 °C for water.

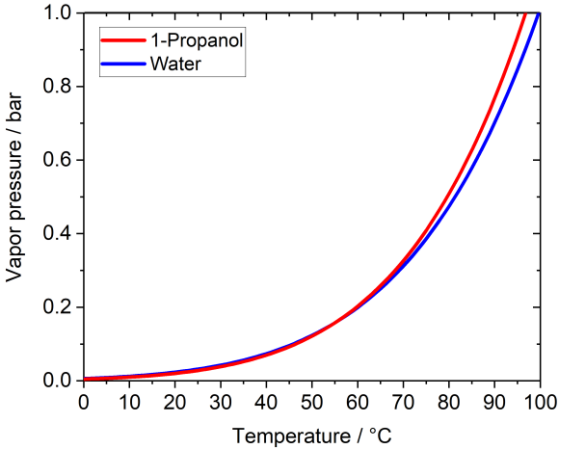

Figure 62: Vapor pressure curves of 1-propanol and water between 0 and 100 °C.

When considering the vaporization or evaporation of a solvent mixture, the interactions between the solvents must be taken into account. This is done in the form of activity coefficients γ_i which depend on the solvent composition. In a hypothetical ideal mixture behavior, these are set to a constant value of 1. In real behavior, however, they vary greatly, shown in Figure 63 for 1-propanol/water mixtures. This significantly influences the partial pressures of the evaporating components (see Eq. (2.6)). The respective dilute component exhibits high activity coefficients. [192]

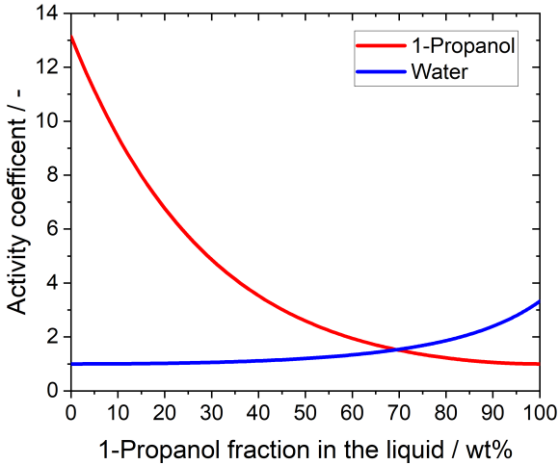

Figure 63: Activity coefficients in 1-propanol/water mixtures as a function of the solvent composition. Calculated according to [192].

Overview of catalyst layer drying literature

The most important literature on fuel cell and electrolyzer ink drying is presented briefly but in more detail than in the main part (see Chapter 1.5).

Using inks with a solvent mixture of 1-propanol and water, Scheepers showed that the composition changes as the film dries [27,76]. They used FTIR spectroscopy to determine the solvent content of the drying air and calculated the actual film composition. In the study from 2018 [76], the starting composition of the catalyst inks and the wet film height were varied. In addition, the study examined the effect of wet film thickness on drying time. As expected, the results demonstrated that a thicker (wet) film requires a longer drying time. However, the course of the 1-propanol content based on a normalized drying time was found to be constant, although no explanation was provided for this. In a further drying study [81], Scheepers et al. varied the drying parameters in the form of the drying temperature, the gas velocity and the preloading of the air with water. They observed an influence of gas velocity and preloading on the drying film and the solvent composition. The effects of temperature

variation are marginal for them. Liu et al. [300] observed a similar effect in their study of the influence of the drying temperature on the layer structure and the resulting cracks.

Koga [149] explored ink drying using grazing incidence small-angle X-ray scattering (GISAXS) and time-resolved attenuated total reflectance Fourier transform infrared (ATR-FTIR) measurements. Correlating with gravimetric measurements, they created a drying curve composed of the proportions of 1-propanol and water. The 1-propanol evaporates completely at the beginning of the drying process, with only residual water evaporating towards the end. However, the focus is on demonstrating the measurement method rather than further investigation of the influence of drying parameters or initial solvent composition.

Hasegawa et al. [94] investigated the solvent composition of drying catalyst inks by extracting the solvents with dehydrated acetonitrile at selected time steps followed by ^{1}H NMR analysis. They also found a change in solvent composition over the drying period. In their experiments, the alcohols ethanol and 1-propanol evaporated preferentially, while water dried more slowly. When the high-boiling-point solvent propylene glycol was added, it remained last in the ink. They further discussed these influences on particle agglomeration during drying and the final layer pattern. ^{1}H NMR analysis was also used by Chen et al. [151] who focused on the drying of the microporous layer, but also observed a preferential evaporation of 2-propanol compared to water and were able to fit component-specific drying rates.

Although Kumano et al. [58] do not vary the drying conditions but investigate different solvent compositions, they discuss drying effects in relatively great detail. They assume a relative enrichment of water in the drying ink due to preferential ethanol or propanol evaporation, thus referring to drying selectivity. They conclude that their water-propanol ink and their water-ethanol(-propanol) ink have similar surface tensions towards the end of drying and argue about cracks induced by capillary forces.

Kusano et al. [319] studied the structural change of agglomerates and the ionomer during drying. However, the focus was not on different drying parameters, nor specific solvent composition, but on the absolute solid content. They observed a decrease in the size of the ionomer shell surrounding the carbon particle during the drying process using contrast-variation small-angle neutron scattering (CV-SANS).

Hoffmann et al. [62] determined drying curves in terms of mass and film height and correlated these with drying stress in the film. At the end of film shrinkage, they observed a significant increase in stress. Depending on the particle material, the addition of Nafion led to longer or sometimes shorter drying times, and the effect is not clearly defined. Solvent composition or variation of drying parameters was not considered.

Suzuki et al. [64] experimented with inks made from 1-propanol and water. They determined drying curves in terms of total mass loss over time. A higher drying temperature results in faster drying. Preloading with water slows down drying. Drying temperature had no effect on film porosity. However, preloading with water during drying resulted in small changes in porosity, even though the pore size distribution remained similar. No effect was observed in performance tests. The effect of solvent composition was not investigated in detail.

When comparing convection drying in an oven with vacuum drying and freeze drying, Talukdar et al. [147,148] revealed the significant impact of drying and the specific drying method on the electrode properties. Significant differences were observed in porosity and performance. However, it should be noted that not all data on the precise drying conditions were provided, which limits the comparability of the results. It remains unclear whether the drying conditions were comparable across all three types of drying to the extent necessary for a fair comparison, such as maintaining a constant drying rate. As a consequence, the data cannot be directly compared. Nevertheless, the data clearly demonstrate that drying has a profound impact on the subsequent layer performance.

Santangelo et al. [150] determined drying curves gravimetrically in a closed air reservoir. They observed curved drying curves for their inks with multiple

solvents. The drying rate decreases with increasing drying time. However, important drying effects in this experimental set-up, such as the effect of air saturation above the film and also the effects of mixture evaporation, are not discussed. This illustrates the need for clarification in this area.

Mauger et al. [91] observed a drying temperature-dependent distribution or local accumulation of ionomer in the dry film, which influences proton conduction during fuel cell operation. Furthermore, they found lower porosities of the catalyst layers with lower drying temperatures. The same trend was also reported by Yang et al. [152] for iridium oxide anodes for electrolyzers and further correlated with performance characteristics in the study.

9.4 Further experiments and considerations for Hypothesis 1

Influence of the rotational speed on ink and layer properties

An important process parameter in ball milling is the rotational speed of the grinding disk. In Chapter 4.1 it is discussed that a high stress number (*SN*), due to longer grinding times, results in increased agglomerate break-up and more smaller particles. According to Eq. (2.4), the particle size can also be reduced by adjusting the speed of the grinding process. In comparison with literature studies [100,103], the study in Chapter 4.1 showed that increased speeds significantly reduced grinding time. It is suggested that this can be taken further: at higher speeds, the same grinding time will result in greater particle breakdown, resulting in fewer cracks in the produced layers.

In Chapter 4.1, the same *SN* experienced by the ink during production are achieved by coordinating the speed and grinding time. The aim is to produce uniform particle size distributions (PSD) despite the variety of ink processing procedures. The rotational speeds required for these tests are compared here using the same grinding time, to provide an initial insight into the effects of rotational speed. No new inks were produced for this purpose. The data comes from the inks used in the test series investigating the influence of grinding time, as well as from the test series with similar *SN* (Inks B and H, see Table 2), and

is only being compared in the new version. Both inks were processed for 3 h, but one at 1000 rpm and the other at 2000 rpm, i.e. twice the speed (Figure 64). With increasing rotational speed, the curve is shifted slightly to smaller particle sizes for constant milling time. Similar results are reported by Liu et al. [100]. The assumption of an increase in *SN* leading to a decrease in particle size at higher speeds seems to be justified.

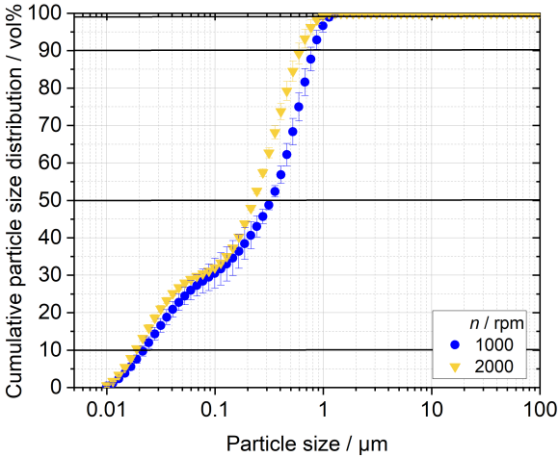

Figure 64: Cumulative particle size distribution (PSD) depending on the rotational speed n during milling for constant 3 h with 1000 and 2000 rpm in a ball mill. With higher rotational speed the PSD shifts to smaller sizes.

When applied directly to the membrane under constant conditions, the inks show a similar crack pattern. Representative sections are shown in Figure 65. There is a slight tendency for the proportion of cracked areas to decrease as the rotational speed increases. The explanation is that the less large agglomerates are beneficial for the crack pattern.

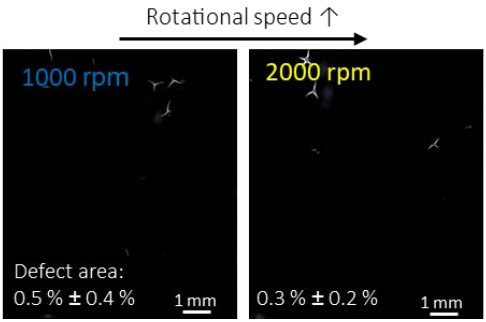

Figure 65: Observed crack pattern of representative catalyst layers with cracks after rotational speeds of 1000 and 2000 rpm and constant milling time of 3 h. All inks were directly coated onto the membrane and dried under similar drying conditions. The dry layer thickness of all layers is 7.4 ± 0.5 µm. The number of cracks and the proportion of cracks observed in the dry layers decrease with higher rotational speed during milling.

This comparison offers a preliminary indication. To make definitive statements, the influence of the rotational speed must be examined in more detail. Slower speeds are generally undesirable as they reduce the stress number and require longer grinding times to compensate. Higher speeds are preferable. However, at speeds over 2000 rpm, air was introduced into the ink, causing coating defects. Degassing steps, such as vacuum or ultrasound, could be added, but they alter the ink due to the additional processing step. This would eliminate the clear correlation between degassed and non-degassed inks. Also, slippage may occur between the rotation disk and the grinding media at a certain speed, reducing the effectiveness of increasing the speed. The differences between the two applied speeds are minor. No significant added value is expected from smaller intermediate steps.

Stress numbers in the literature and this work

The experimental study on the ink processing in a ball mill of this work investigated the influence of the milling time, the rotational speed and the resulting stress number SN. The experimental data are described in Chapter 3.2 and the results are discussed in Chapter 4.1. The grinding media (GM) were driven in

the grinding chamber by a grinding disk. The size of the GM in this work was 6 to 8 µm (according to the supplier) and was calculated with 7 mm. The process parameters were essentially 1000 to 2000 rpm of the grinding disk and 1 to 24 h milling time.

A similar study was conducted by Baez-Cotto et al. [103]. They used a jar mill roller with 5 mm large GM inside the scintillation vial to process the catalyst ink. Because of the relatively low rotational speed of 60 rpm, they milled for 24 to 96 h and therefore several days. An overview of the process parameters in both studies is given in Table 10. Although the bead drive and the systems are different, the basic disintegration mechanisms for the agglomerates into smaller aggregates and primary particles are the same. *SN* is calculated for the inks of both studies according to Eq. (2.4). Table 10 provides an overview of the process conditions for the different inks. The inks are ordered with increasing *SN* from top to bottom. The *SN* is in a same magnitude of order in both studies.

Table 9: Comparison of ink processing parameters for Baez-Cotto et al. [103] and this work. * given; ** calculated with given values; *** assumed.

Parameter	This study	Baez-Cotto et al.
Drive unit	Grinding disk (intern)	Jar mill (outside)
Side of the GM / mm	7	5*
Volumetric filling ratio of grinding media (GM) to ink / ml ml^{-1}	0.5	0.45**
Porosity of the bulk of grinding media / vol%	0.38	0.38***
Volumetric solid content of the product suspension / vol%	3.4	1.6**

Table 10: Stress number *SN* in the studies of Baez-Cotto et al. [103] and of this work on ink processing. With increasing grinding time *t* or increasing rotational speed *n* the stress number *SN* increases. The inks A, B, C and D are from this study (see Table 2), while the Ink-24, Ink-48, Ink-72 and Ink-96 are from Baez-Cotto et al. The inks are ordered according to their *SN*, calculated using Eq. (2.4). *SN* is of the same order of magnitude in both studies.

Ink	***t***	***n***	***SN***
	h	**rpm**	**10^8 m^{-1}**
A	1	1000	1.11
B	3	1000	3.34
Ink-24	24	60	4.16
C	6	1000	6.68
Ink-48	48	60	8.32
Ink-72	72	60	12.5
Ink-96	96	60	16.6
D	24	1000	26.7

Influence of different parameters affecting the stress number

Chapter 4.1 discusses how milling time and rotational speed affect catalyst inks and the layers that result. It's determined that the stress number *SN* is the process function for ball milling catalyst inks. The other stress-number-equation parameters (see Eq. (2.4) in Chapter 2.1) are discussed below.

Volumetric filling ratio of grinding media to ink φ_{GM}: *SN* increases as φ_{GM} increases. One limitation is that if too many grinding beads are added, they no longer mix with the ink, but float on top and do not contribute to comminution.

Volumetric solid content of the product suspension Φ_v: The ink's solid content is not typically optimized for milling, but rather based on other requirements. Different coating processes require different levels of solids (see Chapter 1.3). Changes in ink formulation affect the solid content due to differences in component density (see Appendix 9.2). A higher solid content needs less solvent and requires a shorter drying step if the process allows. According to Eq. (2.4), higher solid content reduces SN, which must be compensated by adjusting other grinding parameters to maintain constant particle size distribution (PSD). Variations in solid content may affect particle-ionomer interactions when

particles are closer together and potentially affect viscosity, flow during milling, and other characteristics. The solid content parameter cannot be considered in isolation without other changes.

Diameter of the grinding media (GM) d_{GM}: Experiments were carried out with larger GM (1.0 – 1.2 mm) than in the experiments presented here (0.6 – 0.8 mm). The resulting PSD was coarser, and the particles were larger with otherwise identical process parameters. This indicates the influence of GM size and its disproportion to the *SN*. To achieve a lower PSD, a higher *SN* and smaller GM should be used. In this study, the GM size was limited by the 0.5 mm mesh size of the strainer at the ink outlet of the milling chamber. As GM diameter decreases, *SI* decreases by the power of three. Minimum diameter is also limited by the need to break particles. Liu et al. [100] demonstrated that using a mixture of different GM sizes is more effective.

Porosity of the bulk of GM ε: This parameter is constant for a monomodal packing. Using mixtures of different GM sizes will influence this parameter.

Surface images of produced catalyst layers

When observing cracks, agglomerates are frequently observed in the immediate vicinity (Figure 66). Due to inhomogeneities in the surrounding area, agglomerates serve as nucleation points for crack formation. Particle sizes and the number of (large) agglomerates decrease with increasing grinding time (see Table 3). Nevertheless, some agglomerates are still found after each grinding time examined. In an industrial process to remove agglomerates, a filtration step could be included in the process.

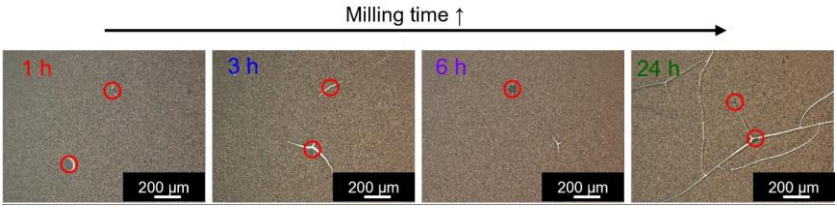

Figure 66: Microscopic images of the surface of different catalyst layers top-light illumination. Agglomerates (circled in red) are common nucleation points for cracks, independent on the milling time of the inks. The number and size of the agglomerates shown are not representative of the inks themselves, but rather serve to illustrate their general appearance. [262]

Ink's particle size and layer's pore diameter distributions

The pore diameter distribution is similar to the particle size distribution (PSD) of the respective inks. In direct comparison (Figure 67), they appear interdependent. The curves' shapes are similar, with both distributions exhibiting a monomodal and bimodal distribution. With the largest agglomerates, the largest significant pores also disappear after 24 h of milling. It is therefore expected that the large pores come from large agglomerates and the smaller pores come from primary particles and small aggregates. Larger agglomerates form larger secondary pores between themselves. At the same time, they also contain larger primary pores. Both disappear when the agglomerate is broken up. At the same time, the (smaller) secondary pores resulting from the now more numerous smaller particles increase. The pores are always smaller than the respective particle agglomerate size.

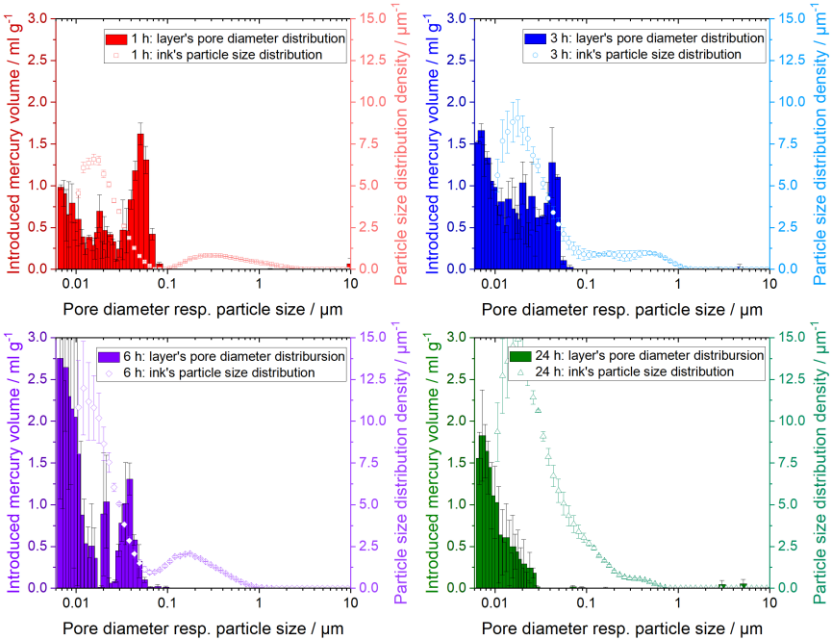

Figure 67: Particle size distribution densities q_3 (data points) of the inks compared to the pore diameter distributions -dV/dlog(d_p) (bars) of the formed layers after 1, 3, 6 and 24 h of ink processing. Shape and qualitative sizes of particles and pores match for each ink. X-axis represents the pore diameter d_p respective the particle size x.[4] If there are no large particles in the ink, there will be no large pores within the respective layers (see 24 h). [262]

Secondary pores of different sizes form between individual primary particles, aggregates and larger agglomerates. In addition, primary pores are present in aggregates and agglomerates. For geometrical reasons, these are generally

[4] Particle size distributions are measured using dynamic light scattering in the diluted ink (see Chapter 3.3). The resolution limit is 0.01 µm at the lower and over 10 µm at the upper end. The pore diameter distributions within the coated layers are determined by means of mercury intrusion (see Chapter 3.5). The measuring range is limited between 0.0064 µm and over 10 µm.

larger in agglomerates than in aggregates. Depending on the type of particles present, different pore sizes are observed in the layer (Figure 68).

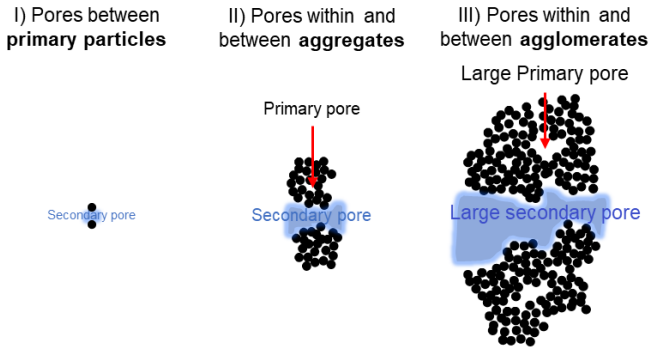

Figure 68: Varying sizes of secondary pores between two I) primary particles, II) aggregates and III) agglomerates. In addition, primary pores occur in aggregates and agglomerates. These are larger in agglomerates. [262]

Influence of *I/C* ratio on particle size and electrode properties

To test the hypothesis that free ionomer acts as crack inhibiting binder, the *I/C* ratio is increased. The effects on the pore diameter distribution are shown in Figure 69. A higher *I/C* results in less pores, in particular large pores vanish. The largest detected pore size is approx. 0.03 µm with *I/C* = 1.0 and only about half as wide for *I/C* = 1.2. The extra ionomer clogs the pores. The reduction in pore size observed here appears to be greater than the improvement in crack area. Ongoing research needs to find the optimum *I/C* ratio and particle size distribution for beneficial pore diameter distribution and system performance. Unfortunately, all of the sample-destructive mercury tests for *I/C* = 1.5 failed due to malfunctions in the measurement protocol. This is why no pore data is available for them.

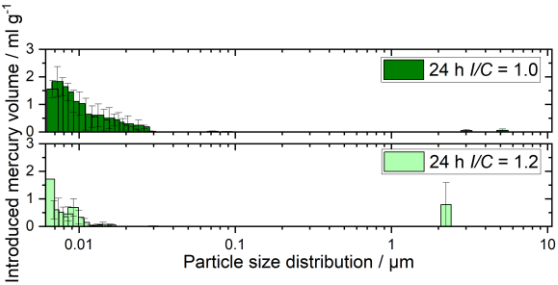

Figure 69: Influence of the ionomer to carbon (*I/C*) ratio on pore diameter distribution. Increasing *I/C* results in less pores, especially less larger pores. [262]

The Influence of the *I/C* on the crack pattern is analyzed. Layers with increased *I/C* show less cracks (Figure 70). The crack pattern of the first row resulting from inks milled for 24 h are known from in Figure 22. After 24 h of ink milling, the crack pattern from the ink with *I/C* = 1.0 shows a pronounced crack network. This is less dense for *I/C* = 1.2 and with *I/C* = 1.5 no crack network is observed. Here, only a few single cracks exist. Also after 3 h of ink milling, the number and size of cracks reduces with increasing *I/C*. In both series, the defect area is reduced to less than 1 % by a sufficiently high *I/C*. The cracks are thus below the critical crack thickness (CCT) according to the pragmatic definition of Hoffmann et al. [62] (see Chapter 4.1). More (free) ionomer reduces crack formation. The milling time resp. coupled particle size distribution and the *I/C* must be considered together.

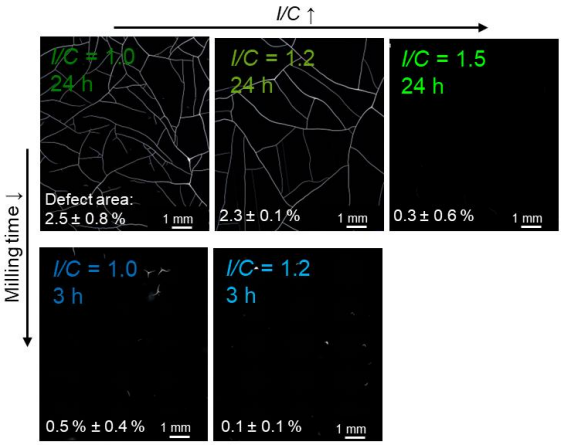

Figure 70: Crack pattern depending on the ionomer to carbon (*I/C*) ratio for inks processed for 3 and 24 h at 1000 rpm. An increased *I/C* leads to less cracks. [262]

9.5 Further experiments and considerations for Hypothesis 2

Influence of the film height on the selectivity in the beaker experiments

Without film-side mass transport resistances, film height should have no effect on drying selectivity. This statement is analyzed by comparing experiments with an initial film height of about 5 and 10 cm for solvent mixtures with $x_{1,0}$ = 40 and 81.5 wt% (Figure 71). The exact film height varies with the composition (see Eq. (3.1)). The initial sample weights were 50 and 100 g respectively. Drying conditions are the same ($NTU_{i,g} \rightarrow 0$). A small difference is the increased distance between the outlet of the dryer nozzle and the film surface. The composition of the films changes very similarly regardless of the initial liquid mass resp. height. Slight variations are within the limits of measurement inaccuracy.

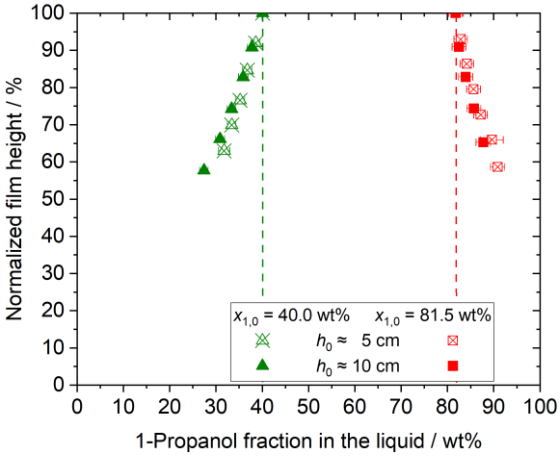

Figure 71: Influence of the (initial) film thickness h_0 on the selectivity of two exemplary 1-propanol/water mixtures with initial 1-propanol fraction of $x_{1,0}$ = 40.0 and 81.5 wt%. It seems that the height of the liquid column does not influence the selectivity. [190]

Proof of concept and accuracy tests of IMRS drying experiments without non-volatile component[5]

Investigating thin films need a new measurement setup and a different analysis. Therefore, in-situ and inverse micro Raman spectroscopy (IMRS) is applied (see Chapter 3.6). In a first step, the 1-propanol/water system is calibrated according to Schabel [231] at 25 °C with 2 – 5 s laser exposure ex-situ, i.e. outside of the dying process, in closed sample vials. The measuring time depends on the maximum Raman peak using one sample of known composition (highest 1-propanol content). The result is a calibration constant of $K_{1,2}$ = 4.97 with 1-propanol in relation to water. The next step is to evaluate the accuracy of the

[5] Results presented in this chapter are published as peer-reviewed article, available under a CC BY-NC 4.0 license, reproduced in accordance with author rights granted by Taylor & Francis: **Quarz P**, Janning L, Zimmerer N, Scharfer P, Schabel W. *Selective evaporation of solvent mixtures in thin films for fuel cell and electrolyser catalyst coatings.* Dry. Technol., 44(3), 346–355. https://doi.org/10.1080/07373937.2026.2616748, referred to in this work as [271].

solvent to solvent calibration (see Eq. (3.3)). For this purpose different solvent compositions are weighed, measured, and compared with their values from the initial weight and IMRS measurement using the identified calibration constant (Table 11). The results show a high accuracy with deviations below ± 0.52 wt%. This is more accurate than other Raman spectroscopic analyses of solvent mixtures in literature [239,241].

Table 11: Calibration analysis for Raman measurements of the binary solvent system at 25 °C (ex-situ up to 5 s exposure time). Weighted mass fractions of 1-propanol $x_{1,\mathrm{weighted}}$ are shown, as well as the corresponding predicted and from the calibration calculated composition from the Raman measurements $x_{1,\mathrm{IMRS}}$ incl. deviation D. For the aimed investigations these deviations are negligible. [271]

$x_{1,\mathrm{weighted}}$	$x_{1,\mathrm{IMRS}}$	$x_{1,\mathrm{IMRS}} - x_{1,\mathrm{weighted}}$ (D)eviation
wt%	wt%	wt%
0.00	0.00	0.00
4.82	4.91	+0.10
9.04	9.22	+0.17
16.65	16.89	+0.24
28.66	28.35	-0.32
37.62	37.81	+0.19
44.53	44.85	+0.32
49.89	50.41	+0.52
55.68	55.73	+0.05
62.48	62.51	+0.03
71.52	71.52	0.00

The previous IMRS measurements were performed ex-situ with closed sample vial. For the actual in-situ drying experiments, shorter laser exposure times (1 s) are required for accurate resolution. Schabel [231] postulated that ex-situ results for polymer films can be transferred to in-situ measurements. To evaluate this for the 1-propanol/water system, the same samples are measured with longer ex-situ laser exposure times and shorter in-situ exposure times in the reservoir used later in the drying tests. A very good transferability is found

with a deviation between 0.2 and 1.2 wt% (Table 12). The in-situ drying experiments can be analyzed with a high quantitative accuracy.

Table 12: Transferability from the ex-situ calibration measurements to the in-situ drying experiments. The deviation D is between 0.2 and 1.2 wt%, meaning the solvent composition is quantitatively determined with high accuracy in-situ during drying. [271]

$x_{1,\mathrm{ex-situ}}$	$x_{1,\mathrm{in-situ}}$	$x_{1,\mathrm{in-situ}} - x_{1,\mathrm{ex-situ}}$ $(D)eviation$
wt%	wt%	wt%
28.28	27.73	-0.54
50.31	49.09	-1.23
71.62	71.42	-0.20

Concentration profile in a non-selectively drying 1-propanol/water composition

The solvent composition within a thin film of a 1-propanol/water mixture is measured with inverse micro Raman spectroscopy (IMRS). Figure 72 shows deep scans of the arheotropic composition without integral composition changes at distinct times during film drying. If the integral composition remains constant, then the composition at different heights within the film is also expected to remain constant. This is expected because an depletion of one composition is needed as an driving force for an accruing gradient. Accordingly, the observed compositions are all constant over the height.

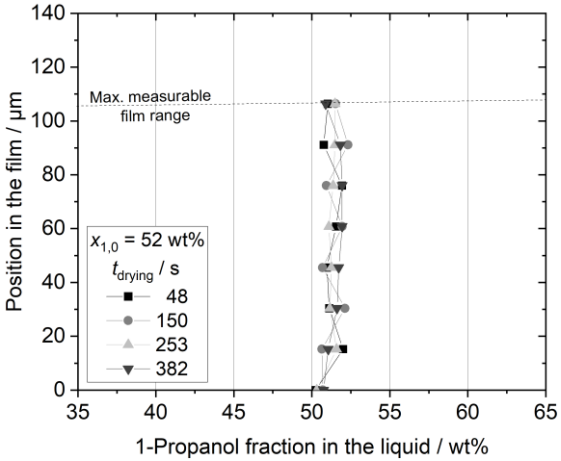

Figure 72: Liquid compositions in the film (along the film height) for an overall non-selectively drying mixture ($x_{1,0}$ = 52 wt%) at different drying times. With increasing drying time the integral and local compositions keep constant. For the first time it is experimentally shown that there are no concentration profiles over the film height. [271]

9.6 Further experiments and considerations for Hypothesis 3

Double-sided membrane direct coating

Finally, the coating of the whole catalyst-coated membrane (CCM) with both electrodes is in focus of the investigation. To differentiate between the first and second sides more easily, the terms "anode" and "cathode" are used below. Note that this assignment does not necessarily refer to the final type of electrode they will be used for. After producing the first catalyst layer (cathode), the backing foil is peeled off and the second side (anode) is coated in the clamping setup (see Chapter 3.4). This produces a CCM that is directly coated on both sides. The experiments correspond to what is illustrated in Figure 44 II a) and III) regarding the occurring solvent mass flows from the ink after ink application.

The anode (second layer) is coated with the same ink, using the same coating and drying parameters as the cathode (first layer), in clamped mode (see Figure 8). No anomalies occur. Similar to the process of coating and drying the cathode without a backing foil (see Figure 48 and Figure 49), the membrane deforms during drying of the anode and then shrinks to its original size.

The focus is on coating quality, which is discussed in terms of cracks. Looking at the produced CCM, it is noticeable that there are almost no cracks in back-light illumination. This may seem surprising at first, but it is easy to explain. Therefore in Figure 73, a CCM with offset of the first layer is shown. The left side of the image shows the membrane with a single catalyst layer applied to one side (cathode), whereas the right side shows the membrane after coating on both sides (CCM). While some defects are visible in the single catalyst layer, there are noticeably fewer cracks in the area of the CCM (overlapping layers). It seems unlikely that the defects on the first side will simply disappear as a result of subsequent process steps. Instead, for the CCM the back-light illumination for crack analysis is no longer suitable to make the defects visible. To be visible as white areas in the back-light, two defects must overlap. In most cases, however, a defect is covered by an intact area in the opposite layer. With an assumed defect rate of approx. 1 % on both sides, there is a mathematical probability of 0.01 % that two defects will overlap. This is the main reason why the CCM appears to nearly crack-free in the back-light illumination.

In consequence, microscopic analysis with top illumination is carried out on the CCM to examine cracks in detail, independently of the underlying layers. Initially, the focus is on the cathode first layer applied, the cathode. Therefore a layer is coated on the membrane with backing foil first. This one was deliberately made slightly thinner (4.7 ± 1.8 µm) than previous coatings. The purpose of this adjustment was to reduce the defects and make them easier to identify after the second coating had been applied. Two characteristic sections of the layer with cracks are shown in Figure 74. These have a good recognition value in the further examination. As expected, the analysis revealed the presence of cracks, particularly concentrated around agglomerates. The

agglomerates appear slightly darker in the top-light illumination than the surrounding area due to the different distance from the microscope.

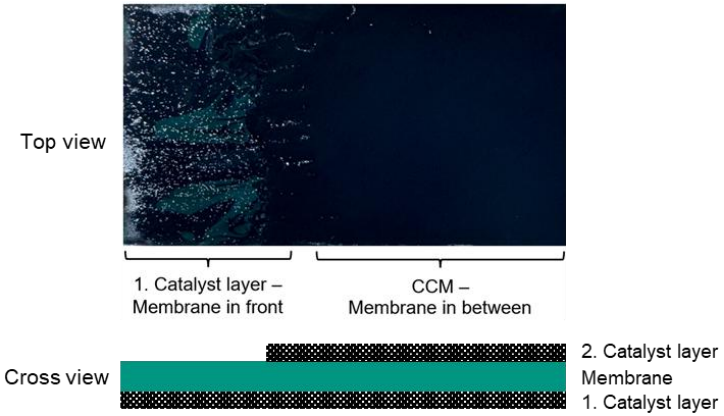

Figure 73: Crack pattern of a CCM coated on both sides including an offset only showing one coating (offset on the left) and the entire CCM (overlap on the right) photographed with back-light illumination. Only some defects are observable white. The other layer usually covers cracks in the CCM area. The schematic cross view of the CCM is shown below.

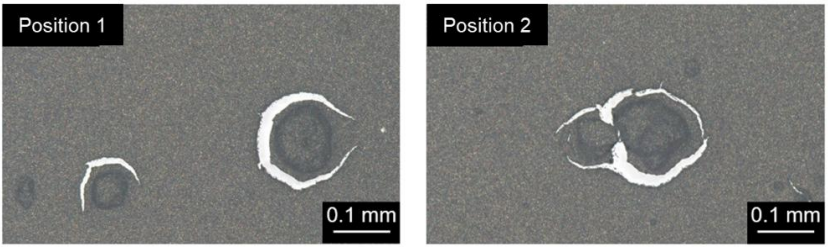

Figure 74: Microscopic images of the cracks in two different positions (Position 1, Position 2) on the first side of a CCM (with the backing foil underneath) before coating the second side on the back of the membrane. The images are taken in top-light illumination. As previously observed, agglomerates are the nuclei for cracks.

The second side (anode) is coated directly onto the membrane and then examined. The anode, exhibits no visible cracks (Figure 75). Despite this layer is slightly thicker (6.7 µm) than the first, it remains crack-free. Even the agglomerate observed at the bottom left does not lead to cracks. This crack-free pattern aligns with the single layer on the membrane without backing foil (see Figure 47), suggesting the first layer does not influence the second coating. The more important factor for reducing cracking is the freedom of movement of the membrane.

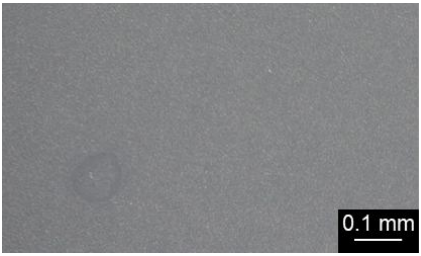

Figure 75: Microscopic image of the second coated electrode of a CCM in top-light illumination. Almost no cracks are observed.

The question arises whether the second coating affects the first layer. Due to the high solvent absorption of the membrane, the membrane could deform and break the dried first catalyst layer on its back. However, it is also possible that the solvent could penetrate through the membrane into the first layer and partially dissolve it. To investigate the consequences on the crack pattern of the first layer, this is observed next.

Between the observation of the first layer before and after the application of the second layer, several intermediate steps take place, all of which can affect the first layer: Removing the backing foil, coating the opposite side with a doctor blade (resulting in solvent contact), and an additional drying step are also part of the CCM manufacturing process.

The two areas (Position 1 and Position 2) previously inspected after the first coating (see Figure 74) are now inspected again after the direct coating of the

second layer (Figure 76). Comparing the images taken before and after the second coating reveals that the crack morphology was maintained. The differences in the brightness of the cracks are probably due to changes in the exposure and, above all, reflection properties of the membrane with and without the first layer underneath. Even with further processing, potential solvent contact from the anode coating and increased stress, the cracks in the cathode do not grow. (The central white areas within the circular agglomerates (darker circles) are not defects but the peaks of these agglomerates.)

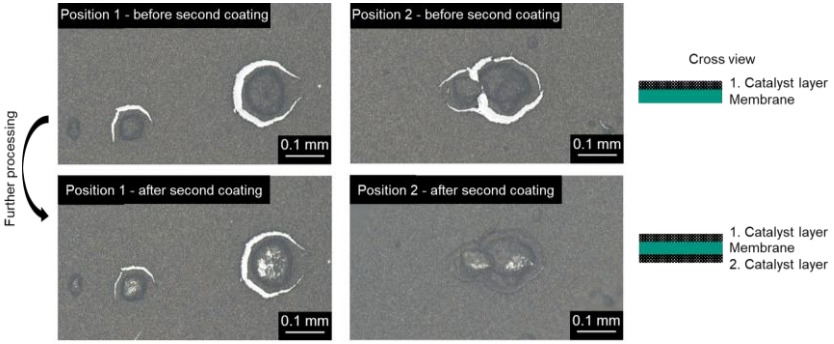

Figure 76: Microscopic images of cracks at different positions 1 and 2 on the first catalyst layer of a CCM before and after coating the second side of the membrane in top-light illumination.

Appling tensile stresses on the membrane

If the backing foil is removed, the stress on the membrane changes in the free-hanging setup (see Chapter 3.4) due to different tensile stresses. Less material is exposed to the same web tension. This may affect the resulting crack pattern. In general, the influence of tensile stress is also important for an industrial roll-to-roll (R2R) process.

In order to investigate this parameter, different tensile stresses were applied to the substrate. The application aimed to achieve a lower web tension (LWT) below typical levels of R2R systems and a higher web tension (HWT) that represents industrial web tensions. Web tensions vary depending on the system

and cannot be generalized. An R2R coating system from the Fraunhofer IPA, which can be operated at a tensile force starting at 10 N with a substrate width of 200 mm [282], serves as reference (50 N m^{-1}). Since the substrate width in these tests was about 100 mm, a minimum of 5 N of tensile force was required to achieve higher web tension for an accurate comparison. This is implemented by suspending different weights (70 g and 570 g) from the membrane. Assuming no frictional losses in the deflection roller, the weight force divided by the substrate width gives the web tension (Eq. (9.10)). To take account of the two different substrate thicknesses, the web tension is divided by their thicknesses and the tensile force is related to the cross-sectional area of the substrate (Eq. (9.11)). Tensions, here up to 116 N cm^{-2}, are in the elastic range of a (dry) NR212 membrane which is up to around 1400 N cm^{-2} [283]. However, this decreases significantly in solvent-swollen membranes. For example, the E-moduli of a N115 Nafion membrane were measured as 221 MPa in the dry state, 160 MPa when swollen with water, 2.59 MPa in isopropanol, and 22.2 MPa when swollen with a 20 vol% solution of isopropanol and 80 wt% water [321]. The overview can be found in Table 13. In principle, it is expected that the membrane with backing foil can withstand higher mechanical stresses.

$$WT = \frac{m \cdot g}{w} \tag{9.10}$$

WT	Web tension per width in N cm^{-1}
m	Attached weight in g
g	Gravitational constant in m s^{-2}
w	Width of the substrate in mm

$$\sigma = \frac{m \cdot g}{w \cdot s_i} \tag{9.11}$$

σ	Tensile stress per cross area in N cm^{-2}
s_i	Thickness of the substrate in µm

Table 13: Data for determining the substrate width- and area-related higher (HWT) and lower (LWT) web tension of the membranes coated in this test setup with (M w/ S) and without (M w/o S) supporting backing foil.

	Membrane w/ support [6]		**Membrane w/o support**	
	M w/ S-LWT	**M w/ S-HWT**	**M w/o S-LWT**	**M w/o S-HWT**
Thickness / µm	126	126	51	51
Attached weight / g	70	570	70	570
Applied force / N	0.7	5.6	0.7	5.6
Web tension per width / N cm^{-1}	0.07	0.59	0.07	0.59
Web tension per total cross area / N cm^{-2}	5.75	47.79	14.23	115.87

[6] The web tension per width and per cross-sectional area is calculated using the entire substrate thickness (membrane and backing foil). It is possible that the backing foil receives most of the applied force/tension and that the membrane itself is only slightly affected by the applied tension. The following values would only have to be divided by 75 µm (thickness of the backing foil) instead of 126 µm. This would make the values 1.68 times higher than specified. Compared to values without a backing foil (M w/o S), however, they would still be smaller.

9.7 Information on works linked to this thesis and the author

Publications

(1) **Quarz P**, Janning L, Zimmerer N, Scharfer P, Schabel W. *Selective Evaporation of Solvent Mixtures in Thin Films for Fuel Cell and Electrolyser Catalyst Coatings*. Dry. Technol., 44(3), 346–355. https://doi.org/10.1080/07373937.2026.2616748.

(2) Zimmerer N, **Quarz P**, Janning L, Scharfer P, Schabel W. *In-situ investigation of crack formation during drying of catalyst layers for polymer electrolyte membrane (PEM) fuel cells and electrolyzer*. Colloids and Surfaces A: Physicochemical and Engineering Aspects 2026;728:138807. https://doi.org/10.1016/j.colsurfa.2025.138807

(3) **Quarz P**, Zimmerer N, Janning L, Steck A-M, Scharfer P, Schabel W. *Ink Processing and its Influence on Particle Size Distribution, Ionomer Requirements and Electrode Properties in Polymer Electrolyte Membrane Fuel Cell and Electrolyzer Catalyst-coated membranes*. Energy Tech 2025:e202501844. https://doi.org/10.1002/ente.202501844.

(4) Rojas-Núñez C, **Quarz P**, Gracia-Medrano-Bravo VA, Kapp J, Käufer F, Sommer T, Kreyschenulte C, Lukassek V, Scharfer P, Wartmann J, Schabel W, Kuth A. *Novel In-Liquid-Plasma Synthesis and Coating Process for Graphene-Coated Perfluorosulfonic Acid-Based Membranes for Application in High-Performance Direct Methanol Fuel Cells*. Energy Tech 2025:e202501447. https://doi.org/10.1002/ente.202501447.

(5) Zimmerer N, **Quarz P**, Terhorst E, Janning L, Scharfer P, Schabel W. *Influence of Ink Formulation and Drying Parameters on Component Composition during Drying of Catalyst Layers for Polymer Electrolyte Membrane Fuel Cells and Electrolyzers*. Energy Tech 2025:2500516. https://doi.org/10.1002/ente.202500516.

(6) Zimmerer N, **Quarz P**, Janning L, Risinger J, Scharfer P, Schabel W. *Processing of hierarchically structured electrodes with varying catalysts for PEM fuel cells*. Wasserstofftechnologien. Effizient produziert., vol. 1, Chemnitz, Germany: Verlag Wissenschaftliche Scripten; 2024, p. 204–21. https://doi.org/10.60687/2025-0067.

(7) **Quarz P**, Zimmerer N, Janning L, Mannes F, Scharfer P, Schabel W. *From Decal coating to membrane direct coating in catalyst-coated membrane (CCM) production*. Wasserstofftechnologien. Effizient produziert., vol. 1, Chemnitz, Germany: Verlag Wissenschaftliche Scripten; 2024, p. 135–44. https://doi.org/10.60687/2025-0065.

(8) **Quarz P**, Zimmerer N, Scharfer P, Schabel W. *About drying phenomena of fuel cell and electrolyzer CCM inks: selectivity of the evaporation of 1-propanol/water mixtures*. Wiley Fuel Cells 2024;24:108–21. https://doi.org/10.1002/fuce.202300252.

(9) **Quarz P**, Zimmerer N, Steck A-M, Scharfer P, Schabel W. *Carbon Nanotubes (CNT) as an additive towards crack-free catalyst-coated membranes (CCM)*. Int J Hydrogen Energy 2024;57:789–97. https://doi.org/10.1016/j.ijhydene.2024.01.049.

(10) Schmidt D, Gartner P, Berezkin I, Rudat J, Bilger M, Grünert T, Zimmerer N, **Quarz P**, Scharfer P, Brückel J, Jung A, Singh P, Pooja P, Maier B, Stahlberger M, Schabel W, Bräse S, Lanze G, Nestrov-Mueller A. *Selective Peptide Binders to the Perfluorinated Sulfonic Acid Ionomer Nafion*. Adv Funct Materials 2024;34:2214932. https://doi.org/10.1002/adfm.202214932.

(11) Gartner P, Lanza G, Rudat J, Bilger M, Grünert T, Nesterov-Mueller A, Zimmerer N, **Quarz P**, Scharfer P, Schabel W, Jung A, Stahlberger M, Bräse S. *Self-healing Fuel Cells by Biological Actuators*. Procedia CIRP 2023;116:161–6. https://doi.org/10.1016/j.procir.2023.02.028.

(12) Ma L, Zimmerer N, Schäfer J, **Quarz P**, Heckmann T, Scharfer P, Schabel W, Fleischer J. *Investigation on a micro-environment concept for MEA production process supported by numerical simulations* 2022. https://nbn-resolving.org/urn:nbn:de:bsz:ch1-qucosa2-764450.

Conference contributions

(1) **Quarz P**, Zimmerer N, Janning L, Scharfer P, Schabel W. *Influences of process parameters in the membrane direct coating of catalyst-coated membranes for PEM fuel cells* (**Talk**) European Coating Symposium (ECS), 16. – 18.09.2025, A Coruña, Spain

(2) **Quarz P**, Zimmerer N, Janning L, Scharfer P, Schabel W. *From Decal Coating to Membrane Direct Coating in Catalyst-coated*

membrane (CCM) Production (**Talk**) Fuel Cell Conference Chemnitz (FC³), 12. – 13.11.2024, Chemnitz, Germany

(3) **Quarz P**, Zimmerer N, Scharfer P, Schabel W. *Mass transport phenomena in decal and membrane direct coating in fuel cell CCM production* (**Talk**) International Coating Science and Technology Symposium (ISCST), 08. – 11.09.2024, Atlanta, USA

(4) **Quarz P**, Zimmerer N, Scharfer P, Schabel W. *Optimization potentials during production of catalyst layers for PEM fuel cells and electrolysers* (**Poster**) International Coating Science and Technology Symposium (ISCST), 08. – 11.09.2024, Atlanta, USA

(5) **Quarz P**; Zimmerer N; Scharfer P; Schabel W. *Processing of catalyst-coated membranes for fuel cell applications* (**Talk**) 8th Thin Film Technology Forum, 06. – 07.06.2024, Karlsruhe, Germany

(6) Zimmerer N; **Quarz P**; Scharfer P; Schabel W. *Crack formation during drying of catalyst layers for PEM electrolysis* (**Talk**), DECHEMA Jahrestagung Trocknungstechnik, 11. – 13.03.2024, Magdeburg, Germany

(7) Zimmerer N, **Quarz P**, Scharfer P, Schabel W. *Mass Transport Phenomena During Production of Catalyst Layers for PEM Fuel Cells and PEM Electrolysis* (**Poster**), DECHEMA Jahrestagung Trocknungstechnik, 11. – 13.03.2024, Magdeburg, Germany

(8) **Quarz P**, Zimmerer N, Scharfer P, Schabel W. *Challenges in membrane direct coating in fuel cell production* (**Talk**), European Coating Symposium (ECS), 13. – 15.09.2023, Paris, France

(9) **Quarz P**, Zimmerer N, Scharfer P, Schabel W. *About the production of catalyst layers for PEM fuel cells and PEM electrolysis* (**Poster**), European Coating Symposium (ECS), 13. – 15.09.2023, Paris, France

(10) **Quarz P**, Zimmerer N, Scharfer P, Schabel W. *Advances in processing of catalyst-coated membranes (CCM) for PEM electrolysis* (**Talk**), International Conference on Electrolysis (ICE), 27.08. – 01.09.2023, Sun City, South Africa

(11) **Quarz P**, Zimmerer N, Scharfer P, Schabel W. *Catalyst-coated membranes for fuel cell applications* (**Talk**), 7th Thin Film Technology Forum, 06. – 07.07.2023, Karlsruhe, Germany

(12) **Quarz P**, Zimmerer N, Scharfer P, Schabel W. *Selective Drying Phenomena of Fuel Cell CCM Inks* (**Poster**), Ulm Electro Chemical Talks (UECT), 14. – 15.06.2023, Ulm, Germany

(13) Zimmerer N, **Quarz P**, Scharfer P, Schabel W. *Approaches for the Structural Optimisation of Catalyst Layers for PEM Fuel Cells* (**Poster**), Ulm Electro Chemical Talks (UECT), 14. – 15.06.2023, Ulm, Germany

(14) Zimmerer N; **Quarz P**; Scharfer P; Schabel W. *About the structural optimization of catalyst layers for fuel cells and electrolyzers* (**Poster**), 10th Annual Conference of the KIT Center for Energy, 10.05.2023, Karlsruhe, Germany

(15) **Quarz P**, Zimmerer N, Scharfer P, Schabel W. *Influence of Mass Transport During Processing of Catalyst-coated membranes (CCM) for PEM Fuel Cell Applications* (**Talk**), Jahrestreffen der ProcessNet-Fachgruppe Wärme- und Stoffübertragung, 06. – 08.03.2023, Frankfurt, Germany

(16) **Quarz P**, Zimmerer N, Scharfer P, Schabel W. *Influence of Formulation and Processing on Membrane Direct Coating of Catalyst-coated membranes (CCM)* (**Talk**), International Coating Science and Technology Symposium (ISCST), 11. – 14.09.2022, Minneapolis, USA

(17) **Quarz P**, Zimmerer N, Scharfer P, Schabel W. *About the procedural optimization of CCM production for PEM-FC and PEM-WE* (**Poster**), International Coating Science and Technology Symposium (ISCST), 11. – 14.09.2022, Minneapolis, USA

(18) **Quarz P**, Zimmerer N, Scharfer P, Schabel W. *Mass Transfer During Fabrication of Catalyst-coated membranes (CCM) for Polymer Electrolyte Membrane (PEM) Fuel Cells or Water Electrolysis* (**Talk**), Forum Annual Meeting on Reaction Engineering and ProcessNet Subject Division Heat and Mass Transfer, 18. – 20. 09.2022, Würzburg, Germany

(19) Zimmerer N, **Quarz P**, Scharfer P, Schabel W. *About the mass transport during drying of structural optimized Catalyst-coated membranes for PEM water electrolysers* (**Poster**), Forum Annual Meeting on Reaction Engineering and ProcessNet Subject Division Heat and Mass Transfer, 18. – 20.09.2022, Würzburg, Germany

(20) Ma L, Zimmerer N, Schäfer J, **Quarz P**, Heckmann T, Scharfer P, Schabel W. Fleischer J, *Investigation on a micro-environment concept for MEA production process supported by numerical simulations* (**Talk/Paper**), Fuel Cell Conference Chemnitz (FC³), 31.05. – 01.06.2022, Chemnitz, Germany

(21) **Quarz P**, Zimmerer N, Scharfer P, Schabel W. *Influence of formulation and processing on membrane direct coating of catalyst-coated membranes (CCM)* (**Poster**), European Hydrogen Energy Conference (EHEC), 18. – 20.05.2022, Madrid, Spain

(22) **Quarz P**, Zimmerer N, Scharfer P, Schabel W. *Catalyst-coated membranes for fuel cell applications* (**Talk**), 6th Thin Film Technology Forum, 12. – 13.05.2022, Karlsruhe, Germany

(23) **Quarz P**, Gracia V, Kruth A, Wartmann J, Scharfer P, Schabel W. *Graphene as a Diffusion Barrier for Direct Methanol Fuel Cells (DMFC)* (**Talk**), European Coating Symposium (ECS), 06. – 09.09.2021, Brussels, Belgium

(24) **Quarz P**, Zimmerer N, Scharfer P, Schabel W. *Catalyst-coated membranes for fuel cell applications* (**Talk**), 5th Thin Film Technology Forum, 24. – 25.06.2021, Karlsruhe, Germany

(25) **Quarz P**, Gracia V, Merklein L, Kruth A, Wartmann J, Scharfer P, Schabel W. *Graphen als Diffusionsbarriere für die Direkt Methanol Brennstoffzelle* (**Poster**), Jahrestreffen der ProcessNet-Fachgruppe Wärme- und Stoffübertragung, 24. – 26.02.2021, Online

(26) **Quarz P**, Gracia V, Merklein L, Kruth A, Wartmann J, Scharfer P, Schabel W. *Graphen als Diffusionssperre für die Direkt Methanol Brennstoffzelle* (**Poster**), ProcessNet Jahrestagung, 21. – 24.09.2020, Online

(27) **Quarz P**, Gracia V, Merklein L, Kruth A, Wartmann J, Scharfer P, Schabel W. *Graphenbeschichtungen als Diffusionssperre für*

Membranen für die Direkt Methanol Brennstoffzelle (**Poster**), Jahrestreffen der ProcessNet-Fachgruppe Wärme- und Stoffübertragung, 12. – 13.03.2020, Erfurt, Germany

Awards in context of this thesis

(1) NEO 2023 donated with 20,000 € (finalist, Top 5), the Innovation Award of the TechnologieRegion Karlsruhe, "BioHealing – Selbstheilende Brennstoffzelle", 30.11.2023, Waldbronn, Germany
(2) "Neuland" KIT Idea Award (3rd Place), "BioHealing – Selbstheilende Brennstoffzelle", 06.06.2022, Karlsruhe, Germany
(3) Poster Award (1st Place) of the EnBW Stiftung at the 10th Annual Conference of the KIT Center for Energy, *About the structural optimization of catalyst layers for fuel cells and electrolyzers*, 10.05.2023, Karlsruhe, Germany.

About the author

Philipp Quarz graduated in Chemical Process Engineering at the Karlsruhe Institute of Technology (KIT) in 2019, focusing on food process engineering and product design. During his studies, he specialized in the rheology of particulate suspensions and product-oriented processing. In 2019, he joined the research group Thin Film Technology (TFT) at KIT as a research assistant.

His PhD research focused on fuel cell and electrolyzer MEA processing, specifically catalyst ink processing, membrane direct coating, and solvent evaporation. He independently applied for and managed industrial and publicly funded projects and presented his results at international conferences.

Furthermore, he was involved in teaching, leading exercises and practical courses for *Thermal Mass Transport Processes* and *Mass Transfer 2*, including exam design and grading. In addition to supervising 15 Bachelor's and eight Master's theses, he was actively responsible for organizing the *13th Short Course "Coating and Drying of Thin Films"* and the *6th "Thin Film Technology Forum"* in 2022. He completed his doctorate (Dr.-Ing.) in 2026.